SAPIENZA
UNIVERSITÀ DI ROMA

# Charge-density waves, quantum-anharmonicity, polar responses and resonant Raman in 1D conjugated systems

Scuola Dottorale "Vito Volterra"
Dottorato di Ricerca in Fisica (XXXVI cycle)

**Stefano Paolo Villani**
ID number 1723536

Advisor
Prof. Francesco Mauri

Co-Advisor
Dr. Paolo Barone

Academic Year 2022/2023

**Charge-density waves, quantum-anharmonicity, polar responses and resonant Raman in 1D conjugated systems**

Sapienza University of Rome



This thesis has been typeset by LaTeX and the Sapthesis class.

Author's email: s.p.villani@gmail.com

# Abstract

Systems with reduced dimensionality are known to display many fascinating phenomena, with properties often showing pathological behaviors. In this context, one of the most studied aspects regards the insurgence of a modulation of the electronic charge density, i.e. a charge density wave (CDW). The interest in CDWs physics is extensive as they are present in many systems, ranging from 1D and 2D materials to high Tc superconductors and transition metal dichalcogenides. CDWs usually manifest as a broken-symmetry state, that in 1D chains of atoms results in a bond-length alternation, commonly explained as a consequence of the interplay between an instability of electronic origin and the coupling between electronic and lattice degrees of freedom. It is widely understood that the interplay of these elements in 1D systems regulates the competition between a dimerized, less symmetric, configuration and an undimerized, more symmetric, one. In particular, a diatomic chain of atoms presents a second-order phase transition between these two phases. However, apart from these two ingredients, many other different elements are actually at play in the creation of a CDW. Indeed, there is evidence that the presence of a CDW in the infinitely long straight chains of carbon atoms, called carbyne, is strongly affected by quantum and anharmonic fluctuations, as well as from the effect of an external environment, as we confirm and discuss in our study. The aim of the present work is thus, on one hand, to unveil the contribution of each element to the manifestation of a CDW, and, on the other hand, to study the properties of 1D systems that host CDWs. Indeed, the instability at the boundaries of the structural phase transition suggests the presence of interesting and peculiar polar responses. Following this idea, in our work, we show how 1D systems such as conjugated polymers present a huge enhancement of the effective charges, with values up to 30 times that of the nominal electronic charge at the critical point of the transition, and of the piezoelectric coefficients, which in principle present a diverging behavior in proximity of the phase boundary. In determining the properties of these materials, it is then fundamental to resort to particular experimental techniques, such as resonance Raman spectroscopy. However, to date, a theory that permits accurately describing experimental results on 1D systems is lacking. We address this problem in our work, introducing a framework that allows for the calculation of resonance Raman spectra beyond the commonly adopted Placzek approximation, even in systems beyond the simple 1D case.

# Contents

# Introduction and overview

In this work, we present and discuss our results regarding several properties of 1D conjugated systems. Each Chapter is devoted to a particular topic, which is introduced in detail before being addressed. Results and contents of Chapter 1 and Chapter 3 are partly adapted from our published work of Ref.[1]. Results and contents of Chapter 2, Chapter 4 and Chapter 5 are instead partly adapted from three different works, currently under preparation. In what follows, we introduce the main elements and concepts underlying the properties we focused on, and at the same time, we give an overview of the organization of this work, highlighting the relevant results.

The reason we decided to study 1D systems is that despite their apparent simplicity, they present a multitude of interesting phenomena, with properties often showing pathological behaviours due to the reduced dimensionality. Moreover, the advantage of dealing with 1D systems resides in the fact that it is particularly simple, yet effective, to catch the key elements at play in determining a certain property. Nevertheless, the conclusions one obtains, are often valid beyond the specific 1D case considered. This idea will be followed throughout the whole work, where the common thread among all chapters will be a simple tight-binding 1D toy-model. As we will see in what follows, with just a few parameters, this model correctly accounts for the main ingredients necessary to describe several 1D systems as well as to explain and predict their properties with accuracy comparable with DFT and experimental results.

One of the key aspects we address in the present work regards the physics of charge density waves (CDWs). CDWs are modulations of the electronic charge density distribution which manifest as broken symmetry states in materials, and, as such, are strictly related to their structural configuration. Understanding the properties of CDWs, and unveiling the mechanisms that concur to their manifestation, is one of the open problems of modern condensed matter physics, as CDWs are ubiquitous, even beyond simple 1D systems. To cite some of the most relevant cases, CDWs occur in systems ranging from 2D materials[2, 3] to high-$T_c$ superconductors[4] and transition metal dichalcogenides[5]. For this reason, in Chapter 1 we start with a review of some of the most relevant aspects of CDWs physics. In particular, with the aid of

the 1D model, we examine how different elements come into play. We will describe how Peierls electronic instability, together with the presence of a strong enough electron-lattice coupling compete with the presence of an atoms-equivalence breaking mechanism in these systems, resulting in a second-order structural phase transition between a less symmetric, dimerized structure, and a more symmetric, undimerized one, with a concomitant manifestation of CDWs with different characters. Even if the results we will discuss are peculiar to these 1D systems, the conclusions we present on the interplay between the key ingredients involved in the description of CDWs physics are valid beyond the 1D case.

As they are both related to the electronic density distribution and the structure of a system, the study of CDWs in 1D systems cannot be separated from the study of their polar properties. Indeed, it is argued that manifestations of broken symmetry states due to CDWs formations may result in ferroelectric behaviours, especially in low-dimensional materials or in materials with a strong coupling between electronic and lattice degrees of freedom, as in some layered superconductors[6] or transition metal dichalcogenides[7, 8, 9]. This is particularly true in the 1D systems we address, where the insurgence of a bond-centered CDW, concomitant with the second order structural phase transition, results in the manifestation of a ferroelectric behaviour, as we will discuss in Chapter 1. Polar properties of 1D systems, however, also present an interest *per se*. Indeed, as detailed in Chapter 1, in the framework of the model it is possible to show that these 1D systems offer the possibility for a concrete realization of the adiabatic charge transport mechanism of the Thouless pump[10], observed e.g. in ultracold fermions[11] and ultracold bosons[12].

Understanding the properties of 1D systems is relevant also for applications in the field of organic electronics. Indeed, conjugated polymers, which can be imagined as (quasi-)1D organic materials, are characterized by the presence of delocalized electrons along the backbone chain, resulting in many interesting and useful optical and electronic applications[13, 14, 15, 16]. The model adopted in this work perfectly describes the physics of delocalized electrons, offering a suitable playground to predict and interpret the properties of conjugated polymers, and in this sense we will talk about 1D conjugated systems. We follow this idea along all the present work, where we resort to specific conjugated polymers to test the predictions obtained in the framework of the model, or, vice-versa, we exploit the simplified and effective picture of the model to explain experimental or DFT results obtained on these materials. In particular, the main system we will address is carbyne, an infinitely-long straight chain of carbon atoms. Carbyne is, at the same time, a physical manifestation of a 1D CDW, with two competing phases characterized by different structures, and a conjugated polymer, thus incarnating the perfect system for our study.

Several recent works[17, 18, 19, 20] have established that in order to correctly describe the structural properties of many materials, it is paramount to correctly account for the quantum nature of the ions as well as for effects of anharmonicity in their interaction. In particular, this is true in the presence of light atoms, as

in carbyne and in conjugated polymers in general, or when a system is close to a displacive phase transition, such as a ferroelectric- or a CDW-instability, as in the 1D systems described by the model. For these reasons, in Chapter 2 we study the effects of quantum-anharmonicity on the structural properties of 1D conjugated systems in the framework of the model. In particular, with model's parameters fitted in order to describe the properties of carbyne, we study the role of quantum anharmonic effects in determining the character of the CDW in this polymer as well as the effects on the related second order structural phase transition.

Another interesting aspect of these 1D systems regards their polar response properties, i.e. those quantities that can be defined in terms of variation of polarization with respect to an external perturbation, as we discuss in Chapter 3. Indeed, the reduced dimensionality, the connection to the the topological phenomenon of the Thouless pump, and the presence of both a CDW- and a ferroelectric-instability, point to the presence of peculiar behaviours of polar responses. We will focus on two prototypical polar responses: the effective charges and piezoelectricity, which may be manifested in 1D systems if specific conditions are met, as in a dimerized chain with inequivalent atoms. As we describe in Chapter 3, in proximity to the critical point of the structural phase transition, both responses present a huge enhancement in the framework of the model. In order to test these hypotheses, we resort to DFT calculations on prototypical conjugated polymers, finding a striking agreement with the behaviour predicted by the model. The ultimate reason for this peculiar behaviour is to be found in the topological nature of effective charges enhancement, which guarantees its stability even against quantum-anharmonic effects.

After having assessed the importance of structural properties on the polar responses enhancement mechanism manifested in these 1D conjugated systems, it comes natural to ask how to determine these properties with experiments. In particular, obtaining information on systems configuration is essential for their characterization. For instance, the presence of dimerization in a 1D system with inequivalent atoms may result in the insurgence of properties, e.g. ferroelectricity or piezoelectricity, otherwise absent. In this task, one of the most used experimental techniques is vibrational Raman spectroscopy, based on the inelastic scattering of light with a vibrational quantum. Chapter 4 will be devoted to the study of the Raman response in 1D systems. In particular, we will describe different levels of approximations usually adopted in the theoretical description of Raman scattering. However, in order to correctly reproduce experimental results on 1D systems, we will see that, on one hand, it becomes essential to account explicitly for resonance effects due to the matching condition between the energy of the impinging laser and the energy of the transition between states of the system and, on the other hand, to even go beyond the commonly adopted Placzek approximation of neglecting the energetic contribution of the vibrational excitations involved in the scattering process.

In order to compute the resonant Raman response of a system beyond the Placzek approximation, it is however necessary to develop a novel theoretical framework.

This is the topic of the last Chapter 5, dedicated to the derivation of the time-dependent density matrix perturbation theory (TDDMPT), a technique that allows the computation of responses of a system with respect to an external perturbation at any given perturbative order. The central idea of this approach is to quantify the responses in terms of perturbation of the electronic density matrix, instead of the standard wave-function perturbation theories. In this way, we avoid gauge-dependence problems and have a well-defined framework to treat perturbations with respect to an external uniform electric field, a notoriously difficult task in periodic crystals due to the ill-definition of the position operator in terms of periodic Bloch-type wave-functions. Another advantage of this approach is that it gives a compact and elegant formulation for an ab-initio implementation in the framework of density-functional theory codes. For this reason, after having applied this approach to the calculation of the resonant Raman response beyond the Placzek approximation in the framework of the model (that does not require ab-initio codes), we focus on the implementation of the Raman response within the TDDMPT formalism in the Quantum ESPRESSO code and conclude presenting the related results.

# Chapter 1

# Structural and polar properties

## Chapter overview

Chapter 1 is organized as follows: first, in section 1.1 we give a brief overview of some of the most relevant aspects of 1D systems, such as Peierls transition and charge density waves, and how they are related to structural and polar properties. Then, in section 1.2 we introduce a model for 1D systems that we will refer to throughout all the present work. We discuss the structural properties of the model in section 1.2.1, focusing on the competition between a higher symmetric phase with equidistant atoms and a lower symmetric one where atoms are not equidistant. In section 1.2.2, we introduce electronic polarization in the model and discuss a peculiar polar-related property typical of these 1D systems: Thouless adiabatic charge pumping. Then, we discuss the relation between structural and polar properties of 1D systems in section 1.2.3. Finally, section 1.3 is dedicated to conjugated polymers, a class of organic materials that can be imagined as a physical realization of 1D chains. In particular, focusing on one of the simplest conjugated polymers – a linear chain of carbon atoms called carbyne – we fit model's parameters on ab-initio density functional theory (DFT) calculations in order to have a working model with a real counterpart for the following Chapters. Conclusions are drawn in section 1.4.

## 1.1 Introduction: one dimension, many properties

The theoretical description of physical systems with many interacting elements is a complex problem, often requiring approximations of some kind. The effectiveness of a given approximation depends on the balance between the accurate description of reality, namely of experimental results, and the reduction of complexity to a few key elements that account for and explain the underlying mechanisms at play. The main ingredients used in condensed matter physics to describe matters are electrons, nuclei and all their interactions – electrons with other electrons, nuclei with other nuclei and electrons with nuclei. The way we treat and mix these ingredients to create a *model*, determines the level and the goodness of the approximation. Over the years,

many models for 1D and quasi-1D materials have been introduced, allowing the description of different properties. What the vast majority of these models have in common, is that they are based on a simple description in terms of 1D linear chains of infinite length, where atoms may form bonds with their nearest neighbors only. In order to describe specific phenomena, one can then add different ingredients to this simple picture. Let's start considering the simplest case of a chain where all atoms are equivalent, e.g. because they are of the same atomic species and form the same bonds with other atoms. Since, apparently, there is no reason to distinguish one neighbor from the other, one could intuitively think that the optimal, stable, structure of such a system would be the one where all the atoms are equidistant. However, if we dig a little deeper, fascinating but less intuitive properties arise, as we discuss in what follows.

For the moment, let's neglect interactions between electronic and ionic degrees of freedom. In his seminal works[21, 22], Rudolf Peierls showed that when subject to an external periodic potential of wave number $q$, the electronic bands structure of a 1D chain of equivalent atoms presents a gap opening at the Fermi level $\pm k_{\mathrm{F}}$, if $q = 2k_{\mathrm{F}}$. The resulting modulation of the electronic charge density gives rise to what is usually called a *charge density wave* (CDW). This phenomenon is a consequence of an instability of electronic nature – also known as Peierls instability – typical of a 1D free-electron gas and highlighted by a divergence of the density-density Lindhard static response function at the Fermi-surface nesting condition $q = 2k_{\mathrm{F}}$[23], as shown in Figure ???. Now, if we consider each atom of the chain contributing with one valence electron, and neglect electron-electron interactions, a system with equidistant atoms would have a half-filled band and therefore be a metal. The Fermi-surface nesting condition $q = 2k_{\mathrm{F}}$ and the consequent opening of the gap, however, would make the system insulating. For this reason, this phenomenon is also a prototypical example of metal-insulator transition[24].

A part for electronic properties, the presence of a charge density modulation is also related to the structural properties of the system, i.e. on atoms' arrangement along the chain. Following the argument of Peierls, this becomes evident if we allow in the 1D chain with equivalent atoms for even an infinitesimally small coupling between electronic and lattice degrees of freedom, namely an electron-phonon (e-ph) coupling. Indeed, in this case, the opening of the gap in the electronic bands can be induced by a $2k_{\mathrm{F}}$ periodic lattice distortion, which acts as an external periodic potential. In this sense, the argument of Peierls predicts a structural transition with a spontaneous symmetry breaking signalled by a bond length alternation (BLA) in the chain, allowing the distinction between a shorter and a longer bond. As a consequence of the BLA, a $2k_{\mathrm{F}}$ modulation of the electronic density also arises, i.e., a CDW. The metal-insulator transition that occurs as a consequence of the periodic lattice distortion and the concomitant CDW is what characterizes the so-called Peierls transition. From its first theorization[22, 25], this phenomenon drew much interest and was later observed in many 1D systems, as in 1D conductors[26] or in

charge-transfer organic salts[27, 28]. However, the interest goes beyond 1D systems, as CDWs occur in many other different systems, from 2D materials[2, 3] to high-$T_c$ superconductors[4] and transition metal dichalcogenides[5]. For this reason, the understanding of this phenomenon is paramount in many different fields.

All the properties discussed above for a chain of equivalent atoms can be described in the framework of the well-known SSH model[29], a tight-binding model of non-interacting electrons, initially introduced by Su, Schrieffer, and Heeger to study solitons in polyenes chains, e.g. polyacetylene, as further discussed in section 1.3. For the sake of generalizing the descriptive power of the model, one can then take a step further and allow for the breaking of atoms equivalence. It is possible to do so, e.g., introducing an onsite energy term in the tight-binding description, allowing the distinction between an atom and its neighbors, or stated in other words, considering a chain with two inequivalent atoms alternating in space. Breaking atoms equivalence also determines the opening of a gap in the electronic bands structure, counteracting Peierls electronic instability and the formation of a CDW. The periodic lattice modulation, therefore, would now require the presence of a finite and strong enough e-ph coupling in order to manifest. It is possible to study the competition between these two gap-opening mechanisms in the framework of the Rice-Mele model, a generalisation of the SSH model introduced to study soliton excitations of linearly conjugated diatomic polymers[30]. In practice, this translates to studying the competition between a dimerized, lower symmetric structure, characterized by a BLA and a bond-centered charge density modulation consequence of the electronic instability, and an undimerized, higher symmetric structure, where all atoms are equidistant but inequivalent and a site-centered charge density modulation is present.

In addition to describing the physics of CDWs and Peierls transition, 1D chains have drawn also attention for their polar properties, becoming prototypical models for 1D ferroelectricity[31, 32]. This property is indeed strictly related to the structure of the chain in terms of symmetries. For ferroelectricity to manifest, a necessary condition is to break centrosymmetry in the chain, a requirement met, for example, in a chain with inequivalent atoms and in presence of BLA. From this point of view, it appears evident that the correct characterisation of ferroelectricity in a 1D system cannot be separated from the study of its structural properties. Moreover, polarization in 1D chains has been put forward as an example of manifestation of topological effects in condensed matter, as discussed e.g. for the quantization of the dipole moment in end charges of push-pull polymers[33], or for Thouless adiabatic charge transport[34, 35].

In conclusion, despite the apparent simplicity, 1D conjugated systems present an abundance of interesting phenomena. In what follows, we introduce the model for 1D conjugated systems that we will adopt for most of the present work and, in this framework, illustrate all the above mentioned effects, in order to provide a common ground as well as the notations for the next Chapters.

## 1.2 A model for 1D conjugated systems

In this section, we provide a detailed description of a diatomic-chain model, following the lines of Rice and Mele[30]. We consider an infinitely long, one-dimensional, linear chain made by the repetition of a unit cell, of length $a$, containing two atoms, one of type $A$ and the other of type $B$. Electronic properties of the system are described in a nearest-neighbors tight-binding approximation. We assume one electronic orbital per atom and adopt the notation $|\alpha, R\rangle$ to indicate that the orbital of atom $\alpha = A, B$ is located at $r_\alpha + R$, $R = na$ ($n \in \mathbb{Z}$) being the position of the atom's cell along the chain. Without loss of generality, we take $r_A = -a/4 + \delta r_A$ and $r_B = +a/4 + \delta r_B$. If $\delta r_\alpha = 0$, all atoms would be equidistant, so $\delta r_\alpha$ indicates the displacement of atom $\alpha$ from the position it would have in a chain with equidistant atoms. For simplicity, we consider longitudinal displacements only, parallel to the linear-chain direction. The basis set of the orbitals $\{|\alpha, R\rangle\}$ is orthonormal and it holds:

$$\langle \alpha, R \,|\, \alpha', R' \rangle = \delta_{\alpha,\alpha'} \delta_{R,R'}. \tag{1.1}$$

We define the onsite energy terms of the tight-binding electronic Hamiltonian $H_\mathrm{e}$ as

$$\langle A, R \,|\, H_\mathrm{e} \,|\, A, R' \rangle = -\langle B, R \,|\, H_\mathrm{e} \,|\, B, R' \rangle = -\Delta \delta_{R,R'}, \text{ with } \Delta \geq 0. \tag{1.2}$$

We want to take into account also the energetic contribution due to the overlap between an atom's orbital and the orbitals of its left and right nearest neighbors. In general, the overlap energy term between two electronic orbitals is a function of the distance $r$ between the atoms and is referred to as the hopping energy $-t(r)$, $t > 0$. For convenience, we indicate with $r_1$ the distance between atoms in the same cell and with $r_2$ the distance between neighboring atoms in adjacent cells, namely:

$$r_1 \equiv (r_B + R) - (r_A + R) = \frac{a}{2} + \delta r_B - \delta r_A, \tag{1.3}$$

$$r_2 \equiv (r_A + R) - (r_B + R - a) = \frac{a}{2} + \delta r_A - \delta r_B \tag{1.4}$$

and it holds $r_1 + r_2 = a$. We can now define the hopping energy between orbitals of atoms in the same cell $-t_1 \equiv -t(r_1)$ and the hopping energy between atoms in adjacent cells $-t_2 \equiv -t(r_2)$. With the same notation of Equation (1.2) we write:

$$\langle A, R \,|\, H_\mathrm{e} \,|\, B, R' \rangle = \langle B, R' \,|\, H_\mathrm{e} \,|\, A, R \rangle^* = -t_1 \delta_{R,R'} - t_2 \delta_{R-a,R'}. \tag{1.5}$$

We define, using Equation (1.3) and (1.4), an adimensional fractional coordinate $u$:

$$u = \frac{r_1 - r_2}{a} = \frac{\delta r_B - \delta r_A}{a/2}. \tag{1.6}$$

This term quantifies deviations of the relative displacement of atoms $A$ and $B$ from the equally spaced chain ($u = 0$), allowing us to express bond lengths with the

following compact expression:

$$r_i = \frac{a}{2}\left[1 + (-1)^{i+1}u\right],\ i = 1, 2. \tag{1.7}$$

With the above definitions, at linear order in atoms' displacement we have

$$t_i = t(r_i) \simeq t\left(\frac{a}{2}\right) + \left.\frac{\mathrm{d}t}{\mathrm{d}r}\right|_{\frac{a}{2}} \cdot \left(r_i - \frac{a}{2}\right), \tag{1.8}$$

which allows us to define the two terms

$$t = \frac{t_1 + t_2}{2} = t\left(\frac{a}{2}\right), \tag{1.9}$$

$$\delta t = \frac{t_1 - t_2}{2} = -\left.\frac{\mathrm{d}t}{\mathrm{d}r}\right|_{\frac{a}{2}} \cdot \frac{a}{2}u. \tag{1.10}$$

The former term $t$ quantifies the hopping energy that equidistant atoms would have while the latter term $\delta t$ describes the variation with respect to $t$ caused by atoms' relative displacement. At linear order in atoms' displacement it holds:

$$\delta t = -t\beta u, \tag{1.11}$$

where we defined the adimensional parameter $\beta > 0$ as

$$\beta = -\frac{a}{2t}\left.\frac{\mathrm{d}t}{\mathrm{d}r}\right|_{\frac{a}{2}}. \tag{1.12}$$

This term quantifies the variation of the hopping energy due to a variation of the distance between the atoms and as such it acts as an electron-phonon coupling term. A schematic representation of the model is shown in Figure 1.1. We notice that if $\Delta = 0$, namely if the atoms are equivalent, we recover the SSH model[29, 36].

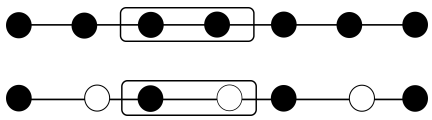

**Figure 1.1.** Two representative diatomic chains described by the tight-binding model are shown. The unit cell, which contains two atoms and has length $a$, is highlighted for both. In the chain on the top, atoms are both equivalent and equidistant. In the model this is described by an onsite energy difference $\Delta = 0$ and equal hopping energies $-t$. Moreover, since the bond lengths are equal, it holds $u = (r_1 - r_2)/a = 0$, where $r_1$ and $r_2$ are the distances between atoms in the same unit cell or in adjacent unit cells, respectively. In the chain on the bottom, atoms are inequivalent (onsite energy difference $\Delta \neq 0$) and there is a bond length alternation with $r_1 \neq r_2$, implying $u \neq 0$. In this sense, $u$ is an adimensional parameters that quantifies atoms displacement with respect to the positions they would have if they were equidistant. The presence of bond length alternation is also reflected by different hopping energies $-t_1$ and $-t_2$, which can be related to $u$ via an electron-phonon coupling parameter $\beta$, as described in the text.

### 1.2.1 Structural properties: second order phase transition

As we are interested in the structural properties at $T = 0\ K$, we study the total energy per unit cell $E_{\text{tot}}(u) = E_{\text{L}}(u) + E_{\text{e}}(u)$, where $E_{\text{L}}(u)$ and $E_{\text{e}}(u)$ are the lattice and electronic contribution, respectively. In particular, we aim to characterize the behaviour of the optimal displacement $\overline{u}$, defined as the one which minimizes $E_{\text{tot}}(u)$ given a set of material-dependent parameters. Lattice dynamics being neglected, we write the lattice contribution, which accounts for the displacement of the atoms with respect to their position in a uniformly spaced chain:

$$E_{\text{L}}(u) = \frac{1}{2}\text{K}\left(\delta r_A - \delta r_B\right)^2 + \frac{1}{2}\text{K}\left(\delta r_B - \delta r_A\right)^2 = \frac{1}{4}\text{K}a^2u^2, \tag{1.13}$$

where we used Equation (1.6) and K is an elastic constant term.

To compute the electronic energy per unit cell $E_{\text{e}}(u)$, we imagine the linear chain as made of $N$ copies of the unit cell and adopt periodic boundary conditions. This allows us to define a basis $\{|\alpha, k\rangle\}$ in the reciprocal $k$-space:

$$|\alpha, k\rangle \equiv \sum_R \frac{\text{e}^{\text{i}(r_\alpha + R)k}}{\sqrt{N}} |\alpha R\rangle\,, \tag{1.14}$$

where $k$ is defined over the first Brillouin zone, namely

$$k = \frac{n}{N}\frac{2\pi}{a}, \quad n = 0, \pm\frac{1}{2}, \pm 1, \ldots, \pm\frac{N}{2}, \tag{1.15}$$

and it holds

$$\langle \alpha', k' \,|\, \alpha k\rangle = \delta_{\alpha,\alpha'}\delta_{k,k'}. \tag{1.16}$$

From Equation (1.2), (1.5) and (1.14) we obtain the matrix elements of the electronic Hamiltonian in the reciprocal space:

$$\langle A, k \,|\, H_{\text{e}} \,|\, A, k'\rangle = -\Delta\delta_{k,k'}, \tag{1.17}$$

$$\langle B, k \,|\, H_{\text{e}} \,|\, B, k'\rangle = \Delta\delta_{k,k'}, \tag{1.18}$$

$$\langle A, k \,|\, H_{\text{e}} \,|\, B, k'\rangle = -\left[t_1 \text{e}^{\text{i}\frac{a}{2}k}\text{e}^{\text{i}k(\delta r_B - \delta r_A)} + t_2\text{e}^{-\text{i}\frac{a}{2}k}\text{e}^{\text{i}k(\delta r_B - \delta r_A)}\right]\delta_{k,k'} \tag{1.19}$$

$$\equiv -T_k\delta_{k,k'}, \tag{1.20}$$

$$\langle B, k \,|\, H_{\text{e}} \,|\, A, k'\rangle = \langle A, k' \,|\, H_{\text{e}} \,|\, B, k\rangle^* = -T_k^*\delta_{k,k'}. \tag{1.21}$$

The above results allow to write in the reciprocal space basis a $2 \times 2$ electronic Hamiltonian matrix $H_{\text{e},k}$ for each $k$-point:

$$H_{\text{e},k} = \begin{pmatrix} -\Delta & -T_k \\ -T_k^* & \Delta \end{pmatrix}. \tag{1.22}$$

Diagonalising the matrix of Equation (1.22) we find the eigenvalues

$$\varepsilon_k^{\pm} = \pm\sqrt{\Delta^2 + |T_k|^2} \tag{1.23}$$

with the respective eigenvectors, namely the Bloch wave-functions

$$|\psi_k^{\pm}\rangle = \begin{pmatrix} \frac{\pm\left(\varepsilon_k^{\pm}-\Delta\right)}{\sqrt{\left(\varepsilon_k^{\pm}-\Delta\right)^2+|T_k|^2}} \\ \frac{-T_k^*}{\sqrt{\left(\varepsilon_k^{\pm}-\Delta\right)^2+|T_k|^2}} \end{pmatrix}, \tag{1.24}$$

where using Equation (1.9), (1.10) and 1.19 we have that

$$|T_k|^2 = 4t^2\cos^2 k\frac{a}{2} + 4\delta t^2 \sin^2 k\frac{a}{2}. \tag{1.25}$$

For each $k$-point, Equation (1.23) allows to distinguish between a lower and a higher energy level, indeed, as shown in Figure 1.2, the chain present two energy bands. We assume that only the lower energy band is filled with electrons and will hereafter refer to it as the occupied – or valence – band, in contrast with the unoccupied – or conduction – higher energy band. From Equation (1.23) we obtain the value of the energy gap $E_{\text{gap}}$ between the occupied and unoccupied band:

$$E_{\text{gap}} = \sqrt{(4\delta t)^2 + (2\Delta)^2}. \tag{1.26}$$

Aiming for the total energy, we consider the contribution of all the occupied states to the electronic energy per unit cell. In particular it holds

$$E_{\text{e}} = \frac{2}{N}\sum_k \varepsilon_k^- = -\frac{2}{N}\sum_k \sqrt{\Delta^2 + 4t^2\cos^2\frac{ka}{2} + 4\delta t^2\sin^2\frac{ka}{2}} \tag{1.27}$$

where the factor of 2 accounts for the spin degeneracy. In the limit of an infinite linear chain, namely for $N \to +\infty$, the eigenvalues and the eigenvectors' coefficients become continuous functions of $k$ and the sum becomes an integral over the first Brillouin zone:

$$E_{\text{e}} = -2a\int_{-\pi/a}^{\pi/a}\frac{\mathrm{d}k}{2\pi}\sqrt{\Delta^2 + 4t^2\cos^2\frac{ka}{2} + 4\delta t^2\sin^2\frac{ka}{2}}. \tag{1.28}$$

Finally, using Equation (1.11), (1.13) and (1.28), we write the total energy per unit cell as a function of the fractional coordinate $u$:

$$E_{\text{tot}}(u) = \frac{1}{4}\mathrm{K}u^2a^2 - 2a\int_{-\pi/a}^{\pi/a}\frac{\mathrm{d}k}{2\pi}\sqrt{\Delta^2 + 4t^2\cos^2\frac{ka}{2} + 4\beta^2t^2u^2\sin^2\frac{ka}{2}}. \tag{1.29}$$

As we are interested in the optimal structure at $T = 0\ K$, we can now study the

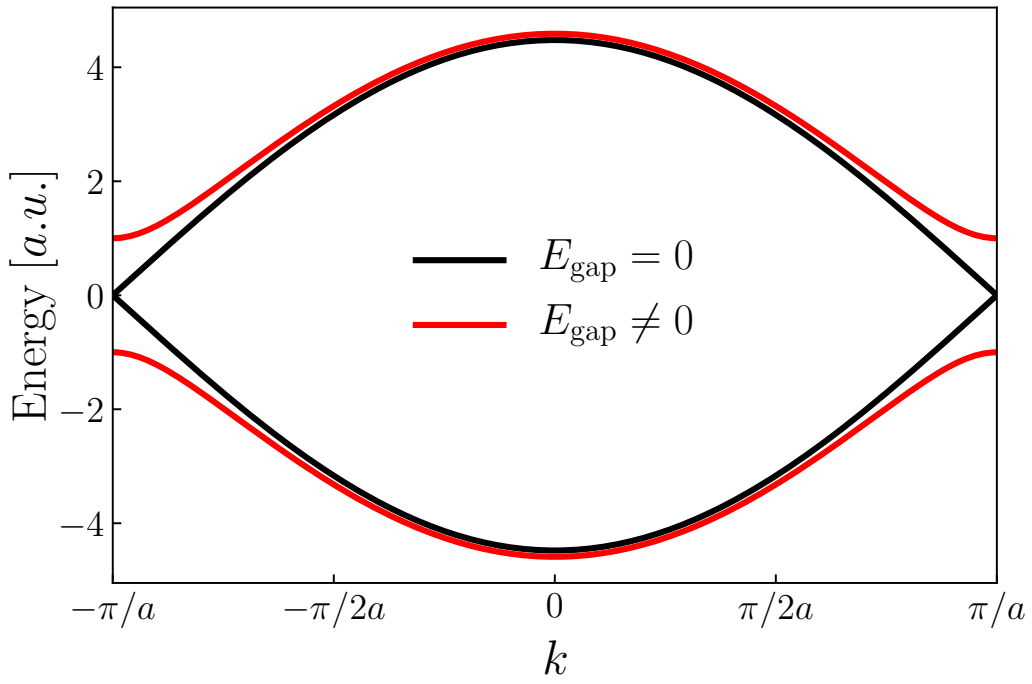


**Figure 1.2.** Electronic bands structure of the model. If $E_{\mathrm{gap}} = 0$, the bands have linear dispersion at the edges of the Brillouin zone, reminding the behaviour of graphene. We assume that the lower energy bands only are occupied with electrons. As summed-up in Equation (1.26), there are two mechanisms that contribute to the opening of the gap: the dimerization of the chain, consequence of the electronic instability and of the electron-phonon coupling, manifested as a bond energy difference $\delta t$; breaking the equivalence between atoms, e.g. with different on-site energies, accounted for by the parameter $\Delta$.

structural properties of the system, encompassed in the optimal displacement $\overline{u}$, defined as the one which minimizes $E_{\mathrm{tot}}(u) = E_{\mathrm{L}}(u) + E_{\mathrm{e}}(u)$ given a set of material-dependent parameters $t$, K, $\Delta$ and $\beta$. With the substitution $z = ka/2$ and exploiting the parity of the integrand in Equation (1.29), the first derivative of the total energy with respect to $u$ reads:

$$\frac{\mathrm{d}E_{\mathrm{tot}}}{\mathrm{d}u} = \frac{1}{2}\mathrm{K}a^2 u - \frac{u}{\pi}\int_{-\pi/2}^{0} \mathrm{d}z \frac{16\beta^2 t^2 \sin^2 z}{\sqrt{\Delta^2 + 4t^2\cos^2 z + 4\beta^2 t^2 u^2 \sin^2 z}}. \tag{1.30}$$

One of the stationary point of Equation (1.30) is in $u = 0$, whereas the others are the solutions of the following equation in $u$:

$$\mathrm{K}a^2\pi = \int_{-\pi/2}^{0} \mathrm{d}z \frac{32\beta^2 t^2 \sin^2 z}{\sqrt{\Delta^2 + 4t^2\cos^2 z + 4\beta^2 t^2 u^2 \sin^2 z}}. \tag{1.31}$$

To solve this integral, we expand the functions $\sin z$ and $\cos z$ at the lower edge of the Brillouin zone, namely in $k = -\pi/a$, in a similar fashion to the conic approximation

in graphene. By doing so, we arrive at

$$\Delta^2 + 4\beta^2 t^2 u^2 = \frac{t^2\pi^2}{\sinh^2 \frac{\mathrm{K}a^2\pi}{8\beta^2 t}}. \tag{1.32}$$

Supposing that $\Delta$ is the parameter which guides the transition, we define

$$\Delta_\mathrm{c} = \frac{t\pi}{\sinh\left(\frac{\mathrm{K}a^2\pi}{16\beta^2 t}\right)}. \tag{1.33}$$

As we are interested in the real solutions only, the above equations tells that if $\Delta \leq \Delta_\mathrm{c}$, the solution of Equation (1.32) provides two symmetric stationary points for $E_\mathrm{tot}(u)$. Indicating with $\overline{u}$ the value which minimizes $E_\mathrm{tot}(u)$, it is straightforward to verify, e.g. computing the second order derivative of $E_\mathrm{tot}(u)$, that

$$\begin{cases} \overline{u} \propto |\Delta - \Delta_\mathrm{c}|^{1/2}, & \text{if } \Delta \leq \Delta_\mathrm{c} \\ \overline{u} = 0, & \text{if } \Delta > \Delta_\mathrm{c}. \end{cases} \tag{1.34}$$

Moreover, it is also immediate to verify that the second order derivative of $E_\mathrm{tot}(u)$ computed at $u(\Delta_\mathrm{c}) = 0$ is a saddle point. These results show that the chain undergoes a second order phase transition in $\Delta$ with $\overline{u}$ as order parameter: when $\Delta > \Delta_\mathrm{c}$, the atoms are equidistant ($\overline{u} = 0$), while for $\Delta \leq \Delta_\mathrm{c}$ the chain displays a bond length alternation that breaks the inversion symmetry of the cell. Finally, in the SSH limit, i.e. when $\Delta = 0$, we recover inversion symmetry, in particular with respect to bonds centers. Stated in other words, the presence of a staggered on-site potential induces a site-centered CDW, counterposed to the bond-centered CDW due to Peierls electronic instability. Figure 1.3 displays two representative energy profiles, one for each phase, obtained from Equation (1.29): the two minima of a double-well energy landscape in the distorted phase collapse into a single minimum when $\Delta \geq \Delta_\mathrm{c}$, i.e., when the local maximum at $u = 0$ turns into a global minimum, signature of the second order transition.

It is interesting to notice that the left-hand side of Equation (1.32) is equal to $E_\mathrm{gap}^2/4$, implying that in the distorted phase, as $\Delta$ varies, $\overline{u}(\Delta)$ varies in a way that keeps the energy gap constant. This implies that the knowledge of the energy gap gives also information on the phase diagram of the system and vice versa. We also notice that in the SSH limit of equivalent atoms, namely for $\Delta = 0$, the first derivative in Equation (1.30) becomes discontinuous in $u = 0$, hence the only possible stationary solutions are for $\overline{u} \neq 0$. This results is coherent with the original argument for the Peierls transition, where a finite $\overline{u} \neq 0$ is allowed by an infinitely small e-ph interaction, conjuring with a Fermi-surface nesting and Peierls electronic instability to produce a dimerized phase with bond-length alternation and the opening of a gap in the energy spectrum $E_\mathrm{gap} = 4|\delta t| = 4\beta t\overline{u}$.

Discussion above sums up the main ideas present in the literature of the Rice-Mele

model about the Peierls transition and related structural properties. In particular, we saw how the competition between two mechanisms to counteract the electronic instability results in a second order structural phase transition. However, the parameter $\Delta$ is not the only handle available to drive the transition, that may be tuned by other model parameters at fixed $\Delta$ (a trivial one being the elastic stiffness K). For instance, it is reasonable that a sufficiently large e-ph coupling may induce a bond dimerization in the gapped chain at a finite $\Delta$. The optimal $\bar{u} \neq 0$ as a function of $\beta$ is given in closed form in Equation (1.32). As the e-ph coupling constant enters in the hyperbolic function, an explicit expression for $\bar{u}$ can be derived by assuming $\mathrm{K}a^2\pi \ll 8\beta^2 t$, which allows to retain only the lowest order term of the Taylor expansion of $\sinh(x)$. With this hypothesis, and defining the term

$$\beta_{\mathrm{c}}^2 = \frac{\mathrm{K}a^2}{8t^2}\Delta, \tag{1.35}$$

in analogy with the previous case, we obtain

$$\begin{cases} \overline{u} \propto |\beta - \beta_{\mathrm{c}}|^{1/2}, & \text{if } \beta > \beta_{\mathrm{c}} \\ \overline{u} = 0, & \text{if } \beta \leq \beta_{\mathrm{c}}. \end{cases} \tag{1.36}$$

This result shows that another way to control the structural transition of the chain in the model, given a finite $\Delta \neq 0$, is through the electron-phonon coupling term $\beta$. Both the behaviours of optimal $\overline{u}(\Delta)$ and $\overline{u}(\beta)$ are shown in the right panel of Figure 1.4.

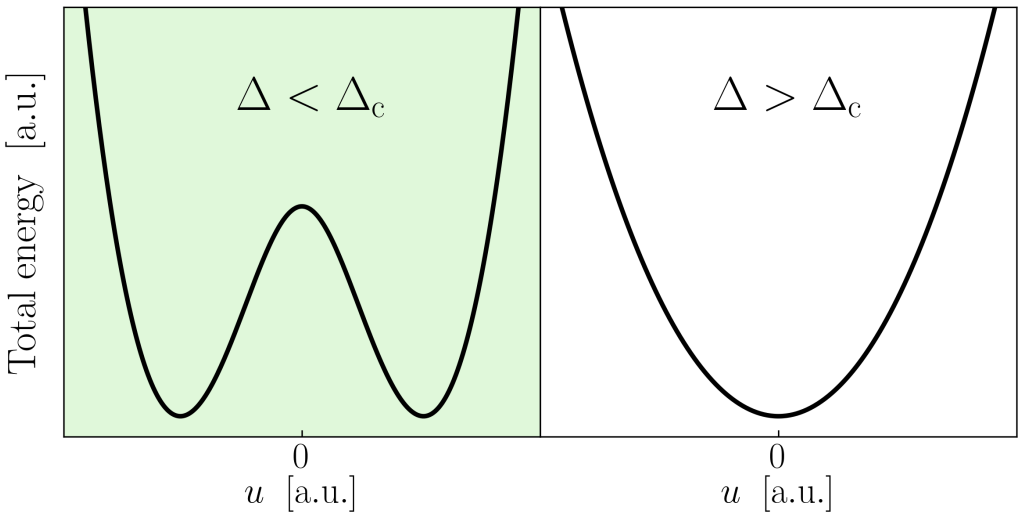


**Figure 1.3.** Behaviour of the total energy per unit cell $E_{\mathrm{tot}}$ with respect to the fractional coordinate $u$. If $\Delta < \Delta_{\mathrm{c}}$, there are two symmetric minima $\overline{u} \neq 0$ and the equilibrium structure present a bond length alternation. If $\Delta > \Delta_{\mathrm{c}}$, there is only one minimum in $\overline{u} = 0$ and the atoms are equidistant.

### 1.2.2 Polar properties: electronic polarization and Thouless pump

In this section, we derive the expression of the dipole moment per unit cell $P$ as obtained within the modern theory of polarization[37]. In this framework, the wave function of the occupied states is required to be continuous at the edges of the Brillouin zone. To satisfy this requirement, we multiply the wave function of the occupied states of Equation (1.24) by a phase factor and define

$$|\psi_k^{\text{occ}}\rangle \equiv \mathrm{e}^{-\mathrm{i}r_A k}\,|\psi_k^-\rangle \tag{1.37}$$

with $r_A = -a/4 + \delta r_A$. The dipole moment per unit cell $P$ is defined in terms of the Berry phase[38] $\varphi$ as

$$P = \frac{-2|e|}{2\pi}\varphi \tag{1.38}$$

where $e$ is the electron's charge, the factor 2 at the numerator accounts for the spin degeneracy and the Berry phase $\varphi$ is defined as

$$\varphi = \mathrm{i}\int_{-\pi/a}^{\pi/a} \mathrm{d}k \left\langle \widetilde{\psi}_k^{\text{occ}} \middle| \frac{\mathrm{d}\widetilde{\psi}_k^{\text{occ}}}{\mathrm{d}k} \right\rangle . \tag{1.39}$$

We indicated with $|\widetilde{\psi}_k^{\text{occ}}\rangle$ the periodic part of the wave function $|\psi_k^{\text{occ}}\rangle$ and from Equation (1.14), (1.24) and (1.37) it holds

$$|\widetilde{\psi}_k^{\text{occ}}\rangle = \mathrm{e}^{-\mathrm{i}r_A k}\sum_R \sum_\alpha c_{\alpha,k}\,|\alpha R\rangle\,, \tag{1.40}$$

where

$$\begin{cases} c_{A,k} &= \frac{\Delta-\varepsilon_k^-}{\sqrt{\left(\Delta-\varepsilon_k^-\right)^2+|T|^2}}, \\ c_{B,k} &= \frac{-T^*}{\sqrt{\left(\Delta-\varepsilon_k^-\right)^2+|T|^2}}. \end{cases} \tag{1.41}$$

As the scalar product in Equation (1.39) is taken over a single unit cell, without loss of generality we consider only the contribution for $R = 0$ in Equation (1.40) and obtain

$$\varphi = \frac{2\pi}{a} r_A + \int_{\pi/a}^{\pi/a} \mathrm{d}k \frac{(\delta r_B - \delta r_A)\,|T|^2 + 2t\delta t a}{(\Delta - \varepsilon_k^-)^2 + |T|^2}. \tag{1.42}$$

From the gap Equation (1.26), we notice that the insulating/metallic character of the system can be visualised in a 2D parametric $(\Delta, \delta t)-$space, where the origin of the axes correspond to a metallic system with $E_{\text{gap}} = 0$, while every other point corresponds to an insulating system with $E_{\text{gap}} \neq 0$. In this space, we define a parameter $\theta$ that allows to identify each point with the polar coordinates $(E_{\text{gap}}, \theta)$,

with the change of coordinates defined by

$$2\Delta = E_{\text{gap}} \sin\theta \tag{1.43}$$

$$4\delta t = E_{\text{gap}} \cos\theta. \tag{1.44}$$

Applying this change of coordinates in Equation (1.42), in the limit $E_{\text{gap}} \ll t$ it can be demonstrated that it holds

$$P = -\frac{|e|}{\pi}\theta. \tag{1.45}$$

This property can be appreciated in Figure 1.4, where we compare, for different values of $E_{\text{gap}}/t$, the behaviour with respect to $\theta$ of the dipole moment $P$, obtained computing Equation (1.38) numerically without further approximations. Values of model's parameters used for numerical calculations were obtained fitting the DFT energy of carbyne, as further explained in section 1.3. As $\theta$ varies, so do the terms $\Delta$ and $\delta t$. In particular, a full rotation of $2\pi$ implies that the system has returned in its initial state, while the dipole moment $P$ has acquired a quantum of $-2|e|$. This property is more general: if the system undergoes an adiabatic evolution along any loop enclosing the origin of the 2D space, a quantised charge is always pumped out. This phenomenon is known as adiabatic charge transport or Thouless' pump[10] and the key ingredient is the presence of the metallic point in the domain enclosed by the loop: in this sense, it is an example of topological phenomenon. In Chapter 3 we will demonstrate how this peculiar topology-related property affects polar responses of the system.

### 1.2.3 Relation between structural and polar properties

Finally, we discuss the relation between polar and structural properties in the model, with the aid of the 2D space, in particular focusing on the possibility to have ferroelectricity in the chain. A necessary condition for the system to manifest ferroelectricity is to be non-centrosymmetric. In order to meet this requirement in the chain, conditions $\Delta \neq 0$ and $\delta t \neq 0$ must be satisfied simultaneously. Indeed, if both $\Delta = 0$ and $\delta t = 0$ – the origin of the axis – the system is metallic and it is not possible to define a polarization. If only one between $\Delta$ and $\delta t$ is non-zero – the horizontal and vertical axes, respectively – the system is still centrosymmetric. In the case $\Delta \neq 0$ and $\delta t = 0$, we have inequivalent but equidistant atoms, and the chain is symmetric for the inversion with respect to atoms sites. In the other case $\Delta = 0$ and $\delta t \neq 0$, instead, we have a BLA between equivalent atoms, hence the chain is symmetric for the inversion with respect to bonds centers. In both cases it is possible to define a dipole moment per unit cell, but symmetry forbids the presence of a *spontaneous* polarization for the bulk system, namely a polarization present even in absence of an external electric field. Finally, if both $\Delta \neq 0$ and $\delta t \neq 0$ – a generic point in the space, a part from the axis and the origin –, the system is not centrosymmetric, with a spontaneous polarization due to the presence

of a mixed bond- and site-centered charge density modulation. From Figure 1.4, we notice that the structural phase transition takes place between a centrosymmetric and a non-centrosymmetric structure: in this sense, this 1D diatomic linear chain model describes a prototypical ferroelectric transition.

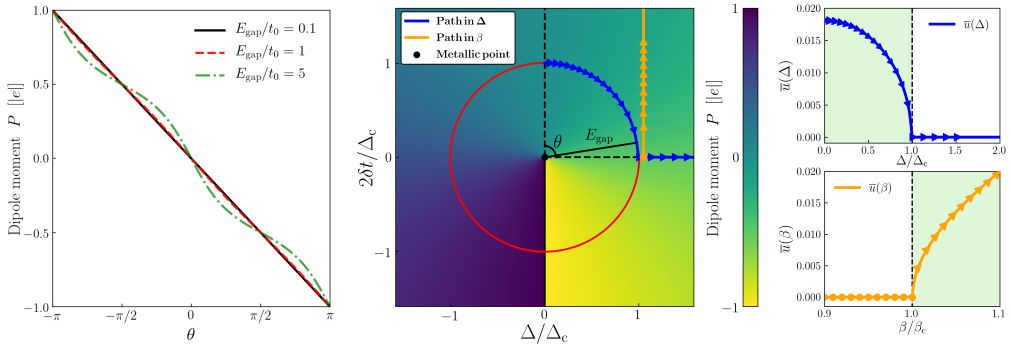


**Figure 1.4.** On the left panel, behaviour of the dipole moment per unit cell $P$ with respect to $\theta$ for different values of $E_{\rm gap}/t$. As expected, in the small-gap limit ($E_{\rm gap} \lesssim t$) we observe the linear behaviour $P \propto -\theta$ predicted in Equation (1.45). On the central panel, values of $P$ are displayed in the 2D parametric $(\Delta, \delta t)-$space, where each point correspond to a physical realization of the model. We highlight that $\theta$ is defined clockwise with respect to the positive vertical semi-axis. From the color-map, we deduce that an adiabatic evolution along a loop containing the origin of the axes – which correspond to a metallic system – pumps out a quantised charge of $-2|e|$, as expected from Thouless argument[10]. Finally, it is interesting to visualize the phase transitions of $\overline{u}(\Delta)$ and $\overline{u}(\beta)$, displayed separately in the two right panels, also as paths in the 2D parametric space. Being $\Delta$ and $\beta$ the independent parameters, and being $\delta t \propto \beta\overline{u}$, one finds that the transition in $\Delta$ from the dimerized ($\overline{u} \neq 0$, hence $\delta t \neq 0$) to the undimerized ($\overline{u} = 0$, hence $\delta t = 0$) phase, happens on a circumference with fixed $E_{\rm gap}$, whereas the evolution with respect to $\beta$ in the dimerized phase corresponds to a vertical line, the undimerized phase corresponding to a single point at fixed $\Delta \neq 0$ and $\delta t = 0$. Arrows on the two paths in the 2D space correspond, respectively, to the arrows in the right panels whereas all the dots of the lower right panel correspond to a single point in the 2D space in $(\Delta = 1.05\Delta_c, \delta t = 0)$.

## 1.3 Conjugated polymers as prototypical 1D systems

In this section, we introduce a class of materials where the concepts discussed above find a physical realization: conjugated polymers (CPs). CPs are organic materials characterized by a backbone chain of atoms, usually carbon atoms, to which other elements and/or functional groups may bond. The property that makes them stand out among other organic compounds is the presence of delocalized electrons along the chain, consequence of the overlap between p-orbitals of atoms in the backbone. This peculiar characteristic results in interesting and useful optical and electronic properties, with many applications in the field of organic electronics[13, 39], some of the most notable being for organic solar panels[40, 14], organic light-emitting diodes (OLED)[41, 15], organic field-effects transistors (OFETs)[42] and

bioelectronics[43, 16].

To have an intuitive understanding of the phenomenon of delocalization, let's consider a prototypical CP: polyacetylene (PA). Since its first synthesis in 1958 by Giulio Natta[44, 45], PA has been object of many studies. In particular, the discovery of its high electrical conductivity upon doping[46] has paved the road to the field of organic conductive polymers and has been awarded with the Nobel Prize in 2000[47]. It is composed by a chain of carbon atoms, each of which is bound to one hydrogen atom, hence it can be schematized as an infinite repetition of the unit $C_2H_2$. From a chemical point of view, a carbon atom has four valence electrons involved in bonds formation. In PA, three of them form the so-called $sp^2$ hybrid orbitals: one of the orbital creates a $\boldsymbol{\sigma}$-bond with the valence electron of the hydrogen atom, whereas each of the other two creates a $\boldsymbol{\sigma}$-bond with one $sp^2$ orbitals of one of the two neighboring carbons. These bonds determine the geometry of the chain, in particular, PA has two isomeric structures, named *cis* and *trans*. Our analysis will focus on the trans one, shown in Figure 1.5, since it's the most stable structure. However, the peculiarity of PA, and of CPs in general, stems from the behaviour of the last valence electrons. Intuitively, since each carbon atom uses three of the four valence electrons to form bonds with an hydrogen atom and with two carbon atoms along the chain, the last electron may form bonds only with one of the two neighboring carbons. Electrons involved in this bonds are in p-orbitals perpendicular to the plane determined by the $sp^2$ orbitals, resulting in $\boldsymbol{\pi}$-bonds. Taking the $C_2H_2$ unit as a reference, this bond can be between carbons in the same unit or between carbons in adjacent units, however resulting in both cases in an alternation of double and single bonds. These two possible realizations of the structure are completely equivalent and in chemistry are usually called *resonance structures*[48]. The resulting electronic structure is a hybrid of these two realizations, meaning that the electrons are not confined to a bond, but rather they are *delocalized* over several atoms along the chain, as depicted in Figure 1.5.

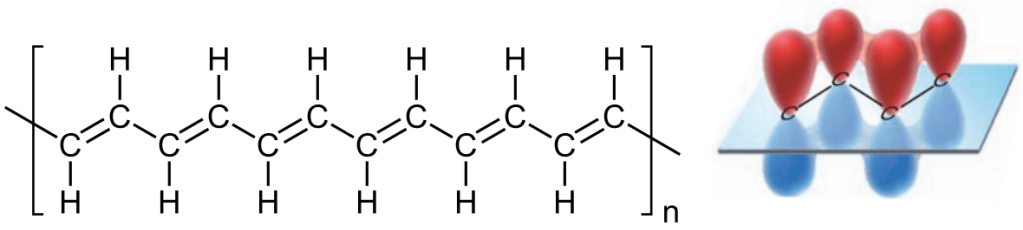


**Figure 1.5.** On the left panel, structure of polyacetylene (PA) in its trans configuration. On the right panel, schematic representation of how a delocalized electronic distribution arises from the overlap between p-orbitals of atoms along the backbone of a conjugated polymer like PA.

This intuitive idea we illustrated for PA is behind all CPs in general. Indeed, all CPs are characterized by resonating structures, which result in electronic delocalization. As a consequence of delocalization, electrons involved posses high mobility

along the chain, giving CPs their peculiar electronic and optical properties. As the electronic delocalization in CPs is a property of the atoms in the backbone chain, 1D models as the one we discussed above are suitable to describe the main features of CPs. For instance, the SSH model of a chain with equivalent atoms[29, 36], has been widely used to describe the properties of PA, as the two carbon atoms in the $C_2H_2$ unit are electronically equivalent (the $\Delta = 0$ case in the model of section 1.2). The Rice-Mele model of a diatomic chain with inequivalent atoms (the $\Delta \neq 0$ case in the model of section 1.2), instead, is suitable to describe substituted polyacetylenes (SPA)[49, 50, 51, 52], a class of conjugated polymers formed by inequivalent monomers which can be obtained substituting (one of) the atoms in the $C_2H_2$ unit of PA with some element(s) or compound(s).

### 1.3.1 Carbyne

A very peculiar example of 1D system and CP is *carbyne*, an infinitely long linear chain of carbon atoms. As such, carbyne is a 1D allotrope of carbon[53], just like graphene in 2D, and diamond and graphite in 3D. Following the intuitive picture used for PA, we recall that, from a chemical point of view, a carbon atom has four valence electrons involved in bonds. In carbyne, in particular, two electrons per atom form $sp-$hybridized orbitals which are involved in $\boldsymbol{\sigma}$-bonds with the other $sp-$orbitals of neighboring carbons, giving to carbyne its perfectly linear structure. The remaining two electrons per atom give rise to two possible realisations of carbyne[54]: on one hand, each electron may form a second bond with one neighbor, resulting in a structure where all carbons form double bonds and are equidistant. Due to the cumulative presence of double bonds, such system is also called *cumulene*. On the other hand, both the two electrons may bond with only one of the two neighbors, resulting in an alternation of single and triple bonds, reflected in a structure with BLA. Following chemistry nomenclature, this realisation of carbyne is called *polyyne*. In Figure 1.6 both cumulene and polyyne structures are shown. At date, the cumulenic phase has never been synthesized and even if its presence has been hypothesized, e.g., in interstellar clouds[55, 56], its actual existence is still debated[57, 58]. Indeed, as discussed in previous sections, a linear chain of equivalent and equidistant atoms would undergo a phase transition in favor of a distorted and insulating phase, in this case the polyynic one. As such, carbyne is also a prototypical example of a physical realization of the Peierls metal-insulator transition, and consequently of a (bond-centered) CDW system. In next Chapter 2, we will further discuss the competition between these two realizations of carbyne, including also quantum-anharmonic effects.

From a practical point of view, the synthesis of carbyne is highly challenging[60] and requires particular care. The most recent advances, with chains composed of up to $\sim$ 6000 atoms, were obtained through the encapsulation of the linear chain inside carbon nanotubes, which act as stabilizing and protective materials[61]. Nevertheless, there is a strong interest in the realization of this material because

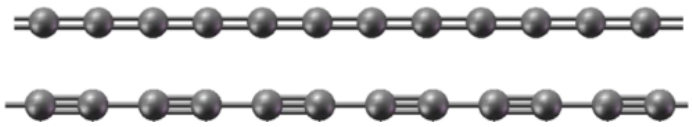

**Figure 1.6.** Carbyne, an infinite length chain of carbon atoms, has two different structural realizations, classified according to the bonds formed by the atoms. The cumulative presence of double bonds is what defines cumulene, characterized by equidistant atoms as shown in the top structure. If instead the chain is characterized by an alternation of single and triple bonds, we are in presence of polyyne. The inequivalence between bonds is reflected by a bond length alternation, as shown in the bottom structure. Both figures are adapted from Ref.[59].

of the incredible properties theoretically predicted. In particular, it is thought to be the strongest material known, with a Young's modulus per density assumed to be twice as large as that of graphene and a predicted specific tensile strength of $6.0 - 7.5 \times 10^7$ Nm/kg[62], where, e.g., for diamond it is $2.5 - 6.5 \times 10^7$ Nm/kg, for graphene is $4.7 - 5.5 \times 10^7$ Nm/kg and for carbon nanotubes is $4.3 - 5.0 \times 10^7$ Nm/kg. Moreover, uses of carbyne were also proposed for convertible energy storage and batteries[63, 64].

### 1.3.2 Fit of the model on carbyne

Being a straight, linear, 1D system, carbyne is the perfect physical realization of the 1D chain model we discussed. Thus, with the aim of having a working-model with a real counterpart, we fitted model's parameters in order to reproduce properties of carbyne obtained with DFT calculations. The choice of an hybrid exchange-correlation functional with an adequate mixing parameter has become the standard for DFT calculations of CPs as they allow to correctly account for the long-range effects due to the delocalized nature of electrons and also for the presence of a surrounding dielectric environment, as can be nanotubes' walls for carbyne[65, 66, 67]. Recent works[68, 17] established the PBE0 functional as a reliable standard for PA and carbyne, with results in agreement with those of more advanced techniques as $G_0W_0$ for the electronic structure and with the experimentally measured BLA of carbyne in carbon nanotubes of Ref.[61]. For these reasons, we adopted the PBE0 functional to compute, with the CRYSTAL code[69, 70], the total energy of carbyne as a function of atoms relative displacement. Computational details on the parameters used in the calculations are given in Appendix C. The physical properties we are interested to reproduce are the BLA, the energy gain $E_{\text{gain}}$ of the stable, distorted polyyne phase with respect to the unstable, undistorted, cumulenic one, and the energy of the longitudinal optical phonon at zero wave-length $\omega_{\text{LO}}(\Gamma)$, which is proportional to the curvature of the total energy profile at its minimum, in order to correctly account for the longitudinal phonon which guides the Peierls transition. Aiming to reproduce these three quantities, we chose three free parameters of the model: the hopping energy parameter between equidistant

atoms $t$, the electron-phonon coupling parameter $\beta$ and the elastic constant term K. Reminding that carbon atoms in carbyne are equivalent in both the cumulene and polyyne realizations, we have $\Delta = 0$. Finally, the cell length parameter $a = 2.534\,\text{Å}$ is taken from a PBE0 unit-cell relaxation calculation.

The optimal values for $t$, $\beta$ and K were obtained minimising a cost function $\mathcal{L}$ defined as

$$\mathcal{L}(t, \beta, \mathrm{K}) = \sum_i w_i \left[Q_i(t, \beta, \mathrm{K}) - Q_i^*\right]^2 \tag{1.46}$$

where the sum runs over the quantities $Q_i$ used for the fit (i.e. the BLA, the $E_{\text{gain}}$ and $\omega_{\text{LO}}(\Gamma)$), $Q_i(\beta, \mathrm{K}, t)$ is the value of the quantity $Q_i$ calculated in the framework of the toy-model with parameters $t$, $\beta$ and K, $Q_i^*$ is the value of the quantity taken as reference from the DFT calculation and $w_i$ is a weight used to rescale to the same order of magnitude all the contributions to $\mathcal{L}$, in particular we put $w_i = 1/Q_i^{*2}$. The results of the fitting procedure are reported in Table 1.1 whereas in Figure 1.7 we show the comparison between total energy profiles obtained with DFT and with the fitted model.

| | | |
|---|---|---|
| $E^*_{\text{gain}}$ (meV) | BLA$^*$ (Å) | $\omega^*_{\text{LO}}(\Gamma)$ (cm$^-$1) |
| 33.86570 | 0.10011 | 1986.57 |
| $E_{\text{gain}}$ (meV) | BLA (Å) | $\omega_{\text{LO}}(\Gamma)$ (cm$^-$1) |
| 33.86572 | 0.10010 | 1986.50 |
| $t_{\text{best}}$ (eV) | $\beta_{\text{best}}$ (eV/Å) | $\mathrm{K}_{\text{best}}$ (eV/Å$^2$) |
| 2.384554 | 7.203604 | 127.976590 |

**Table 1.1.** First line: DFT@PBE0 values for the energy gain $E^*_{\text{gain}}$ between the most stable polyyne phase and the less stable cumulene one, for the bond length alternation BLA$^*$ and for the longitudinal optical phonon energy $\omega^*_{\text{LO}}(\Gamma)$, taken as references for the fitting procedure. Second line: values for the same quantities obtained within the best-fitted model. Last line: values of model's parameters obtained from the fitting procedure described in the text. The value of the cost function defined in Equation (1.46) is $\mathcal{L}(t_{\text{best}}, \beta_{\text{best}}, \mathrm{K}_{\text{best}}) < 10^{-8}$.

### 1.3.3 Validation of the fit

The results of the fitting procedure gives remarkably accurate agreement with DFT target values, putting forward the model as a reliable framework to study properties of 1D systems, in this particular case of carbyne, with results as good as DFT-level ones. In Figure 1.8 we compare the electronic energy bands dispersions obtained ab-initio and with the fitted-model, finding a quite good agreement in describing the occupied band. We also find an energy gap $E_{\text{gap}} \simeq 1.45$ eV in the model, to compare with the ab-initio one $E_{\text{gap}}^{\text{PBE0}} \simeq 2.03$ eV.

The major strength of the model lies however in the fact that the parameters have

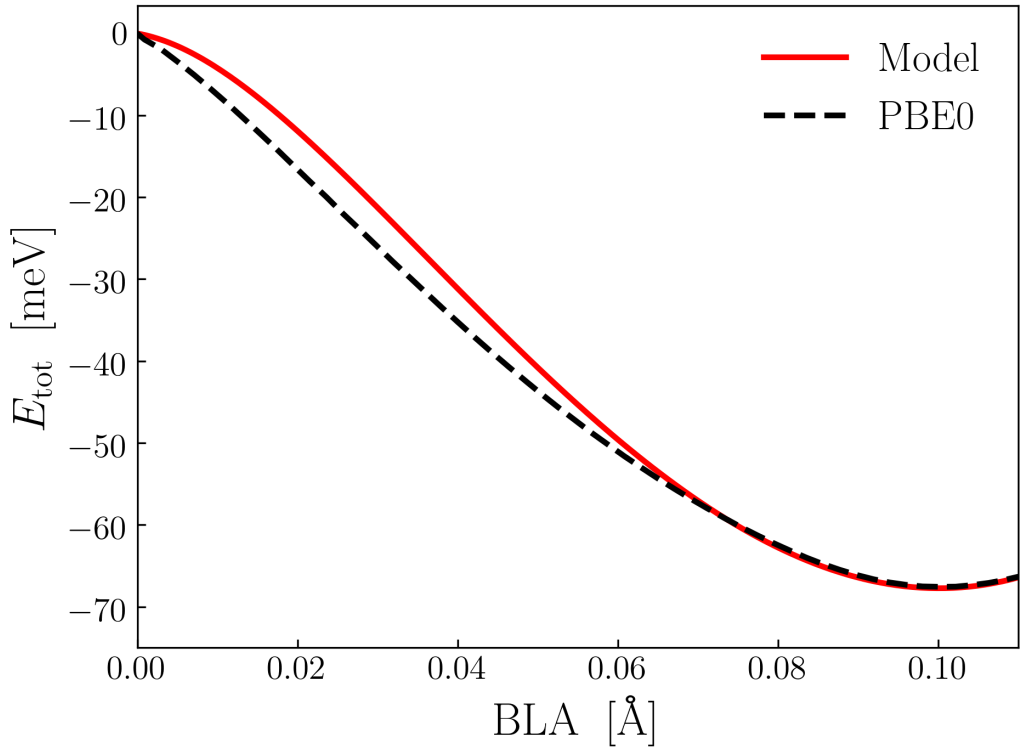


**Figure 1.7.** Comparison between the energy profile of carbyne obtained ab-initio with DFT@PBE0 level calculation and the energy profile obtained with the fitted-model. Aiming to reproduce the depth of the potential well, the position of the minimum and the curvature in the minimum, a remarkable agreement is noticed.

a clear physical meaning, implying that we can describe different physical realizations of carbyne with only slight adjustments. For instance, synthesis of carbyne is only possible inside carbon nanotubes, which may have different properties such as different diameter lengths, different chiralities and so on. These differences are known to strongly affects properties of the carbyne chains they host, e.g. their BLA or their electronic energy gap. As we will thoroughly discuss in Chapter 3, it has been argued that the underlying reason is a renormalization of the e-ph interaction in the chain as a consequence of the dielectric environment of the nanotubes[61, 71]. The framework of the model offers the possibility to test these ideas. Indeed, we can vary the e-ph coupling parameter $\beta$ and verify if specific behaviours experimentally observed are captured by the model. In particular, in Ref.[71] Shi et al. observed a linear relation between the electronic energy gap $E_{\text{gap}}$ with respect to the raman shift in carbyne chains hosted in double-walled carbon nanotubes with different diameters. To verify if the model correctly captures this behaviour and at the same time to test the hypothesis that the main mechanism at play is a renormalization of the electron-phonon interaction, we proceed as follows. Varying the value of the parameter $\beta$ in the model around the fitted value, we compute the values of the energy gaps and of

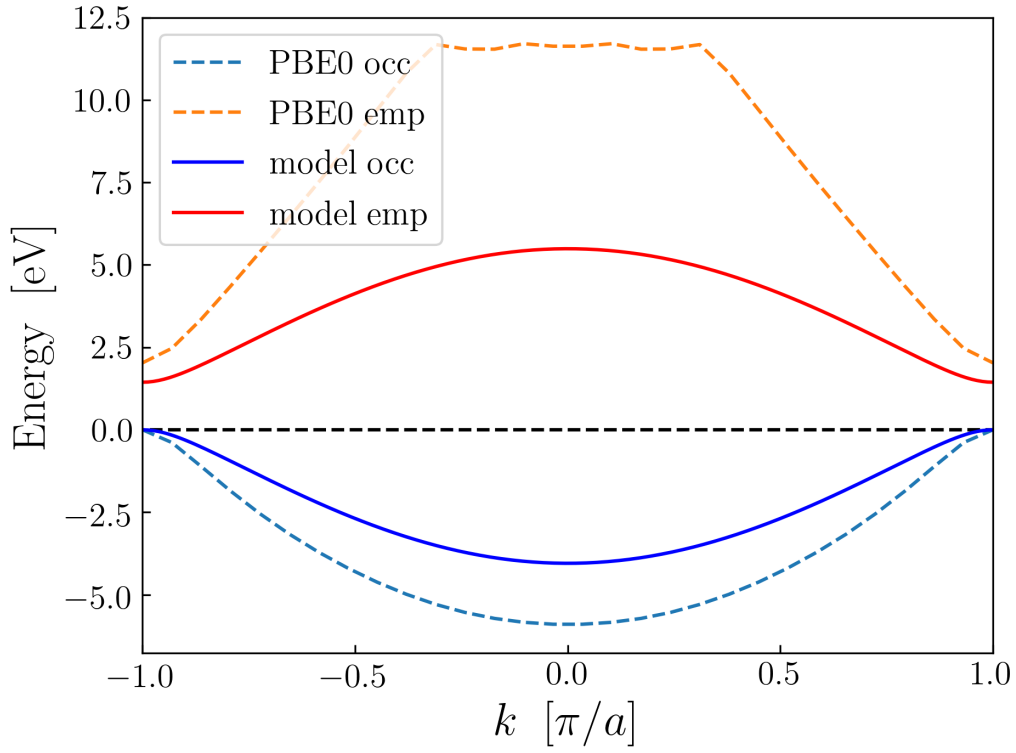


**Figure 1.8.** Electronic energy bands dispersion for carbyne obtained ab-initio and within the fitted-model. Despite the striking conceptual differences between a tight-binding approach and a DFT model with an hybrid functional like the PBE0, there is quite a good agreement in the description of the occupied band and in particular of the energy gap opening at the borders of the Brillouin zone.

the $\omega_{\mathrm{LO}}(\Gamma)$ that a Raman experiment would measure. In Figure 1.9 we compare our results with the experimental data of Ref.[71], obtained with resonance Raman spectroscopy. We remark how, despite the systematic underestimation of the energy gap, the model perfectly captures the linear relation between $E_{\mathrm{gap}}$ and $\omega_{\mathrm{LO}}(\Gamma)$. On one hand, this result validates the fitted-model as a reliable tool for the study of carbyne, on the other, it is also a confirmation that nanotubes' walls strongly affects e-ph interaction of the carbyne chains they contain.

Finally, it would be useful to exploit the fitted-model beyond carbyne, in order to study the structural and polar properties discussed in previous sections. To do so, we need to break the equivalence between carbon atoms. To attain this goal while at the same time keeping a real physical counterpart, we decided to put six helium atoms around one carbon atom every two, in the following way: the six helium atoms are positioned at the vertices of an hexagon which lies in a plane perpendicular to the linear chain direction. At the center of this hexagon is the carbon atom, equidistant from all helium atoms. At the end, there will be an hexagon of heliums around one carbon atom every two, so that this system still falls in the framework of

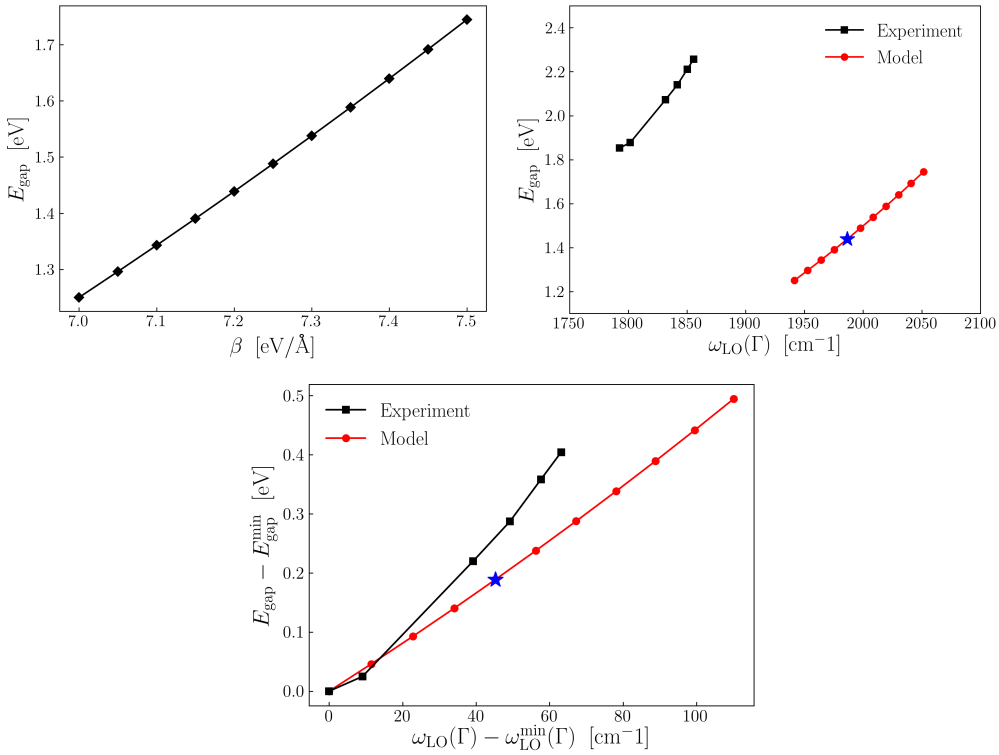


**Figure 1.9.** On the top left, it is possible to observe how the variation of the e-ph coupling parameter $\beta$ modifies the electronic energy gap $E_{gap}$. As expected from Equation (1.26), we find a linear behaviour. Having chosen the handle to control the energy gap, on the top right panel we show the comparison between values of $E_{gap}$ and of the longitudinal optic phonon at $\Gamma$, $\omega_{LO}(\Gamma)$, obtained with the fitted-model on carbyne and from resonance Raman experiments on carbyne inside different carbon nanotubes[71]. The star indicates the results obtained for the $\beta$ of Table 1.1. Despite the systematical underestimation of the energy gap, the model correctly captures the linear relation observed experimentally, indirectly confirming the idea that the dielectric environment around carbyne chains strongly affects their e-ph interaction. This is confirmed by the comparison of the same quantities with rescaled axis in the lower panel. In particular, we subtracted to each value of $E_{gap}$ and of $\omega_{LO}(\Gamma)$, their respective lowest values – indicated with the label $^{min}$ – so that both the experimental and model curves start form the point (0,0).

the diatomic chain model. Indeed, as we vary the distance $d$ between the vertices of the hexagon and its center, the closed-shells of the helium atoms locally modify the electronic charge density distribution of carbyne due to static Coulomb interaction, acting as an effective onsite energy term $\Delta$. A part from the theoretical utility of this system, the philosophy of decorating carbon chains with elements and compounds in order to attain particular properties has been explored also for practical purposes. For instance, studies have shown how networks of carbyne's chains decorated with calcium or lithium atoms hold very promising properties in terms of hydrogen storage capabilities[63, 72]. Even if we are not going to investigate carbyne as an hydrogen storage candidate, we want to stress on the interest in studying these carbyne-based

materials beyond a purely theoretical appeal.

In practice, we perform ab-initio PBE0 calculations on carbyne decorated with helium atoms for various He-C distances $d$. In particular, for a fixed value of $d$ we study how the energy gain and the BLA are affected by the presence of the heliums. Then, keeping fixed the values of the fitted-model parameters of Table 1.1, for each different $d$ we perform a fit using the DFT reference values for $E_{\text{gain}}(d)$ and BLA($d$) in order to retrieve the best values of $\Delta$ for each $d$. Results are shown in the left panel of Figure 1.10. To test the accuracy of this extended fitted-model, we compare the ab-initio effective charges $Z^*$ of helium-decorated carbyne with the ones obtained from the model, finding a good agreement as shown in the right panel of Figure 1.10. As a final remark, testing the validity of model's prediction in the case of the effective charges is instrumental for the results we discuss in Chapter 3 on polar responses of 1D systems.

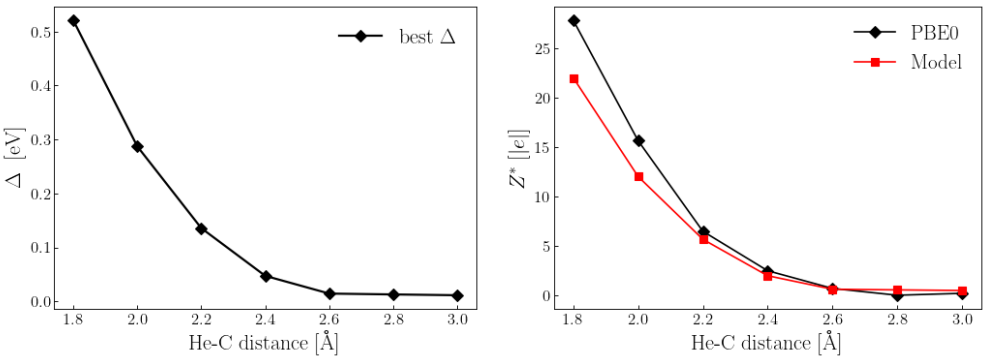


**Figure 1.10.** On the left panel we show the best values of onsite energy $\Delta$, obtained from the fitting procedure described in the text, as a function of the distance between helium and carbon atoms. On the right panel, the comparison between effective charges $Z^*$ obtained from DFT@PBE0 calculations and within the fitted-model, as a function of He-C distance confirm the model as a fast and reliable tool to obtain DFT-level results.

## 1.4 Conclusions

To sum up, in this Chapter we gave an overview on some relevant aspects about structural and polar properties of 1D conjugated systems, in relation with phenomena such as charge density waves and ferroelectricity. In particular, in the framework of a simple tight-binding model of a diatomic linear chain, we first explored the competition between two different structural realizations of the chain: a more symmetric configuration where all atoms are equidistant is counterposed to a less symmetric one characterized by a bond-length alternation. The optimal configuration is determined by physical properties encompassed in specific model's parameters, which guide a second order structural phase transition between the two phases. In particular, a possible knob to control the transition is the strength of the electron-phonon coupling, that, as we will see, may also account in the model for the effects

of dielectric environment surrounding these 1D systems.

Then, strictly related to their configuration, we focused on polar properties of 1D systems. In particular, studying the behaviour of electronic polarization in the model, we shown how the structural transition is also a prototypical ferroelectric phase transition. Moreover, systems described by the model were shown to be realizations of the adiabatic charge transport mechanism of the Thouless pump, with consequences that will be discussed in Chapter 3.

Successively, we introduced the class of conjugated polymers, organic 1D materials with very peculiar optoelectronic properties. The defining characteristic of these materials is the presence of delocalized electrons along a backbone chain, a characteristic that can be perfectly captured in the framework of the model. Following this idea and in order to have a working-model with a physical counterpart, we fitted model parameters with DFT calculations of carbyne, an infinite linear chain of carbon atoms which has drawn a lot of interest for its predicted properties. Fitted-model results show great agreement both with ab-initio calculations and experimental observations, putting forward this simple model as a fast and reliable tool to study properties of 1D systems such as conjugated polymers. In particular, the agreement with experimental results on the linear relation between the electronic energy gap $E_{\mathrm{gap}}$ and the zone-center longitudinal optical phonon energy $\omega_{\mathrm{LO}}(\Gamma)$, suggests that the e-ph parameter $\beta$ of the model correctly captures the effects of a dielectric environment around carbyne, e.g. carbon nanotubes, as argued before.

# Chapter 2

# Quantum-anharmonic effects

## Chapter overview

Chapter 2 is organized as follows. In section 2.1, we describe what quantum-anharmonic effects are and their fundamental role for the correct treatment of many systems. Next, in section 2.2, we present the self-consistent harmonic approximation, a variational theory that allows for a non-perturbative treatment of quantum-anharmonicity in materials. In particular, we discuss its stochastic implementation and how we use it in the 1D model. As a first application, we study the effects of quantum-anharmonicity and temperature on the CDW of carbyne in section 2.3. Next, in section 2.4, we do a similar study on quantum-anharmonic effects on carbyne-derived systems. Finally, conclusions are drawn in section 2.5.

## 2.1 Introduction: the importance of ionic quantum-anharmonic effects

In the previous Chapter, we introduced a model to describe structural and polar properties of 1D conjugated systems, as well as their interplay. In particular, we characterized a second order structural phase transition with respect to model's parameters and discussed the connection with the insurgence of phenomena such as charge density waves and ferroelectricity, neglecting lattice dynamics and at zero temperature. In the present Chapter, we go beyond this hypothesis and include both temperature effects and ionic dynamics in the model.

Even if, in general, the energy of ionic fluctuations is smaller with respect to that of electronic degrees of freedom, in order to understand and correctly reproduce many physical and chemical properties of materials and molecules, it is often necessary to consider vibrations of ions[73], which oscillate even at $T = 0\,K$ because of the zero-point motion energy. Since electron dynamics is much faster than the ionic one, usually one assumes the Born–Oppenheimer (BO) approximation to describe the motion of ions. Namely, one considers the ions subject to the BO potential

$V(\boldsymbol{R})$, given by the electronic ground state energy at any ionic configuration $\boldsymbol{R}$. From this starting point, the standard approach to treat lattice dynamics consists then in Taylor-expanding the BO potential up to second-order around the $\boldsymbol{R}_0$ ionic positions that minimize $V(\boldsymbol{R})$. In this way, the resulting Hamiltonian is harmonic and exactly diagonalizable in terms of phonons, vibrational quanta that within the harmonic approximation are well-defined quasiparticles with an infinite lifetime. In reality, however, phonons do acquire a finite life-time due to their anharmonic interaction with other phonons or because of other types of interactions such as the electron-phonon coupling. When higher-order anharmonic terms are small compared to harmonic ones, one can treat anharmonicity within perturbation theory[74, 75, 76] and correctly account for finite-lifetime effects and/or temperature dependence of phonons energy. However, if anharmonic terms of the BO potential are of the same order of magnitude or even larger than the harmonic ones in the range sampled by ionic fluctuations, perturbative approaches fail and are not valid anymore[77]. This is often the case when light ions are present and/or when the system is close to a displacive phase transition, such as a ferroelectric- or a CDW-instability.

These considerations are particularly relevant for 1D systems described by our model, as they may present at the same time light atoms, anharmonicity and CDW instability. Indeed, the BO potential of the model, namely the total energy $E_{\text{tot}}$ defined in Chapter 1, is strongly anharmonic in proximity of the critical points of the phase transition. Moreover, in the case e.g. of conjugated polymers, the presence of carbon atoms – with light masses $\sim 12$ times that of hydrogen – in the polymers backbone may yield to remarkable zero-point energy renormalization, as already highlighted e.g. in carbyne[17]. Furthermore, as recently shown in several compounds[78, 79, 19, 17], ionic positions can be strongly altered by quantum-anharmonic effects (QAE), even at zero Kelvin. These structural changes are important for both internal degrees of freedom, related to system's symmetries, and for the lattice parameters. Hence, as a final remark, we notice that QAE may also affect polar properties, as they are intertwined with the structural ones (we leave the study of this problem for next Chapter 3).

Driven by these motivations, in what follows we study the effects of quantum-anharmonicity on model's properties. In particular, we use the values of the parameters obtained in section 1.3 to reproduce DFT properties of carbyne. Indeed, being an infinite-length straight chain of carbon atoms, carbyne can be regarded as a physical realization of a one-dimensional CDW. Generally, electron-phonon interaction favors the formation of CDW, while quantum-anharmonicity tends to dampen them. The accurate estimation of quantum-anharmonic effects, however, remains scarce in literature due to its non-perturbative nature and because the quantum behavior of ions, in particular for light atoms, poses challenges for conventional density functional theory (DFT) or standard molecular dynamics approaches. Thus, comprehending the finite temperature quantum-anharmonic phase diagram of carbyne holds pivotal significance in understanding the physics of CDWs.

Moreover, as already discussed, it is possible to vary some of the parameters of the carbyne-like model while still keeping a real physical counterpart, e.g. carbyne decorated with helium atoms or in different dielectric environments. In this way, we can study the effects of quantum-anharmonicity also on the competition between the formation of a bond-centered CDW, driven by the Peierls electronic instability, and a site-centered one, favored e.g. when breaking atoms equivalence. Finally, we argue that since the model may describe many 1D systems beyond carbyne, e.g. other conjugated polymers, the conclusions we present below, hold significance as general results regarding the effects of QAE on properties of 1D systems.

## 2.2 The self-consistent harmonic approximation

In recent years, several methods have been developed to calculate vibrational properties of solids beyond perturbation theory or with the inclusion of quantum effects. A common approach consists in using ab-initio molecular dynamics (AIMD) to extract phonon frequencies or force constants[80, 81, 82]. However, these methods often fail to consistently account for quantum effects, hence the AIMD trajectories needs to be substituted by more expensive path-integral molecular dynamics (PIMD) ones[83]. Other methods, based on variational principles and vibrational self-consistent fields[84, 85], have often successfully incorporated the effect of anharmonicity beyond perturbation theory in different materials. However, they usually lack a consistent procedure to properly capture both quantum effects and anharmonicity in the compound, as many of them simply correct the free energy and/or the phonon frequencies assuming that the ions remain fixed at the $\boldsymbol{R}_0$ classical positions.

Among theories based on variational principles, the Self-Consistent Harmonic Approximation[86, 87] and in particular its stochastic implementation (SSCHA)[20, 18, 73], has recently emerged as a powerful and unique technique that allows to derive thermodynamic properties of materials, incorporating at the same time quantum and anharmonic effects. Indeed, thanks to the SSCHA it is possible to optimize crystal structures, compute thermal expansion, and accurately determine conditions for second-order phase transitions at an affordable computational cost, overcoming limitations of AIMD and PIMD simulations. In this section, we briefly discuss the main ideas behind this theory and its stochastic implementation.

We consider nuclei and electrons in the Born-Oppenheimer (BO) approximation and focus on the quantum problem for the nuclei, expressed in terms of the BO Hamiltonian

$$H = K + V(\boldsymbol{R}), \tag{2.1}$$

where $K$ is the kinetic operator for the nuclei, $V(\boldsymbol{R})$ is the BO potential, derived from the electronic energy in a given atomic configuration and $\boldsymbol{R}$ is a vector with all the $3N_{\text{at}}$ coordinates for the $N_{\text{at}}$ atoms. A system of finite volume, temperature and number of particles, is at equilibrium when it is at the minimum of the free energy

$F = E - TS$, where $E$ is the internal energy of the system, $T$ the temperature and $S$ the entropy, defined in terms of numbers of microstates corresponding to the same macrostate of the system. In a classical picture, microscopic states of the system are determined by the classical probability distribution of atoms $\rho_{\text{cla}}(\boldsymbol{R})$. In the case of a quantum system, in theory this can be done using the exact many-body density matrix. However, the task of computing the exact free energy of a generic quantum system is far from being easy and one usually need to rely on some kind of approximations. When doing so, it is useful to exploit Gibbs-Bogoliubov variational principle on the free energy, which states that given a generic trial density matrix $\tilde{\rho}$, the free energy functional $\mathcal{F}[\tilde{\rho}]$ is bounded by the true free energy $F$ of the system:

$$\mathcal{F}[\tilde{\rho}] = E[\tilde{\rho}] - TS[\tilde{\rho}] \geq F \tag{2.2}$$

where $S[\tilde{\rho}]$ is the entropy and

$$E[\tilde{\rho}] = \langle K + V(\boldsymbol{R}) \rangle_{\tilde{\rho}} \tag{2.3}$$

is the total energy of the system calculated with the trial density matrix $\tilde{\rho}$, where we defined the quantum average for a generic operator $\cdot$ as $\langle \cdot \rangle_{\tilde{\rho}} = \text{Tr}[\tilde{\rho}\, \cdot]$. It is thus possible, in theory, to obtain the true free energy $F$ of the system minimising the functional $\mathcal{F}[\tilde{\rho}]$. However, performing the optimization on any possible trial density matrix is an unfeasible task due to its many-body character. In order to ensure a reliable estimate of $F$, the choice for $\tilde{\rho}$ should be guided by physical intuition while at the same time yielding an optimal parametrization for the minimization procedure.

The intuition behind the SCHA is that atoms vibrate around fixed equilibrium positions even in the most strongly anharmonic crystals, hence the best candidate for the variational principle is the Gaussian distribution, as it is the least biased quantum distribution, with fixed average positions and fluctuations[73]. Following this idea, the SCHA approach consists in considering only Gaussian distributions $\tilde{\rho}_{\boldsymbol{\mathcal{R}},\boldsymbol{\Phi}}$ among all the possible trial density matrices. The indexes $\boldsymbol{\mathcal{R}}$ and $\boldsymbol{\Phi}$ are the variational parameters: the former, called *centroids*, correspond to the average atomic positions whereas the latter correspond to the quantum-thermal fluctuations around them. Just like any Gaussian is defined by the average and mean square displacement, these parameters allow to uniquely identify the Gaussian density matrix $\tilde{\rho}_{\boldsymbol{\mathcal{R}},\boldsymbol{\Phi}}(\boldsymbol{R}) = \langle \boldsymbol{R} | \tilde{\rho}_{\boldsymbol{\mathcal{R}},\boldsymbol{\Phi}} | \boldsymbol{R} \rangle$ which determines the probability to find the atoms in the configuration $\boldsymbol{R}$ and can be imagined as the quantum analogue of $\rho_{\text{cla}}(\boldsymbol{R})$. An advantage of this approach stems from the the fact that it gives an intuitive physical interpretation. Indeed, any Gaussian density matrix $\tilde{\rho}_{\boldsymbol{\mathcal{R}},\boldsymbol{\Phi}}$ that describes a physical system is the equilibrium solution of an harmonic Hamiltonian $\hat{\mathcal{H}}_{\boldsymbol{\mathcal{R}},\boldsymbol{\Phi}}$ defined as

$$\hat{\mathcal{H}}_{\boldsymbol{\mathcal{R}},\boldsymbol{\Phi}} = K + \frac{1}{2} \sum_{a,b}^{3N_{\text{at}}} \left( \hat{R}_a - \mathcal{R}_a \right) \Phi_{a,b} \left( \hat{R}_b - \mathcal{R}_b \right), \tag{2.4}$$

where $\hat{\boldsymbol{R}}$ is the position operator, the centroids $\boldsymbol{\mathcal{R}}$ correspond to the average atomic positions and $\boldsymbol{\Phi}$ to a positive-definite force constant tensor. In particular, at a given temperature $\beta$, the relation between $\tilde{\rho}_{\boldsymbol{\mathcal{R}},\boldsymbol{\Phi}}$ and $\hat{\mathcal{H}}_{\boldsymbol{\mathcal{R}},\boldsymbol{\Phi}}$ is:

$$\tilde{\rho}_{\boldsymbol{\mathcal{R}},\boldsymbol{\Phi}} = \frac{\exp\{-\beta\hat{\mathcal{H}}_{\boldsymbol{\mathcal{R}},\boldsymbol{\Phi}}\}}{Z_{\boldsymbol{\mathcal{R}},\boldsymbol{\Phi}}}, \tag{2.5}$$

with

$$Z_{\boldsymbol{\mathcal{R}},\boldsymbol{\Phi}} = \mathrm{Tr}\left[\exp\{-\beta\hat{\mathcal{H}}_{\boldsymbol{\mathcal{R}},\boldsymbol{\Phi}}\}\right]. \tag{2.6}$$

A part for the intuitive physical picture it gives, the introduction of an auxiliary harmonic Hamiltonian allows us to have an analytical expression for both the kinetic part $\langle K\rangle_{\tilde{\rho}_{\boldsymbol{\mathcal{R}},\boldsymbol{\Phi}}}$ and the entropy $S[\tilde{\rho}_{\boldsymbol{\mathcal{R}},\boldsymbol{\Phi}}]$, entering in the variational principle in Equation (2.2), in terms of $\boldsymbol{\Phi}$ only. The power of the SCHA, hence, relies on the fact that the only resource-demanding quantity to calculate is the average value of the potential

$$\langle V(\boldsymbol{R})\rangle_{\tilde{\rho}_{\boldsymbol{\mathcal{R}},\boldsymbol{\Phi}}} = \int \mathrm{d}\boldsymbol{R} V(\boldsymbol{R})\tilde{\rho}_{\boldsymbol{\mathcal{R}},\boldsymbol{\Phi}}(\boldsymbol{R}). \tag{2.7}$$

We highlight that this approach allows us to include quantum effects because of the quantum nature of $\tilde{\rho}_{\boldsymbol{\mathcal{R}},\boldsymbol{\Phi}}$ and to include effects of anharmonicity at all orders since the BO potential entering Equation (2.7) is exact.

### 2.2.1 Stochastic implementation

To sum up, thanks to the SCHA, the most time-consuming part of the problem of finding the free energy of a system, accounting also for quantum and anharmonic fluctuations of the ions, is reduced to the calculation of the quantum average of the Born-Oppenheimer energy landscape $V(\boldsymbol{R})$ with respect to a gaussian density matrix. In order to obtain the equilibrium configuration of the system in the SCHA, it is necessary to minimize the free energy functional with respect to the free parameters. To do so, the minimization algorithm requires both the values of the functional and of its derivatives with respect to $\boldsymbol{\mathcal{R}}$ and $\boldsymbol{\Phi}$. The procedure and the code adopted to obtain the results presented in this work is described in Ref.[73], that we now briefly illustrate. Starting with an initial guess on $\boldsymbol{\mathcal{R}}$ and $\boldsymbol{\Phi}$, the algorithm proceeds as follows:

- extracts an ensemble of $N_\mathrm{C}$ random nuclear configurations in a supercell, using the trial Gaussian probability distribution function $\tilde{\rho}_{\boldsymbol{\mathcal{R}},\boldsymbol{\Phi}}(\boldsymbol{R})$;
- computes the total energies and the forces for each nuclear configuration in the ensemble. This can be done with an external code, e.g. an ab-initio engine or a force field;
- knowing the total energy and the forces, it computes the free energy functional and its derivatives with respect to the free parameters $\boldsymbol{\mathcal{R}}, \boldsymbol{\Phi}$;

- updates $\boldsymbol{\mathcal{R}}$ and $\boldsymbol{\Phi}$ to minimize the free energy.

These steps are repeated until the minimum of the free energy is found, in particular it can be demonstrated that the optimal free energy is reached when the following self-consistent equations are satisfied:

$$\left\langle \frac{\partial^2 V}{\partial R_a \partial R_b} \right\rangle_{(0)} = \Phi^{(0)}_{a,b} \tag{2.8}$$

$$\langle f_a \rangle_{(0)} = 0 \tag{2.9}$$

where (0) indicates equilibrium quantities and

$$\boldsymbol{f}(\boldsymbol{R}) = -\frac{\partial V(\boldsymbol{R})}{\partial \boldsymbol{R}} \tag{2.10}$$

are the forces. The integrals of space-dependent quantities $O(\boldsymbol{R})$, e.g. the quantum averages of energies and forces, are computed with a Montecarlo approach:

$$\int \mathrm{d}\boldsymbol{R} O(\boldsymbol{R}) \tilde{\rho}_{\boldsymbol{\mathcal{R}},\boldsymbol{\Phi}}(\boldsymbol{R}) \simeq \frac{1}{N_\mathrm{C}} \sum_{\mathcal{I}=1}^{N_\mathrm{C}} O(\boldsymbol{R}_{(\mathcal{I})}), \tag{2.11}$$

where $\boldsymbol{R}_{(\mathcal{I})}$ is one of the randomly extracted configurations. To further cut down the computational cost of the algorithm, one can reduce the number of calls to the force-energy engine calculator – the most expensive part – using techniques such as histogram reweighting to exploit the same values of forces and energies for multiple steps: for more details see Ref.[73]. Alternatively, another way to speed-up the computation is to use reliable force-fields instead of ab-initio codes when this is possible, as in the case of the 1D chain model.

### 2.2.2 Self-consistent harmonic approximation on the model

In order to account for quantum fluctuations, anharmonicity and finite-temperature effects on the properties of 1D systems, we use the stochastic implementation of the SCHA on the 1D model. In this framework, the BO energy surface is the total energy computed in the tight binding approximation described in Chapter 1. As discussed in the previous section, the minimization procedure requires to generate several supercells with atoms arranged according to a Gaussian probability distribution. As a starting guess, we uses the dynamical matrices of the system, computed with the standard approach of expanding the BO energy surface in the harmonic approximation around minima of the potential. In this way, we are ensured that the starting distribution are Gaussian. After the generation of the first ensemble of configurations, all subsequent calculation of energy and forces are done keeping all perturbative orders of the BO potential, in the spirit of the SCHA. Details on how to compute dynamical matrices in the harmonic approximation in the model are described in Appendix A. As previously discussed, values of model parameters

used for SSCHA calculations are obtained fitting quantities of the model on DFT calculations of carbyne, as described in section 1.3. The advantage of using the fitted-model as a force-field for SSCHA calculations relies in a significant reduction in terms of time needed for the calculations, while keeping the same accuracy as with ab-initio engines on real systems. Numerical details regarding the minimization procedure are also described in Appendix A.

## 2.3 Effects on carbyne

Being a physical realization of a 1D CDW, carbyne is a perfect system for studying the physics of this phenomenon. Indeed, the interest in understanding the behaviour of CDWs is transverse as they manifest in many other 1D systems such as conductors[26] or in charge-transfer organic salts[27, 28], as well as in 2D materials[2, 3], high-$T_c$ superconductors[4] and transition metal dichalcogenides[5]. In this section we study the role of quantum-anharmonicity on the CDW in carbyne with the aid of the SSCHA on the toy-model.

### 2.3.1 Zero-point energy renormalization

To test the predictive power of SSCHA results obtained with the fitted model, we study QAE on the energetic competition between the cumulene and the polyyne phases in carbyne, where we remind that cumulene is the high-symmetric structure where carbon atoms are equidistant whereas polyyne is the low-symmetric one, characterized by a bond-length alternation. Indeed, as recently pointed out in Ref.[17] using ab-initio plus SSCHA calculations, even at zero temperature QAE in carbyne reduce the energy gain of the polyyne phase with respect to the cumulene one by $\sim 70\%$, due to zero-point energy renormalization. To check whether the fitted-model correctly reproduce this behaviour, we study the $T = 0\,K$ energy profile of the chain as a function of atoms relative displacement, quantified by the BLA. In Figure 2.1 it can be observed that the results obtained including QAE in the model show good agreement with those taken from [17], obtained instead with ab-initio forces and energies. This result confirms the model as a reliable tool for accurate QAE-corrected calculations, as reliable as ab-initio ones, while ensuring a significant reduction of the computational time. Finally, we also notice how the value of relative displacement which minimizes the energy is also affected by QAE, implying that in order to correctly describe structural properties, it is necessary to account for quantum-anharmonicity, as will be further explored in next sections.

### 2.3.2 Temperature effects on the charge density wave

After having assessed the magnitude of QAE on the energetic competition between cumulene and polyyne in the limiting case of zero temperature, in this section we study the role of finite temperature in carbyne with the aim of characterising the

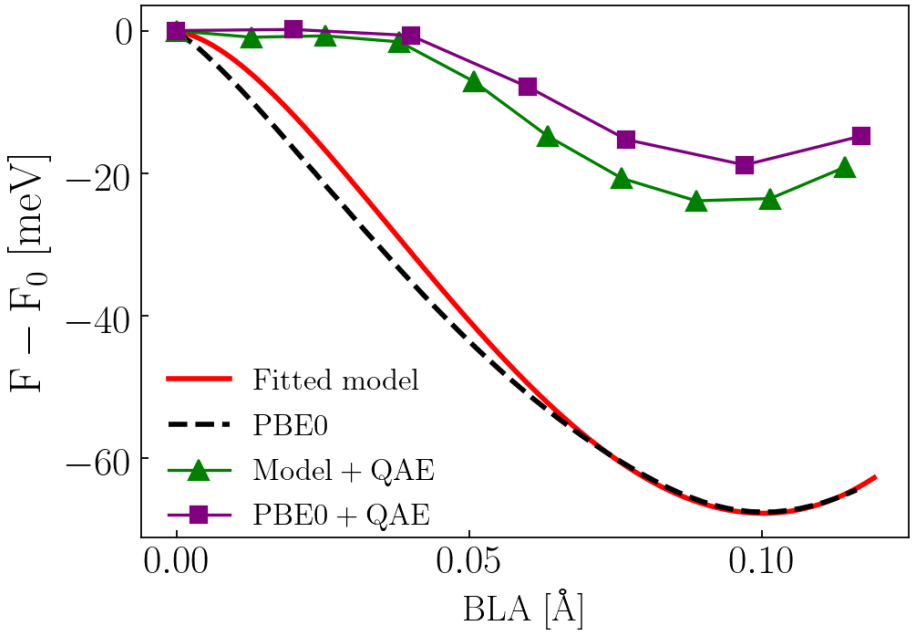


**Figure 2.1.** The inclusion of quantum-anharmonic effects at $T = 0\,K$ reduces the energy gain of the polyyne phase with respect to cumulene of $\sim 70\%$. The treatment of QAE is thus fundamental in the characterization of systems with light atoms and highly anharmonic potentials such as carbyne. In doing this, the 1D toy-model is a reliable tool as it allows for a reduction of the computational cost while yielding results as good as those obtained ab-initio (PBE0+QAE data are taken from Ref.[17]).

temperature-behaviour of its CDW. It is generally understood, e.g. in the framework of the Frölich model[25, 24], that for temperatures below a critical value $T_{\mathrm{CDW}}$, carbyne manifests in the polyynic distorted phase as a consequence of the Peierls electronic instability and of the finite e-ph coupling, whereas the cumulene phase can be stabilized only at $T > T_{\mathrm{CDW}}$. According to the Landau-Peierls picture[88, 89, 21], this metal-insulator transition is of second order. However, at date, it has never been observed and cumulene remains an elusive state of carbyne. Recent calculations performed including QAE on PBE0 results[17], seem to point in a completely different direction: it is argued that the metal-insulator transition is actually of *first order*, with the polyyne phase stable for temperatures much higher than the predicted $T_{\mathrm{CDW}} \simeq 75\,K$. This result would explain the difficulty in finding the cumulenic phase. In order to verify this hypothesis, we exploit the computational advantage guaranteed by the fitted-model with respect to ab-initio codes to study the temperature-dependent behaviour of the CDW in carbyne. In particular, since the signature of the CDW in this system is the resulting periodic lattice modulation, we study how the BLA of the systems varies with temperature.

To start, we perform the first structural minimization at $T = 0\,K$ and, as expected, we find that the polyyne phase is the most stable. Successively, in order to correctly account for the presence of meta-stable states, as it should be done

to characterize first-order phase transitions, for increasing values of $T$, we use the final dynamical matrices of the previous temperature-dependent minimization as the starting probability distribution for the following one. As shown in Figure 2.2, at $T \simeq 5000\,K$ the cumulene phase becomes eventually energetically favorable and the BLA disappears. Then, from the undistorted phase, we perform minimizations for decreasing temperatures, up to $T = 0\,K$. Interestingly, it appears that cumulene is (meta-)stable up to $T \simeq 600\,K$, when the electronic instability eventually makes the polyyne phase the optimal one and the site-centered CDW appears again. These results are consistent with the fact that cumulene has never been experimentally detected, as even in its (meta-)stable phase does not survive at room temperature $T_{\text{room}} = 300\,K$. We also remark how the two temperatures where the transitions occur differ of one order of magnitude, as highlighted by the wide hysteresis cycle in Figure 2.2, and consistently with the picture of a first-order phase transition where two distinct phases may coexist. Finally, we also study the temperature dependence of the free energy differences $\delta F = F_{\text{cooling}} - F_{\text{heating}}$ between minimized free energies $F_{\text{cooling}}$ obtained from the *cooling* cycle with respect to the $F_{\text{heating}}$ obtained from the *heating* one. In the range of temperatures where the phases coexist, the energy of the cumulene phase is generally higher with respect to that of the polyyne one, as shown in Figure 2.2. From a linear fit we identify the critical value $T_{\text{CDW}}^{\text{QAE}} \simeq 4300\,K$, where for $T > T_{\text{CDW}}^{\text{QAE}}$ cumulene is stabilized and becomes the most favorable configuration. Our results give an assessment of the robustness of the CDW, which survives up to high temperatures, much higher than $T_{\text{room}}$.

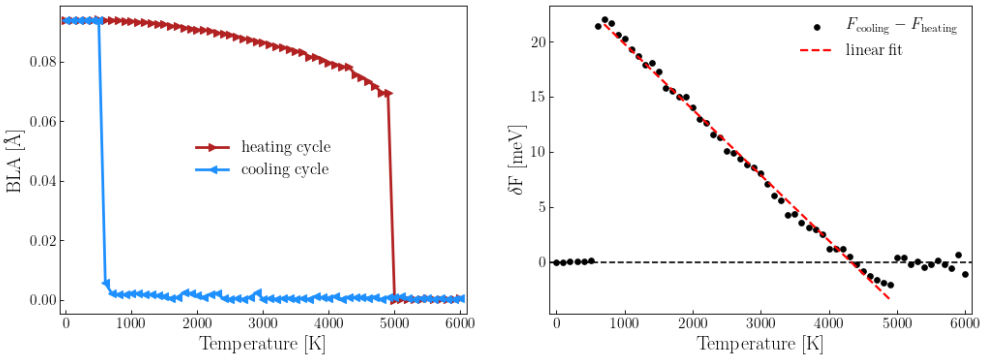


**Figure 2.2.** On the left panel, temperature dependence of the BLA in carbyne with the inclusion of QAE. Results suggest that the polyyne/cumulene transition is of *first order*, in contrast with the common Landau-Peierls picture. On the right panel, behaviour of free energy differences between structures obtained in the cooling cycle and structures from the heating cycle, as described in the text. From a linear fit, we deduce a $T_{\text{CDW}}^{\text{QAE}} \simeq 4300\,K$ above which the CDW melts and cumulene becomes stable.

## 2.4 Effects on carbyne-derived systems

From the results presented above, it appears evident that the inclusion of QAE is essential to study the properties of 1D systems and 1D CDWs. With this in mind, in this section we take a step further and study QAE on the structural properties predicted by the model for 1D chains. As discussed in section 1.2, breaking the equivalence between atoms ($\Delta \neq 0$) also contribute to the stabilization of the electronic instability, which in this case may induce a periodic lattice distortion only for finite and high-enough e-ph coupling. In absence of QAE, this competition results in a CDW with mixed site/bond-centered character, with consequences also on the polar properties of the system[32]. It the framework of the model, this competition manifests in a second order structural phase transition that can be controlled by model's parameter such as $\Delta$ and $\beta$. Since, as we have seen, structural properties and CDWs robustness are affected by QAE and temperature, in this section we focus on the role of quantum-anharmonicity on these phenomena.

As discussed in section 1.3, it is possible to break atoms equivalence in carbyne (at least theoretically). For this reason and for consistency with the above presented results, we still adopt the parameters of the fitted-model for what follows. Indeed, we argue that the fact that the model may accurately describe many other 1D systems similar to carbyne (e.g. other conjugated polymers as PA and SPA) guarantees that the results here presented can be regarded as a reliable indication – at least qualitatively – of the impact of QAE on such 1D systems.

### 2.4.1 Zero-point energy effects on the structural phase transition

We remind that, in the framework of the model, the optimal configuration – namely the optimal relative displacement between neighbouring atoms – is quantified by the $\overline{u}$ which minimizes the total energy of the system $E_{\text{tot}}(u)$ for a given set of parameters. This is still the case if we add QAE with the SSCHA, the only difference being that now the optimal $\overline{u}$ is obtained minimizing the free energy $F(u)$ for a given set of parameters. However, for consistency with the previous section, we will quantify atoms relative displacement using the BLA, a quantity with dimensions of a length proportional to $\overline{u}$ via the relation $\text{BLA} = 2a\overline{u}$, where $a$ is the unit cell length.

As a first step, we perform SSCHA minimizations at zero temperature, varying $\Delta$ or $\beta$ separately, in order to quantify the zero-point energy effects on the transition, or stated in other words to account for the quantum behaviour of the atoms. First, keeping $\beta$ fixed at the value obtained from the fitting procedure, we study the behaviour of $\overline{u}(\Delta)$ and show the results in Figure 2.3. In particular, the first minimization is done for pure carbyne ($\Delta = 0$), using as a starting probability distribution the dynamical matrices obtained in the harmonic approximation on the model. Similarly to the case where QAE are neglected, we found a finite $\overline{u} \neq 0$, however its value has changed, as a result of accounting for the quantum

nature of nuclei. Successively, we perform minimizations for increasing values of $\Delta > 0$, adopting as a starting guess for each minimization the final dynamical matrices obtained at the end of the previous one. For a high enough value of $\Delta$, we observe that the optimal configuration of the system becomes the high-symmetric undimerized one ($\overline{u} = 0$), hinting the presence of a phase transition. To have a complete characterization of the QAE-behaviour of $\overline{u}(\Delta)$, starting from the undimerized phase, we then perform minimizations for decreasing values of $\Delta$, up to $\Delta = 0$. We observe that eventually the system breaks the spatial symmetry to end up in the distorted phase ($\overline{u} \neq 0$). However, as can be observed in Figure 2.3, this $\Delta$-decreasing transition takes place at a different value of onsite energy with respect to the $\Delta$-increasing one, as highlighted by the presence of an hysteresis cycle.

To have an estimate of the new $\Delta_c^{\mathrm{QAE}}$, we compare the minimized free energies of the system obtained at each step of the hysteresis cycle. In Figure 2.3, it can be observed that in the range of values where the system present a coexistence of phases, the free energy $F_{\mathrm{decr.}}$ of the $\Delta$-decreasing path is higher with respect to the $F_{\mathrm{incr.}}$ of the $\Delta$-increasing one up to the value of $\Delta \simeq 0.47$ev, after which it becomes smaller. The two free energies eventually coincide again starting from $\Delta \simeq 0.5\,\mathrm{eV}$. From a linear fit, we estimate a $\Delta_c^{\mathrm{QAE}} \simeq 0.47\,\mathrm{eV}$ which separates the distorted phase from the undistorted one. Comparing this result with the value $\Delta_c \simeq 0.71\,\mathrm{eV}$, obtained without the inclusion of QAE, we conclude that quantum-anharmonicity renormalizes the critical value of the second order structural phase transition of more than 30%.

As described in section 1.2.1, keeping a fixed $\Delta \neq 0$ it is possible to control the transition acting also on the e-ph coupling parameter $\beta$. So, with a similarly procedure as the one described above, we performed SSCHA minimizations for different values of $\beta$ in order to characterize the quantum-anharmonic behaviour of $\overline{u}(\beta)$. The results are shown in Figure 2.3 (for $\Delta = 0.72\,\mathrm{eV} > \Delta_c$), and we observe that as in the previous case, the inclusion of QAE shifts the critical point of the transition to $\beta_c^{\mathrm{QAE}} \simeq 7.75\,\mathrm{eV/\AA}$.

### 2.4.2 Quantum-anharmonic phase diagram

Finally, we relax the $T = 0\,K$ hypothesis and compute the quantum-anharmonic finite-temperature phase diagram of this carbyne-derived systems. With the term phase diagram, we mean that for different realizations of the system, namely changing the parameters $\Delta$ and $\beta$ separately, we study the favorable configuration between the distorted and the undistorted phases for different temperatures. In practice, we perform the same procedure described in section 2.3.2, each time for a different value of $\Delta$, at fixed value of $\beta$, or of $\beta$, at fixed value of $\Delta$. In this way we obtain different values of the critical temperatures $T_{\mathrm{CDW}}^{\mathrm{QAE}}$, because of the role played by $\Delta$ and $\beta$ in the CDW, as already discussed. In Figure 2.4, for some representative cases, it can be observed how varying $\Delta$ or $\beta$ affects the temperature behaviour of the BLA. In particular, the closer we get to $\Delta_c^{\mathrm{QAE}}$ or $\beta_c^{\mathrm{QAE}}$ from the distorted phases, the

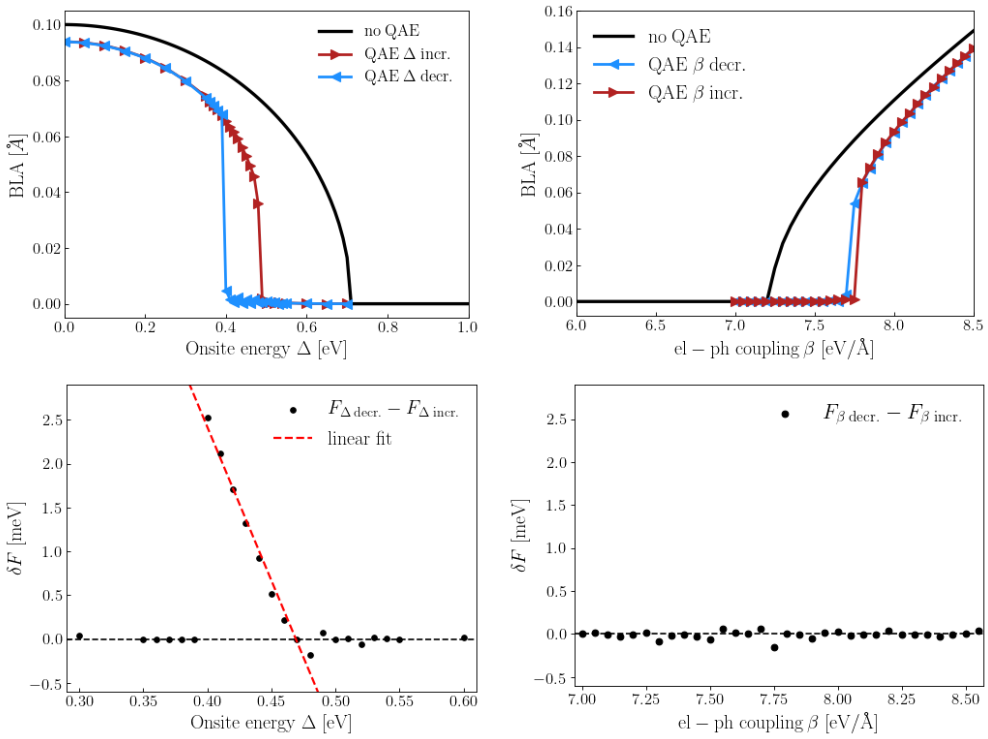


**Figure 2.3.** At $T = 0\,K$, effects of quantum-anharmonicity on the optimal structure of the model fitted for carbyne-derived systems. Pushed from the results obtained for the temperature-dependent behaviour of the CDW in pure carbyne, we performed $\Delta$-increasing and $\Delta$-decreasing cycles (same for $\beta$), as described in the text, in order to test the presence of meta-stable states. On top-left panel, behaviour of atoms relative displacement (quantified by the optimal BLA) for different values of onsite energies $\Delta$, with and without the inclusion of QAE. On top-right panel, the same behaviour is studied varying the e-ph coupling parameter $\beta$ keeping a fixed $\Delta = 0.72\,\text{eV}$. In both cases, inclusion of QAE shifts the critical value of the structural phase transition. For the transition in $\Delta$, a new critical value $\Delta_c^{\text{QAE}} \simeq 0.47\,\text{eV}$ is obtained from a linear fit of the free energy differences between the $\Delta$-decreasing and the $\Delta$-increasing cycles, as detailed in the text and shown in the lower left panel. For the transition in $\beta$, free energy differences shown in the lower right panels are of the order of 0.1 meV. Indeed, the range of phases coexistence is small enough to deduce a $\beta_c^{\text{QAE}} \simeq 7.75\,\text{eV/Å}$.

lower the critical $T_{\text{CDW}}^{\text{QAE}}$ for the melting of the bond-centered CDW becomes. The collection of all the different critical temperatures allow for the definition of two phase diagrams, presented in Figure 2.5, one obtained varying $\Delta$ with fixed $\beta$, the other varying $\beta$ with fixed $\Delta$.

From a practical point of view, the results here discussed – whose validity, we argue, holds beyond the case of carbyne-based systems – suggest a mechanism to control structural properties of 1D systems acting on parameters such as the chemical composition of a conjugated polymer, the dielectric environment and temperature. As will be shown in next Chapter, polar properties, in particular polar responses such as effective charges and piezoelectricity, can be greatly enhanced in proximity

of the critical points of the structural phase transition, putting these 1D systems forward as promising functional materials.

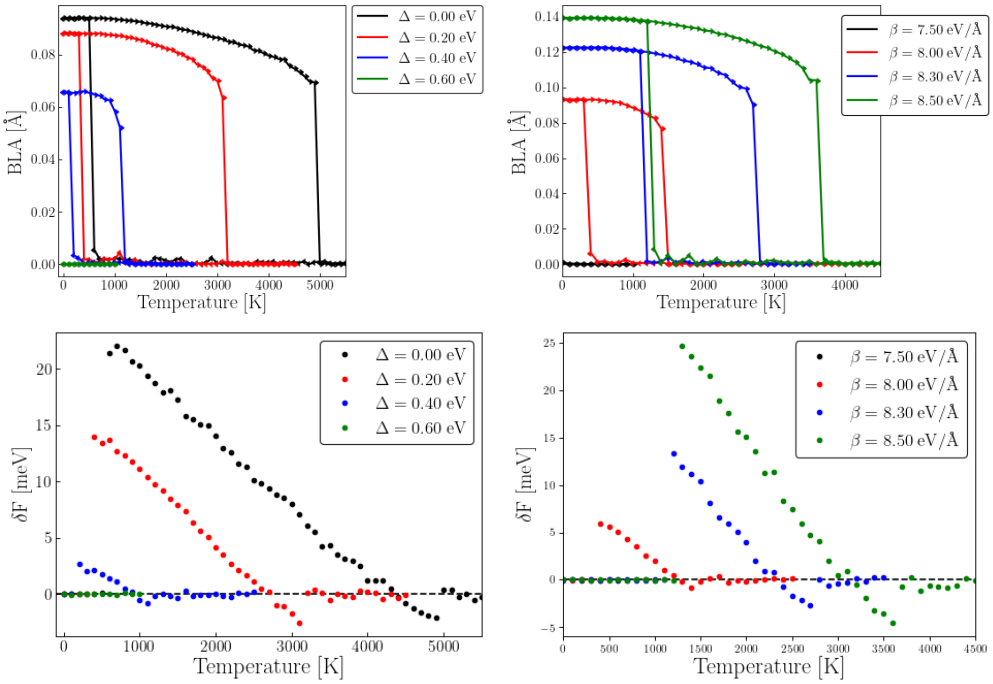


**Figure 2.4.** Effects of temperature on the optimal structure of carbyne-derived systems. On the top left and right panels, for different values of onsite energy $\Delta$ and e-ph coupling parameter $\beta$ respectively, are shown the behaviours of the BLA with respect to the temperature for both heating and cooling cycles. We observe how the closer we get to the respective critical values $\Delta_c^{\mathrm{QAE}} \simeq 0.47\,\mathrm{eV}$ and $\beta_c^{\mathrm{QAE}} \simeq 7.75\,\mathrm{eV/Å}$, the weaker the CDW becomes and the cumulene phase may be stabilized at lower temperatures. From the study of the free energy differences between the structures obtained from the cooling cycle and those obtained from the heating cycles, lower left and right panels, we deduce the behaviour of $T_{\mathrm{CDW}}^{\mathrm{QAE}}(\Delta)$ and $T_{\mathrm{CDW}}^{\mathrm{QAE}}(\beta)$.

## 2.5 Conclusions

In this Chapter we presented our results on the effects of quantum-anharmonicity on the properties of 1D systems, obtained applying the stochastic self-consistent harmonic approximation on the fitted-model. For the prototypical case of carbyne, we found that QAE are responsible for a renormalization of $\sim 70\%$ of the energy gain between the distorted polyyne phase with respect to the undistorted cumulene one. Moreover, polyyne is found to be the most favorable configuration for a wide range of temperatures up to $T_{\mathrm{CDW}}^{\mathrm{QAE}} \simeq 4300\,K$, where cumulene finally becomes stable. In particular, the transition between these two phases, theorized but never observed, is found to be of first order, in contrast with the common Landau-Peierls picture of a second order phase transition. It is however still possible to stabilize a high-symmetric phase in carbyne-derived systems exploiting other mechanisms,

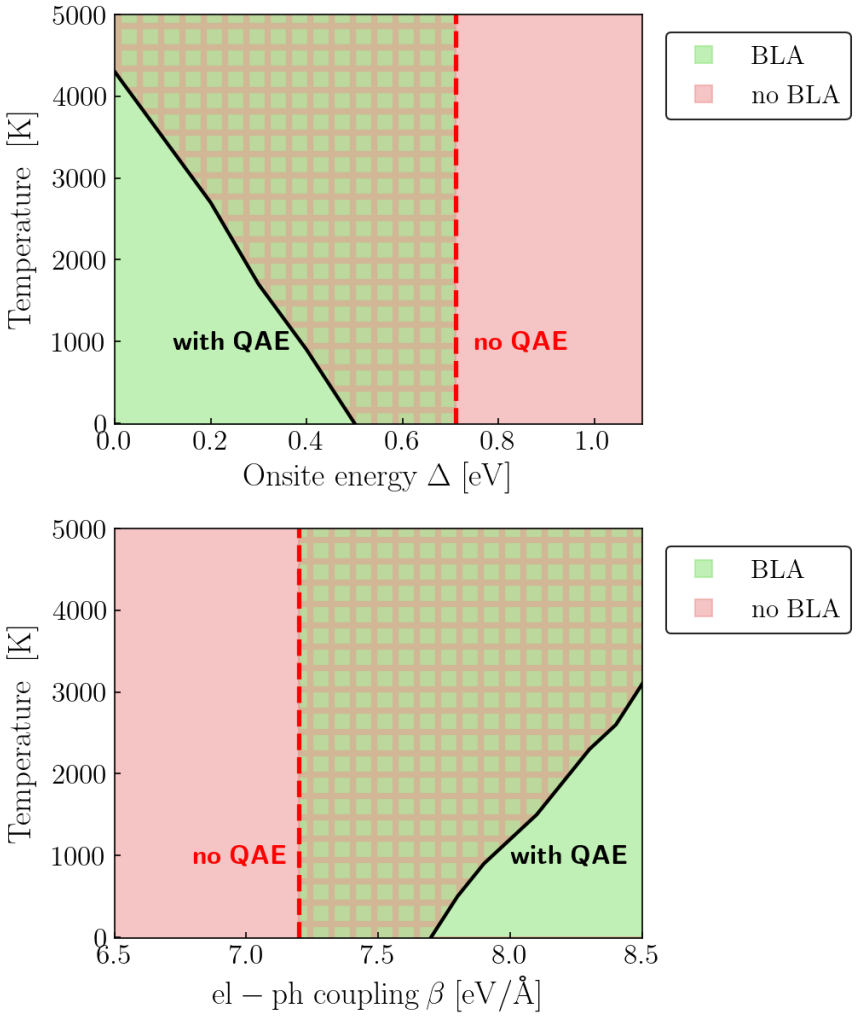


**Figure 2.5.** In the upper panel, phase diagram obtained varying $\Delta$ while keeping $\beta$ fixed at the value obtained form the fit of section 1.3. In the lower panel, phase diagram obtained varying $\beta$ with a fixed $\Delta = 0.72$ eV. Different colors correspond to different structures. Regions with overlapping colors indicate that the predictions are different if we account for QAE or not. The black lines correspond to the behaviour of $T_{\text{CDW}}^{\text{QAE}}(\Delta)$ and $T_{\text{CDW}}^{\text{QAE}}(\beta)$, obtained as described in the text. The vertical red lines are in correspondence of the critical values obtained from the $T = 0\ K$ calculations without QAE in the model.

e.g. breaking the equivalence between carbon atoms or varying the electron-phonon coupling. Moreover, QAE are also found to contribute stabilizing Peierls electronic instability even at $T = 0\,K$, as highlighted by the reduction of the critical value $\Delta_c^{\text{QAE}}$ of the second order structural phase transition. The validity of these results is guaranteed by a comparison with ab-initio plus SSCHA results on carbyne[17]. Finally, we argue that the conclusions we presented, hold even for other systems beyond carbyne, given that they are described by the 1D model, e.g. polyacetylene and substituted polyacetylenes.

# Chapter 3

# Polar responses

## Chapter overview

In Chapter 3 we present our results on the behaviour of polar response properties in 1D conjugated systems. In section 3.1 we briefly discuss what we intend with polar responses and their relation with the concepts introduced in previous Chapters. Then, in section 3.2 we focus on the response of polarization with respect to an atomic displacement, quantified by the so-called effective charges. We show how the intrinsically topological nature of polarization in the model gives rise to a peculiar enhancement of the effective charges in correspondence of the critical point of the phase transition. Next, in section 3.3, we analyze the response of the system with respect to a homogeneous deformation, namely a strain. Quantified by the so-called piezoelectric coefficients, the electro-mechanical response of these systems benefits both from the topological enhancement of the effective charges and from the second order structural phase transition. As discussed in Chapter 2, quantum-anharmonic effects have a huge impact on the properties of the model. In section 3.5 we discuss how they affect previously introduced polar responses. Finally, in section 3.6, we test predictions of the model with numerical calculations in the framework of density-functional theory on prototypical conjugated polymers. Conclusions are drawn in section 3.7.

## 3.1 Introduction: polar responses and charge density waves

In previous Chapters, we explored relevant properties of 1D systems, analyzing the underlying elements at play. A particular aspect we discussed is what determines atoms disposition in a linear diatomic chain and how this is related to the manifestation of a charge density wave, namely a modulation of the electronic charge density distribution. Strictly connected both to the way atoms are arranged and to the character of the CDW in these 1D systems, we find their polar properties. For

instance, we saw how if specific requirements are satisfied, some 1D linear chains may become ferroelectric, displaying a spontaneous polarization. Given these evidences on the strong relation between structural and polar properties in 1D systems, it comes natural to further explore this aspect and study polar responses of 1D systems. For a *polar response*, we intend a phenomenon that can be ascribed to a change in the distribution of electric dipoles within a material, as a consequence of an external perturbation such as atoms displacement, a mechanical stress, or also an applied electric field. From a practical point of view, the effects of these external perturbations can be quantified as linear variations of polarization in the material. Following this approach, in what's next we define polar responses as derivatives of polarization.

Several ingredients are at play in determining polar responses of a system, depending on material properties as well as on the specific perturbation considered. In general, it is a known fact that CDWs have the effect of enhancing polar responses in materials through mechanisms that involve symmetry breaking, strong electron-phonon coupling[90, 6], as well as external tuning via strain or electric fields[91]. The interplay between CDWs formation and polar response is particularly pronounced in materials where these effects are intrinsically coupled, as the conjugated systems we are analyzing, often resulting in functional properties useful for advanced electronic and optoelectronic applications.

To give a practical example of these concepts, let's consider the case of conjugated polymers. If specific symmetry-lowering effects allowing, e.g., for piezoelectricity and ferroelectricity are met in a CP, one may expect a large polar response of electronic origin due to the redistribution of the responsive $\pi-$electronic density along the polymer's backbone. Because of the delocalized nature of conjugated $\pi-$state (of Bloch-type in an infinite periodic chain), small changes of atomic positions may lead to a global shift of electrons, revealing the strong nonlocal and ultimately topological character of electronic polarization in these quasi-1D systems[92, 31]. Indeed, conjugated polymers have been theoretically put forward as a potential new class of "electronic ferroelectrics"[93].

Finally, we remark that, as thoroughly discussed in Chapter 2, quantum-anharmonic effects have a significant impact on the properties of these systems. For this reason, a complete study of polar responses in 1D conjugated systems cannot be done without including QAE, as we eventually do in the present Chapter.

## 3.2 Effective charges

When a large number of interacting atoms is considered, e.g. in molecules and crystals, the correct description and understanding of the properties of matter is often challenging. For example, defining the electric charges of isolated, non-interacting ions is quite straightforward. The same can be said for the electric current generated when these isolated ions move in space. If we now consider a molecule or a crystal,

defining an electric charge associated to a single ion is a much more complicated problem because of the presence of interactions. During time, several definitions have been proposed, inspired by the description of different physical phenomena and based on various models, which, however, lead to different results[94]. The main concepts behind these different definitions can be classified into two categories: one one hand we wave approaches based on the idea of *static* charges, whereas on the other we have the *dynamical* charges. The former concept of a static ionic charge is based on the intuitive idea of partitioning the ground-state electronic density into different contributions, each attributed to a different atom. This approach is particularly reliable when it is possible to delimit regions around ions in such a way that the electron density between different regions is small compared to the reciprocal of the volume enclosed. If this is the case, an unambiguous experimental determination can be done, e.g., with X-rays diffraction[95]. However, if for example we consider a crystal with covalent bonding, this *static* definition would depend on the choice of the partitioning, resulting in ambiguity in the definition of the atomic charge. The concept of dynamical charge, instead, is directly related to the change of polarization (or dipole moment, for molecules) induced by an atomic displacement. The advantage of this approach is that, in principle, the change of polarization can be experimentally measured as an electric current, giving the dynamical charge a well-defined and unambiguous character. For this reason, in our work we follow the idea of assigning an *effective charge* to the atoms quantifying how rigidly the electronic charge distribution follows the displacement of the nuclei. In particular, for each atom in a molecule or in a crystal it is possible to associate a rank-2 tensor of effective charges $Z^*_{I,\alpha\beta}$, where the index $I$ refers to the ions in the molecule or in the crystal cell, whereas Greek letters indicate directions in the Cartesian space. This quantity can be decomposed in two contributions: a trivial one is due to the rigid shift of the nominal ionic charges; the non-trivial contribution is instead due to the redistribution of the electronic charge density as a consequence of the interaction with ionic vibrations. In ordered periodic collections of atoms arranged in a lattice structure, namely in solid crystals, this is the so-called electron-phonon interaction that we already discussed.

Being involved in the response of the electronic charge density distribution to atomic displacements, effective charges play a crucial role in the understanding of many phenomena. One of the most studied is the interaction between external electromagnetic fields and ionic vibrations. In particular, given that phononic frequencies typically reside in the infrared spectral region, these charges are essential for studying systems' interaction with infrared light. Indeed, as discussed e.g. in Ref.[23] about absorption and transmission spectra, incorporating effective charges is vital for matching theoretical predictions with experimental results. Another phenomenon where the effective charges are relevant is piezoelectricity, the property of a material to generate a finite tension across its surfaces in response to a finite strain, as we will further discuss in section 3.3.

As described e.g. in Ref.[96], there are two principal mechanisms that account for the redistribution of electronic charge density due to atomic displacements: one is the rigid displacement of the electronic density, following the moving ion; the other consists in the interatomic charge transfer of electrons involved in the bonds, as discussed for example in Ref.[97]. Which mechanism is predominant depends on the characteristics of the system, as shown for example in Ref.[98] for perovskite oxides. This competition is particularly interesting in linear chains with a resonant bonding, such as conjugated polymers: in Ref.[92], e.g., it is shown how resonating systems may present a huge interatomic charge transfer. In what follows, we will study the effective charges in the chain 1D toy-model, showing how the enhancement of the polar response has an ultimately topological origin, directly related to the mechanism of Thouless adiabatic pumping we discussed in section 1.2.2.

### 3.2.1 Topological effects

As already discussed, systems described in the framework of the model introduced in Chapter 1 can be imagined as 1D crystals made by the repetition of a unit cell with two atoms, $A$ and $B$. A part from the case where these atoms are at the same time equidistant ($\overline{u} = 0$) and equivalent ($\Delta = 0$), a condition that as we have seen is prevented by the insurgence of the structural phase transition, the chain is always insulating. Hence, in what follows, our discussion will focus on the theory of effective charges in insulators only. Moreover, we consider the case of zero macroscopic electric field, allowing us to define the so-called Born, or transverse, effective-charges[99], a central quantity in many phenomena, e.g., in the LO-TO splitting of optical phonons modes. Following the works of Ref.[100, 101, 37] and the idea discussed in the introduction to this Chapter, we define effective charges for the atoms in the chain as first derivatives of the electronic polarisation with respect to atomic displacement. In particular, for atom $\alpha = A, B$ in the model, it holds

$$Z^*_\alpha = a\frac{\partial P}{\partial \delta r_\alpha}. \tag{3.1}$$

where since we are considering displacements along the chain only, the rank-2 tensor becomes a scalar and all the other terms have the meaning defined in Chapter 1: $a$ is the unit cell length, $\delta r_\alpha$ is the displacement of atom $\alpha$ with respect to the position it would have in a chain of equidistant atoms, and $P$ is the electric dipole per unit cell. Exploiting net charge neutrality ($Z^*_A + Z^*_B = 0$) and Equation (1.6) we can define a single effective charge $Z^*$ for the system, which is convenient to express in terms of the fractional coordinate $u = 2(\delta r_B - \delta r_A)/a$, namely:

$$Z^* = 2\frac{\partial P}{\partial u}. \tag{3.2}$$

We remind that the term $u$ has the meaning of relative displacement between the atoms, with respect to the high symmetry positions they would have if they were

equidistant: it holds $u = 0$ for equidistant atoms and $u \neq 0$ in presence of bond-length alternation. There are different ways to compute the first derivatives of $P$: analytically, with finite differences of polarization, with linear perturbation theory and so on. It is however interesting to recall the discussion of Chapter 1 on how the behaviour of $P$ in the model is strictly related to the adiabatic charge transport mechanism of the Thouless pump[10]. An aid to visualise this property comes from the 2D parametric $(\Delta, \delta t)-$space, where the origin of the axes correspond to a metallic system with $E_{\text{gap}} = 0$, while every other point correspond to an insulating system with $E_{\text{gap}} \neq 0$. As discussed in Chapter 1, if the system undergoes an adiabatic evolution along any loop enclosing the origin of this 2D space, a quantized charge is pumped out. The key ingredient is the presence of the metallic point in the domain enclosed by the loop: in this sense, it is an example of topological phenomenon. As we are interested in derivatives of polarization with respect to $u$ and considering that $\delta t \propto u$, intuitively we can visualize the slope of $P$ in the 2D-space as color gradients along lines parallel to the vertical axis: from Figure 3.1, it can be noticed that the quantization of polarization implies that the slope of $P$ depends from the distance with respect to the origin. In particular, the closer we get to the singularity from the undistorted structure ($\delta t = 0$), the higher the slope – i.e. the color gradient – becomes. We can formalize this idea as follows. In Equation (1.44) and (1.43) we introduced a change of coordinates that allows to identify each point in the 2D-space with the polar coordinates $(E_{\text{gap}}, \theta)$. Moreover, in the limit $E_{\text{gap}} \ll t$, the dipole moment per unit cell $P$ and $\theta$ are directly proportional, as reported in Equation (1.45), which we rewrite for convenience:

$$P \propto -\frac{|e|}{\pi}\theta. \tag{3.3}$$

This behaviour can be appreciated in Figure 1.4. Aiming to compute the derivative of $P$ with respect to $u$ – Equation (3.2) – we notice how the effect of a small displacement on a system with a finite $\Delta \neq 0$ is to span an angle $\mathrm{d}\theta$ in the space, starting from $\theta = 0$, i.e. the undistorted structure. Considering that $\delta t \propto u$ (Equation (1.10)) and that, with a suitable choice of the axis, the points on a circumference in this space correspond to systems with the same $E_{\text{gap}}$, we have that $\mathrm{d}\theta \propto u/E_{\text{gap}}$. From Equation (3.3), it holds $\mathrm{d}P \propto \mathrm{d}\theta$, hence we obtain

$$Z^* \propto \frac{1}{E_{\text{gap}}}, \tag{3.4}$$

implying that as we get closer to the origin of the axis – hence $E_{\text{gap}}$ goes to 0 – even an infinitesimal atomic displacement causes a huge redistribution of the charge density. This geometric argument can also be appreciated in Figure 3.1.

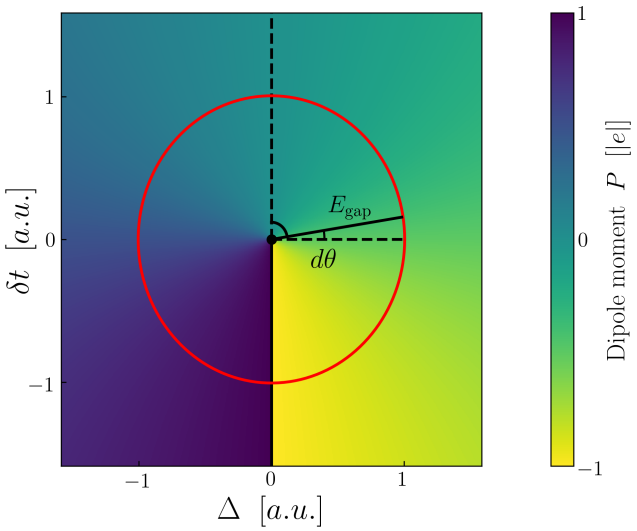


**Figure 3.1.** With the aid of the 2D parametric $(\Delta, \delta t)-$space introduced in the text, it is possible to appreciate the geometric argument that yields Equation (3.4). Being the polarization proportional to the angle $\theta$ spanning the space along a circumference with radius $E_{\text{gap}}$, as $\delta t \propto u$ (Equation (1.10)), it follows that in the undimerized phase $E_{\text{gap}} d\theta \propto du$, hence $Z^* = \partial P/\partial u \propto \partial\theta/\partial u \propto 1/E_{\text{gap}}$.

### 3.2.2 Effective charges and phase transition

The geometric argument presented above suggests using the energy gap $E_{\text{gap}} = \sqrt{(4\delta t)^2 + (2\Delta)^2}$ as a guiding principle in the design of systems with arbitrarily high effective charges. However, as discussed in Chapter 1, the optimal structure of the system is determined by the $\overline{u}$ which minimises the total energy $E_{\text{tot}}(u)$ for a given a set of parameters $\Delta$, $\beta$, $t$ and K. This implies that the energy gap, and consequently the effective charges, of a system at equilibrium at $T = 0\ K$, would depend on $\overline{u}$, namely on the specific realization of the chain, whether dimerized or undimerized. In particular, we remind that the system undergoes a second-order structural phase transition between a dimerized ($\overline{u} \neq 0$) phase and a phase with equidistant atoms ($\overline{u} = 0$). As shown in Chapter 1, it is possible to control the transition acting on the free parameters of the model, e.g. $\Delta$ and $\beta$. For convenience, we display again in Figure 3.3**a** and 3.3**b** the behaviour of $\overline{u}$ with respect to $\Delta/\Delta_{\text{c}}$ and $\beta/\beta_{\text{c}}$, respectively.

With this in mind, plugging Equation (1.10) in Equation (1.45), we obtain an explicit expression for the effective charge in both the dimerized and undimerized phases:

$$Z^*(\overline{u}) = \frac{|e|}{\pi} 4\beta t \frac{\sin\theta(\overline{u})}{E_{\text{gap}}(\overline{u})} \tag{3.5}$$

where we recall that $\sin\theta = 2\Delta/E_{\text{gap}}$. The evolution of $Z^*$ as a function of $\Delta/\Delta_{\text{c}}$ and $\beta/\beta_{\text{c}}$ is shown in Figure 3.3**c** and 3.3**d**. Even though the system always displays a finite gap preventing the metallic divergence of the effective charge, with the values

of the parameters fitted on carbyne as discussed in section 1.3, $Z^*$ reaches the giant value of $\sim 30\,|e|$ at the critical points. Such anomalously large effective charges can not be ascribed only to a mixed covalent-ionic character of the system, as in other cases[96]. As discussed in next section, tuning the bond character can indeed lead to a finite enhancement of the effective charges, which however is typically only few times the value of the nominal charge[96]. The origin of the enhancement of the effective charge in the model is thus different and lies in the topological character of polarization in the system, namely on the Thouless pump mechanism discussed in Chapter 1.

### 3.2.3 Comparison with dynamical charges of a heteropolar diatomic molecule

In this section we compute the dynamical charge of a heteropolar diatomic molecule along the lines discussed in Ref.[96], in order to contrast our predicted topological enhancement of effective charges in the model with the contribution of the mixed ionic-covalent character to "anomalous" Born effective charges. Let's consider a diatomic molecule with two monovalent atoms $A$ and $B$ positioned along the $x$-axis at a distance $d_{AB} = R_B - R_A > 0$. In a LCAO tight-binding approach, the electronic Hamiltonian $H_\mathrm{e}$ reads

$$H_\mathrm{e} = E_A\,|A\rangle\langle A| + E_B\,|B\rangle\langle B| - t(d_{AB})\,(|A\rangle\langle B| + |B\rangle\langle A|) \tag{3.6}$$

where $t(d_{AB})$ is the hopping energy between the atoms, that will in general depend on some power of the inverse distance. For the sake of clarity and without loss of generality, we assume $t(d_{AB}) \propto 1/d_{AB}^2$. We can find the occupied electronic orbital $|\psi_\mathrm{e}^\mathrm{occ}\rangle$ diagonalising $H_\mathrm{e}$:

$$|\psi_\mathrm{e}^\mathrm{occ}\rangle = \sqrt{\frac{1+x}{2}}\,|A\rangle + \sqrt{\frac{1-x}{2}}\,|B\rangle \tag{3.7}$$

with $x = \Delta/\sqrt{\Delta^2 + 4t^2}$ and $\Delta = E_B - E_A$. This allows us to define the dipole moment $D(d_{AB})$ of the molecule as

$$D(d_{AB}) = R_A Z_A^v + R_B Z_B^v - 2\,\langle\psi_\mathrm{e}^\mathrm{occ}|\,\hat{r}\,|\psi_\mathrm{e}^\mathrm{occ}\rangle \tag{3.8}$$

where $Z_A^v = Z_B^v = +1|e|$ are the valence charges of atom A and B, respectively, and $\hat{r}$ is the position operator, whose matrix elements are well defined in an isolated molecule. The dynamical charge $Z_\alpha^*$ of atom $\alpha = A, B$ is defined as the derivative of $D(d_{AB})$ with respect to the atomic displacement $R_\alpha$, and using all the above

definitions we obtain (in units of $|e|$)

$$Z^*_\alpha = \frac{\partial D(d_{AB})}{\partial R_\alpha} \tag{3.9}$$

$$= \frac{(-1)^{i_\alpha}\Delta}{\sqrt{\Delta^2+4t^2}}\left(1+\frac{8t^2}{\Delta^2+4t^2}\right) \tag{3.10}$$

$$= \frac{2X}{\sqrt{1+4X^2}}\left(1+\frac{2}{1+4X^2}\right) \tag{3.11}$$

where $i_A = 1$ and $i_B = 2$. The above equations tell us that acting on the ionic-covalent character of the bond, accounted for by the term $X = \Delta/t$, one can tune the values of the dynamical charges. Albeit the expression of Eq. 3.10 apparently reminds the dependence on the gap of the effective charge in the undimerized 1D chain provided in Eq. 3.4, as it inversely depends on the difference between molecular energy levels, from Eq. 3.11 it is clear that the effective charge is always limited and shows no diverging behaviour. The dynamical charges of atoms $A$ and $B$, which obeys the charge-neutrality sum rule $Z^*_A + Z^*_B = 0$, are displayed in Figure 3.2 as a function of the ionic-covalent character $X = \Delta/t$. The maximum enhancement is indeed found for finite values of $X$, i.e., arising from the mixed ionic-covalent character of the bond, reaching however a finite value that is roughly $\sim 1.5$ the nominal value, consistently with the enhancement reported in [96]. We contrast this result with the enhancement of up to 30 times the nominal charge that we find in the 1D chain and highlight the differences with the analytical behaviour found in the model, namely with Equation (3.4) and (3.5).

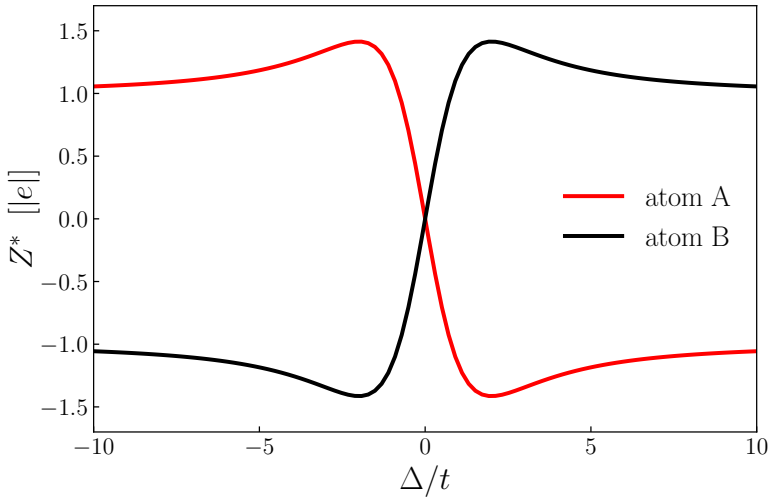


**Figure 3.2.** Dynamical charges of atoms $A$ and $B$ of a dimer molecule. Tuning the ionic/covalent character of the bond through the ratio $\Delta/t$ allows for a maximum enhancement of $\sim 1.5$ times the valence charge of $1|e|$, in stark contrast with the enhancement of up to 30 times we find in the chain.

## 3.3 Piezoelectricity

Piezoelectricity is a well known phenomenon characterising those materials with the property to generate a surface charge, and hence an electric tension, when subject to a stress, or conversely to deform elastically in response to an external electric field. Thanks to the possibility they offer to convert mechanical energy into electrical energy and vice-versa, piezoelectric materials are of great interest in various fields and for many applications, from macro- to microscopic electromechanical devices, to energy harvesting and much more[102, 103]. The most widely used piezoelectric materials are inorganic perovskites, such as lead zirconate titanate (PZT), for their high electromechanical response[104, 105, 106]. However, inorganic materials have very low mechanical flexibility, high fabrication costs and often are toxic because of the lead they contain. These facts motivated an intense research activity aimed at developing and identifying lead-free piezoelectric ceramics[106, 107]. A promising alternative is to exploit piezoelectric properties of organic materials, a route that has been trodden with some success since early 1990s, mostly focusing on the wide class of organic polymers displaying high flexibility, low fabrication costs and bio-compatibility[108, 109, 110, 111]. In this context, the most studied organic piezoelectric is polyvinylidene fluoride (PVDF)[109, 112], a saturated polymer derived from polyethylene and comprising molecular units with net (electrical) dipole moments, thus giving rise to ferroelectricity of conformational origin due to the rotation of chains' segments from non-polar to polar isomers.

Despite the intense research efforts and the progress made in the field of organic piezoelectrics, to date inorganic ceramics still display much better piezoelectric performance than organic counterparts. The piezoelectric response in PZT and related inorganic materials is strongly enhanced at morphotropic phase boundaries (MPB), marking a composition-driven structural transition between two competing, nearly energetically degenerate phases with distinct symmetries[113, 114, 115]. On general grounds, the properties enhancement close to such phase transition may be traced back to the flattening of free-energy surfaces, easing polarization extension and/or rotation, as extensively discussed and observed mostly in perovskite oxides[116]. Recently, the concept of MPB has been loosely extended to the family of P(VDF-TrFE) copolymers[117, 118]. Here, the introduction of different TrFE monomers in the semicrystalline PVDF structure has been proposed to lead to an enhanced conformational competition reminiscent of the structural competition realized at MPB, further suggesting an optimal chemical composition for maximizing the piezoelectric coefficient. Even though at the optimal "morphotropic" composition the piezoelectric coefficient roughly doubles the typical values of PVDF, it is still smaller by one order of magnitude compared to characteristic piezoelectric coefficients of inorganic oxide ceramics such as PZT.

Beside saturated polymers as PVDF and P(VDF-TrFE), whose ferroelectric and piezoelectric properties rely on the ordering of built-in molecular dipoles and as such require appropriate poling treatments, a natural alternative choice is represented by

the conjugated polymers we described in section 1.3. Characterised by a delocalised $\pi-$orbital along their backbone, these polymers are widely studied for their peculiar electronic properties[119, 120]. If specific symmetry-lowering effects allowing for piezoelectricity and ferroelectricity are met in a conjugated polymer, one may expect a large polar response of electronic origin due to the redistribution of the responsive $\pi-$electronic density along the polymer's backbone. In next sections, we study piezoelectricity in 1D systems such as conjugated polymers using our model.

### 3.3.1 Inclusion of strain in the model

In this section we provide an extension of the Rice-Mele model that enables the description of strain effects. Let's consider again the infinitely long one-dimensional diatomic chain. The only possible strains in 1D are contractions or dilatations of the unit cell. Defining the adimensional parameter $\epsilon$, the effects of strain on the unit cell length is

$$a(\epsilon) = a_0(1+\epsilon), \tag{3.12}$$

where $a_0 = a(0)$ indicates the length of the unit cell at zero strain. The introduction of strain in the model affects all spatial-dependent quantities. In particular, as we are interested in the effects of strain and of atoms' displacement, we rewrite the definition of the adimensional fractional coordinate of Equation (1.6) including also the effect of strain $\epsilon$:

$$u(\epsilon) = \frac{r_1 - r_2}{a(\epsilon)} = \frac{\delta r_B - \delta r_A}{a(\epsilon)/2}. \tag{3.13}$$

In analogy with Chapter 1, this term allows us to express bond lengths in a compact expression which accounts also for effects of strain, allowing us to generalize Equation (1.7) as follows:

$$r_i = \frac{a(\epsilon)}{2}\left[1 + (-1)^{i+1}u(\epsilon)\right],\ i = 1, 2. \tag{3.14}$$

With the above definitions, at linear order in atoms' displacement we have

$$t_i = t(r_i) \simeq t\left(\frac{a(\epsilon)}{2}\right) + \left.\frac{\mathrm{d}t}{\mathrm{d}r}\right|_{\frac{a(\epsilon)}{2}} \cdot \left(r_i - \frac{a(\epsilon)}{2}\right), \tag{3.15}$$

which allow us to generalize also Equations (1.9) and (1.10):

$$t(\epsilon) = \frac{t_1 + t_2}{2} = t\left(\frac{a(\epsilon)}{2}\right), \tag{3.16}$$

$$\delta t(\epsilon) = \frac{t_1 - t_2}{2} = -\left.\frac{\mathrm{d}t}{\mathrm{d}r}\right|_{\frac{a(\epsilon)}{2}} \cdot \frac{a(\epsilon)}{2}u(\epsilon). \tag{3.17}$$

The term $t(\epsilon)$ quantifies the effect of strain on the hopping energy between equidistant atoms whereas the term $\delta t(\epsilon)$ describes the variation with respect to $t(\epsilon)$ caused by atoms' relative displacement. In absence of strain ($\epsilon = 0$) we recover the quantities

defined in Chapter 1, whereas at linear order in $\epsilon$ it holds:

$$t(\epsilon) = t\left(\frac{a_0}{2}(1+\epsilon)\right) \simeq t\left(\frac{a_0}{2}\right) + \left.\frac{\mathrm{d}t}{\mathrm{d}r}\right|_{\frac{a_0}{2}} \cdot \left.\frac{\mathrm{d}a(\epsilon)}{\mathrm{d}\epsilon}\right|_{\epsilon=0} \cdot \frac{\epsilon}{2} = \tag{3.18}$$

$$= t_0(1-\beta\epsilon) \tag{3.19}$$

where we defined $t_0 \equiv t(a_0/2)$ and where the adimensional parameter $\beta > 0$, defined as

$$\beta = -\frac{a_0}{2t_0}\left.\frac{\mathrm{d}t}{\mathrm{d}r}\right|_{\frac{a_0}{2}}, \tag{3.20}$$

quantifies the variation of the hopping energy due to a variation of the distance between the atoms at zero strain, and in this sense it has the same meaning of the electron-phonon coupling term defined in Equation (1.12). With an analogous procedure, we obtain

$$\delta t(\epsilon) = -t_0\beta'(1+\epsilon)u(\epsilon), \tag{3.21}$$

where we defined another adimensional e-ph parameter $\beta' > 0$ as

$$\beta' = -\frac{a_0}{2t_0}\left.\frac{\mathrm{d}t}{\mathrm{d}r}\right|_{\frac{a(\epsilon)}{2}}. \tag{3.22}$$

which differs from the definition given in Equation (3.20) as the derivative is evaluated at $a(\epsilon)/2$. Even though the two e-ph parameters $\beta'$, $\beta$ can differ at finite values of the strain, at the lowest order one can safely assume that they coincide, hence hereafter we will consider $\beta' = \beta$.

As in Chapter 1, we are interested in the structural properties at $T = 0\,K$. The strain $\epsilon$ enters in the total energy both explicitly as a parameter and implicitly through strain-dependent quantities. Structural properties are hence enclosed in the optimal $\overline{u}$ which minimises the total energy per unit cell $E_{\mathrm{tot}}$ given a set of parameters $t_0$, $\beta$, K, $\Delta$ and a strain $\epsilon$. To study the behaviour of the order parameter $\overline{u}$ we follow the same approach described in Chapter 1, the only difference being that now we explicitly include the effects of strain on model's quantities. We obtain the following generalization of Equation (1.29) for the total energy per unit cell

$$E_{\mathrm{tot}}(u) = \frac{1}{4}\mathrm{K}u^2a(\epsilon)^2 - 2a\int_{-\pi/a}^{\pi/a}\frac{\mathrm{d}k}{2\pi}\sqrt{\Delta^2 + 4t^2(\epsilon)\cos^2\frac{ka}{2} + 4\beta^2t_0^2(1+\epsilon)^2u^2\sin^2\frac{ka}{2}}. \tag{3.23}$$

Equating to 0 the first derivative of $E_{\mathrm{tot}}$ with respect to $u$, we find again that a stationary point is in $u = 0$, whereas the others are the solutions of the following equation in $u$, obtained with the same procedure described in Chapter 1:

$$\Delta^2 + 4\beta^2t_0^2(1+\epsilon)^2u^2 = \frac{t_0^2(1-\beta\epsilon)^2\pi^2}{\sinh^2\frac{\mathrm{K}a_0^2\pi(1-\beta\epsilon)}{8\beta^2t_0}}. \tag{3.24}$$

Above Equation, which generalized Equation (1.32), summarises the effects of strain in determining the optimal configuration and hence on the structural phase transition. Supposing that $\Delta$ is the guiding parameter of the transition, we can define a strain-dependent critical parameter $\Delta_c(\epsilon)$ which generalizes Equation (1.33):

$$\Delta_c(\epsilon) = \frac{t_0(1-\beta\epsilon)\pi}{\sinh\left(\frac{\mathrm{Ka}_0^2\pi(1-\beta\epsilon)}{16\beta^2 t_0}\right)}, \tag{3.25}$$

where it still holds

$$\begin{cases} \overline{u} \propto |\Delta - \Delta_c(\epsilon)|^{1/2}, & \text{if } \Delta \leq \Delta_c(\epsilon) \\ \overline{u} = 0, & \text{if } \Delta > \Delta_c(\epsilon). \end{cases} \tag{3.26}$$

An analogous result holds if we consider $\beta$ as order parameter, in particular

$$\begin{cases} \overline{u} \propto |\beta - \beta_c(\epsilon)|^{1/2}, & \text{if } \beta > \beta_c(\epsilon) \\ \overline{u} = 0, & \text{if } \beta \leq \beta_c(\epsilon). \end{cases} \tag{3.27}$$

In Figure 3.3**a** and **b** are shown the behaviours of the optimal parameter $\overline{u}$ as a function of parameters $\Delta/\Delta_c$ and $\beta/\beta_c$, respectively. Finally, we remark that strain affects also polarization $P$ both explicitly and implicitly through strain-dependent quantities. In particular, given a system in its optimal configuration $\overline{u}(\epsilon)$, in the limit $E_{\mathrm{gap}}(\epsilon) \ll t(\epsilon)$, it holds

$$P(\epsilon, \overline{u}(\epsilon)) = -\frac{|e|}{\pi}\theta(\epsilon, \overline{u}(\epsilon)) \tag{3.28}$$

### 3.3.2 Morphotropic-like enhancement of the piezoelectric response

In general, the electromechanical response of a system is quantified by the piezoelectric coefficients, defined in terms of variations of polarization with respect to an applied homogeneous strain. In order to have a non-trivial piezoelectric response, the chain must not have points of inversion symmetry, a requirement that is met when the equivalence between atoms is broken in a distorted chain, i.e. both $\Delta \neq 0$ and $\overline{u} \neq 0$. In this case, the chain becomes also ferroelectric with a net dipole moment per unit cell $P$[32]. When defining the electromechanical response of a ferroelectric system which presents a spontaneous polarization, in general one needs to distinguish between a *proper* and an *improper* contribution to the response. Indeed, as the piezoelectric response is usually measured as the electric current which flows in the sample in response to a time-dependent strain, a correct theoretical description needs to account for spurious contribution due to, e.g., homogeneous rotation of the dipole moment. In Appendix B this idea is formalized in the Berry-phase picture following the lines of Ref.[121]. Moreover, we show that in the case we are interested in, i.e. effects of strains on a purely 1D chain, the distinction between proper and

improper contribution to piezoelectricity does not apply. Thus, we can safely define the piezoelectric coefficient of the chain, $c_{\text{piezo}}$, as the derivative of $P$ due to the strain $\epsilon$, namely

$$c_{\text{piezo}} = \left.\frac{\mathrm{d}P(\epsilon, \overline{u}(\epsilon))}{\mathrm{d}\epsilon}\right|_{\epsilon=0} = c_{\text{piezo}}^{\text{c.i.}} + c_{\text{piezo}}^{\text{i.r.}} \tag{3.29}$$

where the derivative of $P$ is decomposed in two contributions. The first one is the so-called *clamped ions* term

$$c_{\text{piezo}}^{\text{c.i.}} = \left.\frac{\partial P(\epsilon, \overline{u}(\epsilon))}{\partial \epsilon}\right|_{\epsilon=0} \tag{3.30}$$

which is obtained keeping fixed the relative position of the ions in the unit cell, i.e., for fixed internal fractional coordinate $\overline{u}_0 = \overline{u}(\epsilon = 0)$. Using Equation (3.17) and (3.28) we have

$$c_{\text{piezo}}^{\text{c.i.}} = -\frac{|e|}{2\pi}\beta \sin 2\theta(0, \overline{u}_0) \tag{3.31}$$

where we notice that $|c_{\text{piezo}}^{\text{c.i.}}| \leq |e|\beta/2\pi$, the maximum achievable value being directly proportional to the e-ph coupling constant $\beta$. The second term of Equation (3.29) takes into account the effect of strain on the internal coordinate $\overline{u}(\epsilon)$ and defines the *internal relaxation* contribution

$$c_{\text{piezo}}^{\text{i.r.}} = Z^*(\overline{u}_0)\left.\frac{\partial \overline{u}(\epsilon)}{\partial \epsilon}\right|_{\epsilon=0} \tag{3.32}$$

where $Z^*(\overline{u}_0)$ is the effective charge of the system in the optimal configuration $\overline{u}_0$, while the second factor, called *internal-strain*, quantifies the variation of the optimal internal parameter $\overline{u}(\epsilon)$ with respect to strain. As discussed in the previous section, the inclusion of strain in the Rice-Mele model affects explicitly the critical values of the phase transition. Considering for the moment $\Delta$ as the guiding parameter, from Equation (3.26) it follows that:

$$\left.\frac{\partial \overline{u}(\epsilon)}{\partial \epsilon}\right|_{\epsilon=0} \propto \frac{1}{|\Delta - \Delta_{\text{c}}(0)|^{1/2}}. \tag{3.33}$$

Equation (3.33) implies that the internal relaxation term diverges as we approach the critical point $\Delta_{\text{c}}(\epsilon)$ from the distorted phase, in analogy with the MPB mechanism at play in some ferroelectric oxides. Indeed, as the $\Delta$ parameter of the Rice-Mele model accounts for the composition of the system, it allows to continuously tune a morphotropic-like phase transition from the distorted phase (lower symmetry, ferroelectric) to the undistorted one (higher symmetry, paraelectric). On the other hand, at a fixed $\Delta \neq 0$ suppressing the Peierls electronic instability, the second-order phase transition can be driven by the e-ph coupling, as discussed in Chapter 1 and

shown e.g. in Figure 3.3**b**. Thus, from Equation (3.27) it holds

$$\left.\frac{\partial \bar{u}(\epsilon)}{\partial \epsilon}\right|_{\epsilon=0} \propto \frac{1}{|\beta - \beta_{\rm c}(0)|^{1/2}}, \tag{3.34}$$

i.e., a diverging internal strain when approaching the critical point from the dimerized phase.

In principle, the diverging behaviour of the internal strain, Equation (3.33) or (3.34), guarantees the existence of piezoelectric 1D systems, such as conjugated polymers, with arbitrarily high response when close to a morphotropic-like phase boundary, irrespective of the prefactor, namely the effective charge $Z^*$. However, this specific enhancement is a consequence of the second order transition. As discussed in Chapter 2, quantum-anharmonic effects may change the order of the structural phase transition, therefore damping the diverging behaviour of $c^{\rm i.r.}_{\rm piezo}$. A robust enhancement of the piezoelectric coefficient against QAE would depend, therefore, on the strength of the polar response embodied by $Z^*$. Unlike the MPB-related enhancement of the internal strain, shown in Figures 3.3**c** and 3.3**d**, the topological behaviour of $Z^*$ is expected to be much more stable with respect to QAE, as we will see in what follows, guaranteeing the enhancement of the electromechanical response. The total piezoelectric coefficient, comprising both the clamped ion and internal relaxation contributions, is shown in Figures 3.3**e** and 3.3**f** as a function of parameters $\Delta/\Delta_{\rm c}(0)$ and $\beta/\beta_{\rm c}(0)$. Insets highlight how the piezoelectric coefficient is mostly contributed by the internal-relaxation contribution, that is strongly enhanced by the combined effect of diverging internal strain $\partial\bar{u}/\partial\epsilon$ and anomalously large effective charges. We remark the importance of both mechanisms, since anomalous effective charges alone in general do not guarantee piezoelectric effects if inversion symmetry is kept, as in centrosymmetric $CaTiO_3$ and $SrTiO_3$[96], or if the internal strains are small, as in 2D hexagonal systems and gapped graphene[122].

## 3.4 Comparison with polar responses in 2D systems

We contrast the results on effective charges and piezoelectricity in 1D systems with the predicted behaviour for polar responses in 2D gapped graphene, where both piezoelectric coefficient and effective charges were found to be independent on the band-gap amplitude[122]. Indeed, electron-strain/lattice couplings in 2D hexagonal crystals can be described as gauge fields [123, 122] whose effect is to shift the Dirac cone of an amount proportional to the coupling constants, causing the latter to be the only relevant quantities determining the strength of polar responses. In the 1D chain, instead, the e-ph interaction contributes, through dimerization, to the gap opening, thus directly affecting the Thouless-pump topological enhancement of effective charge. We further remark that the absence of a structural transition in gapped graphene causes the piezoelectric response to be mostly due to the clamped-ion contribution, the internal-relaxation one contributing roughly 25% to the total

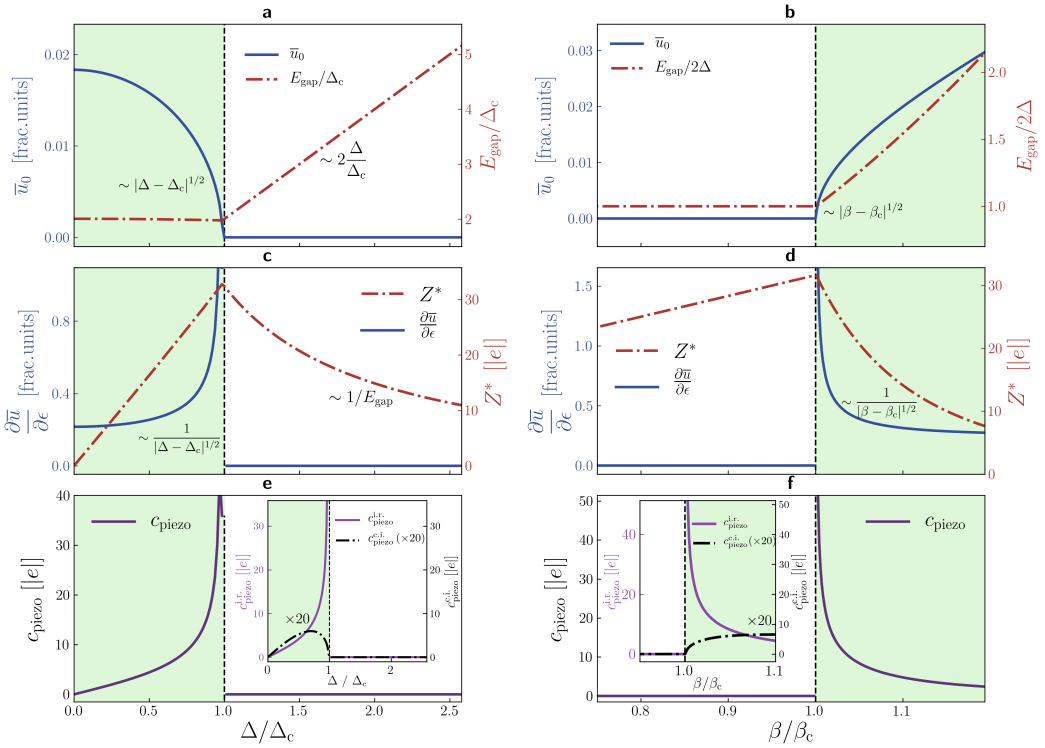


**Figure 3.3.** Panels **a** and **b**: structural phase transition with order parameter $\overline{u}$ as a function of the onsite energy difference $\Delta$ and of the e-ph coupling $\beta$. As shown in Figure 1.3, when $\Delta < \Delta_{\rm c}$ ($\beta > \beta_{\rm c}$) the total energy $E_{\rm tot}(u)$ has a double-well profile with two minima at $|\overline{u}| \neq 0$, resulting in a distorted chain with bond-length alternation. When $\Delta > \Delta_{\rm c}$ ($\beta < \beta_{\rm c}$) the minimum of $E_{\rm tot}(u)$ is at $\overline{u} = 0$ and the atoms become equidistant. The behaviour of the order parameter is typical of second order phase transitions, being $\overline{u} \propto |\Delta - \Delta_{\rm c}|^{1/2}$ ($\overline{u} \propto |\beta - \beta_{\rm c}|^{1/2}$), and the system remains insulating in both phases with gap $E_{\rm gap} = 2\sqrt{\Delta^2 + 4(\beta t_0 \overline{u})^2}$. Panels **c** and **d**: internal strain and effective charge across the phase transition. The inclusion of strain $\epsilon$ in the model affects the critical value $\Delta_{\rm c}(\epsilon)$ ($\beta_{\rm c}(\epsilon)$) and, as expected in a second order transition, the internal strain displays a diverging behaviour close to the critical point, $\partial\overline{u}/\partial\epsilon \propto |\Delta - \Delta_{\rm c}|^{-1/2}$ ($\partial\overline{u}/\partial\epsilon \propto |\beta - \beta_{\rm c}|^{-1/2}$). Near the critical point a huge polar response is also present, quantified by the effective charge $Z^* \propto \beta\Delta/E^2_{\rm gap}$ (Equation (3.5)). Approaching the critical point from the undimerized phase, $Z^*$ is inversely proportional to the gap $E_{\rm gap}(\overline{u} = 0) \equiv \Delta$, panel **c**, and linear in $\beta$, panel **d**. Since the gap is constant as a function of $\Delta$ and linear in $\beta$ when approaching the critical point from the dimerized phase, $Z^*$ displays a linear behaviour in $\Delta$, panel **c**, and it is inversely proportional to $\beta$, panel **d**. Panels **e** and **f**: the piezoelectric coefficient diverges when approaching the critical point from the dimerized phase. As shown in the inset, the major contribution is due to the internal relaxation term of Equation (3.32). The topological nature of the enhancement guarantees its stability.

response[122].

## 3.5 Quantum-anharmonic effects on polar responses

One of the main messages of previous sections is that polar responses in our 1D systems are strictly connected to their structural properties, presenting interesting enhancements in proximity of the critical points of the structural phase transition between the dimerized and the undimerized phases. However, in Chapter 2, we saw that quantum-anharmonicity plays a key role in this competition, renormalizing both the energy gain between the most and the less stable phases, as well as the critical values of the transition. It thus comes natural to ask how much QAE affects polar responses. As a consequence of its topological nature, we expect the enhancement of the effective charges to be stable against quantum fluctuations and anharmonic effects. Our hypothesis is confirmed, as can be seen in the right panel of Figure 3.4, where we show the behaviour of $Z^*$, computed on the fitted-model both with and without QAE, as a function of the onsite energy difference $\Delta$. In particular, to account for QAE, effective charges were computed on the optimal structures obtained from the SSCHA minimization as described in section 2.4. We highlight that not only the enhancement is robust against QAE, but rather it is further augmented by their inclusion. The reason is that as the value of the critical point is reduced by the inclusion of QAE, so are the values of the energy gap of these systems when approaching the renormalized critical point, as shown in the left panel of Figure 3.4. Hence, as a direct consequence of the fact that the topological nature of the enhancement of the effective charges is manifested through the inverse proportionality of $Z^*$ with respect to $E_{\text{gap}}$, Equation (3.4), we deduce that QAE contribute to the enhancement of $Z^*$ by reducing the energy gap.

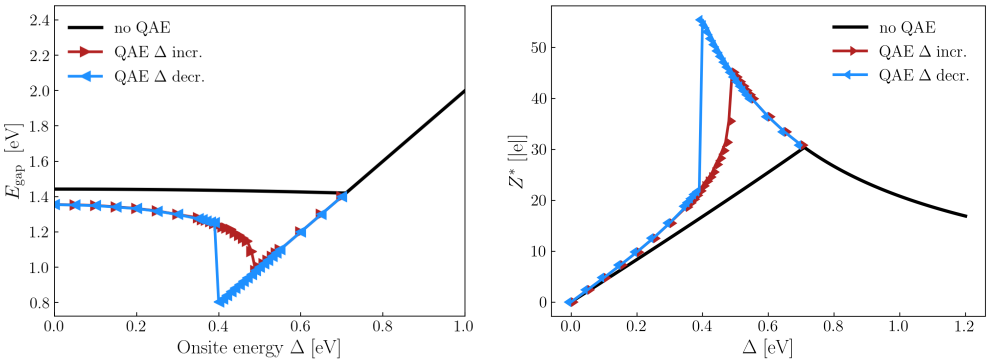


**Figure 3.4.** In the left panel, we show the behaviour of the energy gap $E_{\text{gap}}$, computed in the fitted model as a function of the onsite energy difference $\Delta$, obtained both with and without the inclusion of QAE. As a consequence of the renormalization of the value of the critical point due to quantum-anharmonic effects, the system admits lower values of $E_{\text{gap}}$. This is reflected by an enhancement of the effective charges $Z^*$, shown in the right panel, as a consequence of Equation (3.4). From this result, we deduce that not only the topological nature of the enhancement of the effective charges in these 1D systems guarantees their stability against QAE, but it is also responsible for a further enhancement obtained when we include effects of quantum-anharmonicity.

## 3.6 Ab-initio numerical results

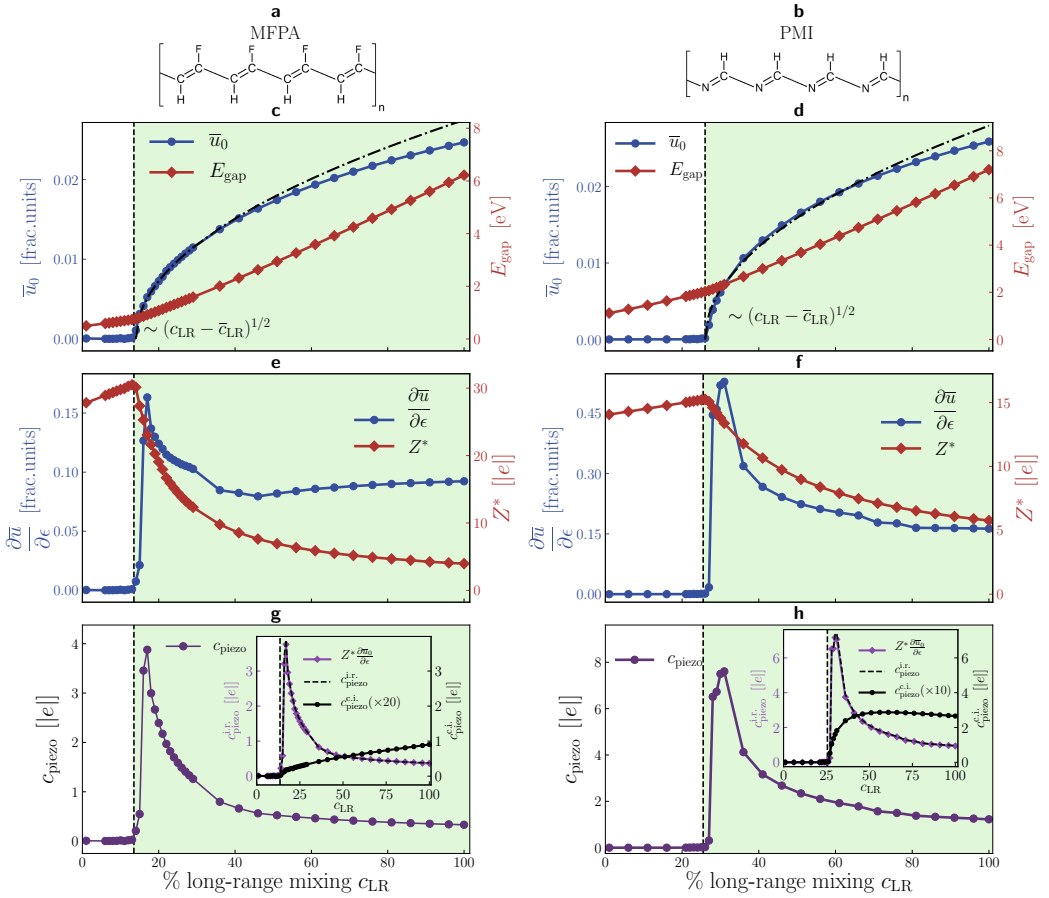


**Figure 3.5.** Panel **a**: mono-fluorinated polyacetylene (MFPA). Panel **b**: polymethineimine (PMI). In panels **c** and **d** for MFPA and PMI, respectively, is shown the behaviour of the internal coordinate $\overline{u}_0$ for different values of the long-range mixing parameter $c_{\rm LR}$ put in the range-separated xc-functional in the DFT calculations. Consistently with the prediction of the model, we observe the behaviour $\overline{u} \simeq |c_{\rm LR} - \bar{c}_{\rm LR}|^{1/2}$, with $\bar{c}^{\rm MFPA}_{\rm LR} \simeq 14\%$ and $\bar{c}^{\rm PMI}_{\rm LR} \simeq 26\%$. In panels **e** and **f**, for MFPA and PMI respectively, the behaviour of $\partial\overline{u}_0/\partial\epsilon$ is reported, along with the values of the effective charge $Z^*$. For each polymer, we chose $Z^* = Z^*_{{\rm C},xx}$ (for MFPA the C bound to the F). In agreement with the model, on the one hand we observe a further hint of the morphotropic-like nature of the transition while on the other hand the huge values of $Z^*$ stands out, in particular in the region near the critical points. In panels **g** and **h** is shown how the piezoelectric coefficient is greatly enhanced when reaching the critical points from the less symmetric phase. The comparison between $c^{\rm c.i.}_{\rm piezo}$ and $c^{\rm i.r.}_{\rm piezo}$, in the insets, highlights the internal-relaxation origin of the enhancement. Furthermore, the comparison with the results obtained putting the values of **e** and **f** in Equation (3.32) shows that the model very well describes the nature of the enhancement.

We performed ab initio calculations in the framework of density functional theory to validate our model predictions, choosing two conjugate polymers representative of the broad class of SPA. One is monofluorinated polyacetylene (MFPA), made

by the repetition of the unit CH-CF and obtained by substituting one hydrogen atom of the $C_2H_2$ unit of PA with fluorine. The other is polymethineimine (PMI), obtained substituting a CH pair with a nitrogen atom to obtain the unit N-CH. For simplicity, we considered the all-trans structures shown in Figure 3.5**a** and 3.5**b**, whose fundamental physical properties are captured by the model. Even though controlling the fraction of substituted atoms may in principle induce a morphotropic-like transition, this approach poses many challenges both from the computational and experimental side: to our specific purposes, it wouldn't allow to study the phase transition and the associated predicted enhancement of piezoelectric effect by varying with continuity an external parameter (as $\Delta$ in the model). As discussed in sections 3.3.2 and 3.2.1, the internal-strain and the effective-charge enhancements may be also induced by tuning the parameter $\beta$. To achieve this computational task, we take advantage of the effect of screened Coulomb vertex corrections to the dressing of the e-ph coupling[124], leading to an enhancement of e-ph itself especially strong in low-dimensional materials and when phonons at zone boundary are involved [125, 126, 127, 128]. Such screened-Coulomb-mediated e-ph enhancement can be captured by hybrid functionals incorporating a fraction of the exact exchange [126, 129]. Its inclusion has been proven essential for describing the bond-length alternation of trans-polyacetylene [130, 68] and related 1D polymers [17, 131], whose BLA is typically underestimated by standard local-density or generalized-gradient approximations, indirectly pointing to an enhancement of the e-ph coupling due to electron-electron interaction. Range-separated hybrid (RSH) functionals represent an ideal choice for our purpose, as they have been designed to better account for the screened Coulomb vertex corrections. The latter can be effectively tuned by acting on the long-range (LR) mixing parameter $c_{\mathrm{LR}}$ that accounts for the fraction of LR exact exchange in RSH functionals, thus providing a computational knob to continuously vary $\beta$. We further remark that the strength of e-ph enhancement due to screened Coulomb effects can be ideally controlled by modifying the screening itself, as proposed for doped graphene [132]. Since the optimal mixing parameter $c_{\mathrm{LR}}$ is inversely proportional to the scalar dielectric constant of the environment in order to enforce the correct asymptotic potential [133, 67, 134, 135, 66], we speculate that controlling the dielectric environment may represent a viable strategy, alternative and complementary to controlling the fraction of substituted atoms, for tuning and optimising the piezoelectric response of conjugated polymers. These considerations are also consistent with the results on carbyne discussed in section 1.3, where we argued that effects of different carbon nanotubes, namely different dielectric environments, used in experiments to confine and stabilize carbyne chains, are correctly accounted for in the model via the e-ph coupling parameter $\beta$.

Motivated by these reasons, we performed structural optimization of both MFPA and PMI for different values of the LR mixing parameter $c_{\mathrm{LR}}$. For consistency with the model, we considered the coordinates of the C and N atoms along the principal axis of the chain, which we take as the $x$-axis, to compute the internal coordinate $u$.

More details on the effect of $c_{\mathrm{LR}}$ on polymers' structures are provided in Appendix C. The evolution of $\overline{u}_0$ displayed in Figure 3.5**c** and 3.5**d**, clearly hints to the presence of a second order phase transition triggered by $c_{\mathrm{LR}}$ for both polymers: the dimerized phase is suppressed by lowering the fraction of mixing, the order parameter showing the expected behaviour as it approaches the second-order phase-transition critical point, in excellent qualitative agreement with model results shown in Figure 3.3**b**, 3.3**d** and 3.3**f** and confirming a posteriori the direct proportionality between $c_{\mathrm{LR}}$ and $\beta$. The second-order character of the phase transition is further confirmed by the softening of the corresponding optical phonon found in the higher-symmetry phase when increasing $c_{\mathrm{LR}}$, shown in Figure 3.6, signalling the onset of a dynamical instability of the undimerized structure.

In Figure 3.5**e** and 3.5**f** the behaviour of $Z^*$ and of $\partial\overline{u}/\partial\epsilon$ calculated from first principles is shown. For MFPA we took $Z^* = Z^*_{\mathrm{C_F},xx}$ where $C_F$ is the carbon atom bound to the fluorine, while for PMI $Z^* = Z^*_{\mathrm{C},xx}$. The full tensors of the effective charges of all the atoms are reported in Appendix C, Table C.1, C.2 and C.3. We highlight the qualitative agreement with the prediction of the model, in particular the huge enhancement of the effective charges around the critical point $\overline{c}_{\mathrm{LR}}$, reaching the strongly anomalous values of $\sim 30\,|e|$ and $\sim 15\,|e|$ in correspondence of $\overline{c}_{\mathrm{LR}}$ for MFPA and PMI, respectively. The covalent character of bonds along the chain prevents a precise definition of the nominal reference value for C, that can be however assumed to be of the order of $1|e|$, as the nominal ionic charges for H and F are respectively $+1|e|$ and $-1|e|$. Effective charges of carbon in both considered chains are strongly anomalous for all considered long-range mixing parameters, displaying values between $5|e|$ and $30|e|$ even for band gaps exceeding 6 eV. These anomalous values exceed even those reported in oxide ferroelectrics, where effective charges are typically two or three times larger than nominal reference values[96]. Figure 3.5**g** and 3.5**h** display the behaviour of the piezoelectric coefficients computed ab initio taking into account also the effects of transverse displacements. In the insets, the different contributions $c^{\mathrm{i.r.}}_{\mathrm{piezo}}$ and $c^{\mathrm{c.i.}}_{\mathrm{piezo}}$ are compared, highlighting the internal-relaxation origin of the enhancement. We also compare the values of $c^{\mathrm{i.r.}}_{\mathrm{piezo}}$ computed with DFT calculations on the polymers, with those obtained using Equation (3.32) of the model, plugging in the the ab initio values of $Z^*$ and $\partial\overline{u}/\partial\epsilon$ of Figure 3.5**e** and 3.5**f**. The agreement between the two approaches is both qualitatively and quantitatively excellent, notwithstanding the simplifying description provided by the Rice-Mele model, that neglects structural details specific of the two considered polymers as well as transverse displacements. We highlight that despite the behaviour $\partial\overline{u}/\partial\epsilon \propto |c_{\mathrm{LR}} - \overline{c}_{\mathrm{LR}}|^{-1/2}$, the main contribution to the piezoelectric coefficient is given by the effective charges. The large values attained in a finite range around the second-order critical point and their ultimately topological origin suggest that the piezoelectric effect is robust against quantum and anharmonic effects that may change the order of the phase transition, as predicted in carbyne[17] and discussed in the previous Chapter 2.

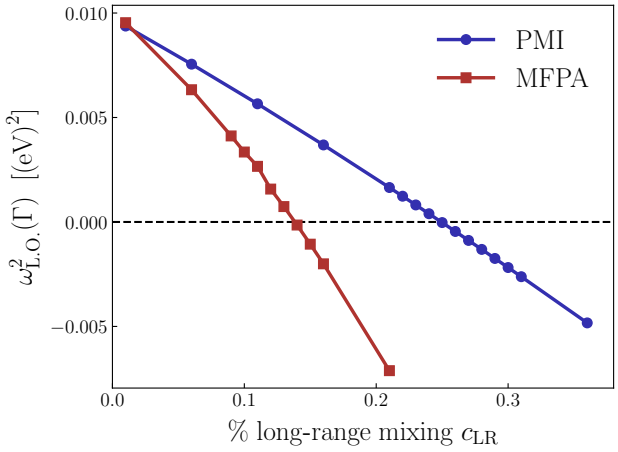


**Figure 3.6.** Behaviour of the LO eigenvalue $\omega^2_{\mathrm{LO}}$, calculated at $\Gamma$ in the undistorted configurations of MFPA and PMI, for different values of the long-range mixing parameter $c_{\mathrm{LR}}$. The change from positive to negative values, signalling a dynamical instability of the system toward the dimerized phase, corresponds to the change of curvature of the total energy at $u = 0$.

### 3.6.1 Comparison with state-of-the-art piezoelectric polymers

Finally, we compare the results for the piezoelectric coefficients of MFPA and PMI with those of the best and most widely used piezoelectric PVDF polymer, made by the repetition of the unit $CF_2$-$CH_2$. The Rice-Mele model fails to capture its main properties, this polymer being not conjugated. Its piezoelectricity indeed derives from the presence of a net dipole moment transverse to the chain, whereas the electromechanical response predicted in conjugated polymers is longitudinal to the chain and ultimately due to the topological-morphotropic enhancement. To have a consistent comparison with available experimental data for PVDF, we computed ab initio the *converse* piezoelectric coefficient $d_{\mathrm{piezo}}$, which measures the response with respect to an external stress, rather than a strain. In particular, $d_{\mathrm{piezo}}$ is linearly related to $c_{\mathrm{piezo}}$ through the elastic constants tensor $\mathbb{C}$, namely $c_{\mathrm{piezo}} = d_{\mathrm{piezo}}\mathbb{C}$. As far as 1D systems are concerned, only a single scalar elastic constant is required, and it can be evaluated as the second derivative of the energy with respect to the strain, i.e. $\mathbb{C} = \partial^2 E_{\mathrm{tot}}/\partial\epsilon^2$. The results for the converse piezoelectric coefficients of PVDF are compared with those of MFPA and PMI in Figure 3.7 and are consistent with the values computed in Ref. [136]. Even though the calculated $d_{\mathrm{piezo}}$ is smaller than reported experimental values, a direct comparison to experiments is hardly drawn because, e.g., of the polymorphic character or low crystallinity of experimental samples, as noticed also in Ref. [136]. We remark that piezoelectric response in PVDF is found to be independent on the fraction of exact exchange, confirming the utterly different nature of the electromechanical response in such non-conjugated polymer. We finally mention that mildly anomalous effective charges have been also reported for PVDF[137], the carbon effective charge however not exceeding

1.5|$e$|, consistently with our results provided in Table C.3 of Appendix C. On the other hand, both MFPA and PMI display a rather large range of values that are larger than calculated $d_{\text{piezo}}$ of PVDF, with up to a six-fold enhancement for PMI close to the dimerization point. The robustness of the enhancement mechanism is confirmed also by the comparison with the piezoelectric coefficients calculated in packed MFPA chains, as shown in Figure 3.8. Even though the selected prototypical SPAs may not be the most efficient ones for practical realization and engineering of their functional properties, the comparison with first-principles estimate of one of the best available piezoelectric polymer alongside the general validity of the proposed model and consequent robustness of its electromechanical response put forward the broad class of $\pi$-conjugated polymers as a promising field for organic piezoelectrics with enhanced functionalities. Additionally, its inverse proportionality to the band gap provides a possible material-design principle for driving the quest of organic polymers with enhanced piezoelectric response.

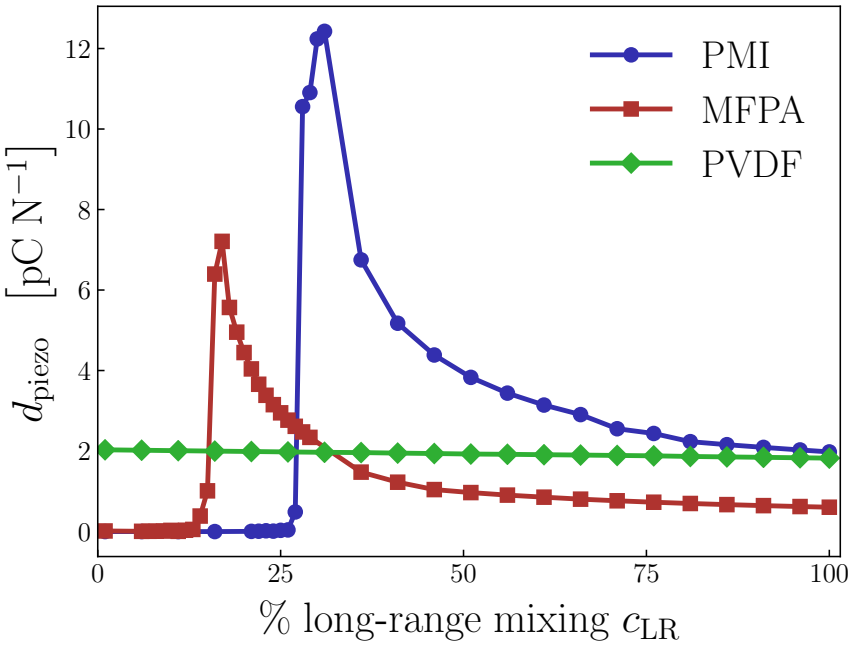


**Figure 3.7.** Comparison of the converse piezoelectric coefficients of MFPA and PMI with respect to PVDF, the current best and most widely used organic piezoelectric. In principle, the mechanism of the morphotropic-topological enhancement allows to outperform the state-of-the-art.

## 3.7 Conclusions

In this Chapter we presented our results on polar responses, i.e. those phenomena that can be defined in terms of linear variations of polarization, in 1D systems. Pushed by the idea that the presence of charge density waves may reflect in enhanced

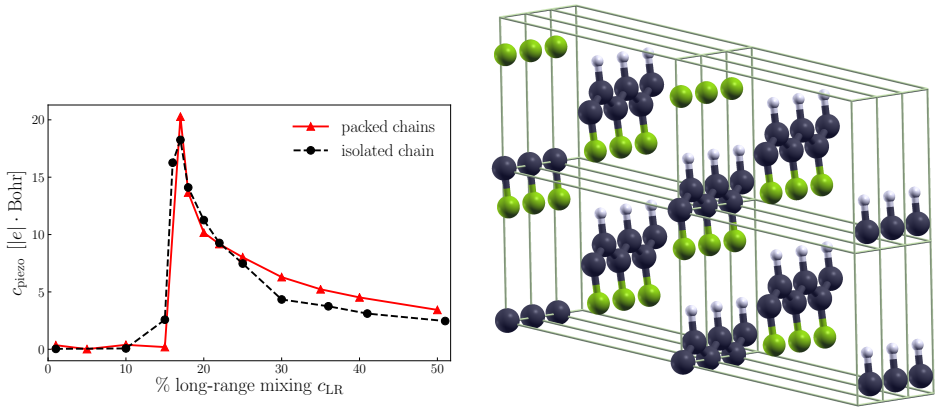


**Figure 3.8.** On the left panel, piezoelectric coefficients of MFPA in its isolated polymeric chain configuration are compared to those obtained for packed chains. The 3D structure adopted, realized with XCrySDen[138] and displayed on the right panel, is similar to the one adopted for PVDF in Ref.[136]. The agreement between the results highlight the robustness of the enhancement mechanism.

polar responses in presence of a strong coupling between structural and polar properties, we focused on two prototypical polar responses: the effective charges $Z^*$, which quantify the effects of ions displacement on the electronic charge density distribution; piezoelectricity, i.e. the response to a strain, which comprises also a contribution proportional to $Z^*$.

In the framework of the model, we found a huge enhancement of both responses in proximity of the critical points of the structural phase transition, with the internal-relaxation contribution to the piezoelectric coefficient showing a diverging behaviour at the critical point. While this latter result is strictly connected to the transition order, which as we have seen may be strongly affected by quantum-anharmonic effects, the enhancement of $Z^*$ is robustness against perturbing effects such as fluctuations or external environments. We trace back this peculiar behaviour to the ultimately topological nature of the effective charges in the model, highlighted by an inverse proportionality between $Z^*$ and the electronic energy gap $E_{\text{gap}}$, as argued also in Ref.[31]. Thus, we expect this topological nature to guarantee stability of the effective charges enhancement against quantum-anharmonic effects. Performing calculations of polar responses with the inclusion of QAE, not only we confirmed this idea, but surprisingly, we found that QAE actually strengthen the enhancement, as a consequence of the fact that quantum-anharmonicity renormalizes the critical values of the phase transition, thus reducing the energy gap.

Finally, theoretical predictions were tested with DFT calculations on prototypical conjugated polymers. We chose to perform calculations varying the long-range mixing parameter entering a range-separated hybrid functional motivated by the fact that, on one hand, it is related to the external dielectric environment, and, on the other hand, it is known to account for screened Coulomb vertex corrections to the dressing of the e-ph coupling. Following this idea, we found a remarkable agreement between

DFT's and model's results, consistently with our discussion on the role of the external environment on the e-ph coupling in conjugated polymers presented in section 1.3. Moreover, we showed that state-of-the-art organic piezoelectric are outperformed by piezoelectric conjugated polymers, mostly thanks to strongly anomalous effective charges of carbon, larger than $5e$ – ordinary values being of the order of $1e$ – and reaching the giant value of $30e$ for band gaps of the order of 1 eV. Our results put forward conjugated polymers, and in general 1D conjugated systems, as a class of functional materials with tunable and enhanced polar response properties.

# Chapter 4

# Resonant Raman response

## Chapter overview

This Chapter is dedicated to the study of the Raman response of 1D systems. First, in section 4.1, we motivate the interest in this topic discussing the importance of Raman spectroscopy in characterizing these systems, with a particular focus on the resonant version of this technique. Aiming for a theoretical description of Raman scattering in 1D systems, in section 4.2 we present the most relevant aspects of the theory for Raman scattering, identifying different levels of approximations and how we treat them: non-resonant, resonant and beyond the Placzek approximation. Finally, in section 4.3, we present our results on the Raman response obtained with different approximations on a prototypical 1D system, the fitted-model for carbyne. Conclusions are drawn in section 4.4.

## 4.1 Introduction: the role of resonance Raman spectroscopy in 1D systems

One of the main messages from past chapters is that the properties of 1D systems are strictly related to their symmetries. Obtaining information on systems configuration is thus essential for their characterization. For instance, the presence of a BLA in a chain of inequivalent atoms – namely, reducing spatial symmetry – may result in the insurgence of properties, e.g. ferroelectricity or piezoelectricity, otherwise absent. There are several experimental techniques that allow determining systems' structure and properties: one of the most powerful and widely used is Raman spectroscopy, based on the process of inelastic scattering of a monochromatic beam of light impinging on a system[139, 100]. A Raman scattering process is thus characterized by the presence of an incoming and an outgoing photon. In particular, the energy of the scattered photon is shifted up or down with respect to the energy of the incident photon as a consequence of the interaction with the system. This energy shift indicates that the initial and final states of the system are not the same. Many

different mechanisms may be responsible for this inelastic scattering, however Raman processes are usually classified depending on which states of the system are involved. If the transition takes place between two different electronic states, one usually talks about *electronic* Raman. Instead, if it happens between vibrational energy levels of the same electronic state (usually the ground state), we are in presence of *vibrational* Raman. In what follows, we will focus on this latter case.

Energy shifts of vibrational Raman lie in a range from tens to thousands of $cm^{-1}$, thus providing information about vibrational, rotational, and other low-frequency modes in materials. Since these modes are strictly related to the structure of a system, Raman spectroscopy is a suitable tool to obtain this information. For instance, the appearance of new Raman-active modes in a spectrum, may signal a phase change in the system under observation. Moreover, specific vibrational modes are often associated with specific features of the system, e.g. a particular bond: thus, one can use Raman spectroscopy to characterize the composition of a substance. Another interesting aspect is the fact that if a molecule (or the unit cell of a crystal) possesses a center of symmetry, then, no normal vibrational mode can be at the same time both Raman active and infrared active. This means that, in some cases, Raman spectroscopy is the only technique that allows us to gather information on specific systems, e.g. in polyacetylene or carbyne.

Aiming to detect Raman signals, there are however some practical problems that need to be addressed. Intensities of Raman peaks are several orders of magnitude lower than those of elastically scattered photons – as e.g. in Rayleigh scattering – thus requiring special filters and particular experimental setups. It is however possible to enhance the response of a Raman-active mode if the energy of the impinging light beam, i.e. the energy of the laser, matches the energy of the electronic transition to which the vibrational mode is coupled. Since the photon energy is resonant with an electronic transition, this technique is called *resonance* Raman spectroscopy[140, 141] (RRS). In this process, the intermediate state of the scattering is not a virtual one, as in the common understanding of the Raman scattering, but rather a real physical state of the system[1]. The resonance condition results in an enhancement of the scattering amplitude for that particular process, with the effect of a much stronger signal of that given vibrational mode, up to several orders of magnitude higher than the signal obtained with another laser frequency not resonant with that electronic transition.

To sum up, RRS is often the preferred choice thanks to its enhanced sensitivity, allowing to overcome limitations due e.g. to the small volume of the sample or its low concentration. Due to the possibility of resonating with specific frequencies, RRS is also a unique tool to determine the electronic structure of a system. As far as 1D systems are concerned, it is widely used to characterize organic and biological materials[142, 143, 144], but also in carbon-derived systems such as

[1]This description may resemble the phenomenon of fluorescence, however the time-scales of these two processes are very different, the Raman being several orders of magnitude faster.

graphite, graphene and carbon nanotubes[145, 146, 147]. For instance, it is used on conjugated polymers to determine how different functional groups affect electronic and vibrational properties, or vice-versa to detect the presence of a particular functional group via the insurgence of a specific resonant Raman signal otherwise absent[148, 149]. In carbon-based 1D systems such as nanotubes, RRS can be used to determine several properties, e.g. the chirality of the nanotube, its diameter, or its breathing radial mode[150, 151, 152]. Moreover, RRS has proved to be essential for the characterization of properties of linear carbon chains such as their electron-phonon coupling, the presence of a Peierls distortion and their vibrational properties[153, 154, 155]. Finally, RRS is paramount for studying long linear carbon chains encapsulated in carbon nanotubes, as it allows for the selective enhancement of vibrational modes specific to the chain, allowing to selectively reduce the background noise due to the presence of the nanotube[61, 71].

In order to have a complete and comprehensive understanding of experimental results, a correct theoretical picture is indispensable. A good theoretical framework should allow, at the same time, to interpret but also predict experimental results. Ab-initio approaches, coupled with numerical techniques implemented e.g. in the framework of DFT codes, have proved to be reliable instruments in this quest. The development of an ab-initio theory for the resonance Raman response of solids will be the main focus of the next Chapter 5. In what's next, we limit to set the ground giving a brief overlook on the theory for (resonant) Raman scattering, discussing the limitations of existing approaches and how to overcome them, and present our results on the fitted-model for carbyne, which has proven to give reliable, DFT-level results.

## 4.2 Remarks on the theory of Raman scattering

The aim of this section is not to give a comprehensive and exhaustive derivation of the theory for Raman scattering, but rather to identify and discuss the key elements in which we are interested. The theoretical description of Raman scattering is based on the treatment of the interaction between light and matter, that exchange both energy and momentum. The electro-magnetic radiation is usually regarded as a perturbation acting on a system of ions and electrons, e.g. a molecule or a crystal. In this way, the Raman response can be treated as a linear response property and, in this sense, it gives information on the unperturbed system. There are several approaches to the treatment of the scattering due to light-matter interaction[156, 100, 139]. In what follows, we briefly review the most common approximations on which light-matter interaction, in general, and Raman scattering, in particular, are based.

In theory, the electromagnetic radiation interacts both with nuclei and electrons, so a complete description should treat the interaction of light with nuclei and light with electrons on the same ground[2]. However, due to the fact that electrons' mass is

[2]This path has been trodden e.g. in Ref.[157], via a minimal coupling involving both ions and

much smaller than ions' mass, one can safely assume that only the electrons interact directly with the electromagnetic field, whereas the interaction of ions with light is mediated through the electron-ion interaction. Another common assumption is based on the fact that wave-length $\lambda$ of lasers usually adopted in experiments is much larger than typical interatomic distances $a$. This allows for the schematization of light-electron interaction as a collection of electric dipoles interacting with a uniform electric field, i.e. the renowned *dipole approximation*. Moreover, in the specific case we are interested in of the vibrational Raman process where one phonon is involved in the inelastic scattering of light from a solid, due to the relation $q = 2\pi/\lambda$ between the wave-length and the wave-vector modulus $q$ of a monochromatic electromagnetic wave, one can safely assume that $q \ll 2\pi/a$, $a$ being typical interatomic distances. Stated in other words, this assumption means that, in vibrational Raman, we can consider no momentum transfer from photons to phonons, hence only (optical) vibrational excitations at the Brillouin zone center $\Gamma$ are involved.

In general, the vast majority of approaches to the theory of Raman scattering are based on these approximations. Differences may instead rise in how the electromagnetic interaction is treated. A possible choice is to adopt the vector potential $\mathbf{A}$ to describe the electromagnetic field and proceed with the usual scattering theory solved in the interaction picture with a diagrammatic approach, as done e.g. in Refs.[139, 140, 156]. Another approach, followed for example by Brüesch[100], is instead that of introducing the electromagnetic interaction via an external electric field $\mathbf{E}$ which is coupled with the electric-dipole moment operator $\mathbf{M}$, and then doing perturbation theory on the total wave function of the matter. Which approach is more convenient may depend on the specific situation one wants to address: we limit here to remark that, under the same approximations, both approaches must yield to the same results as a consequence of the gauge-invariance of electromagnetism. In what follows, we adopt the approach of Brüesch, as it is known to be a more convenient choice for developing an ab-initio theory of the Raman response[158, 159].

### 4.2.1 Vibrational Raman in the Placzek approximation

Let's now go deeper in the description of vibrational Raman, where the energy difference between the incoming and outgoing photons comes from the creation (Stokes process) or annihilation (anti-Stokes process) of a quantum of vibrational energy. The standard framework commonly used to treat these processes was defined by Placzek[160], which, under certain hypothesis, gives a recipe to compute the vibrational Raman spectra of a solid or a molecule, while at the same time providing a clear and intuitive interpretation of this process. The assumptions under the Placzek approximation are the following:

- the adiabatic approximation must be valid;

electrons momenta.

- the ground state is both the initial and final electronic state of the process and it must be non-degenerate;
- the frequency of the incoming light $\omega_{\text{in}}$ must be lower than any electronic transition frequency of the system, but much larger than any vibrational frequency.

First requirement is what is usually done in the standard Born-Oppenheimer approximation, which allows separating the matter wave function in an electronic part, obtained for fixed nuclear positions, and a nuclear part, obtained considering the electronic energy as an effective potential acting on the nuclei. Second condition is what defines a vibrational Raman process, with the additional requirement that the electronic state is the ground state. Third condition rules out the possibility of having resonances in the scattering process. Given these hypothesis, and following, e.g., the approach of Brüesch of doing perturbation theory with an external electric field, one obtains an expression for the intensity $I^\nu$ of the peak correspondent to the (Stokes) process of creation of a phonon of mode $\nu$, which can be observed in the non-resonant Raman spectra of an harmonic solid:

$$I^\nu \propto \left|\mathbf{e_i} \cdot \overleftrightarrow{\mathbf{A}}^\nu \cdot \mathbf{e_s}\right|^2 \frac{1}{\omega_\nu} (n_\nu + 1) \tag{4.1}$$

where $\mathbf{e_i}$ ($\mathbf{e_s}$) is the polarization of the incident (scattered) radiation, $n_\nu = \left[\mathrm{e}^{\hbar\omega_\nu / k_\mathrm{B} T} - 1\right]^{-1}$ is the Bose-Einstein occupation factor at temperature $T$, and the *Raman activity* tensor $\overleftrightarrow{\mathbf{A}}^\nu$ of mode $\nu$ reads

$$A^\nu_{lm} = \sum_{k\tau} \frac{\partial \chi_{lm}}{\partial u_{k\tau}} \frac{\mathrm{w}^\nu_{k\tau}}{\sqrt{M_\tau}} \tag{4.2}$$

where $u_{k\tau}$ is the displacement of the $\tau$-th atom in the $k$-th direction, $M_\tau$ is the atomic mass and $\mathrm{w}^\nu_{k\tau}$ is the orthonormal vibrational eigenmode $\nu$. The term $\chi_{lm}$ is the so-called electronic susceptibility tensor, which quantifies the polar response of the system, in the sense we discussed in the previous Chapter 3, with respect to an external electric field, namely:

$$P_l = \varepsilon_0 \chi_{lm} E_m. \tag{4.3}$$

A part for giving a compact expression to compute the Raman response of an insulator, above Equation (4.2) has also an immediate pictorial interpretation: the Raman response of a system in the Placzek approximation is the response to an external electric field and it is quantified by the modulation of the electronic susceptibility with respect to the vibrations of a given phonon. Usual techniques to compute the derivative in Equation (4.2) rely on a finite differences approach, where one calculates $\chi_{lm}$ for different configurations of the system with atoms displaced of

$\pm\Delta u_{k\tau}$, namely

$$\frac{\partial \chi_{lm}}{\partial u_{k\tau}} \simeq \frac{\chi_{lm}(+\Delta u_{k\tau}) - \chi_{lm}(-\Delta u_{k\tau})}{2\Delta u_{k\tau}}. \tag{4.4}$$

The underlying assumption of this approach, and of the Placzek approximation in general, is that the intensity of the light scattered by a system with vibrating nuclei is the same for each nuclear configuration as the intensity of the light scattered by the system with the nuclei in a fixed configuration, justifying the finite differences approach.

Placzek approximation works very well for large-gap insulators and when excitation energies are e.g. in the visible range. This is reflected by the fact that in above Equations there is no explicit reference to neither the incoming nor the outgoing frequencies. However, there exist many case where these assumptions break down, e.g. in small gap semi-conductors, where the energy of the light beam may resonate with electronic transitions, or when it becomes necessary to explicitly account for the presence of finite phonon frequencies, as in systems with non-negligible phonon energies with respect to electronic-transitions energy scales or in the case of Raman scattering with infrared light. To correctly describe these situations, it is necessary to go beyond the Placzek approximation, as we discuss in next section.

### 4.2.2 How to go beyond the Placzek approximation

As a first step to go beyond the Placzek approximation, we allow for the energy of the incoming photon to match electronic transition energies so as to describe resonance Raman processes, while still considering the energy of the involved phonon much lower and thus negligible. Practically, this translates to considering the frequencies of the incoming and outgoing photons as equal, i.e. $\omega_{\text{in}} = \omega_{\text{out}} = \omega$, and to explicitly include effects of light frequency into the theoretical description. In doing this, the "finite differences" idea that the response of a system with vibrating nuclei is the same as the response of the system with the nuclei in a fixed configuration is still valid[140], allowing us to write the following generalization of Equation (4.2):

$$A^{\nu}_{lm}(\omega) = \sum_{k\tau} \frac{\partial \chi_{lm}(\omega)}{\partial u_{k\tau}} \frac{\mathrm{w}^{\nu}_{k\tau}}{\sqrt{M_\tau}}, \tag{4.5}$$

where the dependence on incoming laser frequency $\omega$ enters through the frequency-dependent susceptibility tensor $\chi_{lm}(\omega)$, which can still be regarded as a polar response property, obeying the relation

$$P_l(\omega) = \varepsilon_0 \chi_{lm}(\omega) E_m(\omega). \tag{4.6}$$

To really go beyond the Placzek approximation, in the sense that the finite differences approach is not valid anymore, we explicitly include the dependence on the phonon frequency $\omega_{\text{ph}}$ in the theoretical description. To obtain a generalized expression for the Raman activity in this case, we resort to the so-called *phenomeno-*

*logical* approach[139], which relates the Raman response to a fluctuation of the energy density of the system. This idea is consistent with the fact that we are treating the Raman response as a linear response property, thus we are in a regime where the fluctuation-dissipation theorem applies. In practice, we write (Equation (2.85) of Ref.[139]):

$$A^{\nu}_{lm}(\omega_{\rm in},\omega_{\rm out},\omega_{\rm ph}) = \sum_{k\tau} \frac{\partial^3 \mathcal{E}^{\rm el}(\omega_{\rm in},\omega_{\rm out},\omega_{\rm ph})}{\partial E_l \partial E_m \partial u_{k\tau}} \frac{{\rm w}^{\nu}_{k\tau}}{\sqrt{M_\tau}} \tag{4.7}$$

where $\mathcal{E}^{\rm el}$ is the electronic ground-state energy of the system, $E_l$ ($E_m$) is the $l$-th ($m$-th) Cartesian component of a uniform electric field and for a Stokes process it holds $\omega_{\rm in} = \omega_{\rm out} + \omega_{\rm ph}$. We remark how in the case $\omega_{\rm ph} = 0$, hence $\omega_{\rm in} = \omega_{\rm out} = \omega$, we recover the known relation between the electronic energy and electronic susceptibility:

$$\chi_{lm}(\omega) = \frac{\partial^2 \mathcal{E}^{\rm el}(\omega)}{\partial E_l \partial E_m}. \tag{4.8}$$

Even if it is in principle possible to go beyond the Placzek approximation following a diagrammatic approach using the vector potential **A** instead of the electric field **E**, there are several advantages in using Equation (4.7) instead. First of all, it is a compact formula which allows avoiding the calculation of many diagrams. Secondly, an expression in terms of derivatives of the electronic ground state energy is the most suitable way for the formulation and numerical implementation of an ab-initio theory for the Raman response beyond the Placzek approximation in the DFT framework. To date, however, there is no ab-initio code for solid-state calculations of the Raman response beyond the Placzek approximation: next Chapter 5 will be devoted to the development and implementation of a theory for the Raman response beyond the Placzek approximation within a DFT approach. Leaving all the technical details to next Chapter, before proceeding we limit here to observe that in order to accomplish this task it is necessary to resort to a different kind of perturbation theory, based on the electronic density $\rho$, instead of the standard perturbation theory on the wave functions. In this framework, derivatives of the electronic energy $\mathcal{E}^{\rm el}$ are computed exploiting the relation

$$\mathcal{E}^{\rm el} = 2{\rm Tr}[H\rho], \tag{4.9}$$

where the factor 2 accounts for the spin and $H$ is a single-particle electronic Hamiltonian as e.g. the Kohn-Sham Hamiltonian or the Hamiltonian of the 1D model.

## 4.3 Raman response in the model

Now that we have discussed the relevant aspects of vibrational Raman scattering theory and introduced the framework we adopt for studying resonance Raman beyond the Placzek approximation, in this section we present a practical application of these concepts with the aid of the fitted-model. In the case of the 1D diatomic

chain, where we have two atoms per unit cell, we expect only one acoustic and one optic vibrational mode. As discussed, a Raman scattering process involving a single phonon happens at approximately zero exchanged momentum, hence only the optic mode at zone-center $\Gamma$ may contribute to the process of energy exchanging. Since we are dealing with 1D systems, we consider electric fields with polarization parallel to the 1D chain direction, as in a back-scattering experiment. In what follows, we first discuss how even in its non-resonant version, Raman scattering can provide useful information on the structural properties of these 1D system. Then, we will take into account the fact that commonly used laser frequencies often match electronic transitions in 1D systems, making necessary to resort to a resonance Raman description. Finally, we will go beyond the Placzek approximation and include also the dependence on the phonon frequency, in order to obtain the best match between theoretical predictions and experimental results on 1D systems.

### 4.3.1 Raman response as signature of the structure

Given the above considerations and using Equation (4.8) for $\omega = 0$, we write Equations (4.1) and (4.2) for the model, respectively:

$$I^{\text{opt.}} \propto |A^{\text{opt.}}|^2 \frac{1}{\omega_{\text{opt.}}} \left(n_{\text{opt.}} + 1\right), \tag{4.10}$$

$$A^{\text{opt.}} = \sum_{\alpha=A,B} \frac{\partial \chi}{\partial \delta r_\alpha} \frac{\mathrm{w}_\alpha^{\text{opt.}}}{\sqrt{M_\alpha}} \tag{4.11}$$

$$= \sum_{\alpha=A,B} \frac{\partial^3 \mathcal{E}^{\text{el}}}{\partial E^2 \partial \delta r_\alpha} \frac{\mathrm{w}_\alpha^{\text{opt.}}}{\sqrt{M_\alpha}}, \tag{4.12}$$

where the sum runs over the two atoms $\alpha = A, B$ in the unit cell, $\delta r_\alpha$ has the meaning of atomic displacement defined in Chapter 1, and the index of the only relevant Cartesian component, the one parallel to the chain, is implied. As anticipated, we compute derivatives of the electronic ground state energy $\mathcal{E}^{\text{el}}$ in terms of perturbations on the electronic density matrix $\rho$, with an approach we will describe in details in next Chapter 5. From Equation (4.9) we obtain

$$\frac{\partial^3 \mathcal{E}^{\text{el}}}{\partial E^2 \partial \delta r_\alpha} = 2\mathrm{Tr}\left[\frac{\partial^2 \rho}{\partial E^2} \frac{\partial H}{\partial \delta r_\alpha}\right], \tag{4.13}$$

however we remark that in this non-resonant case one can also adopt the finite differences approach of Equation (4.4) applied to Equation (4.11).

Even with all the approximations made, the theory presented above for the non-resonant Raman response allows us to interpret and predict properties regarding the structure of the system. As we mentioned, whether a vibrational mode is Raman active or not depends on the symmetries of the system. In particular, if the unit cell

possesses a center of inversion symmetry, modes cannot be at the same time Raman and infrared active. In the case of the 1D chain, symmetries of the unit cell depends on the parameters of the model, which determines whether the system becomes centrosymmetric or not. Considering the on-site energy $\Delta$ as the guiding parameter, we have that the optimal structure in the case of equivalent atoms ($\Delta = 0$, as in carbyne) is the distorted one. Being the atoms equivalent, the system is still centrosymmetric, however for this same reason its optic mode cannot be infrared active: we expect it to be Raman active instead. This idea is confirmed by the fact that, experimentally, the optic mode in carbyne is indeed Raman active. If we break atoms equivalence with a finite $\Delta < \Delta_c$, the optic mode can now be at the same time infrared and Raman active since the chain has both inequivalent atoms and a bond-length alternation. Finally, if $\Delta \geq \Delta_c$ the optimal structure becomes again centrosymmetric, but with inequivalent atoms, so this time the optic mode can be only infrared active. From this qualitative discussion, we conclude that the presence of a BLA in the system must be reflected by the appearance of a signal in the Raman spectrum. To test this idea we study the behaviour of the Raman activity $A^{\text{opt.}}$ of Equation (4.12) calculated on the optimal structures of the fitted-model as a function of $\Delta$. In Figure 4.1 we show that our results confirm the qualitative predictions. For completeness we also show that the finite differences approach and the density-matrix one yield the same results.

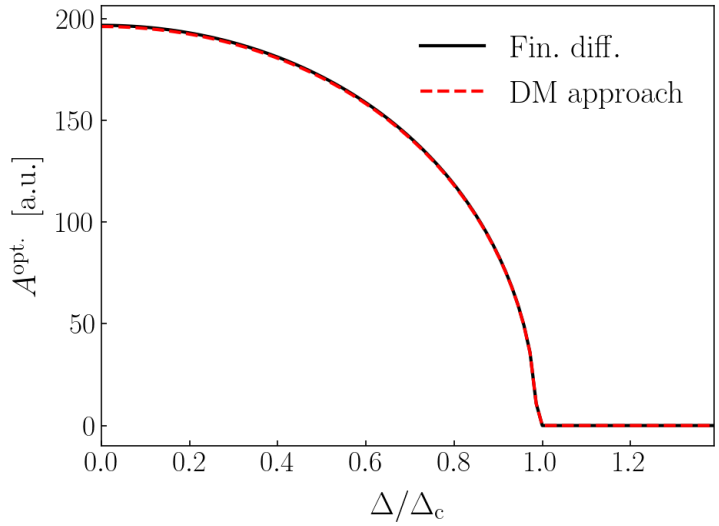


**Figure 4.1.** Behaviour of the Raman activity tensor $A^{\text{opt.}}$ of Equation (4.12) computed both with finite differences of electronic susceptibility with respect to atomic displacement (Equations (4.11) and (4.4)) and with the density matrix (DM) approach of Equation (4.13). Varying the parameter $\Delta$ guiding the structural phase transition, we observe how the Raman signal disappears for $\Delta > \Delta_c$. Reminding the role of $\Delta$ in determining the optimal structure of the system as discussed in section 1.2.1, we conclude that the presence of a Raman response in the model implies that the system is in its distorted structure and vice-versa.

### 4.3.2 Inclusion of resonance effects

As we discussed, it is sometimes convenient to perform Raman experiments with laser energies which matches electronic excitation energies, in particular in 1D systems and carbon based systems, in order to enhance the response. In some other cases it is inevitable for laser frequencies to be very close or even higher than the electronic energy gap of the system. For instance, experimental estimates for the energy gap value of confined carbyne are between 2.253 eV and 1.848 eV[71], where in the fitted-model we found $E_{\text{gap}} \simeq 1.44$ ev and with PBE0 calculation $E_{\text{gap}} \simeq 2.03$ eV. Considering that lasers in range of the visible light have energies from about 1.6 eV to 3.3 eV, it becomes mandatory to account for resonance effects in the theoretical description. To accomplish this task, and analogously to the previous case, we adapt Equation (4.5) in the framework of the 1D model and write

$$A^{\text{opt.}}(\omega) = \sum_{\alpha} \frac{\partial^3 \mathcal{E}^{\text{el}}(\omega)}{\partial^2 E \partial \delta r_\alpha} \frac{\mathrm{w}_\alpha^{\text{opt.}}}{\sqrt{M_\alpha}} \tag{4.14}$$

where using Equations (4.8) and (4.9) it holds:

$$\frac{\partial^3 \mathcal{E}^{\text{el}}(\omega)}{\partial E^2 \partial \delta r_\alpha} = \frac{\partial \chi(\omega)}{\partial \delta r_\alpha} = 2\mathrm{Tr}\left[\frac{\partial \rho(\omega)}{\partial E^2}\frac{\partial H}{\partial \delta r_\alpha}\right]. \tag{4.15}$$

Again, we remark how in this case it is still possible to use both the finite differences approach or the density matrix approach. In the left panel of Figure 4.2, we compare the frequency-dependent Raman activity tensor $A^{\text{opt.}}(\omega)$ computed for the fitted-model on carbyne ($\Delta = 0$) both with the finite differences approach and with the density matrix approach, and show that they yield the same results. On the right panel, instead, we notice how the intensity of the response of the system is enhanced in proximity of $\omega = E_{\text{gap}}$, as a consequence of the resonance. We remark that to avoid divergences in the calculation of the response, we made an analytical extension of the frequency $\omega \to z = \omega + \mathrm{i}\gamma$ where $\gamma$ has the meaning of a dumping term. In the present calculations we put $\gamma = 0.1$ eV, consistently with the values inferred from RRS experiments in Ref.[71]. Also, we considered a finite $T = 300\ K$ in Equation (4.10).

### 4.3.3 Going beyond the Placzek approximation

Finally we relax the hypothesis $\omega_{\text{in}} = \omega_{\text{out}}$ and explicitly treat the dependence on the phonon frequency $\omega_{\text{ph}}$. As we will see, this is necessary in order to correctly reproduce experimental features. Indeed, optical phonon frequencies at zone-center in some 1D systems may have energies up to hundreds of meV ($\omega_{\text{ph}} \simeq 250$ meV in carbyne[71]), meaning that vibrational energies are not negligible with respect to electronic transitions and photon energies ($\omega_{\text{ph}} \simeq 10\%$ of $E_{\text{gap}}$ in carbyne), challenging the assumption behind Placzek approximation. To account for a finite

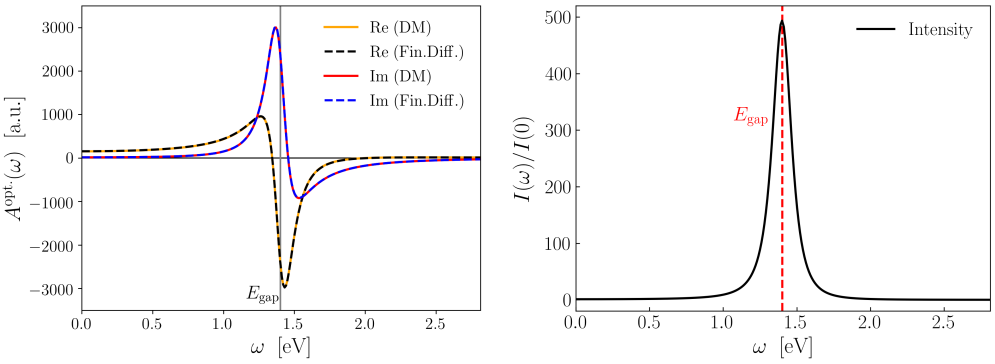


**Figure 4.2.** On the left, behaviour of the Raman activity tensor $A^{\text{opt.}}(\omega)$ of Equation (4.14) computed on the fitted-model for carbyne ($\Delta = 0$) with finite differences and with the density matrix (DM) approach. On the right, we show the Raman intensity $I(\omega)$ computed with Equation (4.10) at room temperature $T = 300\,K$. When then resonance condition $\omega = E_{\text{gap}}$ is met, there is an enhancement in the intensity of the response of up to 500 times the value $I(0)$ obtained neglecting the frequency dependence. For both figures, in order to avoid divergences, we considered a complex frequency $z = \omega + \mathrm{i}\gamma$, where $\gamma$ has the meaning of a dumping term (we put $\gamma = 0.1$ eV as in Ref.[71]): this is reflect by the fact that $A^{\text{opt.}}(\omega)$ acquires a complex character.

$\omega_{\text{ph}}$ in the Raman response of the model, we adapt Equation (4.7) which now reads:

$$A^{\text{opt.}}(\omega_{\text{in}}, \omega_{\text{out}}, \omega_{\text{ph}}) = \sum_{\alpha} \frac{\partial^3 \mathcal{E}^{\text{el}}(\omega_{\text{in}}, \omega_{\text{out}}, \omega_{\text{ph}})}{\partial^2 E \partial \delta r_\alpha} \frac{\mathrm{w}_\alpha^{\text{opt.}}}{\sqrt{M_\alpha}}. \tag{4.16}$$

We remark how in this case the finite differences approach is not doable, hence one must resort to the density matrix one in order to compute energy derivatives and from Equation (4.9) we obtain:

$$\frac{\partial^3 \mathcal{E}^{\text{el}}(\omega_{\text{in}}, \omega_{\text{out}}, \omega_{\text{ph}})}{\partial E^2 \partial \delta r_\alpha} = 2\mathrm{Tr}\left[\frac{\partial \rho(\omega_{\text{in}}, \omega_{\text{out}}, \omega_{\text{ph}})}{\partial E^2} \frac{\partial H}{\partial \delta r_\alpha}\right]. \tag{4.17}$$

If in the previous case, where we considered $\omega_{\text{ph}} = 0$, we observed an enhancement of the response in correspondence of $\omega = E_{\text{gap}}$ as a consequence of a resonance in the system, intuitively, we expect that the presence of a finite $\omega_{\text{ph}} \neq 0$ adds another possible channel for a resonant response to manifest. Indeed, the photon energy may now match both the transition energy between two electronic states or between an electronic state a vibrational state in another electronic state. A rigorous formulation of this idea will be given in next Chapter, we limit here to show in the left panel of Figure 4.3 the appearance of a new peak in the intensity of the Raman spectra of the fitted-model for pure carbyne ($\Delta = 0$) in correspondence of $\omega_{\text{in}} = E_{\text{gap}} + \omega_{\text{ph}}$.

To conclude, we compare our results with the experimental data obtained on other carbon-based 1D systems: carbon nanotubes. In Ref.[161, 152], Duque et al. and Haroz et al. measured the resonance Raman response of carbon nanotubes with different chiralities, varying the frequency of the impinging laser. Results show the

presence of two asymmetric peaks, as can be seen in the right panel of Figure 4.3 for the case of the (7,5)-armchair nanotube. This phenomenon was interpreted as the result of two different resonances: the most intense peak corresponds to the condition $\omega_{\text{in}} = E_{\text{gap}}$, whereas the second less intense peak corresponds to $\omega_{\text{in}} = E_{\text{gap}} + \omega_{\text{ph}}$, where $\omega_{\text{ph}}$ is the energy of the Raman-active phonon associated to that transition, whether it is longitudinal or transverse optic. Even if model's results where obtained with parameters fitted to reproduce carbyne chains, the qualitative agreement with experimental observations suggests that in order to correctly describe and reproduce the effects of RRS in such 1D systems, it is necessary to account for the presence of a finite $\omega_{\text{ph}} \neq 0$. To do this, the model and the expression we derived for the Raman activity beyond Placzek – Equation (4.16) – have proven to be reliable tools.

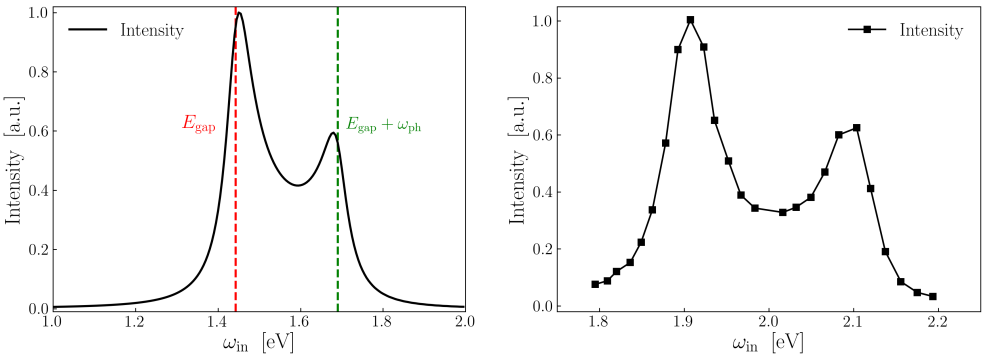


**Figure 4.3.** On the left, as a function of the incoming photon energy $\omega_{\text{in}}$, values of the intensity of the Raman response of the model fitted on carbyne ($\Delta = 0$), computed beyond the Placzek approximation with Equation (4.10) at $T = 300$ K and with the Raman activity of Equation (4.16). We notice two peaks: one for $\omega_{\text{in}} = E_{\text{gap}}$ and the other at $\omega_{\text{in}} = E_{\text{gap}} + \omega_{\text{ph}}$, and we attribute them to the presence of two resonances. For the fitted model we have that $\omega_{\text{ph}} = \omega_{\text{LO}}(\Gamma) \simeq 0.25$ eV. On the right, values of the Raman intensity measured with different laser energies $\omega_{\text{in}}$ on (7,5)-armchair carbon nanotubes taken from Ref.[161]. Even if we are comparing different 1D carbon-based systems, as reflected by the fact that resonances are in different positions, we find a remarkable qualitative agreement as in both cases there are two resonance peaks, separated in energy by the $\omega_{\text{ph}}$ of the longitudinal optic phonon. It is also interesting to notice that the ratio between the intensities of the two peak is in both cases $\sim 0.6$. We conclude that in order to correctly reproduce experimental results in 1D systems, it is necessary to go beyond the Placzek approximation.

## 4.4 Conclusions

Aiming to strengthen the connection between the theoretical description and experimentally measurable properties, in this Chapter we explored the vibrational Raman response of 1D systems under different levels of approximation. The starting point was the Placzek approximation, where one describes the process of Raman scattering neglecting both the frequency of the photons and of the phonon involved. Despite the rough approximation, it is still possible to interpret measured Raman spectra,

indeed the presence or absence of signals is related to specific structural realizations of a system. In many cases, it is however necessary to account at least for a finite photon frequency $\omega$ in order to correctly describe results obtained from resonance Raman spectroscopy. Indeed, in the case of the fitted-model for carbyne, we showed that when the condition $\omega = E_{\text{gap}}$ is met, the response of the system shows a huge enhancement, up to 500 times the value obtained neglecting the frequency dependence. Finally, for a complete theoretical understanding of the Raman response of 1D systems, we considered also the presence of a finite $\omega_{\text{ph}}$ in the process. From the comparison with experimental data obtained on carbon nanotubes, we showed that this inclusion is paramount in order to correctly reproduce the observed behaviour, in particular the insurgence of a second resonance peak in the resonance spectrum.

# Chapter 5

# Time-dependent density matrix perturbation theory

## Chapter overview

In this final Chapter, we present the time-dependent density matrix perturbation theory (TDDMPT), an approach to study the effects of external perturbations on a system, where the central quantity is the electronic density matrix. In the first section 5.1, we motivate the development of this theory and discuss the advantages it offers, in particular in the treatment of a uniform electric field in a crystal. Next, in section 5.2, we derive the central quantities to treat a generic perturbation in the TDDMPT approach. Next, in section 5.3, we focus on the case where the perturbation comes from a uniform electric field. A straightforward application is then given to the Raman response theory, whose formulation in the TDDMPT framework is presented in section 5.4. In particular, we show that in order to go beyond the Placzek approximation, it is necessary to resort to TDDMPT. Finally, in section 5.5, we describe how to implement TDDMPT equations in an ab-initio DFT framework and present our implementation of the Raman response of an insulating crystal in the Quantum ESPRESSO code. Conclusions are drawn in section 5.6.

## 5.1 Introduction: why a perturbation theory on the density matrix

Within the framework of density-functional theory, properties of materials are usually computed as derivatives of the ground state energy. By now, many DFT codes routinely offers the possibility to compute properties such as phonon dispersion, dielectric constants, effective charges, and so on, using linear-response methods, relying on first-order perturbation theory applied to the Kohn-Sham (KS) orbitals[162, 163, 164, 165]. In principle, this methodology can be applied beyond first-order to compute the derivatives of the energy at any order[166]. However, even

if the theoretical ground of wave-function perturbation theory is in principle well set, following this path from a practical point of view poses some challenges. Indeed, even if the final result is invariant with respect to an arbitrary unitary rotation in the space of the occupied KS orbitals, the formulation of the theory depends on the chosen gauge, as becomes apparent in the application of the KS-orbitals orthonormality constraints at high orders[166]. Moreover, the treatment of a perturbing uniform electric field in the case of periodic systems is not trivial, as the position operator is ill-defined in periodic boundary conditions and with Bloch-type orbitals.

An approach that addresses these problems was proposed in Ref.[167], following the idea of not relying on the perturbative series of the single KS orbitals, but rather exploiting a perturbation theory built directly on the electronic density matrix $\rho$. The first advantage of this approach is that the operator $\rho$ is gauge independent by definition, eliminating any possible source of ambiguity or difficulty that the choice of a particular gauge may give. Then, in the case of an insulating system, $\rho$ is a well-behaved, localized operator, in the sense that $\langle r_1 | \rho | r_2 \rangle$ goes to zero exponentially as $|r_1 - r_2|$ goes to infinity[168]. This property allows for a well-defined treatment of a perturbing uniform electric field, solving the problem posed by the ill-definition of the position operator $\hat{r}$ in periodic systems.

As will become more evident in next sections, further qualities of this approach, which we will refer to as Density Matrix Perturbation Theory (DMPT), regards also the computational aspect. Indeed, DMPT equations can be formulated as linear, algebraic (self-consistent) equations, that can be implemented and solved within any DFT code, without any additional cost than that of solving a self-consistent linear system of equations. Moreover, quantities at each order can be expressed in terms of just a finite number of unperturbed orbitals, namely the occupied states. On one hand, this guarantees a straightforward physical interpretation of the different quantities in terms of interaction between states of the unperturbed system, as in many interaction theories. On the other hand, the fact that the explicit knowledge of the unoccupied states is not needed, drastically reduces the computational cost, as in principle the empty states required to achieve converged results may even be infinite.

A practical case where DMPT and its advantages have been exploited is for the calculation of the non-resonant Raman response of an insulator within a DFT scheme[158]. As seen in the previous Chapter, computing the Raman response requires the knowledge of third-order mixed derivatives of the electronic energy with respect to electric fields and atomic displacements. To do so, usual approaches rely on computing the third-order derivatives as finite differences of electronic susceptibilities – i.e. the second-order derivatives with respect to the electric fields – calculated on configurations with displaced atoms. This approach becomes impracticable in situations where the (super)cells of systems are particularly large, or in cases where one needs to compute the Raman response of several (super)cells. The DMPT approach, instead, eliminates this problem since it requires only the calculation of

second-order derivatives of the density matrix, as hinted in Equation 4.13 for the 1D case. From a practical point of view and for the general 3D case, this means that DMPT allows to go from a situation where $36 \times N_{\text{atom}}$ first-order self-consistent calculations are needed for the finite differences approach, to just 6 second-order self-consistent calculations.

Finally, we highlight that the main ideas behind DMPT hold even in the case of a time-dependent perturbation, as can be oscillating electric fields. The aim of the present chapter is thus to extend DMPT to the time-dependent case, enabling the calculation of time-dependent energy derivatives at any order in a DFT framework, while keeping all the advantages outlined above. As a test case, we apply this time-dependent version of DMPT (TDDMPT) to study the resonance Raman response of an insulator beyond the Placzek approximation, justifying the treatment presented in the previous chapter, and also present its implementation in the Quantum ESPRESSO code[169].

## 5.2 Derivation of the time-dependent density matrix perturbation theory

Let's consider a single-particle Hamiltonian $H(t)$ – e.g. the Kohn-Sham Hamiltonian – to describe the electrons of an insulating system in presence of an external, time-dependent perturbation. We distinguish between valence (or occupied) $\{|\psi_v(t)\rangle\}$ and conduction (or unoccupied, or empty) $\{|\psi_c(t)\rangle\}$ eigenstates, for which it holds

$$\mathrm{i}\hbar \frac{\partial |\psi_v(t)\rangle}{\partial t} = H(t) |\psi_v(t)\rangle \,, \tag{5.1}$$

$$\mathrm{i}\hbar \frac{\partial |\psi_c(t)\rangle}{\partial t} = H(t) |\psi_c(t)\rangle \,. \tag{5.2}$$

We define the electronic density matrix of the system as a sum over the valence states:

$$\rho(t) = \sum_v |\psi_v(t)\rangle \langle\psi_v(t)| \,. \tag{5.3}$$

It is evident that when the system is in its ground-state (GS), where all valence states are occupied and all conduction states are unoccupied, the electronic density matrix $\rho(t)$ of Equation (5.3) contains the same information as the $\{|\psi_v(t)\rangle\}$. Indicating with $\lambda$ the (small) parameter associated with the perturbation, we write the perturbative expansions of $H(t)$ and $\rho(t)$ around $\lambda = 0$.

$$H(t) = H^{(0)} + \lambda H^{(1)}(t) + \lambda^2 H^{(2)}(t) + \ldots, \tag{5.4}$$

$$\rho(t) = \rho^{(0)} + \lambda \rho^{(1)}(t) + \lambda^2 \rho^{(2)}(t) + \ldots, \tag{5.5}$$

where it is made explicit that the time-dependence comes from the perturbation only and that the unperturbed $H^{(0)}$ and $\rho^{(0)}$ are time-independent. In the philosophy of

density-functional theory, we are interested in ground-state properties that can be expressed in terms of derivatives of the GS energy. The main idea behind DMPT is that the density matrix yields the same information on the ground state of the system as the valence eigenstates. It is thus possible to compute the response of the system to an external perturbation without resorting to the standard perturbation theory on the wave-functions, avoiding all the problems we discussed. To do so, we exploit the relation in Equation (4.9), which we rewrite:

$$\mathcal{E}(t) = \sum_v \langle \psi_v(t)| \, H(t) \, |\psi_v(t)\rangle = \mathrm{Tr}\left[H(t)\rho(t)\right] \tag{5.6}$$

which relates the ground state energy $\mathcal{E}(t)$ to $\rho(t)$. System's responses to external perturbations are quantified by the derivatives of $\mathcal{E}(t)$ with respect to $\lambda$, hence we write

$$\left.\frac{\partial^n \mathcal{E}(t)}{\partial \lambda^n}\right|_{\lambda=0} = \sum_{i=0}^{n} \mathrm{Tr}\left[H^{(i)}(t)\rho^{(n-i)}(t)\right], \tag{5.7}$$

where the trace $\mathrm{Tr}[\bullet]$ is intended over the complete basis set $\{|\psi_i^{(0)}\rangle\} = \{|\psi_v^{(0)}\rangle\} \cup \{|\psi_c^{(0)}\rangle\}$ of the (unperturbed) eigenstates of $H^{(0)}$.

In order to find an expression for the generic $n$-th order derivative $\rho^{(n)}$ to plug in Equation 5.7, we exploit two relations:

$$\rho^2(t) = \rho(t), \tag{5.8}$$

$$[\rho, H] = \mathrm{i}\hbar\dot{\rho}(t), \tag{5.9}$$

that correspond, respectively, to the idempotence property of the density matrix defined in Equation (5.3) and to von-Neumann equation for the quantum time evolution of the operator $\rho(t)$. It is convenient to define projection operators on the unperturbed valence and conduction states, respectively

$$P_V = \sum_v |\psi_v^{(0)}\rangle \langle \psi_v^{(0)}| = \rho^{(0)} \tag{5.10}$$

$$P_C = \sum_c |\psi_c^{(0)}\rangle \langle \psi_c^{(0)}| = 1 - P_V, \tag{5.11}$$

and it holds $P_V^2 = P_V$ and $P_C^2 = P_C$. This allows us to decompose $\rho(t)$ in the following form

$$\rho(t) = P_C\rho(t)P_C + P_C\rho(t)P_V + P_V\rho(t)P_C + P_V\rho(t)P_V \tag{5.12}$$

$$= \rho_{CC}(t) + \rho_{CV}(t) + \rho_{VC}(t) + \rho_{VV}(t), \tag{5.13}$$

and at each order $n$ it holds:

$$\rho^{(n)}(t) = \rho_{CC}^{(n)}(t) + \rho_{CV}^{(n)}(t) + \rho_{VC}^{(n)}(t) + \rho_{VV}^{(n)}(t). \tag{5.14}$$

In this way, we are able to discriminate between different contributions to the

response of the system involving similar conduction-conduction or valence-valence states or mixed valence-conduction, conduction-valence states. It is possible to express the conduction-conduction and valence-valence operators of Equation (5.13) in terms of the mixed valence-conduction and conduction-valence operators only. For example, from Equation (5.8) projected on conduction-conduction we obtain

$$\rho_{CC}(t) = P_C\rho(t)P_C = P_C\rho^2(t)P_C = P_C\rho(t)(P_C^2 + P_V^2)\rho(t)P_C \tag{5.15}$$

$$= \rho_{CC}(t)\rho_{CC}(t) + \rho_{CV}(t)\rho_{VC}(t). \tag{5.16}$$

A similar operatorial identity holds also for $\rho_{VV}(t)$, and in a compact form we write

$$\rho_{CC}(t) = \frac{1 - \sqrt{1 - 4\rho_{CV}(t)\rho_{VC}(t)}}{2}, \tag{5.17}$$

$$\rho_{VV}(t) = \rho^{(0)} - \frac{1 - \sqrt{1 - 4\rho_{VC}(t)\rho_{CV}(t)}}{2} \tag{5.18}$$

which allow to express each $n$-th order component of Equation (5.14) in terms of $\rho_{CV}^{(i)}(t)$ and $\rho_{VC}^{(i)}(t) = (\rho_{CV}^{(i)}(t))^\dagger$, with $i \leq n$, simply gathering the $n$-th order terms of Equations (5.17) and (5.18) obtained using the expansion

$$\frac{1 - \sqrt{1 - 4x}}{2} \simeq x + x^2 + 2x^3 + \dots . \tag{5.19}$$

For $n = 1$ and $n = 2$, for example, we obtain:

$$\rho^{(1)}(t) = \rho_{CV}^{(1)}(t) + \rho_{VC}^{(1)}(t) \tag{5.20}$$

$$\rho^{(2)}(t) = \rho_{CV}^{(2)}(t) + \rho_{VC}^{(2)}(t) + \left[\rho_{CV}^{(1)}(t), \rho_{VC}^{(1)}(t)\right] \tag{5.21}$$

whereas with some algebraic manipulation one arrives to a compact expression for the generic $\rho^{(n)}(t)$ $(n \geq 2)$:

$$\rho^{(n)}(t) = \rho_{CV}^{(n)}(t) + \rho_{VC}^{(n)}(t) + \sum_{i=1}^{n-1}\left[\rho_{CV}^{(i)}(t), O_{VC}^{(n-i)}(t)\right] \tag{5.22}$$

$$= \rho_{CV}^{(n)}(t) + \rho_{VC}^{(n)}(t) + \sum_{i=1}^{n-1}\left[O_{CV}^{(n-i)}(t), \rho_{VC}^{(i)}(t)\right] \tag{5.23}$$

where

$$O_{VC}(t) = \rho_{VC}(t)\frac{1 - \sqrt{1 - 4\rho_{CV}(t)\rho_{VC}(t)}}{2\rho_{CV}(t)\rho_{VC}(t)} = \frac{1 - \sqrt{1 - 4\rho_{VC}(t)\rho_{CV}(t)}}{2\rho_{VC}(t)\rho_{CV}(t)}\rho_{CV}(t). \tag{5.24}$$

### 5.2.1 Static perturbation

In the case of a static perturbation, we can drop the time-dependence from above expressions. In particular, von-Neumann Equation (5.9) simply becomes:

$$[H, \rho] = 0. \tag{5.25}$$

At each perturbative order, we now define a perturbed-like wave function $|\eta_v^{(n)}\rangle$ such that

$$\rho_{CV}^{(n)} = \sum_v P_c \rho^{(n)} \left|\psi_v^{(0)}\right\rangle \left\langle\psi_v^{(0)}\right| \equiv \sum_v \left|\eta_v^{(n)}\right\rangle \left\langle\psi_v^{(0)}\right|. \tag{5.26}$$

From the perturbative expansion of Equation (5.25), at each order $n$ it holds:

$$\sum_{i=0}^{n} \left[H^{(i)}, \rho^{(n-i)}\right] = 0. \tag{5.27}$$

Applying $P_C$ on the left and $|\psi_v^{(0)}\rangle$ on the right, we obtain

$$\left(H^{(0)} - \varepsilon_v^{(0)}\right) \left|\eta_v^{(n)}\right\rangle = -\sum_{i=1}^{n} P_C \left[H^{(i)}, \rho^{(n-i)}\right] \left|\psi_v^{(0)}\right\rangle, \tag{5.28}$$

where we exploited the relation

$$H^{(0)} \left|\psi_v^{(0)}\right\rangle = \varepsilon_v^{(0)} \left|\psi_v^{(0)}\right\rangle. \tag{5.29}$$

Then, defining the unperturbed Green-function operator projected on conduction states $\{|\psi_c^{(0)}\rangle\}$, with eigenvalues $\{\varepsilon_c^{(0)}\}$

$$\tilde{G}_v = \sum_c \frac{\left|\psi_c^{(0)}\right\rangle \left\langle\psi_c^{(0)}\right|}{\varepsilon_v^{(0)} - \varepsilon_c^{(0)}} \tag{5.30}$$

we finally write:

$$\left|\eta_v^{(n)}\right\rangle = \tilde{G}_v \left(\sum_{i=1}^{n} \left[H^{(i)}, \rho^{(n-i)}\right]\right) \left|\psi_v^{(0)}\right\rangle. \tag{5.31}$$

#### Remarks on DMPT

In principle, we now have all the ingredients to obtain $\rho^{(n)}$ and consequently to compute responses of the system at any given order. We remark that all quantities are expressed in terms of unperturbed orbitals and energies, that need to be computed just once. Plus, exploiting the property $P_C = 1 - P_V$, it is possible to avoid completely the computation of the conduction states, but rather to obtain the perturbed-like wave-functions $|\eta_v^{(n)}\rangle$ solving directly the linear Equation (5.28). Finally, we remark that in the context of DFT, self-consistency stems from the fact that $H^{(n)}$ depends on $\rho^{(n)}$, which in turn depends on $|\eta_v^{(n)}\rangle$, so in this case Equation (5.28) must be solved self-consistently, as we discuss in section 5.5 and in Appendix D.

### 5.2.2 Single monochromatic perturbation

In the case of a generic time-dependent perturbation, it is still possible to follow an approach similar to the one presented above and write $\rho^{(n)}_{CV}(t)$ in terms of the known unperturbed states $\{|\psi^{(0)}_v\rangle\}$ and $\{|\psi^{(0)}_c\rangle\}$, as in Equation (5.28) and (5.31). In the static case this was possible thanks to property (5.25). In the time-dependent case, instead, we exploit von-Neumann Equation 5.9. It is possible to study the case of a generic time dependent perturbation, as we do in Appendix D.1, however, for simplicity, in this section we focus on the case of a monochromatic perturbation.

We consider a perturbative expansion of $H(t)$ where $H^{(i)}(t) = 0 \; \forall i \geq 2$, and

$$H^{(1)}(t) = H^{(1)}(\omega)\left(e^{\mathrm{i}\omega t} + \mathrm{e}^{-\mathrm{i}\omega t}\right) \tag{5.32}$$

Expanding von-Neumann Equation (5.9), we obtain at each perturbative order $n$:

$$\mathrm{i}\hbar\dot{\rho}^{(n)}(t) = \left[H^{(0)}, \rho^{(n)}(t)\right] + \left[H^{(1)}(t), \rho^{(n-1)}(t)\right]. \tag{5.33}$$

Following the principle that at any perturbative order the response of the system is modulated by the perturbation, we plug in Equation (5.33) a trial solution of the form

$$\rho^{(n)}(t) = \sum_{\alpha}\left[\rho^{(n)}(\alpha\omega)\mathrm{e}^{-\mathrm{i}\alpha\omega t} + \rho^{(n)}(-\alpha\omega)\mathrm{e}^{\mathrm{i}\alpha\omega t}\right], \; \alpha = \begin{cases} 0, 2, \ldots, n & \text{if } n \text{ even} \\ 1, 3, \ldots, n & \text{if } n \text{ odd} \end{cases}, \tag{5.34}$$

obtaining

$$\pm\hbar\alpha\omega\rho^{(n)}(\pm\alpha\omega) - \left[H^{(0)}, \rho^{(n)}(\pm\alpha\omega)\right] = \left[H^{(1)}(\omega), \rho^{(n-1)}(\pm(\alpha+1)\omega) + \rho^{(n-1)}(\pm(\alpha-1)\omega)\right] \tag{5.35}$$

where in the case $\alpha = n$ there is only the term of order $(\alpha - 1) = (n - 1)$. Using Equation (5.22) and (5.24) we can again express at each perturbative order the $\rho^{(n)}(\pm\alpha\omega)$ as a combination of projected operators $\rho^{(i)}_{CV}(\pm\alpha\omega)$ with $i \leq n$. In similarity to the static case, we define the perturbed-like valence wave-functions $|\eta^{(n)}_v(\pm\alpha\omega)\rangle$ such that

$$\rho^{(n)}_{CV}(\pm\alpha\omega) = \sum_v P_C\rho^{(n)}(\pm\alpha\omega)\,|\psi^{(0)}_v\rangle \equiv \sum_v |\eta^{(n)}_v(\pm\alpha\omega)\rangle\,\langle\psi^{(0)}_v|\,. \tag{5.36}$$

Applying $P_C$ on the left and $|\psi^{(0)}_v\rangle$ on the right of Equation (5.35) we find

$$\left(H^{(0)} - \varepsilon^{(0)}_v \mp \hbar\alpha\omega\right)|\eta^{(n)}_v(\pm\alpha\omega)\rangle = -P_C\left[H^{(1)}(\omega), \rho^{(n-1)}(\pm(\alpha+1)\omega) + \rho^{(n-1)}(\pm(\alpha-1)\omega)\right]|\psi^{(0)}_v\rangle\,, \tag{5.37}$$

which is the generalization of Equation (5.28) to a monochromatic perturbation.

Defining the frequency-dependent Green function projected on conduction states

$$\tilde{G}_v(\pm\alpha\omega) = \sum_c \frac{|\psi_c^{(0)}\rangle \langle\psi_c^{(0)}|}{\varepsilon_v^{(0)} - \varepsilon_c^{(0)} \pm \alpha\omega}, \tag{5.38}$$

we obtain

$$|\eta_v^{(n)}(\pm\alpha\omega)\rangle = \tilde{G}_v(\pm\alpha\omega)\left[H^{(1)}(\omega), \rho^{(n-1)}(\pm(\alpha+1)\omega) + \rho^{(n-1)}(\pm(\alpha-1)\omega)\right]|\psi_v^{(0)}\rangle\,, \tag{5.39}$$

which generalized Equation (5.31) to the case of a monochromatic perturbation. We again remark that in many cases it is computationally more efficient to solve the linear system of Equation (5.37) instead of diagonalising $H^{(0)}$ to find the $\{\varepsilon_v^{(0)}\}$ and $\{\varepsilon_c^{(0)}\}$ necessary in Equation (5.39).

### Explicit expressions for n=1 and n=2

Aiming to apply TDDMPT for the Raman response, we give here an explicit expression for $\rho^{(1)}(t)$ and $\rho^{(2)}(t)$ in the case of a monochromatic perturbation. We express both quantities in terms of the projected operators:

$$\rho^{(1)}(t) = \rho_{CV}^{(1)}(t) + \rho_{VC}^{(1)}(t) \tag{5.40}$$

$$\rho^{(2)}(t) = \rho_{CV}^{(2)}(t) + \rho_{VC}^{(2)}(t) + \left[\rho_{CV}^{(1)}(t), \rho_{VC}^{(1)}(t)\right]. \tag{5.41}$$

In presence of a monochromatic perturbation, from Equation (5.34) we obtain the trial functions:

$$\rho^{(1)}(t) = \left[\rho^{(1)}(\omega)\mathrm{e}^{-\mathrm{i}\omega t} + \rho^{(1)}(-\omega)\mathrm{e}^{\mathrm{i}\omega t}\right], \tag{5.42}$$

$$\rho^{(2)}(t) = \left[\rho^{(2)}(2\omega)\mathrm{e}^{-\mathrm{i}2\omega t} + \rho^{(2)}(-2\omega)\mathrm{e}^{\mathrm{i}2\omega t} + \rho^{(2)}(0)\right]. \tag{5.43}$$

Exploiting Equations (5.40) and (5.36) we obtain for $n = 1$:

$$\rho^{(1)}(\pm\omega) = \rho_{CV}^{(1)}(\pm\omega) + \rho_{VC}^{(1)}(\pm\omega) \tag{5.44}$$

$$= \sum_v \left(|\eta_v^{(1)}(\pm\omega)\rangle \langle\psi_v^{(0)}| + |\psi_v^{(0)}\rangle \langle\eta_v^{(1)}(\mp\omega)|\right) \tag{5.45}$$

where using Equations (5.38) and (5.39) we can write

$$\rho_{CV}^{(1)}(\pm\omega) = \sum_{c,v} \frac{|\psi_c^{(0)}\rangle \langle\psi_c^{(0)}| \left[H^{(1)}(\omega), \rho^{(0)}\right] |\psi_v^{(0)}\rangle \langle\psi_v^{(0)}|}{\varepsilon_v^{(0)} - \varepsilon_c^{(0)} \pm \hbar\omega}, \tag{5.46}$$

$$\rho_{VC}^{(1)}(\pm\omega) = \sum_{c,v} \frac{|\psi_v^{(0)}\rangle \langle\psi_v^{(0)}| \left[H^{(1)}(\omega), \rho^{(0)}\right]^\dagger |\psi_c^{(0)}\rangle \langle\psi_c^{(0)}|}{\varepsilon_v^{(0)} - \varepsilon_c^{(0)} \mp \hbar\omega} \tag{5.47}$$

$$= \left(\rho_{CV}^{(1)}(\mp\omega)\right)^\dagger \tag{5.48}$$

Analogously, using Equation (5.41) and (5.36), for $n = 2$ we obtain:

$$\rho^{(2)}(\pm 2\omega) = \rho_{CV}^{(2)}(\pm 2\omega) + \rho_{VC}^{(2)}(\pm 2\omega) + \left[\rho_{CV}^{(1)}(\pm\omega), \rho_{VC}^{(1)}(\pm\omega)\right] \tag{5.49}$$

$$= \sum_v \left(|\eta_v^{(2)}(\pm 2\omega)\rangle \langle\psi_v^{(0)}| + |\psi_v^{(0)}\rangle \langle\eta_v^{(2)}(\mp 2\omega)|\right) + \\ + \sum_v |\eta_v^{(1)}(\pm\omega)\rangle \langle\eta_v^{(1)}(\mp\omega)| - \sum_{v,v'} |\psi_v^{(0)}\rangle \langle\eta_v^{(1)}(\pm\omega)|\eta_{v'}^{(1)}(\pm\omega)\rangle \langle\psi_{v'}^{(0)}|, \tag{5.50}$$

$$\rho^{(2)}(0) = \rho_{CV}^{(2)}(0) + \rho_{VC}^{(2)}(0) + \left[\rho_{CV}^{(1)}(\omega), \rho_{VC}^{(1)}(-\omega)\right] + \left[\rho_{CV}^{(1)}(-\omega), \rho_{VC}^{(1)}(+\omega)\right] \tag{5.51}$$

$$= \sum_v \left(|\eta_v^{(2)}(0)\rangle \langle\psi_v^{(0)}| + |\psi_v^{(0)}\rangle \langle\eta_v^{(2)}(0)|\right) + \\ + \sum_v \left(|\eta_v^{(1)}(+\omega)\rangle \langle\eta_v^{(1)}(+\omega)| + |\eta_v^{(1)}(-\omega)\rangle \langle\eta_v^{(1)}(-\omega)|\right) + \\ - \sum_{v,v'} \left(|\psi_v^{(0)}\rangle \langle\eta_v^{(1)}(\pm\omega)|\eta_{v'}^{(1)}(\pm\omega)\rangle \langle\psi_{v'}^{(0)}| + |\psi_v^{(0)}\rangle \langle\eta_v^{(1)}(\pm\omega)|\eta_{v'}^{(1)}(\pm\omega)\rangle \langle\psi_{v'}^{(0)}|\right) \tag{5.52}$$

where using Equation (5.38) and (5.39) we can write

$$\rho_{CV}^{(2)}(\pm 2\omega) = \sum_{c,v} \frac{|\psi_c^{(0)}\rangle \langle\psi_c^{(0)}| \left[H^{(1)}(\omega), \rho^{(1)}(\pm\omega)\right] |\psi_v^{(0)}\rangle \langle\psi_v^{(0)}|}{\varepsilon_v^{(0)} - \varepsilon_c^{(0)} \pm 2\hbar\omega}, \tag{5.53}$$

$$\rho_{VC}^{(2)}(\pm 2\omega) = \sum_{c,v} \frac{|\psi_v^{(0)}\rangle \langle\psi_v^{(0)}| \left[H^{(1)}(\omega), \rho^{(1)}(\pm\omega)\right]^\dagger |\psi_c^{(0)}\rangle \langle\psi_c^{(0)}|}{\varepsilon_v^{(0)} - \varepsilon_c^{(0)} \mp 2\hbar\omega} \tag{5.54}$$

$$= \left(\rho_{CV}^{(2)}(\mp 2\omega)\right)^\dagger, \tag{5.55}$$

$$\rho_{CV}^{(2)}(0) = \sum_{c,v} \frac{|\psi_c^{(0)}\rangle \langle\psi_c^{(0)}| \left[H^{(1)}(\omega), \rho^{(1)}(\omega) + \rho^{(1)}(-\omega)\right] |\psi_v^{(0)}\rangle \langle\psi_v^{(0)}|}{\varepsilon_v^{(0)} - \varepsilon_c^{(0)}} \tag{5.56}$$

$$= \left(\rho_{VC}^{(2)}(0)\right)^\dagger. \tag{5.57}$$

### 5.2.3 Double monochromatic perturbation

With the aim of computing the Raman response beyond the Placzek approximation, we need to account for a finite $\omega_{\text{ph}} \neq 0$. To do so, we consider two monochromatic electric fields, accounting separately for the incoming and outgoing photons. In the framework of TDDMPT, we consider a perturbative expansion of $H(t)$ with $H^{(i)}(t) = 0 \; \forall \; i \geq 2$ and the first order perturbative term $H^{(1)}(t)$ is the sum of two monochromatic terms, namely

$$H^{(1)}(t) = H^{(1)}(\omega_1) \left( e^{\mathrm{i}\omega_1 t} + \mathrm{e}^{-\mathrm{i}\omega_1 t} \right) + H^{(1)}(\omega_2) \left( e^{\mathrm{i}\omega_2 t} + \mathrm{e}^{-\mathrm{i}\omega_2 t} \right) \tag{5.58}$$

This perturbation describes, for example, the incident and outgoing electric fields in a Raman experiment where $|\omega_1 - \omega_2| = \omega_{\text{ph}}$ is the energy of the excited (or absorbed) phonon. We adopted a more general notation with $\omega_1$ and $\omega_2$ instead of $\omega_{\text{in}}$ and $\omega_{\text{out}}$, since this approach may be applied in principle also to other process besides the Raman scattering. Analogously to the single monochromatic case, to obtain the generic $n$-th order response, we proceed as follows:

- we write for the generic $\rho^{(n)}(t)$ a Fourier-like expansion in terms of operators which depend on a linear combination of the frequencies, namely:

$$\rho^{(n)}(\alpha\omega_1 + \beta\omega_2)\mathrm{e}^{\mathrm{i}(\alpha\omega_1 + \beta\omega_2)t}, \tag{5.59}$$

  where $\alpha$ and $\beta$ are integer numbers such that $|\alpha| + |\beta| = n$;

- each of this operators can be written in terms of the projected operators $\rho^{(i)}_{CV}(\alpha'\omega_1 + \beta'\omega_2)$, with $\alpha'$ and $\beta'$ integer numbers such that $|\alpha'| + |\beta'| = i$ and $i \leq n$;

- we express the $\rho^{(i)}_{CV}(\alpha'\omega_1 + \beta'\omega_2)$ in terms of perturbed-like valence wave functions $|\eta^{(i)}_v(\alpha'\omega_1 + \beta'\omega_2)\rangle$, generalizing Equation (5.37) and (5.39).

For the description of Raman scattering, only terms up to $n = 2$ are needed. In what follows we limit to give the final expressions for $n = 1$ and $n = 2$ and address to Appendix D.2 for their explicit derivation. For the former term, there is no mixing of frequencies, so the results is the same of the single monochromatic perturbation case. With the definition of the frequency-dependent Green function projected on conduction states of Equation (5.38) with $\alpha = 1$, we obtain for $j = 1, 2$

$$|\eta^{(1)}_v(\pm\omega_j)\rangle = \tilde{G}_v(\pm\omega_j) \left[ H^{(1)}, \rho^{(0)} \right] |\psi^{(0)}_v\rangle \, . \tag{5.60}$$

which is just Equation (5.39) in the case $n = 1$. For $n = 2$, defining the frequency-dependent Green functions

$$\tilde{G}_v(\alpha\omega_1 + \beta\omega_2) = \sum_c \frac{|\psi^{(0)}_c\rangle \langle\psi^{(0)}_c|}{\varepsilon^{(0)}_v - \varepsilon^{(0)}_c + \hbar(\alpha\omega_1 + \beta\omega_2)}, \tag{5.61}$$

we can write the explicit expression for the generic $|\eta_v^{(2)}(\alpha\omega_1+\beta\omega_2)\rangle$

$$|\eta_v^{(2)}(\alpha\omega_1+\beta\omega_2)\rangle = \tilde{G}_v(\alpha\omega_1+\beta\omega_2)\,\{\bullet\}\,|\psi_v^{(0)}\rangle\,, \tag{5.62}$$

where inside the curly brackets $\{\bullet\}$ there are the proper commutators between $H^{(1)}(\omega_j)$ and $\rho^{(1)}(\pm\omega_l)$ $(j,l\in\{1,2\})$ derived in Appendix D.2 in Equations (D.29 - D.33). We notice how now mixed frequency terms appear in denominators, allowing for more resonances. We remark that, as in the static and in the single monochromatic perturbation case, another way to obtain $|\eta_v^{(2)}(\alpha\omega_1+\beta\omega_2)\rangle$ is by solving linear (self-consistent) systems, reported in Appendix D.2, which may be preferable for numerical implementation as we avoid the explicit calculation of the empty conduction states.

## 5.3 Treatment of electric fields

Having derived a framework that allows for the calculations of time-dependent responses with respect to a perturbation at any given order, in this section we focus on how to treat a uniform electric field in TDDMPT. This is indeed paramount e.g. for the derivation of the Raman response. We follow the idea of Ref.[167] for the static case and then generalize it to the case of a monochromatic field. We consider, without loss of generality, a perturbation due to a uniform monochromatic electric field acting on an insulating crystal along the $z$-axis:

$$H^{(1)}(t) = H^{(1)}(\omega)\left(\mathrm{e}^{\mathrm{i}\omega t}+\mathrm{e}^{-\mathrm{i}\omega t}\right) = -|e|\hat{r}_z E_z(\omega)\left(\mathrm{e}^{\mathrm{i}\omega t}+\mathrm{e}^{-\mathrm{i}\omega t}\right) \tag{5.63}$$

where $|e|$ is the electronic charge and $\hat{r}_z$ is the $z$-component of the position operator $\hat{\boldsymbol{r}}$. As a consequence of our approach based on von-Neumann Equation (5.9) or its time-independent version Equation (5.25), effects of the perturbation appears always inside commutators with derivatives of the electronic density matrix. For this reason, in the case of a perturbation in the form of Equation (5.63), the quantities we need to compute are matrix elements of the commutators between the generic $H^{(1)}(\omega)$ and $\rho^{(n-1)}(\alpha\omega)$ – as e.g. in Equation (5.28), (5.31), (5.60), and (5.62) – which have the form:

$$\langle\psi_c^{(0)}|\left[H^{(1)}(\omega),\rho^{(n-1)}(\alpha\omega)\right]|\psi_v^{(0)}\rangle \propto \langle\psi_c^{(0)}|\left[\hat{r}_z,\rho^{(n-1)}(\alpha\omega)\right]|\psi_v^{(0)}\rangle\,, \tag{5.64}$$

where the commutators between the position operator and the derivative of density matrix are well-defined even in the static limit. By definition, we can express each $\rho^{(i)}(\alpha\omega)$ as a sum of operators of the type

$$D = \frac{1}{\Omega_c}\int \frac{\mathrm{d}^3k}{(2\pi)^3} D_{\mathbf{k}} \tag{5.65}$$

where $\Omega_c$ is the volume of the unit cell of the crystal, $\mathbf{k}$ is defined over the first Brillouin zone, and we can write

$$D_{\mathbf{k}} = \sum_v |\alpha_{\mathbf{k}v}\rangle \langle\beta_{\mathbf{k}v}| \,, \tag{5.66}$$

where $|\alpha_{\mathbf{k}v}\rangle = \mathrm{e}^{\mathrm{i}\mathbf{k}\cdot\mathbf{r}} |\tilde{\alpha}_{\mathbf{k}v}\rangle$ and $|\beta_{\mathbf{k}v}\rangle = \mathrm{e}^{\mathrm{i}\mathbf{k}\cdot\mathbf{r}} |\tilde{\beta}_{\mathbf{k}v}\rangle$ are Bloch-like wave-functions with $|\tilde{\alpha}_{\mathbf{k}v}\rangle$ and $|\tilde{\beta}_{\mathbf{k}v}\rangle$ their lattice-periodic part. If the functions $D_{\mathbf{k}}$ are analytic and periodic in $\mathbf{k}$, it holds

$$\Omega_c \int \frac{\mathrm{d}^3k}{(2\pi)^3} \frac{\partial}{\partial k_z} D_{\mathbf{k}} = 0 \tag{5.67}$$

and exploiting this property it is straightforward to demonstrate that

$$[\hat{r}_z, D] = \mathrm{i}\Omega_c \int \frac{\mathrm{d}^3k}{(2\pi)^3} \sum_v \mathrm{e}^{\mathrm{i}\mathbf{k}\cdot\mathbf{r}} \frac{\partial |\tilde{\alpha}_{\mathbf{k}v}\rangle \langle\tilde{\beta}_{\mathbf{k}v}|}{\partial k_z} \mathrm{e}^{-\mathrm{i}\mathbf{k}\cdot\mathbf{r}}. \tag{5.68}$$

Form this, it follows that in presence of an external (time-dependent) uniform electric field along the $z$-axis, the matrix elements of Equation (5.68) between unperturbed wave-functions $\{|\psi^{(0)}_{\mathbf{k}c}\rangle\}$ and $\{|\psi^{(0)}_{\mathbf{k}v}\rangle\}$ have the form:

$$\frac{1}{N} \langle\psi^{(0)}_{\mathbf{k}c}| \, [\hat{r}_z, D] \, |\psi^{(0)}_{\mathbf{k}v}\rangle = \mathrm{i} \sum_{v'} \langle\tilde{\psi}^{(0)}_{\mathbf{k}c}| \, \frac{\partial \, |\tilde{\alpha}_{\mathbf{k}v'}\rangle \langle\tilde{\beta}_{\mathbf{k}v'}|}{\partial k_z} \, |\tilde{\psi}^{(0)}_{\mathbf{k}v}\rangle \tag{5.69}$$

where $N$ is the number of unit cells and the scalar product on the right-hand side is taken over a single unit cell.

### 5.3.1 Derivatives of polarisation and non-linear optical susceptibilities

The theory developed for TDDMPT and the treatment of uniform electric fields, makes it particularly convenient to compute the derivatives of polarisation $\mathbf{P}$ with respect to a uniform electric field. Indeed, in the most general case, the relation between polarization $\mathbf{P}$ and the electric field $\mathbf{E}$ reads

$$\mathbf{P} = \varepsilon_0 \overleftrightarrow{\chi}(\mathbf{E}) \cdot \mathbf{E}, \tag{5.70}$$

namely the induced polarization $\mathbf{P}$ is related to the electric field $\mathbf{E}$ via a susceptibility tensor $\overleftrightarrow{\chi}(\mathbf{E})$ which depends on the electric field itself. Expanding $\overleftrightarrow{\chi}(\mathbf{E})$ in terms of the electric field we obtain

$$\mathbf{P} = \varepsilon_0 \left( \overleftrightarrow{\chi}^{(1)} \cdot \mathbf{E} + \mathbf{E} \cdot \overleftrightarrow{\chi}^{(2)} \cdot \mathbf{E} + \dots \right), \tag{5.71}$$

where the terms $\overleftrightarrow{\chi}^{(n)}$ are the so-called non-linear optical susceptibilities an it holds

$$\overleftrightarrow{\chi}^{(n)} = \frac{1}{\varepsilon_0} \frac{\partial^n \mathbf{P}}{\partial \mathbf{E}^n} = \mathbf{P}^{(n)}. \tag{5.72}$$

These quantities are particularly relevant in the field of non-linear optics but also e.g. for the Raman response of a polar longitudinal mode in the long-wavelength limit, as will be discussed in next section.

For simplicity of notation, but without losing generality, we consider again a static electric field along the $z$-axis, but the results holds also for a monochromatic field. Thanks to Equation (5.7) we have that:

$$P_z^{(n)} = -\frac{|e|}{N\Omega_c}\frac{\partial^{n+1}\mathcal{E}^{\mathrm{el}}}{\partial E_z^{n+1}} = -\frac{2|e|}{N\Omega_c}\mathrm{Tr}\left[r_z\rho^{(n)}\right], \tag{5.73}$$

where $-|e|$ is the electronic charge, $N$ the number of unit cells and $\Omega_c$ their volume. Exploiting Equation (5.22) and using the property of the trace $\mathrm{Tr}\left[[A,B]C\right] = \mathrm{Tr}\left[A[B,C]\right]$, we obtain:

$$P_z^{(n)} = -\frac{2|e|}{N\Omega_c}\mathrm{Tr}\left[\left[r_z,\rho^{(0)}\right]\rho_{VC}^{(n)} - \left[r_z,\rho^{(0)}\right]\rho_{CV}^{(n)} + \frac{1}{2}\sum_{i=1}^{n-1}\left(\left[r_z,\rho_{CV}^{(i)}\right]O_{VC}^{(n-i)} - \left[r_z,\rho_{VC}^{(i)}\right]O_{CV}^{(n-i)}\right)\right] = \tag{5.74}$$

$$= \frac{2|e|}{N\Omega_c}\sum_{v,v',\mathbf{k}}\mathrm{Im}\left[2\left\langle\tilde{\eta}_{\mathbf{k},v}^{(n)}\right|\frac{\partial\left|\tilde{\psi}_{\mathbf{k},v'}^{(0)}\right\rangle\left\langle\tilde{\psi}_{\mathbf{k},v'}^{(0)}\right|}{\partial k_z}\left|\tilde{\psi}_{\mathbf{k},v}^{(0)}\right\rangle + \sum_{i=1}^{n-1}\left\langle\tilde{\chi}_{\mathbf{k},v}^{(n-i)}\right|\frac{\partial\left|\tilde{\eta}_{\mathbf{k},v'}^{(i)}\right\rangle\left\langle\tilde{\psi}_{\mathbf{k},v'}^{(0)}\right|}{\partial k_z}\left|\tilde{\psi}_{\mathbf{k},v}^{(0)}\right\rangle\right] \tag{5.75}$$

where $n \geq 2$ and the operators $O_{VC}^{(i)}$ are written as

$$O_{VC}^{(i)} = \sum_{\mathbf{k}}\left|\psi_{\mathbf{k},v}^{(0)}\right\rangle\left\langle\chi_{\mathbf{k},v}^{(i)}\right| \tag{5.76}$$

with $\left|\chi_{\mathbf{k},v}^{(i)}\right\rangle = O_{CV}^{(i)}\left|\psi_{\mathbf{k},v}^{(0)}\right\rangle$. If $n = 1$, we recover the usual expression for the (linear) static electronic susceptibility $\chi^{(1)}$:

$$\chi^{(1)} = -\frac{2|e|}{\varepsilon_0 N\Omega_c}\mathrm{Tr}\left\{\left[r_z,\rho^{(0)}\right]\rho_{VC}^{(1)} - \left[r_z,\rho^{(0)}\right]\rho_{CV}^{(1)}\right\} = \tag{5.77}$$

$$= -\frac{4|e|}{\varepsilon_0 N\Omega_c}\mathrm{Re}\left[\sum_{v,c}\frac{\left\langle\psi_{\mathbf{k},v}^{(0)}\right|r_z\left|\psi_{\mathbf{k},c}^{(0)}\right\rangle\left\langle\psi_{\mathbf{k},c}^{(0)}\right|r_z\left|\psi_{\mathbf{k},v}^{(0)}\right\rangle}{\varepsilon_v^{(0)} - \varepsilon_c^{(0)}}\right] \tag{5.78}$$

where for simplicity we neglected the Cartesian indices in the susceptibility tensor.

Following a similar approach, one obtains the expressions for $\omega$-dependent non-linear susceptibilities. For example, from the second derivative with respect to a

monochromatic uniform electric field we obtain:

$$\chi^{(2)}(\omega) = \frac{2e}{\varepsilon_0 N \Omega_c} \sum_{v,v',\mathbf{k}} \Bigg[ 2\mathrm{Im} \left( \langle \tilde{\eta}^{(2)}_{\mathbf{k},v}(0)| \, \frac{\partial \, |\tilde{\psi}^{(0)}_{\mathbf{k},v'}\rangle \, \langle \tilde{\psi}^{(0)}_{\mathbf{k},v'}|}{\partial k_z} \, |\tilde{\psi}^{(0)}_{\mathbf{k},v}\rangle \right) + \mathrm{i} \, \langle \tilde{\eta}^{(1)}_{\mathbf{k},v}(+\omega)| \, \frac{\partial \, |\tilde{\eta}^{(1)}_{\mathbf{k},v'}(+\omega)\rangle \, \langle \tilde{\psi}^{(0)}_{\mathbf{k},v'}|}{\partial k_z} \, |\tilde{\psi}^{(0)}_{\mathbf{k},v}\rangle + \mathrm{i} \, \langle \tilde{\eta}^{(1)}_{\mathbf{k},v}(-\omega)| \, \frac{\partial \, |\tilde{\eta}^{(1)}_{\mathbf{k},v'}(-\omega)\rangle \, \langle \tilde{\psi}^{(0)}_{\mathbf{k},v'}|}{\partial k_z} \, |\tilde{\psi}^{(0)}_{\mathbf{k},v}\rangle \Bigg] . \tag{5.79}$$

The $\chi^{(2)}(\omega)$ tensors are also called *electro-optic* tensors and as we will see in what follows, they play a key role in the Raman response of insulating crystals when the Raman active mode is a longitudinal polar mode in the long-wavelength limit. It is possible to compute ab-initio the $\chi^{(2)}(0)$ in the QE code, where it is implemented exploiting the $2n+1$ theorem[170], however we are currently working on its generalization to the frequency-dependent case using TDDMPT.

## 5.4 Raman response with TDDMPT

In this section we apply the theory introduced above to the case of the vibrational Raman response of an insulating crystal at $T = 0\,K$. For convenience, we sum up here the discussion of previous Chapter 4 on the different levels of approximations one can adopt. In the most general case, to treat the (Stokes) vibrational Raman response of a crystal, we have to account for an inelastic scattering process where an incoming photon of energy $\omega_{\mathrm{in}}$ interacts with the system and exchange an amount of energy $\omega_{\mathrm{ph}}$, used to excite the phonon of a Raman active mode. As a result of the interaction, an outgoing photon with energy $\omega_{\mathrm{out}} = \omega_{\mathrm{in}} - \omega_{\mathrm{ph}}$ is emitted. In the Placzek approximation, we consider a process where $\omega_{\mathrm{in}}$ is smaller than electronic transition energies and much higher than vibrational energies, so that one can consider $\omega_{\mathrm{in}} = \omega_{\mathrm{out}} = 0$. Sometimes it is instead necessary to account for the fact that laser frequencies are close or even matches electronic transitions, and this can be done considering $\omega_{\mathrm{in}} = \omega_{\mathrm{out}} = \omega$, but still neglecting $\omega_{\mathrm{ph}} = 0$. Finally, in specific situations one has to include a finite $\omega_{\mathrm{ph}} \neq 0$, as we shown in section 4.3 for 1D systems as carbyne or carbon nanotubes. TDDMPT formalism offers a compact and elegant framework to compute fully ab initio Raman responses at different level of approximations, allowing also for the inclusion of non-linear optic effects of macroscopic electric fields generated by lattice polar vibrations of longitudinal optical phonons in the long wave-length limit.

### 5.4.1 Static response in the Placzek approximation

Using TDDMPT in its time-independent version, we study the Raman response of an insulating system in the Placzek approximation. The object of interest is

the Raman activity tensor of Equation (4.2), which we rewrite here making use of Equation (4.8) with $\omega = 0$ to express it in terms of derivatives of the electronic ground state energy $\mathcal{E}^{\text{el}}$:

$$A^{\nu}_{lm} = \sum_{k\tau} \frac{\partial^3 \mathcal{E}^{\text{el}}}{\partial E_l \partial E_m \partial u_{k\tau}} \frac{\mathrm{w}^{\nu}_{k\tau}}{\sqrt{M_\tau}}. \tag{5.80}$$

We remind that $E_l$ ($E_m$) is the $l$-th ($m$-th) Cartesian component of a uniform electric field, $u_{k\tau}$ is the displacement of the $\tau$-th atom in the $k$-th direction, $M_\tau$ is its atomic mass and $\mathrm{w}^{\nu}_{k\tau}$ is the orthonormal vibrational eigenmode $\nu$. In the DMPT framework, the third-order derivative of the electronic energy becomes:

$$\frac{\partial^3 \mathcal{E}^{\text{el}}}{\partial E_l \partial E_m \partial u_{k\tau}} = 2\mathrm{Tr}\left[\frac{\partial^2 \rho}{\partial E_l \partial E_m} \frac{\partial H}{\partial u_{k\tau}}\right]. \tag{5.81}$$

We remark that, in this case, one can also calculate the third-order derivatives as finite differences of electronical susceptibility $\chi_{lm} = \partial^2 \mathcal{E}^{\text{el}} / \partial E_l \partial E_m$ (which can be computed using standard linear response techniques), namely:

$$\frac{\partial^3 \mathcal{E}^{\text{el}}}{\partial E_l \partial E_m \partial u_{k\tau}} \simeq \frac{\chi_{lm}(+\Delta u_{k\tau}) - \chi_{lm}(-\Delta u_{k\tau})}{2\Delta u_{k\tau}}. \tag{5.82}$$

However, even in this case of the Placzek approximation it may be convenient to adopt the DMPT approach instead. In the finite-differences case, indeed, one would need $36 N_{\text{atoms}}$ first-order calculation, against the six second-order calculation required to compute the $\rho^{(2)}$ of Equation (5.81). The DMPT approach is thus particularly advantageous when dealing with large systems with many atoms in the unit cell[158].

We conclude this section writing an explicit expression for the third-order derivative in the case of the 1D model (Equation (4.13)), making use of the quantities defined in this Chapter:

$$\begin{aligned}\frac{\partial^3 \mathcal{E}^{\text{el}}}{\partial E^2 \partial \delta r_\alpha} = \frac{2}{N_k} \sum_k \Bigg[ &\sum_v \langle \eta^{(2)}_{v,k} | \frac{\partial H}{\partial \delta r_\alpha} | \psi^{(0)}_{v,k} \rangle - \sum_{v,v'} \langle \eta^{(1)}_{v,k} | \eta^{(1)}_{v',k} \rangle \langle \psi^{(0)}_{v',k} | \frac{\partial H}{\partial \delta r_\alpha} | \psi^{(0)}_{v,k} \rangle \\ &+ \sum_v \langle \psi^{(0)}_{v,k} | \frac{\partial H}{\partial \delta r_\alpha} | \eta^{(2)}_{v,k} \rangle + \sum_v \langle \eta^{(1)}_{v,k} | \frac{\partial H}{\partial \delta r_\alpha} | \eta^{(1)}_{v,k} \rangle \Bigg],\end{aligned} \tag{5.83}$$

where in the model we have one valence (occupied) band only and the $\{|\eta^{(i)}_{s,k}\rangle\}$ ($s = v, v'$; $i = 1, 2$) can be computed with Equation (5.31) or (5.28).

### 5.4.2 Resonant Raman response

Analogously to the previous case, we first write the expression for the Raman activity tensor in the resonant case (Equation (4.5)) making use of Equation (4.8) to express

it in terms of derivatives of the energy:

$$A^{\nu}_{lm}(\omega) = \sum_{k\tau} \frac{\partial^3 \mathcal{E}^{\mathrm{el}}(\omega)}{\partial E_l \partial E_m \partial u_{k\tau}} \frac{\mathrm{w}^{\nu}_{k\tau}}{\sqrt{M_\tau}}, \tag{5.84}$$

where in the TDDMPT approach it can be demonstrated that:

$$\frac{\partial^3 \mathcal{E}^{\mathrm{el}}(\omega)}{\partial E_l \partial E_m \partial u_{k\tau}} = \frac{\partial \chi_{lm}(\omega)}{\partial u_{k\tau}} = 2\mathrm{Tr}\left[\frac{\partial^2 \rho(0)}{\partial E_l \partial E_m} \frac{\partial H}{\partial u_{k\tau}}\right]. \tag{5.85}$$

The term $\rho^{(2)}(0)$, defined in Equation (5.53), comes from the mixing of terms in $+\omega$ and $-\omega$ from the perturbative expansion. Hence, it can be imagined as the quantity which accounts for processes where photons with different, opposing, energies are involved: one is absorbed and the other is emitted, as in the case of Raman scattering. Again, we remark that it is in principle possible to compute the third-order derivative with the finite differences approach, however the same considerations on the convenience of using TDDMPT, especially for large systems with several atoms per cell, applies in this case. Finally we make use of quantities defined in this Chapter to write an explicit expression for the third-order derivatives in the case of the 1D model (Equation (4.15)):

$$\begin{aligned}
\frac{\partial^3 \mathcal{E}^{\mathrm{el}}(\omega)}{\partial E^2 \partial \delta r \alpha} =& 2\mathrm{Tr}\left[\rho^{(2)}(0)\frac{\partial H}{\partial \delta r \alpha}\right] = \\
=& \frac{2}{N_k}\sum_k \Bigg[\sum_v \langle \eta^{(2)}_{v,k}(0)|\frac{\partial H}{\partial \delta r\alpha}|\psi^{(0)}_{v,k}\rangle + \sum_v \langle \psi^{(0)}_{v,k}|\frac{\partial H}{\partial \delta r\alpha}|\eta^{(2)}_{v,k}(0)\rangle \\
&- \sum_{v,v'} \langle \eta^{(1)}_{v,k}(+\omega)|\eta^{(1)}_{v',k}(+\omega)\rangle\langle \psi^{(0)}_{v',k}|\frac{\partial H}{\partial \delta r\alpha}|\psi^{(0)}_{v,k}\rangle + \sum_v \langle \eta^{(1)}_{v,k}(+\omega)|\frac{\partial H}{\partial \delta r\alpha}|\eta^{(1)}_{v,k}(+\omega)\rangle \\
&- \sum_{v,v'} \langle \eta^{(1)}_{v,k}(-\omega)|\eta^{(1)}_{v',k}(-\omega)\rangle\langle \psi^{(0)}_{v',k}|\frac{\partial H}{\partial \delta r\alpha}|\psi^{(0)}_{v,k}\rangle + \sum_v \langle \eta^{(1)}_{v,k}(-\omega)|\frac{\partial H}{\partial \delta r\alpha}|\eta^{(1)}_{v,k}(-\omega)\rangle\Bigg],
\end{aligned} \tag{5.86}$$

where we used Equations (5.53) and (5.56), and the perturbed-like wave-functions can be computed using Equation (5.37) or (5.39).

### 5.4.3 Going Beyond the Placzek approximation

Finally, we write the general expression for the Raman activity tensor beyond the Placzek approximation in the TDDMPT framework. In particular, we start from Equation (5.87), which we rewrite:

$$A^{\nu}_{lm}(\omega_{\mathrm{in}}, \omega_{\mathrm{out}}, \omega_{\mathrm{ph}}) = \sum_{k\tau} \frac{\partial^3 \mathcal{E}^{\mathrm{el}}(\omega_{\mathrm{in}}, \omega_{\mathrm{out}}, \omega_{\mathrm{ph}})}{\partial E_l \partial E_m \partial u_{k\tau}} \frac{\mathrm{w}^{\nu}_{k\tau}}{\sqrt{M_\tau}}. \tag{5.87}$$

We focus on the Stokes process of phonon creation, and adapting to the notation used in the present Chapter, we put $\omega_{\mathrm{in}} = \omega_1$, $\omega_{\mathrm{out}} = \omega_2$ and $\omega_{\mathrm{ph}} = \omega_1 - \omega 2$. Moreover, to simplify the notation for the process we are interested in, we identify

$(\omega_{\text{in}}, \omega_{\text{out}}, \omega_{\text{ph}}) \equiv (\omega_1 - \omega_2)$. With these considerations, we now express the third-order derivative of the energy of above Equation (5.87) in the TDDMPT formalism:

$$\frac{\partial^3 \mathcal{E}^{\text{el}}(\omega_1 - \omega_2)}{\partial E_l \partial E_m \partial u_{k\tau}} = 2\text{Tr}\left[\frac{\partial^2 \rho(\omega_1 - \omega_2)}{\partial E_l \partial E_m}\frac{\partial H}{\partial u_{k\tau}}\right]. \tag{5.88}$$

We remark that in this case it is not possible to compute the third-order derivative as finite differences of electronic susceptibilities, making necessary to resort to other approaches e.g. the TDDMPT one. Analogously to the previous sections, we give an explicit expression for (5.88) in terms of quantities defined in this Chapter (and in Appendix D) for the case of the 1D model:

$$\begin{aligned}
\frac{\partial^3 \mathcal{E}^{\text{el}}(\omega_1 - \omega_2)}{\partial E^2 \partial \delta r_\alpha} =& 2\text{Tr}\left[\rho^{(2)}(\omega_1 - \omega_2)\frac{\partial H}{\partial \delta r_\alpha}\right] = \\
=& \frac{2}{N_k}\sum_k \Bigg[\sum_v \langle \eta^{(2)}_{v,k}(\omega_1 - \omega_2)|\frac{\partial H}{\partial \delta r_\alpha}|\psi^{(0)}_{v,k}\rangle + \sum_v \langle \psi^{(0)}_{v,k}|\frac{\partial H}{\partial \delta r_\alpha}|\eta^{(2)}_{v,k}(\omega_1 - \omega_2)\rangle \\
&+ \sum_{v,v'} \langle \eta^{(1)}_{v,k}(+\omega_1)|\eta^{(1)}_{v',k}(+\omega_2)\rangle\langle \psi^{(0)}_{v',k}|\frac{\partial H}{\partial \delta r_\alpha}|\psi^{(0)}_{v,k}\rangle - \sum_v \langle \eta^{(1)}_{v,k}(+\omega_1)|\frac{\partial H}{\partial \delta r_\alpha}|\eta^{(1)}_{v,k}(+\omega_2)\rangle \\
&+ \sum_{v,v'} \langle \eta^{(1)}_{v,k}(-\omega_2)|\eta^{(1)}_{v',k}(-\omega_1)\rangle\langle \psi^{(0)}_{v',k}|\frac{\partial H}{\partial \delta r_\alpha}|\psi^{(0)}_{v,k}\rangle - \sum_v \langle \eta^{(1)}_{v,k}(-\omega_2)|\frac{\partial H}{\partial \delta r_\alpha}|\eta^{(1)}_{v,k}(-\omega_1)\rangle\Bigg],
\end{aligned} \tag{5.89}$$

where we used Equation (D.25), which we report here

$$\rho^{(2)}(\omega_1 - \omega_2) = \rho^{(2)}_{CV}(\omega_1 - \omega_2) + \rho^{(2)}_{VC}(\omega_1 - \omega_2) + \left[\rho^{(1)}_{CV}(\omega_1), \rho^{(1)}_{VC}(\omega_2)\right] + \left[\rho^{(1)}_{CV}(\omega_2), \rho^{(1)}_{VC}(\omega_1)\right] \tag{5.90}$$

and all perturbed-like wave-functions and projected operators are defined in Appendix D.

### 5.4.4 Raman response with non-linear corrections

To conclude this part on the application of TDDMPT to the study of the Raman response, we take into consideration the case where the optical phonon involved in the process is longitudinal, meaning that its oscillation at $|\mathbf{q}| \sim 0$, the so-called long-wavelength limit, may induce a macroscopic electric electric field if the crystal is polar. If the oscillations of this polar mode are induced by an external electric field, in order to account for system's polar response in this situation, one must resort to the general relation between polarization and electric field given in Equation (5.71), where the so-called non-linear optical susceptibilities terms appears.

As far as the Raman response is concerned, we focus on the cases where the finite differences approach is still valid so that we can write for an insulating crystal:

$$\frac{\partial \chi^{(1)}_{lm}}{\partial u_{k,\tau}} = \left.\frac{\partial \chi^{(1)}_{lm}}{\partial u_{k,\tau}}\right|_{\mathbf{E}=0} - \frac{8\pi}{\Omega_{\text{c}}}\frac{\sum_i Z^*_{ik,\tau} q_i}{\sum_{i,i'} q_i \varepsilon_{ii'} q_{i'}} \sum_i \chi^{(2)}_{lmi} q_i, \tag{5.91}$$

where the first term on the right-hand side is computed at null electric field, $Z^*_\tau$ is the effective charge tensor of atom $\tau$, and $\chi^{(2)}_{lmi}$ is the non-linear optical susceptibility tensor as defined by the expansion in Equation (5.71). In order to correctly describe a Raman process in presence of a polar mode, e.g. in III-V cubic semiconductors as GaAs, it is thus necessary to use the above Equation (5.91) in the calculation of Raman activities. To do so, TDDMPT offers a self-consistent and compact framework, as it allows for the calculation of all the quantities involved.

## 5.5 Implementation of the Raman response in Quantum ESPRESSO

This last section is dedicated to the implementation of the calculation of the resonance Raman response we did in the Quantum ESPRESSO (QE) code[169], using the TDDMPT formalism discussed above. Being QE based on a DFT approach, we must now explicitly account for self-consistent terms given by the dependence of the generic $H^{(n)}$ on $\rho^{(n)}$. As anticipated, for the sake of time-efficiency, but without losing accuracy, it is convenient to avoid the explicit calculation of the (unperturbed) conduction states. In TDDMPT this is possible since the main ingredients can be obtained solving self-consistent linear systems depending on the valence states only.

As a starting point, we adopt the already implemented static Raman response[158], and generalize it in order to account for a time-dependent uniform electric field perturbation. With the TDDMPT approach it is in principle possible to implement in QE the resonance Raman response beyond the Placzek approximation. Even if this is our final goal before a public release, the code that allows this calculation is still under testing, and for this reason we limit here to present our results on the response to a single monochromatic uniform electric field. In what follows, we briefly discuss how self-consistency enters in TDDMPT Equations and finally we test our implementation on the calculation of the Raman tensor of silicon in its zincblende structure. More details on the work-flow of the code and on the routines we used or modified are in Appendix D.3. We also remark that, at the present moment, the implementation supports only local density approximation (LDA) functionals.

### 5.5.1 Self-consistency in TDDMPT

Without losing generality, we address here the case where self consistency stems from a (single particle) time-dependent Kohn-Sham Hamiltonian $H_{\mathrm{KS}}$ that reads

$$H^{[\rho(t)]}_{\mathrm{KS}}(t) = V_{\mathrm{ext.}}(t) + V_{\mathrm{HXC}}[\rho(t)] \tag{5.92}$$

where we made explicit the fact that the time dependence enters in the Hamiltonian both explicitly through the external potential $V_{\mathrm{ext.}}(t)$, which accounts for both the static, ionic (pseudo-)potential and for the time-dependent perturbation, and through the functional dependence of the Hartree-Exchange-Correlation (HXC)

functional potential on the time-dependent electronic density $\rho(t)$. For simplicity, hereafter we will neglect the explicit functional dependence on $\rho(t)$ unless needed, so e.g. we will write $V_{\mathrm{HXC}}[\rho(t)] = V_{\mathrm{HXC}}(t)$. The perturbative expansion comes from the perturbation in $V_{\mathrm{ext.}}(t)$ and we consider $V^{(i)}_{\mathrm{ext.}}(t) = 0$ for $i \geq 2$. In order to obtain the Raman response, the implementation was made considering an external perturbation constituted by a monochromatic electric field, however we want to remark that the results presented in this section are more general and apply for any time-dependent external perturbation. For the sake of a lighter notation, in what follows Cartesian indexes will be neglected unless otherwise stated. Accounting also for self-consistency, von-Neumann Equation (5.33) for the generic $\rho^{(n)}(t)$ becomes:

$$\mathrm{i}\hbar\dot{\rho}^{(n)}(t) = \left[H^{(0)}_{\mathrm{KS}}, \rho^{(n)}(t)\right] + \left[H^{(1)}_{\mathrm{KS}}(t), \rho^{(n-1)}(t)\right] + \left[H^{(2)}_{\mathrm{KS}}(t), \rho^{(n-2)}(t)\right], \tag{5.93}$$

where

$$H^{(1)}_{\mathrm{KS}}(t) = V^{(1)}_{\mathrm{ext.}}(t) + V^{(1)}_{\mathrm{HXC}}(t), \tag{5.94}$$

$$H^{(2)}_{\mathrm{KS}}(t) = V^{(2)}_{\mathrm{HXC}}(t). \tag{5.95}$$

In real-space representation it holds

$$V^{(1)}_{\mathrm{HXC}}(\boldsymbol{r}, t) = \int \mathrm{K}_{\mathrm{HXC}}(\boldsymbol{r}, \boldsymbol{r'})\rho^{(1)}(\boldsymbol{r'}, t)\mathrm{d}^3\boldsymbol{r'} = \int \frac{\delta^2 E_{\mathrm{HXC}}[\rho](\boldsymbol{r}, \boldsymbol{r'})}{\delta\rho(\boldsymbol{r})\delta\rho(\boldsymbol{r'})}\rho^{(1)}(\boldsymbol{r'}, t)\mathrm{d}^3\boldsymbol{r'}, \tag{5.96}$$

$$\begin{aligned} V^{(2)}_{\mathrm{HXC}}(\boldsymbol{r}, t) = &\int \frac{\delta^2 E_{\mathrm{HXC}}[\rho](\boldsymbol{r}, \boldsymbol{r'})}{\delta\rho(\boldsymbol{r})\delta\rho(\boldsymbol{r'})}\rho^{(2)}(\boldsymbol{r'}, t)\mathrm{d}^3\boldsymbol{r'} + \\ &+ \int \frac{\delta^3 E_{\mathrm{HXC}}[\rho](\boldsymbol{r}, \boldsymbol{r'}, \boldsymbol{r''})}{\delta\rho(\boldsymbol{r})\delta\rho(\boldsymbol{r'})\delta\rho(\boldsymbol{r''})}\rho^{(1)}(\boldsymbol{r'}, t)\rho^{(1)}(\boldsymbol{r''}, t)\mathrm{d}^3\boldsymbol{r'}\mathrm{d}^3\boldsymbol{r''}, \end{aligned} \tag{5.97}$$

where $\mathrm{K}_{\mathrm{HXC}}$ is the Hartree-Exchange-Correlation kernel, defined in terms of functional derivatives of the HXC energy functional $E_{\mathrm{HXC}}[\rho]$ with respect to electronic density, as in standard DFT approaches. In the previous Equations we also used the instantaneous approximation, namely we suppose a real and time-independent $\mathrm{K}_{\mathrm{HXC}}(\boldsymbol{r}, \boldsymbol{r'})$. This hypothesis will always be adopted in what follows, implying that the time-dependence of the induced potentials comes from the induced charge densities only. Under the hypothesis we made of $V^{(i)}_{\mathrm{ext.}}(t) = 0$ for $i \geq 2$, the self-consistent terms are those with $n = 1$ and $n = 2$, which are of interest e.g. for the Raman response. Considering a monochromatic perturbation, we substitute in Equation (5.93) the trial solution of Equation (5.34). With some manipulation, we finally obtain the self-consistent linear systems which defines the perturbed-like valence wave functions $\{|\eta^{(1)}_v(\pm\omega)\rangle\}$ and $\{|\eta^{(2)}_v(0)\rangle\}$, needed e.g. for the Raman response (further details on their derivation are in Appendix D.3). For the former it reads:

$$\left(H^{(0)} - \varepsilon^{(0)}_v \mp \hbar\omega\right)|\eta^{(1)}_v(\pm\omega)\rangle = -P_C\left[V^{(1)}_{\mathrm{ext.}}(\pm\omega) + V^{(1)}_{\mathrm{HXC}}(\pm\omega), \rho^{(0)}\right]|\psi^{(0)}_v\rangle, \tag{5.98}$$

where in real-space representation it holds

$$V^{(1)}_{\mathrm{HXC}}(\boldsymbol{r},+\omega) = V^{(1)}_{\mathrm{HXC}}(\boldsymbol{r},-\omega) = \int \frac{\delta^2 E_{\mathrm{HXC}}[\rho](\boldsymbol{r},\boldsymbol{r'})}{\delta\rho(\boldsymbol{r})\delta\rho(\boldsymbol{r'})}\rho^{(1)}(\boldsymbol{r'},\omega)\mathrm{d}^3\boldsymbol{r'}, \tag{5.99}$$

with

$$\rho^{(1)}(\boldsymbol{r},\omega) = \rho^{(1)}_{CV}(\boldsymbol{r},\omega) + \rho^{(1)}_{VC}(\boldsymbol{r},\omega). \tag{5.100}$$

To obtain above Equations, we also exploited the fact that being both $\rho^{(1)}(\boldsymbol{r},t)$ and $\rho^{(1)}(\boldsymbol{r},\omega)$ real, we have that $\rho^{(1)}(\boldsymbol{r},-\omega) = [\rho^{(1)}(\boldsymbol{r},\omega)]^\dagger = \rho^{(1)}(\boldsymbol{r},\omega)$.
For the $\{|\eta^{(2)}_v(0)\rangle\}$ instead it holds

$$\left(H^{(0)} - \varepsilon^{(0)}_v\right)|\eta^{(2)}_v(0)\rangle = -P_C\left\{2\left[V^{(1)}_{\mathrm{ext.}}(\omega) + V^{(1)}_{\mathrm{HXC}}(\omega), \rho^{(1)}(\omega)\right] + \left[V^{(2)}_{\mathrm{HXC}}(0), \rho^{(0)}\right]\right\}|\psi^{(0)}_v\rangle\,, \tag{5.101}$$

where in real-space it holds

$$\begin{aligned} V^{(2)}_{\mathrm{HXC}}(\boldsymbol{r},0) = &\int \frac{\delta^2 E_{\mathrm{HXC}}[\rho](\boldsymbol{r},\boldsymbol{r'})}{\delta\rho(\boldsymbol{r})\delta\rho(\boldsymbol{r'})}\rho^{(2)}(\boldsymbol{r'},0)\mathrm{d}^3\boldsymbol{r'} + \\ &+ 2\int \frac{\delta^3 E_{\mathrm{HXC}}[\rho](\boldsymbol{r},\boldsymbol{r'},\boldsymbol{r''})}{\delta\rho(\boldsymbol{r})\delta\rho(\boldsymbol{r'})\delta\rho(\boldsymbol{r''})}\rho^{(1)}(\boldsymbol{r'},\omega)\rho^{(1)}(\boldsymbol{r''},\omega)\mathrm{d}^3\boldsymbol{r'}\mathrm{d}^3\boldsymbol{r''}, \end{aligned} \tag{5.102}$$

with

$$\rho^{(2)}(\boldsymbol{r},0) = \rho^{(2)}_{CV}(\boldsymbol{r},0) + \rho^{(2)}_{VC}(\boldsymbol{r},0) + \left[\rho^{(1)}_{CV}(\boldsymbol{r},\omega), \rho^{(1)}_{VC}(\boldsymbol{r},-\omega)\right] + \left[\rho^{(1)}_{CV}(\boldsymbol{r},-\omega), \rho^{(1)}_{VC}(\boldsymbol{r},\omega)\right]. \tag{5.103}$$

With these quantities, it is possible to compute the Raman response of an insulating crystal at $T = 0\,K$, as we do in next section for the test case of a silicon crystal.

### 5.5.2 Test on the Raman response of silicon

As described in details in Appendix D.3, we implemented the calculation of the Raman response in the case of a single monochromatic frequency in the QE code. The final goal is to allow going beyond the Placzek approximation, however we limit here to present results obtained with the code tested for the calculation of the $\omega$-dependent Raman activity of Equation (5.84), which we rewrite:

$$A^{\nu}_{lm}(\omega) = \sum_{k\tau} \frac{\partial^3 \mathcal{E}^{\mathrm{el}}(\omega)}{\partial E_l \partial E_m \partial u_{k\tau}} \frac{\mathrm{w}^{\nu}_{k\tau}}{\sqrt{M_\tau}}, \tag{5.104}$$

where the novelty is the calculation of the third-order energy derivative in the TDDMPT approach, namely

$$\frac{\partial^3 \mathcal{E}^{\mathrm{el}}(\omega)}{\partial E_l \partial E_m \partial u_{k\tau}} = \frac{\partial \chi_{lm}(\omega)}{\partial u_{k\tau}} = 2\mathrm{Tr}\left[\frac{\partial^2 \rho(0)}{\partial E_l \partial E_m}\frac{\partial H}{\partial u_{k\tau}}\right]. \tag{5.105}$$

The system we choose for testing is silicon in a zincblende (cubic) crystal structure, with a unit cell with two silicon atoms, labelled Si1 and Si2, placed in crystal positions $(0,0,0)$ and $(1/4,1/4,1/4)$, respectively, defined with respect to the lattice parameter $a = 10.20$ Bohr. We used an LDA functional and pseudo-potentials without non-linear core corrections, with a kinetic energy cutoff of 20 Ry for the wave-functions and 80 Ry for the charge density. We computed the third-order derivative of the energy appearing in Equation (5.105) both with the finite differences approach and with the density-matrix formalism and studied its convergence with respect to the number of inequivalent k-points $N_k^{\text{ineq}}$ in the Brillouin zone. For symmetry reasons related to the crystal structure, and due to the fact that we are dealing with two electronically equivalent atoms Si1 and Si2, it holds

$$\frac{\partial^3 \mathcal{E}^{\text{el}}(\omega)}{\partial E_l \partial E_m \partial u_{k,\text{Si1}}} = -\frac{\partial^3 \mathcal{E}^{\text{el}}(\omega)}{\partial E_l \partial E_m \partial u_{k,\text{Si2}}} = |\epsilon_{lmk}|\mathcal{R}, \tag{5.106}$$

where $\epsilon_{lmk}$ is the Levi-Civita tensor and $\mathcal{R}$ is the value of the olny non-zero component of the response tensor. In Figure 5.1, we compare the values obtained for $\mathcal{R}$ with both approaches and in particular we study their convergence with respect to the number of inequivalent k-points $N_k^{\text{ineq}}$. As it can be observed, both approaches reach the same converged values, confirming the goodness of the code and of the TDDMPT approach. However, it is worth to mention that the TDDMPT methods allows for a faster convergence with respect to the number of k-points.

## 5.6 Conclusions

In this Chapter, we presented the time-dependent density matrix perturbation theory (TDDMPT), a perturbative theory formulated on the electronic density matrix instead of the standard wave-function based approaches. TDDMPT allows for the ab-initio calculation of response properties of materials in a compact and elegant way at any perturbative order, avoiding many problems that affects other approaches. Indeed, by definition the TDDMPT approach is free from gauge-dependency problems and moreover it offers a well-defined framework to treat perturbations coming from a uniform electric field, a notoriously difficult task due to the ill-definition of the position operator in periodic systems. Plus, at any perturbative order, all the quantities needed for a TDDMPT calculation can be obtained solving (self-consistent) linear equations in terms of valence states only, avoiding the calculation of empty states, which in principle may even be infinite. Finally, TDDMPT allows for an impressive time-reduction, when dealing with systems with many atoms, when compared with other approaches based e.g. on finite differences.

After deriving the equations to treat a generic time-dependent perturbation, we focused on the specific case of a uniform electric field. Indeed, TDDMPT allows for a simple and compact derivation of non-linear optical susceptibilities, namely

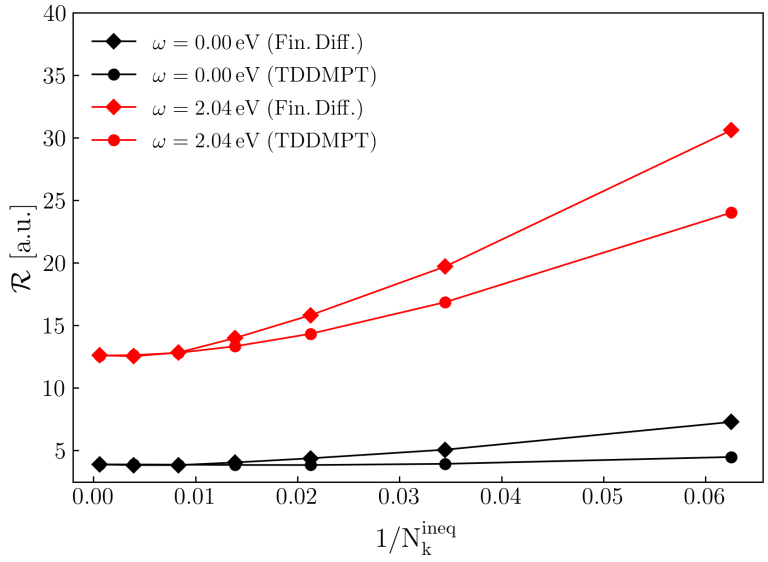


**Figure 5.1.** For the silicon crystal in the cubic structure described in the text, we compare the convergence behaviours of the only non-zero component $\mathcal{R}$ of the Raman response tensor of Equation (5.106) for two representative values of photon frequencies $\omega = 0$ eV and $\omega = 2.04$ eV, where LDA calculation yield a direct energy band gap of $E_{\text{gap}}^{\text{dir}} = 2.56$ eV and and indirect band gap of $E_{\text{gap}}^{\text{indir}} = 0.51$ eV. We highlight the agreement between the converged values obtained with the finite differences approach and the TDDMPT one we implemented in QE. Moreover, we remark how the TDDMPT methods presents a faster convergence with respect to the number of inequivalent k-points $N_k^{\text{ineq}}$.

derivatives of polarization with respect to an electric field, central quantities in many phenomena. We then applied our results to the case of the Raman response, giving, for the first time, a compact and self-consistent approach to compute the Raman response of an insulating crystal beyond the Placzek approximation. Indeed, TDDMPT is a unique tool to accomplish this goal, as it is not possible to resort to usual methods for the calculation of Raman spectra in the Placzek approximation, based on finite differences of electronic susceptibilities. Finally, we showed how to implement TDDMPT equations in a DFT self-consistent framework, paving the road for its implementation in ab-initio codes. In particular, we implemented the calculation of the frequency-dependent Raman response of an insulating crystal in the Quantum ESPRESSO code, and presented the results of the tests on a silicon crystal.

# Conclusions

Despite their apparent simplicity, 1D conjugated systems were found to harbor a multitude of interesting phenomena, resulting from the interplay between few key elements that we identified and discussed in our study. To conclude, in this section we briefly review and sum-up the main results of our work.

The first aspect we focused on, was the study of the manifestation of charge density waves with different characters in 1D system, a feature which is reflected by the competition between two different structural realizations of these systems, resulting from the interplay between a Peierls electronic instability, electron-ion interactions and atom-equivalence breaking mechanisms. With the aid of a simple tight-binding model of a diatomic chain, we analyzed the role played by the electron-phonon coupling, which in the model we found acting as a guiding parameter of a second order structural phase transition between a dimerized, less symmetric, structure, and an undimerized, more symmetric one. Moreover, thanks to the strict relation between polar and structural properties in these systems, we showed how this phase transition is also a prototypical ferroelectric phase transition. Even if these results were obtained in the framework of the model, the conclusions on the importance of the electron-phonon coupling in determining the character of CDWs and ferroelectric properties in 1D systems remain valid even beyond.

A part for its role in CDWs formation, the electron-phonon coupling was also found to be related to, and hence to account for, the presence of a dielectric environment around these systems. This statement is supported by the agreement we found between the behaviour of the electronic energy gap with respect to the zone-center frequency of the longitudinal-optic mode of an infinitely-long straight chain of carbon atoms, i.e. carbyne, obtained on one hand within the framework of the model with parameters fitted to describe carbyne, and on the other hand from resonance Raman spectroscopy experiments on carbyne chains confined inside different carbon nanotubes, taken from Ref.[71]. The fact that the electron-phonon coupling plays a relevant role in these systems is also remarked by the high value of the e-ph coupling term $\beta \simeq 7.20$ eV/Å that we found in the fitted-model. The validity of the results obtained with the fitted-model is also supported by the comparison with DFT calculations on carbyne and carbyne-derived systems, putting forward this simple model as a reliable and versatile tool to describe physics of 1D conjugated systems. Indeed, this model is particularly suitable to describe the main characteristics of

conjugated polymers, a class of carbon-based organic (quasi-)1D materials, such as carbyne and polyacetylene, characterized by a delocalized orbital along a backbone chain, resulting in many interesting and useful optoelectronic applications.

Another element that we found having a fundamental relevance in determining the properties of 1D conjugated systems were the quantum-anharmonic effects. Indeed, results of recent works highlighted the importance of correctly accounting for the quantum nature of ions and for their anharmonic interactions, in particular in systems with light atoms, such as conjugated polymers, and in presence of a displacive phase transition in proximity of a CDW- or a ferroelectric-instability, as is the case of the systems described by the model. In order to include QAE in our theoretical framework, we used the stochastic implementation of the self-consistent harmonic approximation (SSCHA)[18], a variational theory, based on the free energy functional, that allows to determine thermodynamic properties of materials with the inclusion of QAE in a non-perturbative and fully-ab initio approach.

To evaluate the role of QAE on CDWs formation and on the related structural properties, we focused on the prototypical case of carbyne, described in the framework of the fitted-model. We found that QAE are responsible for a renormalization of $\sim 70\%$ of the energy gain between the dimerized phase of carbyne, called polyyne, with respect to the undimerized one, called cumulene. Regarding the competition between these two phases, we also found that, contrary to the common Landau-Peierls picture of a second order phase transition in temperature, the inclusion of QAE reveals that the transition is actually of first order, in agreement with some previous results[17]. In particular, the polyyne phase is found to be the most favorable configuration for a wide range of temperatures, up to $T_{\mathrm{CDW}}^{\mathrm{QAE}} \simeq 4300\,K$, where cumulene finally becomes stable, consistently with the fact that the existence of this high symmetric phase of carbyne was theorized but never observed.

As we discussed, it is however possible to stabilize the undimerized phase in 1D systems exploiting particular mechanisms, e.g. breaking the equivalence between atoms or varying the electron-phonon coupling, which in the framework of the model result in a second order structural phase transition. The impact of QAE on this process in carbyne-derived systems is to shift the critical values of the transition, contributing to the stabilization of the Peierls electronic instability and thus going against the formation of bond-centered CDWs. The validity of the presented results is guaranteed thanks to a comparison with ab-initio plus SSCHA results on carbyne, taken from Ref.[17]. In this way, the model was proven to be a reliable tool for accurate DFT-plus-QAE-level results, while at the same time guaranteeing an impressive computational advantage with respect to ab-initio approaches. We finally argue that even if results were presented for carbyne and carbyne-derived systems, the key message on the impact of QAE holds, at least qualitatively, even for other systems described by the model, e.g. for polyacetylene and substituted polyacetylenes.

After having assessed the role of quantum-anharmonicity in determining the

optimal configuration of 1D conjugated systems, we then turned our attention to the study of their polar responses, i.e. to study those quantities that can be defined in terms of linear variations of polarization with respect to an external perturbation. Indeed, as we discussed, on one hand, polarization in these 1D systems is strictly connected to their structural properties, on the other hand, it is known that CDWs have the effect of enhancing polar responses in materials through mechanisms that involve symmetry breaking and strong electron-phonon coupling.

Following this idea, we studied, in the framework of the model, perturbations where the e-ph coupling play a central role. In particular, we focused on the response with respect to atomic displacements, quantified by the effective charges $Z^*$, and on the response with respect to a strain, quantified by the piezoelectric coefficients. We found that both quantities present a strong enhancement when reaching the critical point of the structural transition from the dimerized configuration, the piezoelectric coefficient showing a diverging behaviour due to the order of the transition and reminiscent of the morphotropic behaviour of piezoelectric perovskites.

Instead, we traced back the enhancement of the effective charges to the mechanism of the adiabatic charge transport of the Thouless pump, which results in an inverse proportionality relation between $Z^*$ and the energy gap $E_{\text{gap}}$. The intrinsically topological character of this mechanism, ensures stability of the enhancement against fluctuations and anharmonicity. Calculations of effective charges with the inclusion of QAE not only confirmed this hypothesis, but even shown that QAE determine a further enhancement of the response as a consequence of the peculiar relation between $Z^*$ and $E_{\text{gap}}$ and of the renormalization of the critical values of the transition due to the impact of QAE.

Our theoretical predictions on the behaviour of polar responses showed a remarkable agreement when compared with DFT results obtained on prototypical conjugated polymers. Having in mind the role of the e-ph coupling parameter as a guiding parameter of the structural phase transition in the model, we decided to perform DFT calculations varying the long-range mixing parameter entering a range-separated hybrid functional. The reason for choosing this computational handle was motivated by results showing how these long-range mixing parameters correctly account for screened Coulomb vertex corrections to the dressing of the e-ph coupling in conjugated systems. Moreover, these mixing parameters are also directly related to the presence external dielectric environment around a system, consistently with our discussion on the role of the external environment on the e-ph coupling in conjugated polymers presented in section 1.3.

Finally, we showed that piezoelectric conjugated polymers outperform, in principle, state-of-the-art organic piezoelectric, mostly thanks to the strongly anomalous effective charges of carbon, larger than $5e$ – ordinary values being of the order of $1e$ – and reaching the giant value of $30e$ for band gaps of the order of 1 eV. Thus, our results put forward conjugated polymers, and in general 1D conjugated systems, as a class of functional materials with tunable and enhanced polar response properties.

Last part of this work was devoted to the task of extending the theoretical framework we developed so as to include the description of Raman response of 1D systems. Aiming to characterize both their vibrational and structural properties, we focused on the vibrational Raman response, one of the most widely used experimental techniques, based on the inelastic scattering between a photon and a phonon. We analyzed this response under different levels of approximation. The main result we found is that in order to correctly reproduce experimental results on 1D conjugated systems, it is necessary to go beyond the commonly adopted Placzek approximation, where one describes the process of Raman scattering neglecting both the frequency of the photon and of the phonon involved, and include effects of resonances in the theoretical description. Indeed, the intensity of the resonant Raman response of the longitudinal optic mode of carbyne obtained with the fitted-model, showed a huge enhancement, up to 500 times the value obtained neglecting laser-frequency dependence. More specifically, these resonances may appear both when the photon energy matches the energy of an electronic transition, or when it matches the energy of a transition between an electronic state a vibrational state in another electronic state, resulting in the presence of two resonant peaks, consistently with experimental results obtained on the resonant Raman response of carbon nanotubes[152].

In order to go beyond the Placzek approximation, it was necessary to resort to a novel approach, since the usually adopted one of calculating the Raman response as finite-differences of electronic susceptibility breaks down. To accomplish this task, we generalized the idea presented in Ref.[167] and developed the time-dependent density matrix perturbation theory (TDDMPT), which enables the calculation of material response properties at any perturbative order in a concise and elegant manner, overcoming many issues found in other methods. The approach we propose of using a perturbative theory formulated on the electronic density matrix instead of the standard wave-function based approaches, presents many advantages both from a theoretical and practical point of view. Indeed, being based of the density matrix, TDDMPT is inherently free from gauge-dependency problems. Moreover, it provides a clear framework to handle perturbations from a uniform electric field, a notoriously challenging task due to the ill-defined position operator in periodic systems. Then, from a practical point of view, TDDMPT quantities can be computed as solutions of self-consistent linear equations involving valence states only, eliminating the need to calculate empty states, which in principle may be even infinite. Additionally, TDDMPT significantly reduces computational costs to obtain responses of large systems containing many atoms, as compared with other approaches. In the case of the Raman tensor, e.g., the TDDMPT approach allows going from $36 \times N_{\text{atoms}}$ first-order calculations, needed for the finite differences approach, to just 6 second-order calculations.

After having derived the equations for a generic time-dependent perturbation, we focused on the case of uniform electric fields and showed how TDDMPT facilitates a straightforward derivation of non-linear optical susceptibilities, crucial quantities in

many phenomena. We then applied our findings to compute the Raman response of an insulating crystal beyond the Placzek approximation. The method we derived is unique in doing this, as traditional methods for Raman spectra calculation based on finite differences cannot be used in this context. Finally, TDDMPT equations are suitable for a straightforward generalization in the framework of density-functional theory, offering a compact and elegant way for ab-initio calculations. We thus implemented TDDMPT equations to calculate the frequency-dependent Raman response of an insulating crystal in the Quantum ESPRESSO code, and presented test results for a silicon crystal.

# Appendix A

# The stochastic self-consistent harmonic approximation in the model

In this Appendix we discuss about the details on the stochastic self-consistent harmonic approximation (SSCHA) applied in the framework of the 1D model. As discussed in chapter 2, to do SSCHA calculations we need several supercells of the system under study, each with a different atomic configuration. Atomic positions in each supercell are chosen according to the Gaussian probability distribution used to compute the free energy of the system, as described in the main text. The optimal configuration of the system at a target temperature $T$ is obtained minimizing the free energy. To do so, we need energies and forces computed on the supercells. In the framework of the model, it is straight-forward to generalize the tight-binding description to the case of a supercell and compute energy and forces at a fraction of time with respect to using DFT codes. We use the dynamical matrices obtained in the harmonic approximation on the supercell as a starting probability distribution for the SSCHA minimization. In what follows, in section A.1 we first derive the expressions for energies, forces and dynamical matrices in the generalized tight-binding model, and then in section A.2 we give more details on the computational parameters used in the free energy minimization process.

## A.1 Generalized tight-binding model

To set the ground, we fix some notations and definitions:

- $N_{\text{cells}}$ is the number of cells in the supercell;
- $n$ is the number of atoms per cell;
- $n_e$ is the number of electrons per atom contributing to the electronic band structure. All atoms contribute equally;

- $N_{\text{at}}$ is the number of atoms in the supercell (it holds $N_{\text{at}} = N_{\text{cells}} \times n$);
- $a$ is the length of the unit cell;
- $L_{\text{s.c.}} = aN_{\text{cells}}$ is the length of the supercell;
- $\Delta$ ($> 0$) is the absolute value of the onsite energy. The atoms of the supercell have values of onsite energy with alternating signs;
- $-t$ ($t > 0$) is the value of the hopping energy between nearest neighbours in the case of equidistant atoms;
- $r_\alpha^{(0)} = \alpha \cdot a/2$ is the position of atom $\alpha$ in the supercell in the case of equidistant atoms, with $\alpha = 1, \ldots, N$;
- $\delta r_\alpha$ is the displacement of atom $\alpha$ from the position $r_\alpha^{(0)}$. It quantifies the displacement of atom $\alpha$ from the position it would have in a chain with equidistant atoms;
- $r_\alpha = r_\alpha^{(0)} + \delta r_\alpha$ is the position of atom $\alpha$ in the supercell;
- $\delta u_\alpha = \delta r_\alpha / a$ is the displacement of atom $\alpha$ from $r_\alpha^{(0)}$ in adimensional units;
- $\beta$ is the electron-phonon coupling parameter, measured in units of energy divided by length. It is the same for every atom;
- $\delta t_\alpha = -\beta(r_{\alpha+1} - r_\alpha - a/2) = -\beta\,(\delta r_{\alpha+1} - \delta r_\alpha)$ is the variation of hopping energy between atoms $\alpha$ and $\alpha + 1$ due to atomic displacements with respect to the equidistant atoms configuration;
- $-t_\alpha = -(t + \delta t_\alpha)$ is the hopping energy between atoms $\alpha$ and $\alpha + 1$;
- $\mathrm{K}_{\text{ela}}$ is the elastic constant parameter used to account for $\boldsymbol{\sigma}$-bonds stiffness between neighbouring atoms. It is the same for every pair of neighbours;
- $N_k$ is the number of k-points used in the electronic calculations.

All results were obtained with $n = 2$ and with periodic boundary conditions (PBC) adopted on the supercell, hence it holds $\bullet_{\alpha+N} \equiv \bullet_\alpha$ for every quantity that depends on the index $\alpha$.

### A.1.1 Electronic Hamiltonian

For the electronic problem, we generalize the first-neighbours tight-binding model of section 1.2. In reciprocal $k$-space, the Hamiltonian of the supercell reads

$$H_k = \begin{bmatrix} \Delta & T_1 & 0 & \dots & 0 & T_N^* \\ T_1^* & -\Delta & T_2 & \ddots & \ddots & 0 \\ 0 & T_2^* & \Delta & \ddots & \ddots & \vdots \\ \vdots & \ddots & \ddots & \ddots & \ddots & 0 \\ 0 & \ddots & \ddots & \ddots & \Delta & T_{N-1} \\ T_N & 0 & \dots & 0 & T_{N-1}^* & -\Delta \end{bmatrix}, \tag{A.1}$$

where

$$T_\alpha = -t_\alpha \mathrm{e}^{\mathrm{i}k(r_{\alpha+1}-r_\alpha)} = [-t + \beta(\delta r_{\alpha+1} - \delta r_\alpha)]\mathrm{e}^{\mathrm{i}k(\delta r_{\alpha+1}-\delta r_\alpha + a/2)} \tag{A.2}$$

and

$$k = \frac{m}{N_k}\frac{2\pi}{L_{\text{s.c.}}} \quad m = 0, 1, \dots, N_k \tag{A.3}$$

We indicate with $\varepsilon_{j,k}$ its eigenvalues and with $\psi_{j,k}$ its eigenvectors, with $j = 1, \dots, N$. Each of the $N$ atoms contribute with $n_e$ electrons and since we are taking into account also the possibility to have degenerate orbitals, as the p-orbitals of carbyne, each band is $n_e$-fold degenerate, hence there are $N_{\text{occ}} = n_e \cdot (N/2)$ occupied bands and $N_{\text{emp}} = n_e \cdot (N/2)$ empty bands. In the particular case where the supercell is just a single unit cell, hence $N_{\text{cells}} = 1$ and $N = n = 2$, it reduces to Equation 1.22:

$$H_k^{(N=2)} = \begin{bmatrix} \Delta & T_1^* + T_N \\ T_1 + T_N^* & -\Delta \end{bmatrix}. \tag{A.4}$$

### A.1.2 Born-Oppenheimer potential

For a given atomic configuration $\{\mathbf{r}\} = \{r_1, r_2, \dots, r_N\}$, in the Born-Oppenheimer approximation, we consider two contributions to the Born-Oppenheimer (BO) potential $V_{BO}(\{\mathbf{r}\})$: one comes from the electronic energy of the occupied bands of the supercell whereas the other accounts for the $\boldsymbol{\sigma}$-bonds stiffness of neighbouring atoms and depends directly on atoms displacement. Namely, we write:

$$V_{BO}(\{\mathbf{r}\}) = E_{\text{I}}(\{\mathbf{r}\}) + E_{\text{e}}(\{\mathbf{r}\}) \tag{A.5}$$

with

$$E_{\text{I}}(\{\mathbf{r}\}) = \frac{1}{2}\mathrm{K}_{\text{ela}} \sum_{\alpha=1}^{N} (\delta r_{\alpha+1} - \delta r_\alpha)^2, \tag{A.6}$$

and

$$E_{\mathrm{e}}(\{\mathbf{r}\}) = \frac{2n_e}{N_k} \sum_{k=1}^{N_k} \sum_{j=1}^{N_{\mathrm{occ}}} \varepsilon_{j,k}(\{\mathbf{r}\}) \tag{A.7}$$

where the factor 2 accounts for the spin. We recall that PBC are adopted, hence $\delta r_{N+1} \equiv \delta r_1$.

### A.1.3 Dynamical matrices in the harmonic approximation

We now compute the dynamical matrices of the supercell in the harmonic approximation. To do so, we need the second order derivative of the BO potential, calculated with respect to the atomic displacements $\delta r_\alpha$, for a given atomic configuration $\{\mathbf{r}\}$. From Equation (A.5), we get two contributions:

$$\frac{\partial^2 V_{BO}(\{\mathbf{r}\})}{\partial \delta r_\alpha \partial \delta r_\beta} = \frac{\partial^2 E_{\mathrm{I}}(\{\mathbf{r}\})}{\partial \delta r_\alpha \partial \delta r_\beta} + \frac{\partial^2 E_{\mathrm{e}}(\{\mathbf{r}\})}{\partial \delta r_\alpha \partial \delta r_\beta}. \tag{A.8}$$

As far as the first contribution is concerned, it is easy to verify that

$$\frac{\partial^2 E_{\mathrm{I}}(\{\mathbf{r}\})}{\partial \delta r_\alpha \partial \delta r_\beta} = \mathrm{K_{ela}} \left(2\delta_{\alpha,\beta} - \delta_{\alpha,\beta+1} - \delta_{\alpha,\beta-1}\right) \tag{A.9}$$

where the $\delta_{\alpha,\beta(\pm 1)}$ on the right-hand side are Kronecker's delta. Regarding the electronic contribution, instead, we use Hellmann-Feynman theorem and static perturbation theory to compute the second order derivative of the electronic energy $E_{\mathrm{e}}(\{\mathbf{r}\})$. In particular, it holds:

$$\frac{\partial^2 E_{\mathrm{e}}(\{\mathbf{r}\})}{\partial \delta r_\alpha \partial \delta r_\beta} = \frac{2n_e}{N_k} \sum_k \sum_i^{\mathrm{occ}} \left\{ \langle \psi_{i,k} | H_{k,\alpha\beta} | \psi_{i,k} \rangle + 2\mathrm{Re} \left[ \sum_j^{\mathrm{emp}} \frac{\langle \psi_{i,k} | H_{k,\alpha} | \psi_{j,k} \rangle \langle \psi_{j,k} | H_{k,\beta} | \psi_{i,k} \rangle}{\varepsilon_{i,k} - \varepsilon_{j,k}} \right] \right\} \tag{A.10}$$

where $H_{k,\alpha}$ ($H_{k,\beta}$) is the derivative with respect to $\delta r_\alpha$ ($\delta r_\beta$) of the electronic Hamiltonian $H_k$ of Equation (A.1), while $H_{k,\alpha\beta}$ is its second order derivative with respect to the displacement of atoms $\alpha$ and $\beta$. It can be verified that it holds:

$$H_{k,\alpha} \equiv \frac{\partial H_k}{\partial \delta r_\alpha} = \begin{bmatrix} 0 & \dots & 0 & 0 & 0 & \dots & 0 \\ \vdots & \ddots & \vdots & \vdots & \vdots & \ddots & \vdots \\ 0 & \dots & 0 & \partial_\alpha T_{\alpha-1} & 0 & \dots & 0 \\ 0 & \dots & \partial_\alpha T^*_{\alpha-1} & 0 & \partial_\alpha T_\alpha & \dots & 0 \\ 0 & \dots & 0 & \partial_\alpha T^*_\alpha & 0 & \dots & 0 \\ \vdots & \ddots & \vdots & \vdots & \vdots & \ddots & \vdots \\ 0 & \dots & 0 & 0 & 0 & \dots & 0 \end{bmatrix} \tag{A.11}$$

where

$$\partial_\alpha T_{\alpha-1} \equiv \frac{\partial T_{\alpha-1}}{\partial \delta r_\alpha} = -\left(\mathrm{i}kt_{\alpha-1} - \beta t\right) \mathrm{e}^{\mathrm{i}k(\delta r_\alpha - \delta r_{\alpha-1} + a/2)}, \tag{A.12}$$

$$\partial_\alpha T_\alpha \equiv \frac{\partial T_\alpha}{\partial \delta r_\alpha} = \left(\mathrm{i}kt_\alpha - \beta t\right) \mathrm{e}^{\mathrm{i}k(\delta r_{\alpha+1} - \delta r_\alpha + a/2)} \tag{A.13}$$

while

$$H_{k,\alpha\beta} \equiv \frac{\partial^2 H_k}{\partial \delta r_\alpha \partial \delta r_\beta} = \delta_{\beta,\alpha-1} \frac{\partial^2 H_k}{\partial \delta r_\alpha \partial \delta r_{\alpha-1}} + \delta_{\beta,\alpha+1} \frac{\partial^2 H_k}{\partial \delta r_\alpha \partial \delta r_{\alpha+1}} + \delta_{\beta,\alpha} \frac{\partial^2 H_k}{\partial \delta r_\alpha^2} \tag{A.14}$$

with

$$\frac{\partial^2 H_k}{\partial \delta r_\alpha \partial \delta r_{\alpha-1}} = \begin{bmatrix} 0 & \dots & 0 & 0 & 0 & \dots & 0 \\ \vdots & \ddots & \vdots & \vdots & \vdots & \ddots & \vdots \\ 0 & \dots & 0 & \partial^2_{\alpha,\alpha-1} T_{\alpha-1} & 0 & \dots & 0 \\ 0 & \dots & \partial^2_{\alpha,\alpha-1} T^*_{\alpha-1} & 0 & 0 & \dots & 0 \\ 0 & \dots & 0 & 0 & 0 & \dots & 0 \\ \vdots & \ddots & \vdots & \vdots & \vdots & \ddots & \vdots \\ 0 & \dots & 0 & 0 & 0 & \dots & 0 \end{bmatrix}, \tag{A.15}$$

$$\frac{\partial^2 H_k}{\partial \delta r_\alpha \partial \delta r_{\alpha+1}} = \begin{bmatrix} 0 & \dots & 0 & 0 & 0 & \dots & 0 \\ \vdots & \ddots & \vdots & \vdots & \vdots & \ddots & \vdots \\ 0 & \dots & 0 & 0 & 0 & \dots & 0 \\ 0 & \dots & 0 & 0 & \partial^2_{\alpha,\alpha+1} T_\alpha & \dots & 0 \\ 0 & \dots & 0 & \partial^2_{\alpha,\alpha+1} T^*_\alpha & 0 & \dots & 0 \\ \vdots & \ddots & \vdots & \vdots & \vdots & \ddots & \vdots \\ 0 & \dots & 0 & 0 & 0 & \dots & 0 \end{bmatrix}, \tag{A.16}$$

$$\frac{\partial^2 H_k}{\partial \delta r_\alpha^2} = \begin{bmatrix} 0 & \dots & 0 & 0 & 0 & \dots & 0 \\ \vdots & \ddots & \vdots & \vdots & \vdots & \ddots & \vdots \\ 0 & \dots & 0 & \partial^2_{\alpha,\alpha} T_{\alpha-1} & 0 & \dots & 0 \\ 0 & \dots & \partial^2_{\alpha,\alpha} T^*_{\alpha-1} & 0 & \partial^2_{\alpha,\alpha} T_\alpha & \dots & 0 \\ 0 & \dots & 0 & \partial^2_{\alpha,\alpha} T^*_\alpha & 0 & \dots & 0 \\ \vdots & \ddots & \vdots & \vdots & \vdots & \ddots & \vdots \\ 0 & \dots & 0 & 0 & 0 & \dots & 0 \end{bmatrix} \tag{A.17}$$

where

$$\partial^2_{\alpha,\alpha-1} T_{\alpha-1} \equiv \frac{\partial^2 T_{\alpha-1}}{\partial \delta r_\alpha \partial \delta r_{\alpha-1}} = -k^2 t_{\alpha-1} \mathrm{e}^{\mathrm{i}k(\delta r_\alpha - \delta r_{\alpha-1} + a/2)}, \tag{A.18}$$

$$\partial^2_{\alpha,\alpha+1} T_{\alpha} \equiv \frac{\partial^2 T_{\alpha}}{\partial \delta r_\alpha \partial \delta r_{\alpha+1}} = -k^2 t_{\alpha+1} \mathrm{e}^{\mathrm{i}k(\delta r_{\alpha+1} - \delta r_{\alpha} + a/2)}, \tag{A.19}$$

$$\partial^2_{\alpha,\alpha} T_{\alpha-1} \equiv \frac{\partial^2 T_{\alpha-1}}{\partial^2 \delta r_\alpha} = k^2 t_{\alpha-1} \mathrm{e}^{\mathrm{i}k(\delta r_\alpha - \delta r_{\alpha-1} + a/2)}, \tag{A.20}$$

$$\partial^2_{\alpha,\alpha} T_{\alpha} \equiv \frac{\partial^2 T_{\alpha}}{\partial^2 \delta r_\alpha} = k^2 t_{\alpha} \mathrm{e}^{\mathrm{i}k(\delta r_{\alpha+1} - \delta r_{\alpha} + a/2)}. \tag{A.21}$$

Substituting everything in Equation (A.8) we can compute the derivative of the BO potential for a given configuration $\{\mathbf{r}\} = \{r_1, r_2, \ldots, r_N\}$ and this allows to define a force-constants matrix $\mathcal{C}_{\alpha\beta}(\{\mathbf{r}\})$:

$$\mathcal{C}_{\alpha\beta}(\{\mathbf{r}\}) = \frac{\partial^2 V_{BO}(\{\mathbf{r}\})}{\partial \delta r_\alpha \partial \delta r_\beta}. \tag{A.22}$$

On a general ground, it can be demonstrated that such a matrix satisfies different properties, such as the translational invariance. To make this properties explicit, we introduce an index $l = 1, \ldots, N_{\text{cells}}$ to indicate a unit cell in space, and with $\tau = 1, \ldots, n$ we refer to the atoms in a given unit cell. For a generic atom $\alpha$ of the supercell, it holds $\alpha = nl + \tau$. Given this definitions, we can make the translational invariance explicit:

$$\mathcal{C}_{\alpha\beta}(\{\mathbf{r}\}) = \mathcal{C}_{nl+\tau, nl'+\tau'}(\{\mathbf{r}\}) = \mathcal{C}_{\tau,\tau'+n(l'-l)}(\{\mathbf{r}\}). \tag{A.23}$$

Moreover, the force constant matrix must also be symmetric, namely

$$\mathcal{C}_{\alpha\beta}(\{\mathbf{r}\}) = \mathcal{C}_{\beta\alpha}(\{\mathbf{r}\}) \tag{A.24}$$

which is a consequence of the invariance of the second order derivatives with respect to the order of derivation.

Finally, we define the dynamical matrices $\mathcal{D}_{\tau\tau'}(q)$ as the discrete Fourier transform of the force-constants matrix over the unit cells of the supercell:

$$\mathcal{D}_{\tau\tau'}(q) = \sum_{l'=1}^{N_{\text{cells}}} \frac{\mathrm{e}^{-\mathrm{i}qa(l-l')}}{\sqrt{M_\tau M_{\tau'}}} \mathcal{C}_{\tau+nl,\tau'+nl'}(\{\mathbf{r}\}) \tag{A.25}$$

$$= \sum_{l'=1}^{N_{\text{cells}}} \frac{\mathrm{e}^{\mathrm{i}qal'}}{\sqrt{M_\tau M_{\tau'}}} \mathcal{C}_{\tau,\tau'+nl'}(\{\mathbf{r}\}) \tag{A.26}$$

where thanks to the translational invariance we put $l = 0$ and the variable $q$ is

defined over a grid of points commensurate with the supercells, namely:

$$q = \frac{m}{N_{\text{cells}}} \frac{2\pi}{a} \quad m = 0, 1, \ldots, N_{\text{cells}}. \tag{A.27}$$

The dynamical matrices are $n \times n$ matrices – $n$ being the number of atoms per unit cell – and satisfies different properties, in particular from the definition it is immediate to see that $\mathcal{D}_{\tau\tau'}(q)$ is Hermitian for each $q$. Consequently, their eigenvalues $\omega_\nu^2(q)$ ($\nu = 1 \ldots n$) are real and can be obtained diagonalising $\mathcal{D}_{\tau\tau'}(q)$ for each $q$.

### A.1.4 Forces and energies

Now that we have defined a way to compute the dynamical matrices of the system, we can do the SSCHA. In particular, the starting configurations are generated using a Gaussian probability distribution derived from the dynamical matrices. Each configuration is a supercell with $N_{\text{cells}}$ and $N_{\text{at}} = N_{\text{cells}} \times n$ atoms, where in the case of carbyne the number of atoms per cell is $n = 2$. Forces and energies must be also computed and in the case of the model we have that for a given atomic configuration $\{\mathbf{r}\} = \{r_1, r_2, \ldots, r_N\}$ the total energy reads:

$$E_{\text{tot}}(\{\mathbf{r}\}) = V_{BO}(\{\mathbf{r}\}) = E_{\text{I}}(\{\mathbf{r}\}) + E_{\text{e}}(\{\mathbf{r}\}), \tag{A.28}$$

where the two contributions $E_{\text{I}}(\{\mathbf{r}\})$ and $E_{\text{e}}(\{\mathbf{r}\})$ are those defined in Equations (A.6) and (A.7), respectively. For the forces, instead, it holds

$$F_\alpha(\{\mathbf{r}\}) = -\frac{\partial V_{BO}(\{\mathbf{r}\})}{\partial \delta r_\alpha} = -\frac{\partial E_{\text{I}}(\{\mathbf{r}\})}{\partial \delta r_\alpha} - \frac{\partial E_{\text{e}}(\{\mathbf{r}\})}{\partial \delta r_\alpha}. \tag{A.29}$$

Regarding the contribution to the forces coming from the ionic configuration, it can be demonstrated that

$$\frac{\partial E_{\text{I}}(\{\mathbf{r}\})}{\partial \delta r_\alpha} = \mathrm{K}_{\text{ela}} \left(2\delta r_\alpha - \delta r_{\alpha+1} - \delta r_{\alpha-1}\right) \tag{A.30}$$

while for the electronic contribution we can use perturbation theory to obtain

$$\frac{\partial E_{\text{e}}(\{\mathbf{r}\})}{\partial \delta r_\alpha} = \frac{2n_e}{N_k} \sum_k \sum_i^{\text{occ}} \langle \psi_{i,k} | H_{k,\alpha} | \psi_{i,k} \rangle, \tag{A.31}$$

with the $H_{k,\alpha}$ defined in Equation (A.11). At the end of the SSCHA minimization we will have that the supercell is just a repetition of the same unit cell and hence we expect the system to be either in a high symmetry phase, in which the atoms are equidistant with $r_{i+1} - r_i = a/2$, or in a low symmetry phase, in which there is a bond-length alternation equal to $2\,|\delta r_{i+1} - \delta r_i|$.

## A.2 Computational details

As explained in section 2.2, in the stochastic implementation of the SCHA, integrals of space-dependent quantities $O(\boldsymbol{R})$, e.g. the quantum averages of energies and forces, are computed with a Montecarlo approach:

$$\int \mathrm{d}\boldsymbol{R} O(\boldsymbol{R}) \tilde{\rho}_{\boldsymbol{\mathcal{R}},\boldsymbol{\Phi}}(\boldsymbol{R}) \simeq \frac{1}{N_\mathrm{C}} \sum_{\mathcal{I}=1}^{N_\mathrm{C}} O(\boldsymbol{R}_{(\mathcal{I})}), \tag{A.32}$$

where $\boldsymbol{R}_{(\mathcal{I})}$ is one of the randomly extracted configurations and $N_\mathrm{C}$ is the total number of configuration generated. Each configuration correspond to a supercell and is generated from a Gaussian probability distribution. The results presented in this work were obtained with $N_\mathrm{C} = 4000$. To decide the optimal number of cells $N_\mathrm{cells}$ and the optimal number of $k$-points $N_k$ for the calculations of energy and forces, we studied the convergence of the order parameter, namely of the BLA, in carbyne ($\Delta = 0$) as a function of these parameters. We chose $N_\mathrm{cells} = 40$ and $N_k = 160$: as shown in Figure A.1 these parameters ensure converged values of the BLA for a wide range of temperatures.

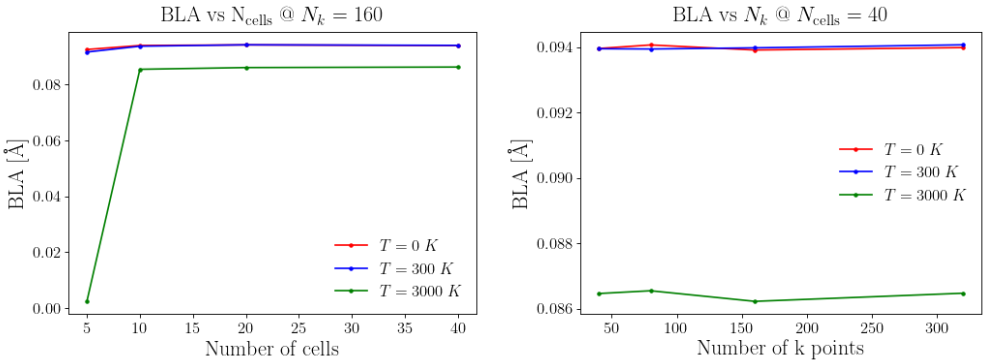


**Figure A.1.** Study of the convergence of the order parameter of the system, namely the bond length alternation, with respect to the number $N_\mathrm{cells}$ of cells per supercell, and to the number $N_k$ of $k$-points.

# Appendix B

# Berry-phase theory of piezoelectricity

In this Appendix, we present the Berry-phase theory of piezoelectricity, following the lines of Ref.[121]. The distinction between a proper and an improper piezoelectric coefficients was given both by Martin[171] and by Nelson and Lax[172, 173] to account, in the response of a dielectric to an external strain, for the effects of spurious contributions due e.g. to homogeneous rotations of spontaneous electric dipoles present in the material. The general relation between the proper and improper piezoelectric coefficients they obtain is:

$$c_{ijk}^{\text{proper}} = c_{ijk}^{\text{improper}} + \delta_{jk} P_i^s - \delta_{ij} P_k^s \tag{B.1}$$

where $\boldsymbol{P}^s$ is the spontaneous polarisation of the material and

$$c_{ijk}^{\text{improper}} = \frac{\mathrm{d}P_i}{\mathrm{d}\epsilon_{jk}} \tag{B.2}$$

with $\epsilon_{jk}$ defined through the relation

$$\mathrm{d}r_j = \sum_k \epsilon_{jk} r_k. \tag{B.3}$$

From the presence of the Kronecker delta $\delta_{jk}$ and $\delta_{ij}$ in Equation (B.1), we immediately notice that in the case of a 1D system, this distinction does not apply. In the last Equation (B.3), $\mathrm{d}r_j$ is the deformation of the medium from its undeformed position $r_j$, and $\epsilon_{jk}$ refers to a generic homogeneous deformation. In Ref.[121], Vanderbilt obtains a way to compute the proper piezoelectric coefficients from first principles adopting the Berry-phase formalism. It is possible to do so thanks to the fact that in modern theory of polarisation we can write[121]

$$\mathbf{P} = \frac{e}{\Omega} \sum_\tau Z_\tau \mathbf{r}_\tau - \frac{e}{\Omega} \sum_n^{\text{occ}} \mathbf{r}_n \tag{B.4}$$

where $e$ is the unit electric charge, $\Omega$ is the volume of the unit cell, $\mathbf{r}_\tau$ is the position of the $\tau$-th ion in the unit cell, $Z_\tau$ its nuclear charge and $\mathbf{r}_n$ is the Wannier centre of the $n$-th electronic band[174].

## B.1 Proper piezoelectric tensor independent on branch choice

In general, the electronic contribution to polarisation is a quantity defined modulo $(e/\Omega)\mathbf{R}$ with $\mathbf{R}$ a real-space lattice vector, so there is an ambiguity in the definition of polarisation: there are more branches, related by

$$\mathbf{P}^{(b')} = \mathbf{P}^{(b)} + \frac{e}{\Omega}\mathbf{R}. \tag{B.5}$$

Vanderbilt demonstrated that the proper piezoelectric tensor is independent on this choice of branch. Indeed, we can write:

$$\mathrm{d}P_i^{(b')} = \mathrm{d}P_i^{(b)} + \frac{e}{\Omega}\mathrm{d}R_i - \frac{e}{\Omega^2}R_i\mathrm{d}\Omega \tag{B.6}$$

where from Equation (B.3) we have that:

$$\mathrm{d}R_i = \sum_l \epsilon_{il}R_l. \tag{B.7}$$

Considering now that $\Omega = a_1 \cdot (a_2 \times a_3)$ we get

$$\mathrm{d}\Omega = \mathrm{d}a_1 \cdot (a_2 \times a_3) + a_1 \cdot (\mathrm{d}a_2 \times a_3) + a_1 \cdot (a_2 \times \mathrm{d}a_3) \tag{B.8}$$

and since from Equation (B.3)

$$\mathrm{d}a_i = \sum_l \epsilon_{il}a_l \tag{B.9}$$

we finally obtain:

$$\mathrm{d}\Omega = \epsilon_{11}a_1 \cdot (a_2 \times a_3) + a_1 \cdot (\epsilon_{22}a_2 \times a_3) + a_1 \cdot (a_2 \times \epsilon_{33}a_3) = \sum_l \epsilon_{ll}\Omega. \tag{B.10}$$

Substituting Equations (B.7) and (B.10) in Equation (B.6) we obtain

$$\mathrm{d}P_i^{(b')} = \mathrm{d}P_i^{(b)} + \frac{e}{\Omega}\sum_l \left(\epsilon_{il}R_l - \epsilon_{ll}R_i\right). \tag{B.11}$$

As in Equation (B.2), we now take the derivative with respect to $\epsilon_{jk}$ and obtain:

$$c_{ijk}^{\mathrm{improper},(b')} = c_{ijk}^{\mathrm{improper},(b)} + \frac{e}{\Omega}\delta_{ij}R_k - \frac{e}{\Omega}\delta_{jk}R_i \tag{B.12}$$

Since from Equation (B.5) we have that:

$$\frac{e}{\Omega}\mathbf{R} = \mathbf{P}^{(b')} - \mathbf{P}^{(b)} \tag{B.13}$$

we can substitute in Equation (B.12) and obtain

$$c_{ijk}^{\text{improper},(b')} = c_{ijk}^{\text{improper},(b)} + \delta_{ij}\left(P_k^{(b')} - P_k^{(b)}\right) - \delta_{jk}\left(P_i^{(b')} - P_i^{(b)}\right) \tag{B.14}$$

which can be rewritten as

$$c_{ijk}^{\text{improper},(b')} + \delta_{jk}P_i^{(b')} - \delta_{ij}P_k^{(b')} = c_{ijk}^{\text{improper},(b)} + \delta_{jk}P_i^{(b)} - \delta_{ij}P_k^{(b)} \tag{B.15}$$

We recognise on each size the proper piezoelectric tensor, as defined in Equation (B.1). This means that the proper piezoelectric tensor does not depend on the choice of the branch.

## B.2 Clamped ions vs internal strain contribution

The piezoelectric tensor can be decomposed into two contributions: one is obtained considering the nuclear coordinates to follow Equation (B.3) exactly and is called *clamped-ion* (CI) contribution. Another contribution comes instead when we consider also the internal relaxation of the nuclear coordinates at fixed strain and can be called *internal-strain* contribution: in this way, we are sure that the system is in the lower energy state after the deformation[1]. As shown for example in Ref.[175] and in Ref.[176], the internal-strain contribution is proportional to the effective charges. From Equations (B.1) and (B.2), indeed, we can write:

$$c_{ijk}^{\text{proper}} = \frac{\mathrm{d}P_i}{\mathrm{d}\epsilon_{jk}} + \delta_{jk}P_i - \delta_{ij}P_k = \tag{B.16}$$

$$= \left.\frac{\partial P_i}{\partial \epsilon_{jk}}\right|_{\mathbf{u}} + \sum_{s,l}\left.\frac{\partial P_i}{\partial u_l^s}\right|_{\epsilon}\frac{\partial u_l^s}{\partial \epsilon_{jk}} + \delta_{jk}P_i - \delta_{ij}P_k = \tag{B.17}$$

$$= c_{ijk}^{\text{proper},C.I.} + \sum_{s,l}\frac{e}{\Omega}Z_{s,il}^{*}\frac{\partial u_l^s}{\partial \epsilon_{jk}} \tag{B.18}$$

where $u_l^s$ is the $l$-th component of the internal coordinate of the $s$-th ion and $Z_{s,il}^*$ is the $il$ component of the effective charge tensor $Z_s^*$ of atom $s$.

Before proceeding, it is worth to point out that that being the internal-strain contribution considered at fixed $\epsilon$, the proper-vs-improper distinction does not applies in this case. Indeed the internal-strain contribution comes just from the relaxation of internal coordinates. In what follows, we will focus only on the clamped ions terms, neglecting the contribution of the internal strain.

[1] An exhaustive treatment of this distinction and how this applies when it comes to DFPT calculations is done e.g. by Wu, Vanderbilt and Hamann in Ref.[175]

## B.3 Ionic contribution to proper piezoelectric tensor

Let's find an expression for the proper piezoelectric coefficient which depends only on the Berry phases. We start from Equation (B.4), which contains a ionic and an electronic contribution. In the clamped ion approximation, ionic coordinates follow Equation (B.3) exactly, and considering also Equation (B.10) we get

$$\mathrm{d}P_i^{\text{ionic}} = \frac{e}{\Omega}\sum_\tau Z_\tau \mathrm{d}r_{\tau,i} - \frac{e}{\Omega^2}\sum_\tau Z_\tau r_{\tau,i}\mathrm{d}\Omega \tag{B.19}$$

$$= \frac{e}{\Omega}\sum_\tau Z_{\tau,l}\left(\epsilon_{il}r_{\tau,l} - \epsilon_{ll}r_{\tau,i}\right) \tag{B.20}$$

which implies

$$c^{\text{improper}}_{\text{ionic},ijk} = \frac{\mathrm{d}P_i^{\text{ionic}}}{\mathrm{d}\epsilon_{jk}} = \frac{e}{\Omega}\sum_\tau Z_\tau\left(\delta_{ij}r_k - \delta_{jk}r_i\right) = \delta_{ij}P_k^{\text{ionic}} - \delta_{jk}P_i^{\text{ionic}} \tag{B.21}$$

hence in the clamped ion approximation the ionic contribution to the proper piezoelectric tensor is zero:

$$c^{\text{proper}}_{\text{ionic},ijk} = c^{\text{improper}}_{\text{ionic},ijk} - \delta_{ij}P_k^{\text{ionic}} + \delta_{jk}P_i^{\text{ionic}} = 0 \tag{B.22}$$

## B.4 Electronic contribution to proper piezoelectric tensor

In the clamped ion approximation, if also the Wannier centres $\mathbf{r}_n$ followed Equation (B.3) exactly, the proper tensor would be identically zero for the same argument exposed for the ions. However, there is no reason to think that the Wannier centres would follow exactly Equation (B.3) when the system is deformed. From this point of view, it is evident that proper piezoelectric response can be regarded as a measure of the degree to which the Wannier centres fail to follow a homogeneous deformation: let's see why. We start by writing the electronic contribution to the polarisation as:

$$P_i^{\text{elec}} = -\frac{e}{\Omega}\sum_n r_{i,n} = -\frac{1}{2\pi}\frac{e}{\Omega}\sum_{n,\alpha}\phi_{n,\alpha}R_{i,\alpha} \tag{B.23}$$

where $\phi_{n,\alpha}$ is the Berry phase of the $n$-th occupied band in direction $\alpha$ and $R_{i,\alpha}$ is the $i$-th component of the $\alpha$-th real space primitive lattice vector.
The electronic contribution to the improper coefficient is:

$$c^{\text{improper}}_{\text{elec},ijk} = \frac{\mathrm{d}P_i^{\text{elec}}}{\mathrm{d}\epsilon_{jk}} = -\frac{e}{2\pi}\sum_{n,\alpha}\frac{\mathrm{d}}{\mathrm{d}\epsilon_{jk}}\left[\frac{\phi_{n,\alpha}}{\Omega}R_{i,\alpha}\right] = \tag{B.24}$$

$$= -\frac{e}{2\pi}\sum_{n,\alpha}\left[\frac{R_{i,\alpha}}{\Omega}\frac{\mathrm{d}\phi_{n,\alpha}}{\mathrm{d}\epsilon_{jk}} + \frac{\phi_{n,\alpha}}{\Omega}\frac{\mathrm{d}R_{i,\alpha}}{\mathrm{d}\epsilon_{jk}} - \frac{R_{i,\alpha}\phi_{n,\alpha}}{\Omega^2}\frac{\mathrm{d}\Omega}{\mathrm{d}\epsilon_{jk}}\right] \tag{B.25}$$

Using Equations (B.3), (B.10) and (B.23) we obtain:

$$c_{\mathrm{elec},ijk}^{\mathrm{improper}} = \frac{\mathrm{d}P_i^{\mathrm{elec}}}{\mathrm{d}\epsilon_{jk}} = -\frac{e}{2\pi}\sum_{n,\alpha}\frac{R_{i,\alpha}}{\Omega}\frac{\mathrm{d}\phi_{n,\alpha}}{\mathrm{d}\epsilon_{jk}} + \delta_{ij}P_k^{\mathrm{elec}} - \delta_{jk}P_i^{\mathrm{elec}} \tag{B.26}$$

which means that:

$$c_{\mathrm{elec},ijk}^{\mathrm{proper}} = c_{\mathrm{elec},ijk}^{\mathrm{improper}} - \delta_{ij}P_k^{\mathrm{elec}} + \delta_{jk}P_i^{\mathrm{elec}} = -\frac{e}{2\pi}\sum_{n,\alpha}\frac{R_{i,\alpha}}{\Omega}\frac{\mathrm{d}\phi_{n,\alpha}}{\mathrm{d}\epsilon_{jk}}. \tag{B.27}$$

Since the ionic contribution in the clamped ions approximation is zero, we finally obtain (Equation (22) of [121]):

$$c_{ijk}^{\mathrm{proper},C.I.} = -\frac{1}{2\pi}\frac{e}{\Omega}\sum_{n,\alpha}\frac{\mathrm{d}\phi_{n,\alpha}}{\mathrm{d}\epsilon_{jk}}R_{\alpha,i} \tag{B.28}$$

where $\Omega$ is the undeformed unit cell volume and $\mathbf{R}_\alpha$ are the undeformed real space primitive lattice vectors. We obtained a formula which relates the proper piezoelectric coefficient to a property of the Berry phase, namely how it varies with a strain $\epsilon$.

# Appendix C

# Computational details on DFT calculations

All DFT calculations of Chapter 1 and 3 were performed using the CRYSTAL code[69, 70], which employs a basis of local Gaussian-type functions. This approach allows for the simulation of truly isolated systems, as the 1D polymers addressed in Chapters 1 and 3, using the hybrid functionals, proven to be essential for accurately reproducing the physics of 1D chains[17, 68]. The Gaussian-type basis set significantly reduces the computational cost of evaluating real-space integrals and, hence, it allows for a drastically reduction of the computational cost when compared, e.g., with state-of-the-art plane-waves based DFT codes. We used triple-$\zeta$-polarised Gaussian-type bases[177] with real space integration tolerances of 10-10-10-15-30 and an energy tolerance of $10^{-10}$ Ha for the total energy convergence. For the results presented in Chapter 1, we adopted the built-in PBE0 functional, whereas for the results of Chapter 3 we customised a range-separated LC-$\omega$PBE hybrid exchange-correlation functional[178] varying the value of the long-range (LR) mixing parameter $c_{\mathrm{LR}}$ which enters in the definition of the LR part of the functional, namely

$$E_{\mathrm{xc}}^{\mathrm{LC}-\omega\mathrm{PBE}} = E_{\mathrm{xc}}^{\mathrm{PBE}} + c_{\mathrm{LR}} \left( E_{\mathrm{x}}^{\mathrm{LR,HF}} - E_{\mathrm{x}}^{\mathrm{LR,PBE}} \right). \tag{C.1}$$

When $c_{\mathrm{LR}} = 0$ the PBE functional is recovered while if $c_{\mathrm{LR}} = 1$ we have pure Hartree-Fock (HF) exchange. The long-range terms in round brackets depend on the range-separation parameter $\omega$ that enters in the decomposition of the Coulomb operator $1/r$ as

$$\frac{1}{r} = \frac{1 - \mathrm{erf}(\omega r)}{r} + \frac{\mathrm{erf}(\omega r)}{r} \tag{C.2}$$

where $\mathrm{erf}(\cdot)$ is the error function; the first and second term in the right-hand side of Eq. C.2 account for the short- and long-range part of the Coulomb operator, respectively. All the presented values were obtained with $\omega = 0.4$ $\mathrm{a}_0^{-1}$. For each $c_{\mathrm{LR}}$, a geometric optimisation was performed and all quantities were computed on the equilibrium configurations. The derivatives $\partial\overline{u}/\partial\epsilon$ of the order parameter

with respect to the strain were computed with finite differences, performing a fixed-cell optimisation for each strained configuration with cell length $a(\epsilon) = a_0(1 \pm \epsilon)$ and $\epsilon = 0.01$, while the effective charges were computed as finite differences of polarization. Values of polarization along the chain (parallel to the $x$-axis) were computed using the Berry phase approach, whereas components transverse to the isolated chain were computed in real space[179, 180]. The piezoelectric coefficients $c_{\text{piezo}}$ and $d_{\text{piezo}}$ of Figure 3.5**g**, 3.5**h** and 3.7, as well as the values of $c^{\text{c.i.}}_{\text{piezo}}$ and of $c^{\text{i.r.}}_{\text{piezo}}$, were computed using the Berry phase approach[121] as implemented in the code[181, 182] and described in Appendix B, which accounts also for transverse displacements. The *converse* piezoelectric coefficient $d_{\text{piezo}}$ is linearly related to $c_{\text{piezo}}$ through the elastic constants tensor $\mathbb{C}$, namely $c_{\text{piezo}} = d_{\text{piezo}}\mathbb{C}$. As far as 1D systems are concerned, only a single scalar elastic constant is required, and it can be evaluated as the second derivative of the energy with respect to the strain, i.e. $\mathbb{C} = \partial^2 E/\partial\epsilon^2$.

For each value of the long-range mixing parameter $c_{\text{LR}}$, a geometric optimisation was performed in order to obtain the equilibrium structures. The unit cell length $a_0$ has a very weak dependence on $c_{\text{LR}}$ for all the polymers studied, as shown in Figure C.1. Signatures of the second order phase transition in MFPA and PMI are provided by the behaviour of the eigenvalues of the dynamical matrix corresponding to the longitudinal optical (LO) mode driving the structural transition, calculated at $\Gamma$ in the undistorted configuration and shown in Figure 3.6, and by the behaviour of the bond lengths and bond angles, reported in Figure C.2. Conversely, the structure of PVDF is not affected by changes in the $c_{\text{LR}}$ parameter, as highlighted in Figure C.3.

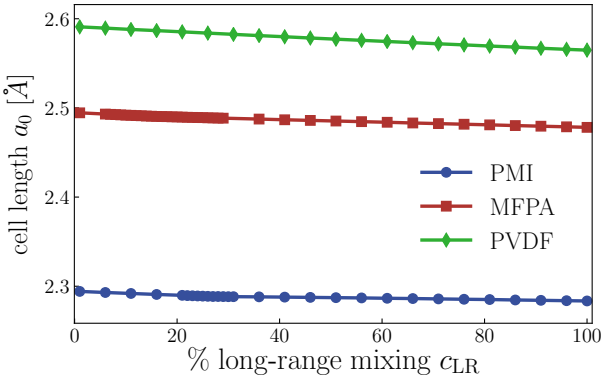


**Figure C.1.** Values of the cell length $a_0$ obtained through cell relaxation calculations show a weak dependence on the value of the long-range mixing parameter $c_{\text{LR}}$.

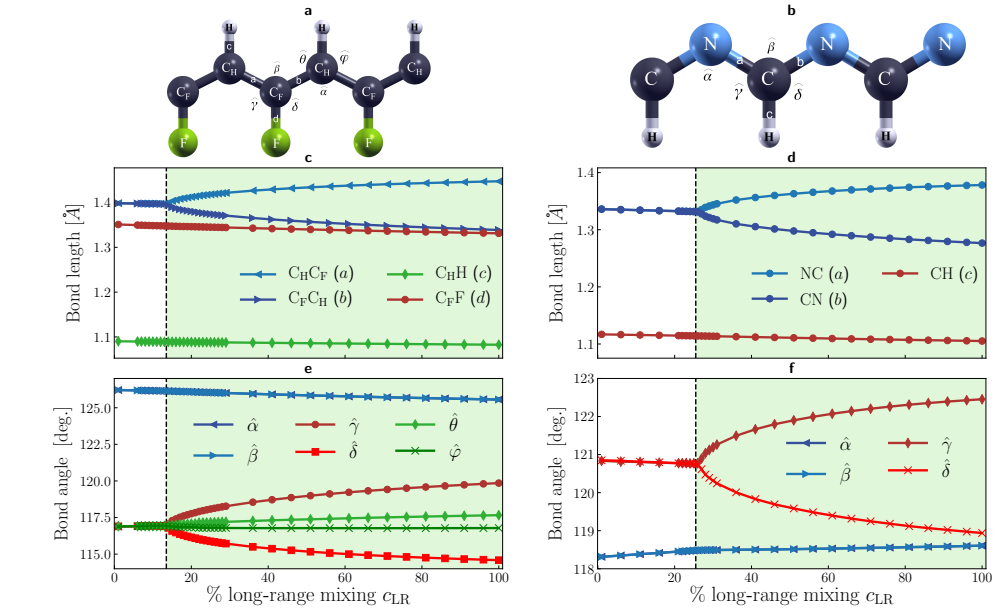


**Figure C.2.** View of the undimerized structure of **a** mono-fluorinated polyacetylene (MFPA) and **b** polymethineimine (PMI), realized with XCrySDen[138]. In **c** and **d** for MFPA and PMI, respectively, we report the values of the bond length between the atoms of the unit cell, calculated with different long-range mixing parameter $c_{\mathrm{LR}}$, whereas in **e** and **f** we report the values of the bond angles for MFPA and PMI, respectively. For MFPA, we use $\mathrm{C_H}$ and $\mathrm{C_F}$ to label carbon atoms bonded to hydrogen and fluorine, respectively. Bond angles are labeled as follows: $\hat{\alpha}$ and $\hat{\beta}$ denote the $\widehat{\mathrm{C_FC_HC_F}}$ ($\widehat{\mathrm{CNC}}$) and $\widehat{\mathrm{C_HC_FC_H}}$ ($\widehat{\mathrm{NCN}}$) bond angles, while $\hat{\gamma}$ and $\hat{\delta}$ label the $\widehat{\mathrm{C_HC_FF}}$ ($\widehat{\mathrm{NCH}}$) and $\widehat{\mathrm{FC_FC_H}}$ ($\widehat{\mathrm{HCN}}$) bond angles. For MFPA only, we also denote by $\hat{\theta}$ and $\hat{\phi}$ the $\widehat{\mathrm{C_FC_HH}}$ and $\widehat{\mathrm{HC_HC_F}}$ bond angles. As expected, the phase transition is signalled by the bond-length alternation as well as in the bifurcation of $\hat{\gamma}$ and $\hat{\delta}$ bond angles.

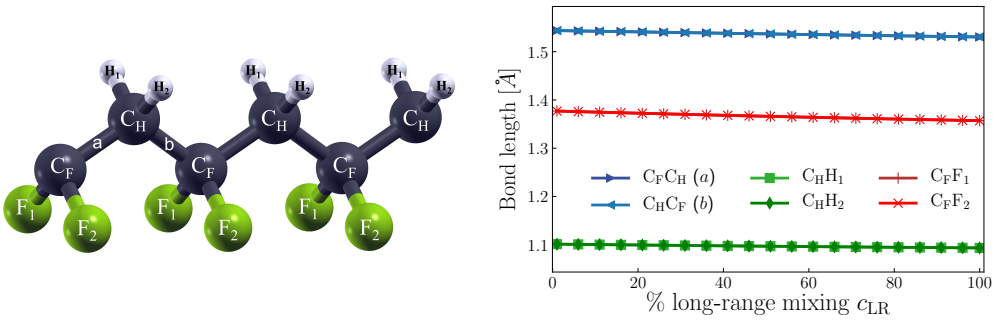


**Figure C.3.** On the left, view of the structure of polyvinylidene fluoride (PVDF), realized with XCrySDen[138]. On the right, behaviour of the bond lengths for different values of $c_{\mathrm{LR}}$. As expected, the structure of PVDF depends very weakly on the long-range mixing parameter, this polymer being not conjugated.

## C.1 Tables with effective charge tensors

In this section we report the full effective-charge tensors of polymers described in Chapter 3.

**Table C.1. Effective charge tensors of MFPA.** For three representative values of the long-range mixing parameter $c_{\mathrm{LR}}$ (including the critical value where the chain dimerization occurs), the components of the effective charge tensors for each atom of the unit cell of MFPA are reported. The $Z^*_{xx}$ component of the carbon atoms reaches strikingly high values, hint of the anomalous polar response of the $\pi$-orbitals along the backbone chain. The sum rule $Z^*_{\mathrm{C_F}} + Z^*_{\mathrm{C_H}} + Z^*_{\mathrm{F}} + Z^*_{\mathrm{H}} = 0$ is also respected.

| $\mathbf{c_{LR} = 1\%}$ | | | | $\mathbf{c_{LR} = 13\% (\simeq \bar{c}_{LR})}$ | | | | $\mathbf{c_{LR} = 100\%}$ | | | |
|---|---|---|---|---|---|---|---|---|---|---|---|
| $Z^*_{\mathrm{C_F}}$ | | | | $Z^*_{\mathrm{C_F}}$ | | | | $Z^*_{\mathrm{C_F}}$ | | | |
| | $x$ | $y$ | $z$ | | $x$ | $y$ | $z$ | | $x$ | $y$ | $z$ |
| $x$ | 27.830 | -0.007 | 0.000 | $x$ | 30.497 | -0.015 | 0.000 | $x$ | 3.969 | -0.901 | 0.000 |
| $y$ | -0.013 | 0.976 | 0.000 | $y$ | -0.029 | 0.991 | 0.000 | $y$ | -0.334 | 1.100 | 0.000 |
| $z$ | 0.000 | 0.000 | 0.168 | $z$ | 0.000 | 0.000 | 0.185 | $z$ | 0.000 | 0.000 | 0.217 |
| $Z^*_{\mathrm{C_H}}$ | | | | $Z^*_{\mathrm{C_H}}$ | | | | $Z^*_{\mathrm{C_H}}$ | | | |
| | $x$ | $y$ | $z$ | | $x$ | $y$ | $z$ | | $x$ | $y$ | $z$ |
| $x$ | -25.533 | -0.001 | 0.000 | $x$ | -28.090 | -0.006 | 0.000 | $x$ | -3.426 | 0.145 | 0.000 |
| $y$ | 0.013 | -0.104 | 0.000 | $y$ | 0.028 | -0.113 | 0.000 | $y$ | 0.316 | -0.154 | 0.000 |
| $z$ | 0.000 | 0.000 | -0.197 | $z$ | 0.000 | 0.000 | -0.214 | $z$ | 0.000 | 0.000 | -0.241 |
| $Z^*_{\mathrm{F}}$ | | | | $Z^*_{\mathrm{F}}$ | | | | $Z^*_{\mathrm{F}}$ | | | |
| | $x$ | $y$ | $z$ | | $x$ | $y$ | $z$ | | $x$ | $y$ | $z$ |
| $x$ | -2.143 | 0.010 | 0.000 | $x$ | -2.240 | 0.028 | 0.000 | $x$ | -0.576 | 0.088 | 0.000 |
| $y$ | 0.001 | -0.865 | 0.000 | $y$ | 0.001 | -0.876 | 0.000 | $y$ | 0.021 | -0.961 | 0.000 |
| $z$ | 0.000 | 0.000 | -0.104 | $z$ | 0.000 | 0.000 | -0.106 | $z$ | 0.000 | 0.000 | -0.118 |
| $Z^*_{\mathrm{H}}$ | | | | $Z^*_{\mathrm{H}}$ | | | | $Z^*_{\mathrm{H}}$ | | | |
| | $x$ | $y$ | $z$ | | $x$ | $y$ | $z$ | | $x$ | $y$ | $z$ |
| $x$ | -0.154 | -0.002 | 0.000 | $x$ | -0.167 | -0.008 | 0.000 | $x$ | 0.031 | -0.124 | 0.000 |
| $y$ | 0.000 | -0.007 | 0.000 | $y$ | 0.000 | -0.002 | 0.000 | $y$ | -0.003 | 0.015 | 0.000 |
| $z$ | 0.000 | 0.000 | 0.132 | $z$ | 0.000 | 0.000 | 0.135 | $z$ | 0.000 | 0.000 | 0.143 |

**Table C.2. Effective charge tensors of PMI.** For three representative values of the long-range mixing parameter $c_{\mathrm{LR}}$ (including the critical value where the chain dimerization occurs), the components of the effective charge tensors for each atom of the unit cell of PMI are reported. The $Z^*_{xx}$ component of the backbone atoms reaches strikingly high values, hint of the anomalous polar response of the $\pi$-orbitals along the backbone chain. The sum rule $Z^*_{\mathrm{C}} + Z^*_{\mathrm{N}} + Z^*_{\mathrm{H}} = 0$ is also respected.

| $\mathbf{c_{LR} = 1\%}$ | | | | $\mathbf{c_{LR} = 25\%\ (\simeq \bar{c}_{LR})}$ | | | | $\mathbf{c_{LR} = 100\%}$ | | | |
|---|---|---|---|---|---|---|---|---|---|---|---|
| $Z^*_{\mathrm{C}}$ | | | | $Z^*_{\mathrm{C}}$ | | | | $Z^*_{\mathrm{C}}$ | | | |
| | $x$ | $y$ | $z$ | | $x$ | $y$ | $z$ | | $x$ | $y$ | $z$ |
| $x$ | 14.063 | 0.000 | 0.000 | $x$ | 15.204 | 0.004 | 0.000 | $x$ | 5.762 | 0.166 | 0.000 |
| $y$ | -0.005 | 0.643 | 0.000 | $y$ | -0.012 | 0.655 | 0.000 | $y$ | -0.268 | 0.638 | 0.000 |
| $z$ | 0.000 | 0.000 | 0.168 | $z$ | 0.000 | 0.000 | 0.186 | $z$ | 0.000 | 0.000 | 0.203 |
| $Z^*_{\mathrm{N}}$ | | | | $Z^*_{\mathrm{N}}$ | | | | $Z^*_{\mathrm{N}}$ | | | |
| | $x$ | $y$ | $z$ | | $x$ | $y$ | $z$ | | $x$ | $y$ | $z$ |
| $x$ | -14.059 | 0.000 | 0.000 | $x$ | -15.217 | -0.001 | 0.000 | $x$ | -5.699 | 0.022 | 0.000 |
| $y$ | 0.005 | -0.427 | 0.000 | $y$ | 0.012 | -0.448 | 0.000 | $y$ | 0.267 | -0.476 | 0.000 |
| $z$ | 0.000 | 0.000 | -0.273 | $z$ | 0.000 | 0.000 | -0.292 | $z$ | 0.000 | 0.000 | -0.318 |
| $Z^*_{\mathrm{H}}$ | | | | $Z^*_{\mathrm{H}}$ | | | | $Z^*_{\mathrm{H}}$ | | | |
| | $x$ | $y$ | $z$ | | $x$ | $y$ | $z$ | | $x$ | $y$ | $z$ |
| $x$ | -0.004 | 0.000 | 0.000 | $x$ | 0.013 | -0.003 | 0.000 | $x$ | -0.063 | -0.188 | 0.000 |
| $y$ | 0.000 | -0.216 | 0.000 | $y$ | 0.000 | -0.206 | 0.000 | $y$ | 0.001 | -0.162 | 0.000 |
| $z$ | 0.000 | 0.000 | 0.105 | $z$ | 0.000 | 0.000 | 0.106 | $z$ | 0.000 | 0.000 | 0.115 |

**Table C.3. Effective charge tensors of PVDF.** Components of the effective charge tensors of the atoms of the unit cell of PVDF. For each component, values reported are obtained as average of those computed with different values of $c_{\mathrm{LR}}$, the highest standard deviation being of the order of $10^{-2}$. The very weak dependence of the effective charges of PVDF on $c_{\mathrm{LR}}$ is a direct consequence of the fact that the structure of PVDF does not depend on $c_{\mathrm{LR}}$, as observed in Figure C.3. Our results for the Born effective charges of PVDF are overall consistent with previously reported values calculated within the generalized-gradient approximation[137]. The sum rule $Z^*_{\mathrm{C_F}} + Z^*_{\mathrm{C_H}} + Z^*_{\mathrm{F_1}} + Z^*_{\mathrm{F_2}} + Z^*_{\mathrm{H_1}} + Z^*_{\mathrm{H_2}} = 0$ is also respected.

| $Z^*_{\mathrm{C_H}}$ | | | |
|---|---|---|---|
| | $x$ | $y$ | $z$ |
| $x$ | -0.603 | 0.000 | 0.000 |
| $y$ | 0.000 | 0.012 | 0.000 |
| $z$ | -0.001 | 0.001 | -0.092 |

| $Z^*_{\mathrm{H_1}}$ | | | |
|---|---|---|---|
| | $x$ | $y$ | $z$ |
| $x$ | 0.069 | 0.000 | 0.000 |
| $y$ | 0.000 | 0.002 | -0.048 |
| $z$ | 0.000 | -0.060 | 0.034 |

| $Z^*_{\mathrm{H_2}}$ | | | |
|---|---|---|---|
| | $x$ | $y$ | $z$ |
| $x$ | 0.069 | 0.000 | 0.000 |
| $y$ | 0.000 | 0.003 | 0.048 |
| $z$ | 0.000 | 0.060 | 0.035 |

| $Z^*_{\mathrm{C_F}}$ | | | |
|---|---|---|---|
| | $x$ | $y$ | $z$ |
| $x$ | 1.333 | 0.000 | 0.000 |
| $y$ | 0.000 | 1.165 | 0.000 |
| $z$ | 0.001 | 0.000 | 0.955 |

| $Z^*_{\mathrm{F_1}}$ | | | |
|---|---|---|---|
| | $x$ | $y$ | $z$ |
| $x$ | -0.434 | 0.000 | 0.000 |
| $y$ | -0.002 | -0.590 | -0.292 |
| $z$ | 0.000 | -0.248 | -0.467 |

| $Z^*_{\mathrm{F_2}}$ | | | |
|---|---|---|---|
| | $x$ | $y$ | $z$ |
| $x$ | -0.434 | 0.000 | 0.000 |
| $y$ | 0.002 | -0.592 | 0.292 |
| $z$ | 0.000 | 0.246 | -0.465 |

# Appendix D

# Details on the time-dependent density-matrix perturbation theory and its implementation

In this Appendix, we discuss about the details of the TDDMPT and its implementation in the QE code. First, we treat the case of a generic time-dependent perturbation in section D.1, then we focus on the case of a double monochromatic perturbation in section D.2. Finally, we describe the DFT implementation of TDDMPT in the QE code in section D.3.

## D.1 Generic time-dependent perturbation

We rewrite Eq. (5.4) highlighting the contribution due to the time-dependent perturbation

$$H(t) = H^{(0)} + V(t) \tag{D.1}$$

where it holds $V^{(i)}(t) = H^{(i)}(t)\ \forall i \geq 1$. It is convenient to adopt the interaction picture, defined with respect to the Schrödinger picture by the transformations

$$|\psi(t)\rangle_I = \mathrm{e}^{\mathrm{i}H_0 t/\hbar} |\psi(t)\rangle\,, \tag{D.2}$$

$$A_I(t) = \mathrm{e}^{\mathrm{i}H_0 t/\hbar} A(t) \mathrm{e}^{-\mathrm{i}H_0 t/\hbar} \tag{D.3}$$

where Equations (D.2) and (D.3) refers to a generic wave function and a generic observable, respectively. With this definitions, it is possible to recast von-Neumann equation (5.9) as follows

$$\mathrm{i}\hbar\dot{\rho}_I(t) = [V_I(t), \rho_I(t)] \tag{D.4}$$

where now the time evolution of $\rho_I(t)$ depends explicitly only on the perturbation $V_I(t) = \mathrm{e}^{\mathrm{i}H_0 t/\hbar} V(t) \mathrm{e}^{-\mathrm{i}H_0 t/\hbar}$. We can now project both sides of Equation (D.4) using $P_C$ and $P_V$ – noticing that they remain unchanged when passing in the interaction

picture – in order to obtain a differential equation for $\rho_{CV,I}(t)$:

$$\mathrm{i}\hbar\dot{\rho}_{I,CV}(t) = P_C\left[V_I(t), \rho_I(t)\right] P_V. \tag{D.5}$$

We can integrate this differential equation with the initial condition

$$\rho_{CV,I}(0) = \rho_{CV}(0) = P_C \sum_v |\psi_v^{(0)}\rangle \langle\psi_v^{(0)}| P_V = 0 \tag{D.6}$$

and obtain

$$\rho_{CV,I}(t) = -\frac{\mathrm{i}}{\hbar}\int_0^t P_C\left[V_I(t'), \rho_I(t')\right] P_V \mathrm{d}t'. \tag{D.7}$$

This integral equation can be expanded perturbatively allowing to solve it iteratively and find:

$$\rho_{CV,I}^{(n)}(t) = -\frac{\mathrm{i}}{\hbar}\int_0^t \sum_{i=1}^{n} P_C\left[V_I^{(i)}(t'), \rho_I^{(n-i)}(t')\right] P_V \mathrm{d}t' \quad \text{for} \quad n \geq 1. \tag{D.8}$$

This expression for $\rho_{CV}^{(n)}(t)$ depends on terms of the perturbative expansion of lower orders (up to the $(n-1)$-th) and holds for every generic time-dependent perturbation. Moreover, it is defined in terms of quantities that depends only on the unperturbed wave functions as will more explicit in what follows.

### D.1.1 Analogy with time-independent case

It is possible to write $\rho_{CV}^{(n)}(t)$ defining a perturbed-like time-dependent valence wave-function $|\eta_v^{(n)}(t)\rangle$:

$$\rho_{CV}^{(n)}(t) = \sum_v |\eta_v^{(n)}(t)\rangle \langle\psi_v^{(0)}|. \tag{D.9}$$

First, we transform Equation (D.8) back to the Schrödinger picture:

$$\rho_{CV}^{(n)}(t) = \mathrm{e}^{-\mathrm{i}H_0 t/\hbar}\left(-\frac{\mathrm{i}}{\hbar}\int_0^t \sum_{i=1}^{n} P_C\left[V_I^{(i)}(t'), \rho_I^{(n-i)}(t')\right] P_V \mathrm{d}t'\right)\mathrm{e}^{\mathrm{i}H_0 t/\hbar}; \tag{D.10}$$

then, with some manipulation, we can write

$$|\eta_v^{(n)}(t)\rangle = \sum_c \mathcal{C}_{cv}^{(n)}(t)\,|\psi_c^{(0)}\rangle \tag{D.11}$$

where

$$\mathcal{C}_{cv}^{(n)}(t) = -\frac{\mathrm{i}}{\hbar}\int_0^t \mathrm{e}^{\mathrm{i}\left(\varepsilon_v^{(0)} - \varepsilon_c^{(0)}\right)t/\hbar} \sum_{i=1}^{n} \langle\psi_c^{(0)}|\left[V_I^{(i)}(t'), \rho_I^{(n-i)}(t')\right]|\psi_v^{(0)}\rangle\,\mathrm{d}t'. \tag{D.12}$$

It is straightforward to verify that if we do the limit to the time-independent case we recover the equations for the static case of section 5.2.1, whereas if we plug a single or

double monochromatic perturbation we recover the respective frequency-dependent equations discussed above.

## D.2 Details on the double monochromatic perturbation case

In this section we derive Equations (5.60) and (5.62). The starting point is the double monochromatic perturbation $H^{(1)}(t)$ defined in Equation (5.58), which we rewrite for convenience:

$$H^{(1)}(t) = H^{(1)}(\omega_1)\left(e^{\mathrm{i}\omega_1 t} + \mathrm{e}^{-\mathrm{i}\omega_1 t}\right) + H^{(1)}(\omega_2)\left(e^{\mathrm{i}\omega_2 t} + \mathrm{e}^{-\mathrm{i}\omega_2 t}\right) \tag{D.13}$$

Plugging $H^{(1)}(t)$ into the perturbative expansion of von-Neumann Equation (5.33), for $n = 1$ we have

$$\mathrm{i}\hbar\dot{\rho}^{(1)}(t) = \left[H^{(0)}, \rho^{(1)}(t)\right] + \left(e^{\mathrm{i}\omega_1 t} + e^{-\mathrm{i}\omega_1 t}\right)\left[H^{(1)}(\omega_1), \rho^{(0)}\right] + \left(e^{\mathrm{i}\omega_2 t} + e^{-\mathrm{i}\omega_2 t}\right)\left[H^{(1)}(\omega_2), \rho^{(0)}\right] \tag{D.14}$$

which suggests that we can decompose $\rho^{(1)}(t)$ as follows:

$$\rho^{(1)}(t) = \rho^{(1)}(\omega_1)e^{-\mathrm{i}\omega_1 t} + \rho^{(1)}(-\omega_1)e^{\mathrm{i}\omega_1 t} + \rho^{(1)}(\omega_2)e^{-\mathrm{i}\omega_2 t} + \rho^{(1)}(-\omega_2)e^{\mathrm{i}\omega_2 t}. \tag{D.15}$$

Each term $\rho^{(1)}(\pm\omega_j)$, $j \in \{1, 2\}$, can be found as in the single monochromatic perturbation case and from Equation (5.40) we have:

$$\rho^{(1)}(\pm\omega_j) = \rho^{(1)}_{CV}(\pm\omega_j) + \rho^{(1)}_{VC}(\pm\omega_j) \quad \text{with} \quad \rho^{(1)}_{VC}(\pm\omega_j) = \left[\rho^{(1)}_{CV}(\mp\omega_j)\right]^\dagger. \tag{D.16}$$

Proceeding as in the other cases, we define a perturbed-like, frequency-dependent, valence wave-function $|\eta^{(1)}_v(\pm\omega_j)\rangle$:

$$\rho^{(1)}_{CV}(\pm\omega_j) = P_C\rho^{(1)}(\pm\omega_j)\,|\psi^{(0)}_v\rangle \equiv \sum_v |\eta^{(1)}_v(\pm\omega_j)\rangle\,\langle\psi^{(0)}_v| \tag{D.17}$$

From Equation (D.14) solved with the trial function (D.15) we obtain for each frequency-dependent term

$$\pm\hbar\omega_j\rho^{(1)}(\pm\omega_j) - \left[H^{(0)}, \rho^{(1)}(\pm\omega_j)\right] = \left[H^{(1)}(\omega_j), \rho^{(0)}\right] \tag{D.18}$$

and applying $P_C$ on the left and $|\psi^{(0)}_v\rangle$ on the right we arrive at:

$$\left(H^{(0)} - \varepsilon^{(0)}_v \mp \hbar\omega_j\right)|\eta^{(1)}_v(\pm\omega_j)\rangle = -P_C\left[H^{(1)}(\omega_j), \rho^{(0)}\right]|\psi^{(0)}_v\rangle\,, \tag{D.19}$$

which is the same results of Equation (5.37). With the definition of the frequency-dependent Green function projected on conduction states of Equation (5.38) with

$\alpha = 1$, we arrive at Equation (5.60)

$$|\eta_v^{(1)}(\pm\omega_j)\rangle = \tilde{G}_v(\pm\omega_j)\left[H^{(1)}, \rho^{(0)}\right]|\psi_v^{(0)}\rangle\,, \tag{D.20}$$

which is just Equation (5.39) in the case $n = \alpha = 1$.
For $n = 2$ we follow the same steps:

- from von-Neumann equation (5.33) we have:

$$\mathrm{i}\hbar\dot{\rho}^{(2)}(t) = \left[H^{(0)}, \rho^{(2)}(t)\right] + \left[H^{(1)}(t), \rho^{(1)}(t)\right] \tag{D.21}$$

- from Equation (D.13) and (D.15) we obtain:

$$\begin{aligned}\rho^{(2)}(t) = &\left[\rho^{(2)}(2\omega_1)e^{-2\mathrm{i}\omega_1 t} + \rho^{(2)}(-2\omega_1)e^{2\mathrm{i}\omega_1 t}\right] + \\ &+ \left[\rho^{(2)}(2\omega_2)e^{-2\mathrm{i}\omega_2 t} + \rho^{(2)}(-2\omega_2)e^{2\mathrm{i}\omega_2 t}\right] + \\ &+ \left[\rho^{(2)}(\omega_1+\omega_2)e^{-\mathrm{i}(\omega_1+\omega_2)t} + \rho^{(2)}(\omega_1-\omega_2)e^{-\mathrm{i}(\omega_1-\omega_2)t}\right] + \\ &+ \left[\rho^{(2)}(-\omega_1-\omega_2)e^{\mathrm{i}(\omega_1+\omega_2)t} + \rho^{(2)}(-\omega_1+\omega_2)e^{\mathrm{i}(\omega_1-\omega_2)t}\right] + \\ &+ \rho^{(2)}(0)\mathrm{e}^{\mathrm{i}0t}\end{aligned} \tag{D.22}$$

  where terms with mixed frequencies are now present;

- from Equation (5.41), (D.15) and (D.16) we obtain an expression for each component of the previous Equation (D.22) in terms of the $\rho_{CV}^{(i)}(\alpha\omega_1 + \beta\omega_2)$ with $i \in \{1, 2\}$ and $\alpha$ and $\beta$ integers obeying $|\alpha| + |\beta| = i$:

$$\rho^{(2)}(\pm 2\omega_1) = \rho_{CV}^{(2)}(\pm 2\omega_1) + \rho_{VC}^{(2)}(\pm 2\omega_1) + \left[\rho_{CV}^{(1)}(\pm\omega_1), \rho_{VC}^{(1)}(\pm\omega_1)\right] \tag{D.23}$$

$$\rho^{(2)}(\pm 2\omega_2) = \rho_{CV}^{(2)}(\pm 2\omega_2) + \rho_{VC}^{(2)}(\pm 2\omega_2) + \left[\rho_{CV}^{(1)}(\pm\omega_2), \rho_{VC}^{(1)}(\pm\omega_2)\right] \tag{D.24}$$

$$\rho^{(2)}(\omega_1 \pm \omega_2) = \rho_{CV}^{(2)}(\omega_1 \pm \omega_2) + \rho_{VC}^{(2)}(\omega_1 \pm \omega_2) + \left[\rho_{CV}^{(1)}(\omega_1), \rho_{VC}^{(1)}(\pm\omega_2)\right] + \left[\rho_{CV}^{(1)}(\pm\omega_2), \rho_{VC}^{(1)}(\omega_1)\right] \tag{D.25}$$

$$\rho^{(2)}(-\omega_1 \pm \omega_2) = \rho_{CV}^{(2)}(-\omega_1 \pm \omega_2) + \rho_{VC}^{(2)}(-\omega_1 \pm \omega_2) + \left[\rho_{CV}^{(1)}(-\omega_1), \rho_{VC}^{(1)}(\pm\omega_2)\right] + \left[\rho_{CV}^{(1)}(\pm\omega_2), \rho_{VC}^{(1)}(-\omega_1)\right] \tag{D.26}$$

$$\begin{aligned}\rho^{(2)}(0) = \rho_{CV}^{(2)}(0) + \rho_{VC}^{(2)}(0) + &\left[\rho_{CV}^{(1)}(\omega_1), \rho_{VC}^{(1)}(-\omega_1)\right] + \left[\rho_{CV}^{(1)}(-\omega_1), \rho_{VC}^{(1)}(\omega_1)\right] + \\ &\left[\rho_{CV}^{(1)}(\omega_2), \rho_{VC}^{(1)}(-\omega_2)\right] + \left[\rho_{CV}^{(1)}(-\omega_2), \rho_{VC}^{(1)}(\omega_2)\right]\end{aligned} \tag{D.27}$$

  and it holds $\rho_{VC}^{(i)}(\alpha\omega_1 + \beta\omega_2) = \left[\rho_{CV}^{(i)}(-\alpha\omega_1 - \beta\omega_2)\right]^\dagger$.

- aiming to find the $|\eta_v^{(2)}(\alpha\omega_1 + \beta\omega_2)\rangle$ such that

$$\rho_{CV}^{(2)}(\alpha\omega_1 + \beta\omega_2) = \sum_v |\eta_v^{(2)}(\alpha\omega_1 + \beta\omega_2)\rangle\langle\psi_v^{(0)}|\,, \tag{D.28}$$

  we solve Equation (D.21) with the trial function of Equation (D.22) and applying again $P_C$ on the left and $|\psi_v^{(0)}\rangle$ on the right we obtain the following

(self-consistent) linear systems:

$$\left(H^{(0)} - \varepsilon_v^{(0)} - \hbar 2\omega_1\right) |\eta_v^{(2)}(2\omega_1)\rangle = -P_C \left[H^{(1)}(\omega_1), \rho^{(1)}(\omega_1)\right] |\psi_v^{(0)}\rangle \quad \text{(D.29)}$$

$$\left(H^{(0)} - \varepsilon_v^{(0)} - \hbar 2\omega_2\right) |\eta_v^{(2)}(2\omega_2)\rangle = -P_C \left[H^{(1)}(\omega_2), \rho^{(1)}(\omega_2)\right] |\psi_v^{(0)}\rangle \quad \text{(D.30)}$$

$$\left(H^{(0)} - \varepsilon_v^{(0)} - \hbar\left(\omega_1 \pm \omega_2\right)\right) |\eta_v^{(2)}(\omega_1 \pm \omega_2)\rangle = -P_C \left\{\left[H^{(1)}(\omega_1), \rho^{(1)}(\pm\omega_2)\right] + \left[H^{(1)}(\omega_2), \rho^{(1)}(\omega_1)\right]\right\} |\psi_v^{(0)}\rangle \quad \text{(D.31)}$$

$$\left(H^{(0)} - \varepsilon_v^{(0)} - \hbar\left(-\omega_1 \pm \omega_2\right)\right) |\eta_v^{(2)}(-\omega_1 \pm \omega_2)\rangle = -P_C \left\{\left[H^{(1)}(\omega_1), \rho^{(1)}(\pm\omega_2)\right] + \left[H^{(1)}(\omega_2), \rho^{(1)}(-\omega_1)\right]\right\} |\psi_v^{(0)}\rangle \quad \text{(D.32)}$$

$$\left(H^{(0)} - \varepsilon_v^{(0)}\right) |\eta_v^{(2)}(0)\rangle = -P_C \left\{\left[H^{(1)}(\omega_1), \rho^{(1)}(\omega_1) + \rho^{(1)}(-\omega_1)\right] + \left[H^{(1)}(\omega_2), \rho^{(1)}(\omega_2) + \rho^{(1)}(-\omega_2)\right]\right\} |\psi_v^{(0)}\rangle\,. \quad \text{(D.33)}$$

Defining the frequency-dependent Green functions

$$\tilde{G}_v(\alpha\omega_1 + \beta\omega_2) = \sum_c \frac{|\psi_c^{(0)}\rangle \langle\psi_c^{(0)}|}{\varepsilon_v^{(0)} - \varepsilon_c^{(0)} + \hbar(\alpha\omega_1 + \beta\omega_2)} \quad \text{(D.34)}$$

we can write the explicit expression for the $|\eta_v^{(2)}(\alpha\omega_1 + \beta\omega_2)\rangle$ of Equation (5.62)

$$|\eta_v^{(2)}(\alpha\omega_1 + \beta\omega_2)\rangle = \tilde{G}_v(\alpha\omega_1 + \beta\omega_2)\,\{\bullet\}\,|\psi_v^{(0)}\rangle \quad \text{(D.35)}$$

where inside the curly brackets $\{\bullet\}$ there are the proper commutators between $H^{(1)}(\omega_j)$ and $\rho^{(1)}(\pm\omega_l)$ $(j, l \in \{1, 2\})$ according to Equation (D.29 - D.33).

## D.3 Details on the implementation in Quantum ESPRESSO

In this section we see in details the derivation of the self-consistent linear systems of Equation (5.98) and (5.101), as well as the work-flow of our implementation in the QE code. We start reviewing the existing work-flow for the static Raman response, which will be the base for the time-dependent case.

### D.3.1 Static case

The **phonon** routine is the main driver of the phonon code in QE (the well-known `ph.x`). It reads all the quantities calculated by the **pwscf** routine (`pw.x`), it checks if some recover file is present and determines which calculations need to be done, depending on the flags in the input file. It calls the subroutine **do_phonon** which can compute the response to an atomic displacement, the dynamical matrix at each q-point as well as the electron-phonon interaction. At $\mathbf{q} = \mathbf{0}$ it can calculate the linear response to an electric field perturbation and hence the dielectric constant, the Born effective charges and the polarizability at imaginary frequencies. At $\mathbf{q} = \mathbf{0}$, it can also calculate the electro-optic and the Raman tensors from second order

response to an electric field[1]. The computation of the different responses to an electric field perturbation is managed by the subroutine **phescf**, called by do_phonon. First, linear-response quantities are computed calling the subroutine **solve_e**[2]. In particular, the perturbed valence wave functions and the induced charge density are obtained solving the self-consistent linear system which defines the variation of the valence wave function due to the perturbation, namely from Equation (5.28) for $n = 1$:

$$(H_{\mathrm{KS}}^{(0)} - \varepsilon_v^{(0)}) \, |\eta_v^{(1)}\rangle = -P_C \left[H_{\mathrm{KS}}^{(1)}, \rho^{(0)}\right] |\psi_v^{(0)}\rangle \,, \tag{D.36}$$

where

$$H_{\mathrm{KS}}^{(1)} = V_{\mathrm{ext.}}^{(1)} + V_{\mathrm{HXC}}^{(1)}, \tag{D.37}$$

and in real-space representation it holds

$$V_{\mathrm{HXC}}^{(1)}(\boldsymbol{r}) = \int \mathrm{K}_{\mathrm{HXC}}(\boldsymbol{r}, \boldsymbol{r'}) \rho^{(1)}(\boldsymbol{r'}) \mathrm{d}^3\boldsymbol{r'} = \int \frac{\delta^2 E_{\mathrm{HXC}}[\rho](\boldsymbol{r}, \boldsymbol{r'})}{\delta\rho(\boldsymbol{r})\delta\rho(\boldsymbol{r'})} \rho^{(1)}(\boldsymbol{r'}) \mathrm{d}^3\boldsymbol{r'}. \tag{D.38}$$

Since $\rho^{(1)}$ depends on the $\{|\eta_v^{(1)}\rangle\}$, the linear system must be solved self-consistently.

At the end of the **solve_e** subroutine, both the $\{|\eta_v^{(1)}\rangle\}$ and $\rho^{(1)}$ have been computed and are stored, including self-consistently the Hartree-Exchange-Correlation part (more details on this are in Section D.3.3). The ground is now set for the calculation of linear-response quantities such as effective charges and dielectric constant but also for second order quantities. The subroutine to perform second order calculation, in particular to compute Raman and electro-optical tensors, is **raman** and it is called inside phescf, after solve_e (**if lraman==.true.**). We focus only on the parts involved in the calculation of the Raman tensors. First, we need to compute the second-order perturbed-like wave functions $\{|\eta_v^{(2)}\rangle\}$. They are defined as the solution of the following self-consistent linear system:

$$(H_{\mathrm{KS}}^{(0)} - \varepsilon_v^{(0)}) \, |\eta_v^{(2)}\rangle = -P_C \left[H_{\mathrm{KS}}^{(1)}, \rho^{(1)}\right] |\psi_v^{(0)}\rangle - P_C \left[H_{\mathrm{KS}}^{(2)}, \rho^{(0)}\right] |\psi_v^{(0)}\rangle \,, \tag{D.39}$$

where $H_{\mathrm{KS}}^{(1)}$ is defined in Equation (D.37), while in real-space representation it holds:

$$\begin{aligned} H_{\mathrm{KS}}^{(2)}(\boldsymbol{r}) = V_{\mathrm{HXC}}^{(2)}(\boldsymbol{r}) = &\int \frac{\delta^2 E_{\mathrm{HXC}}[\rho](\boldsymbol{r}, \boldsymbol{r'})}{\delta\rho(\boldsymbol{r})\delta\rho(\boldsymbol{r'})} \rho^{(2)}(\boldsymbol{r'}) \mathrm{d}^3\boldsymbol{r'} + \\ &+ \int \frac{\delta^3 E_{\mathrm{HXC}}[\rho](\boldsymbol{r}, \boldsymbol{r'}, \boldsymbol{r''})}{\delta\rho(\boldsymbol{r})\delta\rho(\boldsymbol{r'})\delta\rho(\boldsymbol{r''})} \rho^{(1)}(\boldsymbol{r'}) \rho^{(1)}(\boldsymbol{r''}) \mathrm{d}^3\boldsymbol{r'} \mathrm{d}^3\boldsymbol{r''}. \end{aligned} \tag{D.40}$$

From the expression for the second derivative of the density $\rho^{(2)}$, namely

$$\rho^{(2)} = \rho_{CV}^{(2)} + \rho_{VC}^{(2)} + \left[\rho_{CV}^{(1)}, \rho_{VC}^{(1)}\right], \tag{D.41}$$

we can separate the right-hand side of Equation (D.40) in a self-consistent (SCF)

[1] The keyword to put in the input file in order to calculate Raman tensors is **lraman**.

[2] They are are needed also for second order calculations.

and a non-self-consistent (NSCF) part:

$$V^{(2)}_{HXC,\mathrm{SCF}}(\boldsymbol{r}) = \int \frac{\delta^2 E_{\mathrm{HXC}}[\rho](\boldsymbol{r},\boldsymbol{r'})}{\delta\rho(\boldsymbol{r})\delta\rho(\boldsymbol{r'})}\left[\rho^{(2)}_{CV}(\boldsymbol{r'}) + \rho^{(2)}_{VC}(\boldsymbol{r'})\right]\mathrm{d}^3\boldsymbol{r'}, \tag{D.42}$$

$$\begin{aligned} V^{(2)}_{HXC,\mathrm{NSCF}}(\boldsymbol{r}) = &\int \frac{\delta^2 E_{\mathrm{HXC}}[\rho](\boldsymbol{r},\boldsymbol{r'})}{\delta\rho(\boldsymbol{r})\delta\rho(\boldsymbol{r'})}\left[\rho^{(1)}_{CV}(\boldsymbol{r'}), \rho^{(1)}_{VC}(\boldsymbol{r'})\right]\mathrm{d}^3\boldsymbol{r'} + \\ &+ \int \frac{\delta^3 E_{\mathrm{HXC}}[\rho](\boldsymbol{r},\boldsymbol{r'},\boldsymbol{r''})}{\delta\rho(\boldsymbol{r})\delta\rho(\boldsymbol{r'})\delta\rho(\boldsymbol{r''})}\rho^{(1)}(\boldsymbol{r'})\rho^{(1)}(\boldsymbol{r''})\mathrm{d}^3\boldsymbol{r'}\mathrm{d}^3\boldsymbol{r''}. \end{aligned} \tag{D.43}$$

The work-flow of the `raman` subroutine to compute the $\{|\eta^{(2)}_v\rangle\}$ and $\rho^{(2)}$ is divided in three main steps:

**1.** first, it calls the subroutine **`dhdrhopsi`** to compute

$$P_C[H^{(1)}_{\mathrm{KS}}, \rho^{(1)}]\,|\psi^{(0)}_v\rangle = P_C[V^{(1)}_{\mathrm{ext.}}, \rho^{(1)}]\,|\psi^{(0)}_v\rangle + P_C\left[V^{(1)}_{\mathrm{HXC}}, \rho^{(1)}\right]|\psi^{(0)}_v\rangle\,. \tag{D.44}$$

The two terms on the right-hand side are computed separately:

**1.1** the first term involves the position operator $\hat{r}$, which is not well defined in an infinite periodic system. Instead, the commutator with the density operator and its derivatives is well defined and it holds:

$$P_C[V^{(1)}_{\mathrm{ext.}}, \rho^{(1)}]\,|\psi^{(0)}_v\rangle = \mathrm{i}P_C\sum_{v'}\frac{\partial\,|\widetilde{\eta}^{(1)}_{v'}\rangle\,\langle\widetilde{\psi}^{(0)}_{v'}|}{\partial k}\,|\widetilde{\psi}^{(0)}_v\rangle\,, \tag{D.45}$$

where the $\widetilde{\mathrm{o}}$ indicates the periodic part of the wave function. The derivative is computed with finite differences, hence it is necessary to calculate both the $\{|\psi^{(0)}_v\rangle\}$ and the $\{|\eta^{(1)}_v\rangle\}$ at $\mathbf{k} \pm \Delta\mathbf{k}$. This first-order calculations are done by the subroutine **`solve_e_nscf`**, which solves the linear system of Equation (D.36) without the SCF cycle, $\rho^{(1)}$ being already known;

**1.2** using the relation $\rho^{(1)} = \sum_v(|\eta^{(1)}_v\rangle\,\langle\psi^{(0)}_v| + |\psi^{(0)}_v\rangle\,\langle\eta^{(1)}_v|)$, the second term becomes:

$$P_C\left[V^{(1)}_{\mathrm{HXC}}, \rho^{(1)}\right]|\psi^{(0)}_v\rangle = P_C V^{(1)}_{\mathrm{HXC}}\,|\eta^{(1)}_v\rangle - P_C\sum_{v'}|\eta^{(1)}_{v'}\rangle\,\langle\psi^{(0)}_{v'}|\,V^{(1)}_{\mathrm{HXC}}\,|\psi^{(0)}_v\rangle\,, \tag{D.46}$$

where all the terms are already known.

**2.** then, in the subroutine **`dvpsi_e2`**, it computes the non-self-consistent part of the right-hand side of Equation (D.39) using the NSCF potential $V^{(2)}_{HXC,\mathrm{NSCF}}$ of Equation (D.43);

**3.** finally, in the subroutine **`solve_e2`**, the $\{|\eta^{(2)}_v\rangle\}$ are computed self-consistently solving the linear system of Equation (D.39).

Now we have all the ingredients to compute the Raman tensor, defined by:

$$\frac{\partial^3 \mathcal{E}^{\mathrm{el}}}{\partial \mathrm{E}_l \partial \mathrm{E}_m \partial u_\alpha^\tau} = 2\mathrm{Tr}\left[\frac{\partial^2 \rho}{\partial \mathrm{E}_l \partial \mathrm{E}_m}\frac{\partial V_{\mathrm{ext.}}}{\partial u_\alpha^\tau}\right], \tag{D.47}$$

where the factor 2 is for the spin degeneracy, $\mathcal{E}^{\mathrm{el}}$ is the electronic total energy, $\mathrm{E}_l$ and $\mathrm{E}_m$ are, respectively, the $l$-th and $m$-th component of an external electric field and $u_\alpha^\tau$ is the displacement of the $\tau$-th atom of the unit-cell in the $\alpha$-th Cartesian direction. Without loss of generality, hereafter we will consider $\boldsymbol{l = m}$ and will consequently drop the subscripts. Using the definitions of the trace operator and of the second-order derivative of the density matrix $\rho^{(2)}$, we write Equation (D.47) as:

$$\begin{aligned}\frac{\partial^3 \mathcal{E}^{el.}}{\partial E^2 \partial u_\alpha^\tau} = &2\sum_v \langle \eta_v^{(2)} | \frac{\partial V_{\mathrm{ext.}}}{\partial u_\alpha^\tau} | \psi_v^{(0)} \rangle - 2\sum_{v,v'} \langle \eta_v^{(1)} | \eta_{v'}^{(1)} \rangle \langle \psi_{v'}^{(0)} | \frac{\partial V_{\mathrm{ext.}}}{\partial u_\alpha^\tau} | \psi_v^{(0)} \rangle + \\ &+ 2\sum_v \langle \psi_v^{(0)} | \frac{\partial V_{\mathrm{ext.}}}{\partial u_\alpha^\tau} | \eta_v^{(2)} \rangle + 2\sum_v \langle \eta_v^{(1)} | \frac{\partial V_{\mathrm{ext.}}}{\partial u_\alpha^\tau} | \eta_v^{(1)} \rangle. \end{aligned} \tag{D.48}$$

The subroutine **`raman_mat`** computes the different terms in Equation (D.48) using the $\{|\eta_v^{(1)}\rangle\}$ and the $\{|\eta_v^{(2)}\rangle\}$ computed before. The effect of atomic displacement is included calling the subroutine **`dvqpsi_us`**, which applies the derivative of the bare potential $\partial V_{\mathrm{ext.}}/\partial u_\alpha^\tau$ to the wave-functions[3].

### D.3.2 Time-dependent case

We consider a perturbation constituted by a monochromatic electric field:

$$\mathbf{E}(t) = \mathbf{E}\left(\mathrm{e}^{-\mathrm{i}\omega t} + \mathrm{e}^{\mathrm{i}\omega t}\right). \tag{D.49}$$

We rewrite for convenience the von-Neumann Equation (5.93) for the $n$-th derivative $\rho^{(n)}(t)$ of the density matrix:

$$\mathrm{i}\hbar\dot{\rho}^{(n)}(t) = \left[H_{\mathrm{KS}}^{(0)}, \rho^{(n)}(t)\right] + \left[H_{\mathrm{KS}}^{(1)}(t), \rho^{(n-1)}(t)\right] + \left[H_{\mathrm{KS}}^{(2)}(t), \rho^{(n-2)}(t)\right], \tag{D.50}$$

where

$$H_{\mathrm{KS}}^{(1)}(t) = V_{\mathrm{ext.}}^{(1)}(t) + V_{\mathrm{HXC}}^{(1)}(t), \tag{D.51}$$

$$H_{\mathrm{KS}}^{(2)}(t) = V_{\mathrm{HXC}}^{(2)}(t), \tag{D.52}$$

[3]The self-consistent contribution of the variation induced on the charge density by this perturbation is neglected.

and in real-space representation it holds

$$V^{(1)}_{\mathrm{HXC}}(\boldsymbol{r},t) = \int \mathrm{K}_{\mathrm{HXC}}(\boldsymbol{r},\boldsymbol{r'})\rho^{(1)}(\boldsymbol{r'},t)\mathrm{d}^3\boldsymbol{r'} = \int \frac{\delta^2 E_{\mathrm{HXC}}[\rho](\boldsymbol{r},\boldsymbol{r'})}{\delta\rho(\boldsymbol{r})\delta\rho(\boldsymbol{r'})}\rho^{(1)}(\boldsymbol{r'},t)\mathrm{d}^3\boldsymbol{r'}, \quad \text{(D.53)}$$

$$V^{(2)}_{\mathrm{HXC}}(\boldsymbol{r},t) = \int \frac{\delta^2 E_{\mathrm{HXC}}[\rho](\boldsymbol{r},\boldsymbol{r'})}{\delta\rho(\boldsymbol{r})\delta\rho(\boldsymbol{r'})}\rho^{(2)}(\boldsymbol{r'},t)\mathrm{d}^3\boldsymbol{r'} + + \int \frac{\delta^3 E_{\mathrm{HXC}}[\rho](\boldsymbol{r},\boldsymbol{r'},\boldsymbol{r''})}{\delta\rho(\boldsymbol{r})\delta\rho(\boldsymbol{r'})\delta\rho(\boldsymbol{r''})}\rho^{(1)}(\boldsymbol{r'},t)\rho^{(1)}(\boldsymbol{r''},t)\mathrm{d}^3\boldsymbol{r'}\mathrm{d}^3\boldsymbol{r''}. \quad \text{(D.54)}$$

In the previous equations we used the instantaneous approximation, namely we suppose a real and $\omega$-independent $\mathrm{K}_{\mathrm{HXC}}(\boldsymbol{r},\boldsymbol{r'})$. This hypothesis will always be adopted in what follows.
We substitute in Equation (D.50) the trial solution of Equation (5.34), which we rewrite for convenience

$$\rho^{(n)}(t) = \sum_{\alpha}\left[\rho^{(n)}(\alpha\omega)\mathrm{e}^{-\mathrm{i}\alpha\omega t} + \rho^{(n)}(-\alpha\omega)\mathrm{e}^{\mathrm{i}\alpha\omega t}\right],\ \alpha = \begin{cases} 0,2,\ldots,n & \text{if } n \text{ even} \\ 1,3,\ldots,n & \text{if } n \text{ odd} \end{cases} \quad \text{(D.55)}$$

and consider the cases $n = 1$ and $n = 2$. In the former case, Equation (D.55) becomes

$$\rho^{(1)}(t) = \rho^{(1)}(+\omega)\mathrm{e}^{-\mathrm{i}\omega t} + \rho^{(1)}(-\omega)\mathrm{e}^{+\mathrm{i}\omega t} \quad \text{(D.56)}$$

and since both $\rho^{(1)}(\boldsymbol{r},t)$ and $\rho^{(1)}(\boldsymbol{r},\omega)$ are real, we have that $\rho^{(1)}(\boldsymbol{r},-\omega) = [\rho^{(1)}(\boldsymbol{r},\omega)]^\dagger = \rho^{(1)}(\boldsymbol{r},\omega)$. With some manipulation, we arrive at the self-consistent linear system which defines the perturbed valence wave functions $\{|\eta^{(1)}_v(\pm\omega)\rangle\}$ of Equation (5.98):

$$\left(H^{(0)} - \varepsilon^{(0)}_v \mp \hbar\omega\right)|\eta^{(1)}_v(\pm\omega)\rangle = -P_C\left[V^{(1)}_{\mathrm{ext.}}(\pm\omega) + V^{(1)}_{\mathrm{HXC}}(\pm\omega), \rho^{(0)}\right]|\psi^{(0)}_v\rangle, \quad \text{(D.57)}$$

where in real-space representation it holds

$$V^{(1)}_{\mathrm{HXC}}(\boldsymbol{r},+\omega) = V^{(1)}_{\mathrm{HXC}}(\boldsymbol{r},-\omega) = \int \frac{\delta^2 E_{\mathrm{HXC}}[\rho](\boldsymbol{r},\boldsymbol{r'})}{\delta\rho(\boldsymbol{r})\delta\rho(\boldsymbol{r'})}\rho^{(1)}(\boldsymbol{r'},\omega)\mathrm{d}^3\boldsymbol{r'}, \quad \text{(D.58)}$$

with

$$\rho^{(1)}(\boldsymbol{r},\omega) = \rho^{(1)}_{CV}(\boldsymbol{r},\omega) + \rho^{(1)}_{VC}(\boldsymbol{r},\omega). \quad \text{(D.59)}$$

Analogously, for $n = 2$ we have:

$$\rho^{(2)}(t) = \rho^{(2)}(+2\omega)\mathrm{e}^{-\mathrm{i}2\omega t} + \rho^{(2)}(-2\omega)\mathrm{e}^{+2\mathrm{i}\omega t} + \rho^{(2)}(0), \quad \text{(D.60)}$$

where $\rho^{(2)}(2\omega) = \rho^{(2)}(-2\omega)$. The self-consistent linear systems which define the perturbed-like valence wave functions $\{|\eta^{(2)}_v(\pm2\omega)\rangle\}$ and $\{|\eta^{(2)}_v(0)\rangle\}$ are, respectively:

$$\left(H^{(0)} - \varepsilon^{(0)}_v \mp \hbar2\omega\right)|\eta^{(2)}_v(\pm2\omega)\rangle = -P_C\left\{\left[V^{(1)}_{\mathrm{ext.}}(\omega) + V^{(1)}_{\mathrm{HXC}}(\omega), \rho^{(1)}(\omega)\right] + \left[V^{(2)}_{\mathrm{HXC}}(2\omega), \rho^{(0)}\right]\right\}|\psi^{(0)}_v\rangle, \quad \text{(D.61)}$$

and

$$\left(H^{(0)} - \varepsilon_v^{(0)}\right) |\eta_v^{(2)}(0)\rangle = -P_C \left\{ 2 \left[ V_{\text{ext.}}^{(1)}(\omega) + V_{\text{HXC}}^{(1)}(\omega), \rho^{(1)}(\omega) \right] + \left[ V_{\text{HXC}}^{(2)}(0), \rho^{(0)} \right] \right\} |\psi_v^{(0)}\rangle \,, \quad \text{(D.62)}$$

where we recognize the above Equation for the $\{|\eta_v^{(2)}(0)\rangle\}$ as Equation (5.101), and in real-space it holds

$$\begin{aligned} V_{\text{HXC}}^{(2)}(\boldsymbol{r}, 2\omega) = & \int \frac{\delta^2 E_{\text{HXC}}[\rho](\boldsymbol{r}, \boldsymbol{r'})}{\delta\rho(\boldsymbol{r})\delta\rho(\boldsymbol{r'})} \rho^{(2)}(\boldsymbol{r'}, 2\omega) \mathrm{d}^3\boldsymbol{r'} + \\ & + \int \frac{\delta^3 E_{\text{HXC}}[\rho](\boldsymbol{r}, \boldsymbol{r'}, \boldsymbol{r''})}{\delta\rho(\boldsymbol{r})\delta\rho(\boldsymbol{r'})\delta\rho(\boldsymbol{r''})} \rho^{(1)}(\boldsymbol{r'}, \omega)\rho^{(1)}(\boldsymbol{r''}, \omega) \mathrm{d}^3\boldsymbol{r'} \mathrm{d}^3\boldsymbol{r''}, \end{aligned} \quad \text{(D.63)}$$

with

$$\rho^{(2)}(\boldsymbol{r}, 2\omega) = \rho_{CV}^{(2)}(\boldsymbol{r}, 2\omega) + \rho_{VC}^{(2)}(\boldsymbol{r}, 2\omega) + \left[ \rho_{CV}^{(1)}(\boldsymbol{r}, \omega), \rho_{VC}^{(1)}(\boldsymbol{r}, \omega) \right], \quad \text{(D.64)}$$

and

$$\begin{aligned} V_{\text{HXC}}^{(2)}(\boldsymbol{r}, 0) = & \int \frac{\delta^2 E_{\text{HXC}}[\rho](\boldsymbol{r}, \boldsymbol{r'})}{\delta\rho(\boldsymbol{r})\delta\rho(\boldsymbol{r'})} \rho^{(2)}(\boldsymbol{r'}, 0) \mathrm{d}^3\boldsymbol{r'} + \\ & + 2 \int \frac{\delta^3 E_{\text{HXC}}[\rho](\boldsymbol{r}, \boldsymbol{r'}, \boldsymbol{r''})}{\delta\rho(\boldsymbol{r})\delta\rho(\boldsymbol{r'})\delta\rho(\boldsymbol{r''})} \rho^{(1)}(\boldsymbol{r'}, \omega)\rho^{(1)}(\boldsymbol{r''}, \omega) \mathrm{d}^3\boldsymbol{r'} \mathrm{d}^3\boldsymbol{r''}, \end{aligned} \quad \text{(D.65)}$$

with

$$\rho^{(2)}(\boldsymbol{r}, 0) = \rho_{CV}^{(2)}(\boldsymbol{r}, 0) + \rho_{VC}^{(2)}(\boldsymbol{r}, 0) + \left[ \rho_{CV}^{(1)}(\boldsymbol{r}, \omega), \rho_{VC}^{(1)}(\boldsymbol{r}, -\omega) \right] + \left[ \rho_{CV}^{(1)}(\boldsymbol{r}, -\omega), \rho_{VC}^{(1)}(\boldsymbol{r}, \omega) \right]. \quad \text{(D.66)}$$

It is worth to point out that, just like in Equation (D.40), also in Equation (D.63) and (D.65) there is a non self-consistent part and a self-consistent one. In particular, we have:

$$V_{HXC,\text{SCF}}^{(2)}(\boldsymbol{r}, 2\omega) = \int \frac{\delta^2 E_{\text{HXC}}[\rho](\boldsymbol{r}, \boldsymbol{r'})}{\delta\rho(\boldsymbol{r})\delta\rho(\boldsymbol{r'})} \left[ \rho_{CV}^{(2)}(\boldsymbol{r'}, 2\omega) + \rho_{VC}^{(2)}(\boldsymbol{r'}, 2\omega) \right] \mathrm{d}^3\boldsymbol{r'}, \quad \text{(D.67)}$$

$$\begin{aligned} V_{HXC,\text{NSCF}}^{(2)}(\boldsymbol{r}, 2\omega) = & \int \frac{\delta^2 E_{\text{HXC}}[\rho](\boldsymbol{r}, \boldsymbol{r'})}{\delta\rho(\boldsymbol{r})\delta\rho(\boldsymbol{r'})} \left[ \rho_{CV}^{(1)}(\boldsymbol{r'}, \omega), \rho_{VC}^{(1)}(\boldsymbol{r'}, \omega) \right] \mathrm{d}^3\boldsymbol{r'} + \\ & + \int \frac{\delta^3 E_{\text{HXC}}[\rho](\boldsymbol{r}, \boldsymbol{r'}, \boldsymbol{r''})}{\delta\rho(\boldsymbol{r})\delta\rho(\boldsymbol{r'})\delta\rho(\boldsymbol{r''})} \rho^{(1)}(\boldsymbol{r'}, \omega)\rho^{(1)}(\boldsymbol{r''}, \omega) \mathrm{d}^3\boldsymbol{r'} \mathrm{d}^3\boldsymbol{r''}; \end{aligned} \quad \text{(D.68)}$$

$$V_{HXC,\text{SCF}}^{(2)}(\boldsymbol{r}, 0) = \int \frac{\delta^2 E_{\text{HXC}}[\rho](\boldsymbol{r}, \boldsymbol{r'})}{\delta\rho(\boldsymbol{r})\delta\rho(\boldsymbol{r'})} \left[ \rho_{CV}^{(2)}(\boldsymbol{r'}, 0) + \rho_{VC}^{(2)}(\boldsymbol{r'}, 0) \right] \mathrm{d}^3\boldsymbol{r'}, \quad \text{(D.69)}$$

$$\begin{aligned} V_{HXC,\text{NSCF}}^{(2)}(\boldsymbol{r}, 0) = & \int \frac{\delta^2 E_{\text{HXC}}[\rho](\boldsymbol{r}, \boldsymbol{r'})}{\delta\rho(\boldsymbol{r})\delta\rho(\boldsymbol{r'})} \left\{ \left[ \rho_{CV}^{(1)}(\boldsymbol{r'}, \omega), \rho_{VC}^{(1)}(\boldsymbol{r'}, -\omega) \right] + \right. \\ & \left. + \left[ \rho_{CV}^{(1)}(\boldsymbol{r'}, -\omega), \rho_{VC}^{(1)}(\boldsymbol{r'}, \omega) \right] \right\} \mathrm{d}^3\boldsymbol{r'} + \\ & + 2 \int \frac{\delta^3 E_{\text{HXC}}[\rho](\boldsymbol{r}, \boldsymbol{r'}, \boldsymbol{r''})}{\delta\rho(\boldsymbol{r})\delta\rho(\boldsymbol{r'})\delta\rho(\boldsymbol{r''})} \rho^{(1)}(\boldsymbol{r'}, \omega)\rho^{(1)}(\boldsymbol{r''}, \omega) \mathrm{d}^3\boldsymbol{r'} \mathrm{d}^3\boldsymbol{r''}. \end{aligned} \quad \text{(D.70)}$$

Finally, we write the $\omega$-dependent version of Equation (D.47) for $\rho^{(2)}(0)$:

$$\frac{\partial^3 \mathcal{E}^{el.}(\omega)}{\partial E^2 \partial u_\alpha^\tau} = 2\mathrm{Tr}\left[\rho^{(2)}(0)\frac{\partial H}{\partial u_\alpha^\tau}\right], \tag{D.71}$$

and substituting the expression for $\rho^{(2)}(0)$ we obtain

$$\begin{aligned}\frac{\partial^3 \mathcal{E}^{el.}(\omega)}{\partial E^2 \partial u_\alpha^\tau} =& 2\sum_v \left[\langle\eta_v^{(2)}(0)|\frac{\partial H}{\partial u_\alpha^\tau}|\psi_v^{(0)}\rangle + \langle\psi_v^{(0)}|\frac{\partial H}{\partial u_\alpha^\tau}|\eta_v^{(2)}(0)\rangle\right] + \\ &+ 2\sum_v \left[\langle\eta_v^{(1)}(+\omega)|\frac{\partial H}{\partial u_\alpha^\tau}|\eta_v^{(1)}(+\omega)\rangle + \langle\eta_v^{(1)}(-\omega)|\frac{\partial H}{\partial u_\alpha^\tau}|\eta_v^{(1)}(-\omega)\rangle\right] + \\ &- 2\sum_{v,v'} \left[\langle\eta_v^{(1)}(+\omega)|\eta_{v'}^{(1)}(+\omega)\rangle + \langle\eta_v^{(1)}(-\omega)|\eta_{v'}^{(1)}(-\omega)\rangle\right] \langle\psi_{v'}^{(0)}|\frac{\partial H}{\partial u_\alpha^\tau}|\psi_v^{(0)}\rangle.\end{aligned} \tag{D.72}$$

### D.3.3 First order terms

We have all the ingredients for the calculation of the frequency-dependent Raman response defined in terms of perturbed-like wave-functions. In this section we focus on the workflow to compute self-consistently these terms. In the subroutine **`solve_e`** it is implemented the linear-response for both a static and a monochromatic external uniform electric field. We will focus on the frequency-dependent response, but if we put $\omega = 0$ in the following equations we recover the static case. The aim is to compute the perturbed wave functions $\{|\eta_v^{(1)}(\pm\omega)\rangle\}$ solving the self-consistent linear system of Equation (D.57), which we rewrite:

$$\left(H^{(0)} - \varepsilon_v^{(0)} \mp \hbar\omega\right)|\eta_v^{(1)}(\pm\omega)\rangle = -P_C\left[V_{\text{ext.}}^{(1)}(\omega), \rho^{(0)}\right]|\psi_v^{(0)}\rangle - P_C\left[V_{\text{HXC}}^{(1)}(\omega), \rho^{(0)}\right]|\psi_v^{(0)}\rangle. \tag{D.73}$$

Before the self-consistent cycle, the subroutine **`dvpsi_e`** is called to compute the non-self-consistent (NSCF) contribution $|\eta_v^{(1)}\rangle_{\text{NSCF}}$, namely:

$$|\eta_v^{(1)}\rangle_{\text{NSCF}} = -P_C\left[V_{\text{ext.}}^{(1)}(\omega), \rho^{(0)}\right]|\psi_v^{(0)}\rangle, \tag{D.74}$$

which remains unchanged during all the self-consistent cycle[4]. At each step of the cycle, the subroutine **`sternheimer_kernel`** takes in input $|\eta_v^{(1)}\rangle_{\text{NSCF}}$ (called `dvpsi` in the code) and the estimate of the self-consistent potential $V_{\text{HXC}}^{(1)}$ calculated at the previous step[5] (called `dvscfins` in the code) and computes the new estimates for the potential and for the solution vector of the linear system as follows:

1. applies $V_{\text{HXC}}^{(1)}$ to the unperturbed valence wave function $|\psi_v^{(0)}\rangle$ and adds the result to the NSCF vector $|\eta_v^{(1)}\rangle_{\text{NSCF}}$. The result is stored in the variable `dvpsi`;

[4]This is done for each **k**-point and for each polarisation of the perturbing electric field.

[5]At the first step it is zero. Alternatively, it can be read from a recover file in the case of a restart from a previous calculation.

**2.** orthogonalizes `dvpsi` to the valence states with the `orthogonalize` subroutine (this step correspond to the application of the operator $-P_C$);

**3.** calls the subroutine `cgsolve_all` to solve the linear system of Equation (D.73). In particular, it takes in input the right-hand side vector `dvpsi` together with the frequency $\pm\omega$ – hence it is called two times – to compute an estimate of the solution vectors;

**4.** since $\rho^{(1)}(+\omega) = \rho^{(1)}(-\omega)$, it is possible to compute the total variation of the charge density directly using the vector

$$\overline{|\eta_v^{(1)}(\omega)\rangle} = \frac{1}{2}\left(|\eta_v^{(1)}(+\omega)\rangle + |\eta_v^{(1)}(-\omega)\rangle\right), \tag{D.75}$$

which is stored in the variable `dpsi`. We highlight that if $\omega = 0$ we obtain the static $|\eta_v^{(1)}\rangle$ of Equation (D.36). At each step of the cycle, this estimate is used as a starting guess for the left-hand side vector for both frequencies $\pm\omega$;

**5.** the subroutine `incdrhoscf` then computes the variation of the charge density $\overline{\rho^{(1)}}(\omega)$

$$\overline{\rho^{(1)}}(\omega) = \frac{2}{\mathcal{W}} \sum_v |\psi_v^{(0)}\rangle \, \overline{\langle \eta_v^{(1)}(\omega)|}\,, \tag{D.76}$$

where the factor 2 comes from the sum over the conjugate complex of a real quantity and $\mathcal{W}$ is a proper weighting factor which contains the contribution of the spin degeneracy and the normalization over the unit-cell volume.

Now we are back again in `solve_e`, where finally the self-consistent potential is updated through the subroutine `dv_of_drho`, which computes

$$V_{\mathrm{HXC}}^{(1)}(\boldsymbol{r},\omega) = \int \frac{\delta^2 E_{\mathrm{HXC}}[\rho](\boldsymbol{r},\boldsymbol{r'})}{\delta\rho(\boldsymbol{r})\delta\rho(\boldsymbol{r'})} \overline{\rho^{(1)}}(\boldsymbol{r'},\omega)\mathrm{d}^3\boldsymbol{r'}, \tag{D.77}$$

and stores the result in `dvscfout`. The self-consistent potential that will be given in input to the new call of `sternheimer_kernel` through the variable `dvscfins`, is computed mixing the old one and the new one. At the end of the cycle, the final estimates of the solution vector $|\eta_v^{(1)}(\omega)\rangle$ of Equation (D.75) (contained in `dpsi`) and of the self-consistent potential $V_{\mathrm{HXC}}^{(1)}(\omega)$ (contained in `dvscfout`) are stored.

### D.3.4 Second order terms

We focus on the calculation of the second order terms $\{|\eta_v^{(2)}(0)\rangle\}$ and $\rho^{(2)}(0)$. We have to solve the linear system of Equation (D.62), which we rewrite using the $\overline{\rho^{(1)}}(\omega)$ of Equation (D.76) computed in `solve_e`:

$$\left(H^{(0)} - \varepsilon_v^{(0)}\right)|\eta_v^{(2)}(0)\rangle = -2P_C\left[H_{\mathrm{KS}}^{(1)}(\omega), \overline{\rho^{(1)}}(\omega)\right]|\psi_v^{(0)}\rangle + P_C\left[V_{\mathrm{HXC}}^{(2)}(0), \rho^{(0)}\right]|\psi_v^{(0)}\rangle\,. \tag{D.78}$$

**1.** first, it calls the subroutine **`dhdrhopsi`** to compute

$$P_C[H^{(1)}_{\mathrm{KS}}(\omega), \overline{\rho^{(1)}(\omega)}]\,|\psi^{(0)}_v\rangle = P_C[V^{(1)}_{\mathrm{ext.}}(\omega), \overline{\rho^{(1)}}(\omega)]\,|\psi^{(0)}_v\rangle + P_C\left[V^{(1)}_{\mathrm{HXC}}(\omega), \overline{\rho^{(1)}}(\omega)\right]|\psi^{(0)}_v\rangle\,. \tag{D.79}$$

The two terms on the right-hand side are computed separately:

**1.1** in analogy with the static case we have that:

$$P_C[V^{(1)}_{\mathrm{ext.}}(\omega), \overline{\rho^{(1)}}(\omega)]\,|\psi^{(0)}_v\rangle = \mathrm{i}P_C \sum_{v'} \frac{\partial\,|\overline{\widetilde{\eta}^{(1)}_{v'}(\omega)}\rangle\,\langle\widetilde{\psi}^{(0)}_{v'}|}{\partial k}\,|\widetilde{\psi}^{(0)}_v\rangle\,, \tag{D.80}$$

where the $\widetilde{\mathrm{o}}$ indicates the periodic part of the wave function. The derivative is computed with finite differences, hence it is necessary to calculate both the $\{|\psi^{(0)}_v\rangle\}$ and the $\{|\overline{\widetilde{\eta}^{(1)}_v(\omega)}\rangle\}$ at $\mathbf{k} \pm \Delta\mathbf{k}$. The first-order calculations are done by the subroutine **`solve_e_nscf`**, which solves the linear system of Equation (D.36) without the SCF cycle, $\overline{\rho^{(1)}(\omega)}$ being already known;

**1.2** analogously to the static case, the second term is:

$$\begin{aligned} P_C\left[V^{(1)}_{\mathrm{HXC}}(\omega), \overline{\rho^{(1)}(\omega)}\right]|\psi^{(0)}_v\rangle = {} & P_C V^{(1)}_{\mathrm{HXC}}(\omega)\,|\overline{\eta^{(1)}_v(\omega)}\rangle + \\ & - P_C \sum_{v'} |\overline{\eta^{(1)}_{v'}(\omega)}\rangle\,\langle\psi^{(0)}_{v'}|\,V^{(1)}_{\mathrm{HXC}}(\omega)\,|\psi^{(0)}_v\rangle\,; \end{aligned} \tag{D.81}$$

**2.** then, in the subroutine **`dvpsi_e2`**, it computes the non-self-consistent part of the right-hand side of Equation (D.78) using the $V^{(2)}_{HXC,\mathrm{NSCF}}(0)$ of Equation (D.70):

$$\begin{aligned} V^{(2)}_{HXC,\mathrm{NSCF}}(\boldsymbol{r},0) = {} & \int \frac{\delta^2 E_{\mathrm{HXC}}[\rho](\boldsymbol{r},\boldsymbol{r'})}{\delta\rho(\boldsymbol{r})\delta\rho(\boldsymbol{r'})} \Big\{\Big[\rho^{(1)}_{CV}(\boldsymbol{r'},\omega), \rho^{(1)}_{VC}(\boldsymbol{r'},-\omega)\Big] + \\ & + \Big[\rho^{(1)}_{CV}(\boldsymbol{r'},-\omega), \rho^{(1)}_{VC}(\boldsymbol{r'},\omega)\Big]\Big\}\,\mathrm{d}^3\boldsymbol{r'} + \\ & + 2\int \frac{\delta^3 E_{\mathrm{HXC}}[\rho](\boldsymbol{r},\boldsymbol{r'},\boldsymbol{r''})}{\delta\rho(\boldsymbol{r})\delta\rho(\boldsymbol{r'})\delta\rho(\boldsymbol{r''})}\rho^{(1)}(\boldsymbol{r'},\omega)\rho^{(1)}(\boldsymbol{r''},\omega)\mathrm{d}^3\boldsymbol{r'}\mathrm{d}^3\boldsymbol{r''}. \end{aligned} \tag{D.82}$$

From the first order calculations we have the $\{|\overline{\eta^{(1)}_v(\omega)}\rangle\}$ and the $\overline{\rho^{(1)}}(\omega)$. With the latter we can compute:

$$\rho^{(1)}(\boldsymbol{r'},\omega)\rho^{(1)}(\boldsymbol{r''},\omega) = \overline{\rho^{(1)}}(\boldsymbol{r'},\omega)\overline{\rho^{(1)}}(\boldsymbol{r''},\omega). \tag{D.83}$$

However, we need the $\{|\eta^{(1)}_v(\omega)\rangle\}$ and the $\{|\eta^{(1)}_v(-\omega)\rangle\}$ separately in order to compute:

$$\Big[\rho^{(1)}_{CV}(\pm\omega), \rho^{(1)}_{VC}(\mp\omega)\Big] = \sum_v |\eta^{(1)}_v(\pm\omega)\rangle\,\langle\eta^{(1)}_v(\pm\omega)| - \sum_{v,v'} |\psi^{(0)}_v\rangle\,\langle\eta^{(1)}_v(\pm\omega)|\eta^{(1)}_{v'}(\pm\omega)\rangle\,\langle\psi^{(0)}_{v'}|\,. \tag{D.84}$$

We compute them solving the linear system of Equation (D.73) with the subroutine `solve_e_nscf`, $\rho^{(1)}(\omega)$ being known;

3. finally, in the subroutine **`solve_e2`**, the $\{|\eta_v^{(2)}(0)\rangle\}$ are computed self-consistently solving the linear system of Equation (D.78).

We now have all ingredients to compute the Raman response using Equation (D.72) and the `raman_mat` subroutine.

# Bibliography

[1] Stefano Paolo Villani, Marco Campetella, Paolo Barone, and Francesco Mauri. Giant piezoelectricity driven by thouless pump in conjugated polymers. *npj Computational Materials*, 10(1):81, 2024.

[2] Matteo Calandra. Charge density waves go nano. *Nature nanotechnology*, 10(9):737–738, 2015.

[3] Yi Chen, Wei Ruan, Meng Wu, Shujie Tang, Hyejin Ryu, Hsin-Zon Tsai, Ryan L Lee, Salman Kahn, Franklin Liou, Caihong Jia, et al. Strong correlations and orbital texture in single-layer 1t-tase2. *Nature Physics*, 16(2):218–224, 2020.

[4] Eduardo H da Silva Neto, Pegor Aynajian, Alex Frano, Riccardo Comin, Enrico Schierle, Eugen Weschke, András Gyenis, Jinsheng Wen, John Schneeloch, Zhijun Xu, et al. Ubiquitous interplay between charge ordering and high-temperature superconductivity in cuprates. *Science*, 343(6169):393–396, 2014.

[5] Jl A Wilson, FJ Di Salvo, and S Mahajan. Charge-density waves and superlattices in the metallic layered transition metal dichalcogenides. *Advances in Physics*, 24(2):117–201, 1975.

[6] Taner Yildirim. Ferroelectric soft phonons, charge density wave instability, and strong electron-phonon coupling in bis 2 layered superconductors: A first-principles study. *Physical Review B*, 87(2):020506, 2013.

[7] Shuoguo Yuan, Xin Luo, Hung Lit Chan, Chengcheng Xiao, Yawei Dai, Maohai Xie, and Jianhua Hao. Room-temperature ferroelectricity in mote2 down to the atomic monolayer limit. *Nature communications*, 10(1):1775, 2019.

[8] Li Wang, Ying Wu, Yayun Yu, Aixi Chen, Huifang Li, Wei Ren, Shuai Lu, Sunan Ding, Hui Yang, Qi-Kun Xue, et al. Direct observation of one-dimensional peierls-type charge density wave in twin boundaries of monolayer mote2. *ACS nano*, 14(7):8299–8306, 2020.

[9] Giovanni Marini and Matteo Calandra. Light-tunable charge density wave orders in mote 2 and wte 2 single layers. *Physical review letters*, 127(25):257401, 2021.

[10] DJ Thouless. Quantization of particle transport. *Physical Review B*, 27:6083, 1983.

[11] Shuta Nakajima, Takafumi Tomita, Shintaro Taie, Tomohiro Ichinose, Hideki Ozawa, Lei Wang, Matthias Troyer, and Yoshiro Takahashi. Topological thouless pumping of ultracold fermions. *Nature Physics*, 12:296–300, 2016.

[12] Michael Lohse, Christian Schweizer, Oded Zilberberg, Monika Aidelsburger, and Immanuel Bloch. A thouless quantum pump with ultracold bosonic atoms in an optical superlattice. *Nature Physics*, 12(4):350–354, 2016.

[13] Xin Guo, Martin Baumgarten, and Klaus Müllen. Designing $\pi$-conjugated polymers for organic electronics. *Progress in Polymer Science*, 38(12):1832–1908, 2013.

[14] Chu-Chen Chueh, Alex K-Y Jen, et al. Recent advances in molecular design of functional conjugated polymers for high-performance polymer solar cells. *Progress in Polymer Science*, 99:101175, 2019.

[15] Mohamad Saleh AlSalhi, Javed Alam, Lawrence Arockiasamy Dass, and Mohan Raja. Recent advances in conjugated polymers for light emitting devices. *International Journal of Molecular Sciences*, 12(3):2036–2054, 2011.

[16] Erica Zeglio, Alexandra L Rutz, Thomas E Winkler, George G Malliaras, and Anna Herland. Conjugated polymers for assessing and controlling biological functions. *Advanced Materials*, 31(22):1806712, 2019.

[17] Davide Romanin, Lorenzo Monacelli, Raffaello Bianco, Ion Errea, Francesco Mauri, and Matteo Calandra. Dominant role of quantum anharmonicity in the stability and optical properties of infinite linear acetylenic carbon chains. *The Journal of Physical Chemistry Letters*, 12:10339–10345, 2021.

[18] Lorenzo Monacelli, Ion Errea, Matteo Calandra, and Francesco Mauri. Pressure and stress tensor of complex anharmonic crystals within the stochastic self-consistent harmonic approximation. *Physical Review B*, 98(2):024106, 2018.

[19] Lorenzo Monacelli, Ion Errea, Matteo Calandra, and Francesco Mauri. Black metal hydrogen above 360 gpa driven by proton quantum fluctuations. *Nature Physics*, 17(1):63–67, 2021.

[20] Ion Errea, Matteo Calandra, and Francesco Mauri. Anharmonic free energies and phonon dispersions from the stochastic self-consistent harmonic approximation: Application to platinum and palladium hydrides. *Physical Review B*, 89(6):064302, 2014.

[21] R Peierls. Zur theorie der elektrischen und thermischen leitfähigkeit von metallen. *Annalen der Physik*, 396(2):121–148, 1930.

[22] Rudolf Ernst Peierls. *Quantum theory of solids*. Clarendon Press, 1996.

[23] Giuseppe Grosso, Giuseppe; Pastori Parravicini. *Solid State Physics*. Academic Press, 2013.

[24] Jean-Paul Pouget. The peierls instability and charge density wave in one-dimensional electronic conductors. *Comptes Rendus Physique*, 17:332–356, 2016.

[25] Herbert Fröhlich. On the theory of superconductivity: the one-dimensional case. *Proceedings of the Royal Society of London. Series A. Mathematical and Physical Sciences*, 223(1154):296–305, 1954.

[26] R Comes, M Lambert, H Launois, and HR Zeller. Evidence for a peierls distortion or a kohn anomaly in one-dimensional conductors of the type k 2 pt (cn) 4 br 0.30 · x h 2 o. *Physical Review B*, 8:571, 1973.

[27] Seiichi Kagoshima, Hiroyuki Anzai, Koji Kajimura, and Takehiko Ishiguro. Observation of the kohn anomaly and the peierls transition in ttf–tcnq by x-ray scattering. *Journal of the Physical Society of Japan*, 39:1143–1144, 1975.

[28] G Shirane, SM Shapiro, R Comes, AF Garito, and AJ Heeger. Phonon dispersion and kohn anomaly in tetrathiafulvalene-tetracyanoquinodimethane (ttf-tcnq). *Physical Review B*, 14(6):2325, 1976.

[29] W. P. Su, J.R. Schrieffer, and A. J. Heeger. Solitons in polyacetylene. *Physical review letters*, 42:1698, 1979.

[30] M.J. Rice and E.J. Mele. Elementary excitations of a linearly conjugated diatomic polymer. *Physical Review Letters*, 49:1455, 1982.

[31] Shigeki Onoda, Shuichi Murakami, and Naoto Nagaosa. Topological nature of polarization and charge pumping in ferroelectrics. *Physical review letters*, 93:167602, 2004.

[32] Kunihiko Yamauchi and Paolo Barone. Electronic ferroelectricity induced by charge and orbital orderings. *Journal of Physics: Condensed Matter*, 26:103201, 2014.

[33] Konstantin N Kudin, Roberto Car, and Raffaele Resta. Quantization of the dipole moment and of the end charges in push-pull polymers. *The Journal of chemical physics*, 127(19), 2007.

[34] David Vanderbilt and RD King-Smith. Electric polarization as a bulk quantity and its relation to surface charge. *Physical Review B*, 48(7):4442, 1993.

[35] Di Xiao, Ming-Che Chang, and Qian Niu. Berry phase effects on electronic properties. *Reviews of modern physics*, 82:1959, 2010.

[36] W-P_ Su, JR Schrieffer, and AJ Heeger. Soliton excitations in polyacetylene. *Physical Review B*, 22:2099, 1980.

[37] RD King-Smith and David Vanderbilt. Theory of polarization of crystalline solids. *Physical Review B*, 47, 1993.

[38] Michael Victor Berry. Quantal phase factors accompanying adiabatic changes. *Proceedings of the Royal Society of London. A. Mathematical and Physical Sciences*, 392:45–57, 1984.

[39] André Moliton and Roger C Hiorns. Review of electronic and optical properties of semiconducting $\pi$-conjugated polymers: applications in optoelectronics. *Polymer International*, 53(10):1397–1412, 2004.

[40] Serap Günes, Helmut Neugebauer, and Niyazi Serdar Sariciftci. Conjugated polymer-based organic solar cells. *Chemical reviews*, 107(4):1324–1338, 2007.

[41] Markus Gross, David C Müller, Heinz-Georg Nothofer, Ulrich Scherf, Dieter Neher, Christoph Bräuchle, and Klaus Meerholz. Improving the performance of doped $\pi$-conjugated polymers for use in organic light-emitting diodes. *Nature*, 405(6787):661–665, 2000.

[42] Gilles Horowitz. Organic field-effect transistors. *Advanced materials*, 10(5):365–377, 1998.

[43] Sahika Inal, Jonathan Rivnay, Andreea-Otilia Suiu, George G Malliaras, and Iain McCulloch. Conjugated polymers in bioelectronics. *Accounts of chemical research*, 51(6):1368–1376, 2018.

[44] G. Natta, G. Mazzanti, and P. Corradini. Polimerizzazione stereospecifica dell'acetilene. *Atti Accad. Naz. Lincei Cl. Sci. Fis. Mat. Nat. Rend.*, (25):3, 1958.

[45] AM Saxman, R Liepins, and M Aldissi. Polyacetylene: Its synthesis, doping and structure. *Progress in polymer science*, 11(1-2):57–89, 1985.

[46] Hideki Shirakawa, Edwin J Louis, Alan G MacDiarmid, Chwan K Chiang, and Alan J Heeger. Synthesis of electrically conducting organic polymers: halogen derivatives of polyacetylene,(ch) x. *Journal of the Chemical Society, Chemical Communications*, (16):578–580, 1977.

[47] Alan J. Heeger. Nobel lecture: Semiconducting and metallic polymers: The fourth generation of polymeric materials. *Rev. Mod. Phys.*, 73:681–700, Sep 2001.

[48] Andrew Streitwieser, Clayton H Heathcock, Edward M Kosower, and Penelope J Corfield. *Introduction to organic chemistry*, volume 547. Macmillan New York, 1992.

[49] PC Barbé, J-C Brosse, G Cecchin, D Derouet, K Dušek, F Epaillard, T Higashimura, J Kratochvila, G Legeay, M Lesná, et al. Polyacetylenes with substituents: Their synthesis and properties. In *Catalytical and Radical Polymerization*, pages 121–165. Springer, 1986.

[50] Toshikazu Sakaguchi, Yuki Hayakawa, Ritsuka Ishima, and Tamotsu Hashimoto. Synthesis and photoluminescence properties of poly (1-hexyl-2-aryl acetylene) s, poly (1-phenyl-2-fluorenylacetylene), and poly (1-fluorenyl-2-fluorenlacetylene). *Synthetic metals*, 162(1-2):64–69, 2012.

[51] Benedict A San Jose, Satoshi Matsushita, Yasuyuki Moroishi, and Kazuo Akagi. Disubstituted liquid crystalline polyacetylene derivatives that exhibit linearly polarized blue and green emissions. *Macromolecules*, 44:6288–6302, 2011.

[52] Toshio Masuda. Substituted polyacetylenes. *Journal of Polymer Science Part A: Polymer Chemistry*, 45:165–180, 2007.

[53] Yu P Kudryavtsev, SE Evsyukov, MB Guseva, VG Babaev, and VV Khvostov. Carbyne—the third allotropic form of carbon. *Russian chemical bulletin*, 42:399–413, 1993.

[54] RB Heimann, J Kleiman, and NM Salansky. A unified structural approach to linear carbon polytypes. *Nature*, 306(5939):164–167, 1983.

[55] A Greenville Whittaker, Ethel J Watts, Roy S Lewis, and Edward Anders. Carbynes: carriers of primordial noble gases in meteorites. *Science*, 209(4464):1512–1514, 1980.

[56] Th Henning and F Salama. Carbon in the universe. *Science*, 282(5397):2204–2210, 1998.

[57] J Jansta and FP Dousek. Some aspects of existence of elementary carbon with sp-hybridized bonds. *Carbon*, 18(6):433–437, 1980.

[58] PPK Smith and Peter R Buseck. Carbyne forms of carbon: do they exist? *Science*, 216(4549):984–986, 1982.

[59] Carlo S Casari, Matteo Tommasini, Rik R Tykwinski, and Alberto Milani. Carbon-atom wires: 1-d systems with tunable properties. *Nanoscale*, 8(8):4414–4435, 2016.

[60] Bitao Pan, Jun Xiao, Jiling Li, Pu Liu, Chengxin Wang, and Guowei Yang. Carbyne with finite length: The one-dimensional sp carbon. *Science advances*, 1(9):e1500857, 2015.

[61] Lei Shi, Philip Rohringer, Kazu Suenaga, Yoshiko Niimi, Jani Kotakoski, Jannik C Meyer, Herwig Peterlik, Marius Wanko, Seymur Cahangirov, Angel Rubio, et al. Confined linear carbon chains as a route to bulk carbyne. *Nature materials*, 15(6):634–639, 2016.

[62] Mingjie Liu, Vasilii I Artyukhov, Hoonkyung Lee, Fangbo Xu, and Boris I Yakobson. Carbyne from first principles: chain of c atoms, a nanorod or a nanorope. *ACS nano*, 7(11):10075–10082, 2013.

[63] Pavel B Sorokin, Hoonkyung Lee, Lyubov Yu Antipina, Abhishek K Singh, and Boris I Yakobson. Calcium-decorated carbyne networks as hydrogen storage media. *Nano letters*, 11(7):2660–2665, 2011.

[64] Bochao Duan, Weikun Wang, Anbang Wang, Keguo Yuan, Zhongbao Yu, Hailei Zhao, Jingyi Qiu, and Yusheng Yang. Carbyne polysulfide as a novel cathode material for lithium/sulfur batteries. *Journal of materials chemistry A*, 1(42):13261–13267, 2013.

[65] Miguel AL Marques, Julien Vidal, Micael JT Oliveira, Lucia Reining, and Silvana Botti. Density-based mixing parameter for hybrid functionals. *Physical Review B*, 83(3):035119, 2011.

[66] Arun K. Manna, Sivan Refaely-Abramson, Anthony M. Reilly, Alexandre Tkatchenko, Jeffrey B. Neaton, and Leeor Kronik. Quantitative prediction of optical absorption in molecular solids from an optimally tuned screened range-separated hybrid functional. *Journal of Chemical Theory and Computation*, 14:2919–2929, 2018.

[67] Leeor Kronik and Stephan Kümmel. Dielectric screening meets optimally tuned density functionals. *Advanced Materials*, 30:1706560, 2018.

[68] Andrea Ferretti, Giuseppe Mallia, Layla Martin-Samos, Giovanni Bussi, Alice Ruini, Barbara Montanari, and Nicholas M Harrison. Ab initio complex band structure of conjugated polymers: Effects of hydrid density functional theory and GW schemes. *Physical Review B*, 85(23):235105, 2012.

[69] Roberto Dovesi, Roberto Orlando, Alessandro Erba, Claudio M Zicovich-Wilson, Bartolomeo Civalleri, Silvia Casassa, Lorenzo Maschio, Matteo Ferrabone, Marco De La Pierre, Philippe d'Arco, et al. Crystal14: A program for the ab initio investigation of crystalline solids, 2014.

[70] Roberto Dovesi, Alessandro Erba, Roberto Orlando, Claudio M Zicovich-Wilson, Bartolomeo Civalleri, Lorenzo Maschio, Michel Rérat, Silvia Casassa, Jacopo Baima, Simone Salustro, et al. Quantum-mechanical condensed matter simulations with crystal. *Wiley Interdisciplinary Reviews: Computational Molecular Science*, 8:e1360, 2018.

[71] Lei Shi, Philip Rohringer, Marius Wanko, Angel Rubio, Sören Waßerroth, Stephanie Reich, Sofie Cambré, Wim Wenseleers, Paola Ayala, and Thomas Pichler. Electronic band gaps of confined linear carbon chains ranging from polyyne to carbyne. *Physical Review Materials*, 1(7):075601, 2017.

[72] Ekaterina Anikina, Amitava Banerjee, Valery Beskachko, and Rajeev Ahuja. Li-decorated carbyne for hydrogen storage: charge induced polarization and van't hoff hydrogen desorption temperature. *Sustainable Energy & Fuels*, 4(2):691–699, 2020.

[73] Lorenzo Monacelli, Raffaello Bianco, Marco Cherubini, Matteo Calandra, Ion Errea, and Francesco Mauri. The stochastic self-consistent harmonic approximation: calculating vibrational properties of materials with full quantum and anharmonic effects. *Journal of Physics: Condensed Matter*, 33(36):363001, 2021.

[74] AA Maradudin and AE Fein. Scattering of neutrons by an anharmonic crystal. *Physical Review*, 128(6):2589, 1962.

[75] Roger A Cowley. Anharmonic crystals. *Reports on Progress in Physics*, 31(1):123, 1968.

[76] Matteo Calandra, Michele Lazzeri, and Francesco Mauri. Anharmonic and non-adiabatic effects in mgb2: Implications for the isotope effect and interpretation of raman spectra. *Physica C: Superconductivity*, 456(1-2):38–44, 2007.

[77] Ion Errea. Approaching the strongly anharmonic limit with ab initio calculations of materials' vibrational properties–a colloquium. *The European Physical Journal B*, 89:1–13, 2016.

[78] Ion Errea, Matteo Calandra, Chris J Pickard, Joseph R Nelson, Richard J Needs, Yinwei Li, Hanyu Liu, Yunwei Zhang, Yanming Ma, and Francesco Mauri. Quantum hydrogen-bond symmetrization in the superconducting hydrogen sulfide system. *Nature*, 532(7597):81–84, 2016.

[79] Ion Errea, Francesco Belli, Lorenzo Monacelli, Antonio Sanna, Takashi Koretsune, Terumasa Tadano, Raffaello Bianco, Matteo Calandra, Ryotaro Arita, Francesco Mauri, et al. Quantum crystal structure in the 250-kelvin superconducting lanthanum hydride. *Nature*, 578(7793):66–69, 2020.

[80] CZ Wang, Che Ting Chan, and KM Ho. Tight-binding molecular-dynamics study of phonon anharmonic effects in silicon and diamond. *Physical Review B*, 42(17):11276, 1990.

[81] Olle Hellman, Igor A Abrikosov, and Sergei I Simak. Lattice dynamics of anharmonic solids from first principles. *Physical Review B*, 84(18):180301, 2011.

[82] Olle Hellman, Peter Steneteg, Igor A Abrikosov, and Sergei I Simak. Temperature dependent effective potential method for accurate free energy calculations of solids. *Physical Review B*, 87(10):104111, 2013.

[83] David M Ceperley. Path integrals in the theory of condensed helium. *Reviews of Modern Physics*, 67(2):279, 1995.

[84] Joel M Bowman. Self-consistent field energies and wavefunctions for coupled oscillators. *The Journal of Chemical Physics*, 68(2):608–610, 1978.

[85] Bartomeu Monserrat, ND Drummond, and RJ Needs. Anharmonic vibrational properties in periodic systems: energy, electron-phonon coupling, and stress. *Physical Review B*, 87(14):144302, 2013.

[86] DJ Hooton. Li. a new treatment of anharmonicity in lattice thermodynamics: I. *The London, Edinburgh, and Dublin Philosophical Magazine and Journal of Science*, 46(375):422–432, 1955.

[87] Thomas R Koehler. Theory of the self-consistent harmonic approximation with application to solid neon. *Physical Review Letters*, 17(2):89, 1966.

[88] Lev Davidovich Landau. Zur theorie der phasenumwandlungen ii. *Phys. Z. Sowjetunion*, 11(545):26–35, 1937.

[89] Lev Davidovich Landau and Evgeniĭ Mikhaĭlovich Lifshitz. *Course of theoretical physics*. Elsevier, 2013.

[90] Xiaoxiang Xi, Liang Zhao, Zefang Wang, Helmuth Berger, László Forró, Jie Shan, and Kin Fai Mak. Strongly enhanced charge-density-wave order in monolayer nbse2. *Nature nanotechnology*, 10(9):765–769, 2015.

[91] Shang Gao, Felix Flicker, Raman Sankar, He Zhao, Zheng Ren, Bryan Rachmilowitz, Sidhika Balachandar, Fangcheng Chou, Kenneth S Burch, Ziqiang Wang, et al. Atomic-scale strain manipulation of a charge density wave. *Proceedings of the National Academy of Sciences*, 115(27):6986–6990, 2018.

[92] G Lucovsky and RM White. Effects of resonance bonding on the properties of crystalline and amorphous semiconductors. *Physical Review B*, 8(2):660, 1973.

[93] N. Kirova and S. Brazovskii. Electronic ferroelectricity in carbon based materials. *Synthetic Metals*, 216:11–22, 2016.

[94] J Meister and WHE Schwarz. Principal components of ionicity. *The Journal of Physical Chemistry*, 98(33):8245–8252, 1994.

[95] W Cochran. 'effective'ionic charge in crystals. *Nature*, 191(4783):60–61, 1961.

[96] Ph. Ghosez, J.-P. Michenaud, and X. Gonze. Dynamical atomic charges: The case of $ABo_3$ compounds. *Phys. Rev. B*, 58:6224–6240, Sep 1998.

[97] BG Dick Jr and AW Overhauser. Theory of the dielectric constants of alkali halide crystals. *Physical Review*, 112(1):90, 1958.

[98] M Posternak, R Resta, and A Baldereschi. Role of covalent bonding in the polarization of perovskite oxides: the case of knbo 3. *Physical Review B*, 50(12):8911, 1994.

[99] A Smekal, Max Born, and Maria Göppert-Mayer. *Dynamische Gittertheorie der Kristalle*. Springer, 1933.

[100] Peter Brüesch. *Phonons: Theory and Experiments II: Experiments and Interpretation of Experimental Results*, volume 65. Springer Science & Business Media, 2012.

[101] R Resta, M Posternak, and A Baldereschi. Towards a quantum theory of polarization in ferroelectrics: The case of knbo 3. *Physical review letters*, 70(7):1010, 1993.

[102] S Tadigadapa and K Mateti. Piezoelectric mems sensors: state-of-the-art and perspectives. *Measurement Science and technology*, 20:092001, 2009.

[103] Joe Briscoe and Steve Dunn. Piezoelectric nanogenerators–a review of nanostructured piezoelectric energy harvesters. *Nano Energy*, 14:15–29, 2015.

[104] Don Berlincourt. Piezoelectric crystals and ceramics. In *Ultrasonic transducer materials*, pages 63–124. Springer, 1971.

[105] Hans Jaffe. Piezoelectric ceramics. *Journal of the American Ceramic Society*, 41:494–498, 1958.

[106] J. Rödel, W. Jo, K. T. P. Seifert, E.-M. Anton, T. Granzow, and D. Damjanovic. Perspective on the development of lead-free piezoceramics. *Journal of the American Ceramic Society*, 92:1153–1177, 2009.

[107] Y. Saito, H. Takao, T. Tani, and et al. Lead-free piezoceramics. *Nature*, 432:84–87, 2009.

[108] N Setter, D Damjanovic, L Eng, G Fox, Spartak Gevorgian, S Hong, A Kingon, H Kohlstedt, NY Park, GB Stephenson, et al. Ferroelectric thin films: Review of materials, properties, and applications. *Journal of applied physics*, 100:051606, 2006.

[109] Andrew J Lovinger. Ferroelectric polymers. *Science*, 220:1115–1121, 1983.

[110] Khaled S Ramadan, Dan Sameoto, and Sthephane Evoy. A review of piezoelectric polymers as functional materials for electromechanical transducers. *Smart Materials and Structures*, 23:033001, 2014.

[111] Thangavel Vijayakanth, David J. Liptrot, Ehud Gazit, Ramamoorthy Boomishankar, and Chris R. Bowen. Recent advances in organic and organic–inorganic hybrid materials for piezoelectric mechanical energy harvesting. *Advanced Functional Materials*, 32:2109492, 2022.

[112] P. Saxena and P. Shukla. A comprehensive review on fundamental properties and applications of poly(vinylidene fluoride) (PVDF). *Adv Compos Hybrid Mater*, 4:8–26, 2020.

[113] H. Fu and R. Cohen. Polarization rotation mechanism for ultrahigh electromechanical response in single-crystal piezoelectrics. *Nature*, 403:281, 2000.

[114] Z. Kutnjak, J. Petzelt, and R. Blinc. The giant electromechanical response in ferroelectric relaxors as a critical phenomenon. *Nature*, 441:956, 2006.

[115] Muhtar Ahart, Maddury Somayazulu, RE Cohen, P Ganesh, Przemyslaw Dera, Ho-kwang Mao, Russell J Hemley, Yang Ren, Peter Liermann, and Zhigang Wu. Origin of morphotropic phase boundaries in ferroelectrics. *Nature*, 451:545–548, 2008.

[116] Dragan Damjanovic. A morphotropic phase boundary system based on polarization rotation and polarization extension. *Applied Physics Letters*, 97:062906, 2010.

[117] Y. Liu, H. Aziguli, B. Zhang, W. Xu, W. Lu, J. Bernholc, and Wang Q. Ferroelectric polymers exhibiting behaviour reminiscent of a morphotropic phase boundary. *Nature*, 562:96, 2018.

[118] Jiseul Park, Yeong-won Lim, Sam Yeon Cho, Myunghwan Byun, Kwi-Il Park, Han Eol Lee, Sang Don Bu, Ki-Tae Lee, Qing Wang, and Chang Kyu Jeong. Ferroelectric polymer nanofibers reminiscent of morphotropic phase boundary behavior for improved piezoelectric energy harvesting. *Small*, 18:2104472, 2022.

[119] William Barford. *Electronic and optical properties of conjugated polymers*. Oxford University Press, 2013.

[120] Hugo Bronstein, Christian B Nielsen, Bob C Schroeder, and Iain McCulloch. The role of chemical design in the performance of organic semiconductors. *Nature Reviews Chemistry*, pages 1–12, 2020.

[121] David Vanderbilt. Berry-phase theory of proper piezoelectric response. *Journal of Physics and Chemistry of Solids*, 61:147–151, 2000.

[122] Oliviero Bistoni, Paolo Barone, Emmanuele Cappelluti, Lara Benfatto, and Francesco Mauri. Giant effective charges and piezoelectricity in gapped graphene. *2D Materials*, 6:045015, 2019.

[123] H. Rostami, F. Guinea, M. Polini, and R. Roldán. Piezoelectricity and valley chern number in inhomogeneous hexagonal 2d crystals. *npj 2D Mater. Appl.*, 2:15, 2018.

[124] Zhenglu Li, Gabriel Antonius, Meng Wu, Felipe H. da Jornada, and Steven G. Louie. Electron-phonon coupling from ab initio linear-response theory within the *GW* method: Correlation-enhanced interactions and superconductivity in $Ba_{1-x}K_xBiO_3$. *Phys. Rev. Lett.*, 122:186402, May 2019.

[125] D. M. Basko and I. L. Aleiner. Interplay of Coulomb and electron-phonon interactions in graphene. *Phys. Rev. B*, 77:041409, Jan 2008.

[126] Michele Lazzeri, Claudio Attaccalite, Ludger Wirtz, and Francesco Mauri. Impact of the electron-electron correlation on phonon dispersion: Failure of LDA and GGA DFT functionals in graphene and graphite. *Phys. Rev. B*, 78:081406, Aug 2008.

[127] Tommaso Venanzi, Lorenzo Graziotto, Francesco Macheda, Simone Sotgiu, Taoufiq Ouaj, Elena Stellino, Claudia Fasolato, Paolo Postorino, Vaidotas Mišeikis, Marvin Metzelaars, Paul Kögerler, Bernd Beschoten, Camilla Coletti, Stefano Roddaro, Matteo Calandra, Michele Ortolani, Christoph Stampfer, Francesco Mauri, and Leonetta Baldassarre. Probing enhanced electron-phonon coupling in graphene by infrared resonance raman spectroscopy. *Phys. Rev. Lett.*, 130:256901, Jun 2023.

[128] Betül Pamuk, Jacopo Baima, Roberto Dovesi, Matteo Calandra, and Francesco Mauri. Spin susceptibility and electron-phonon coupling of two-dimensional materials by range-separated hybrid density functionals: Case study of $Li_xZrNCl$. *Phys. Rev. B*, 94:035101, Jul 2016.

[129] Jonathan Laflamme Janssen, Michel Côté, Steven G. Louie, and Marvin L. Cohen. Electron-phonon coupling in $C_{60}$ using hybrid functionals. *Phys. Rev. B*, 81:073106, Feb 2010.

[130] Denis Jacquemin, Eric. A. Perpète, Ilaria Ciofini, and Carlo Adamo. Assessment of recently developed density functional approaches for the evaluation of the bond length alternation in polyacetylene. *Chemical Physics Letters*, 405(4):376–381, 2005.

[131] Matteo Barborini, Matteo Calandra, Francesco Mauri, Ludger Wirtz, and Pierluigi Cudazzo. Excitonic-insulator instability and peierls distortion in one-dimensional semimetals. *Phys. Rev. B*, 105:075122, Feb 2022.

[132] Claudio Attaccalite, Ludger Wirtz, Michele Lazzeri, Francesco Mauri, and Angel Rubio. Doped graphene as tunable electron-phonon coupling material. *Nano Letters*, 10(4):1172–1176, 2010.

[133] Nicholas P. Brawand, Márton Vörös, Marco Govoni, and Giulia Galli. Generalization of dielectric-dependent hybrid functionals to finite systems. *Phys. Rev. X*, 6:041002, Oct 2016.

[134] Sivan Refaely-Abramson, Sahar Sharifzadeh, Manish Jain, Roi Baer, Jeffrey B. Neaton, and Leeor Kronik. Gap renormalization of molecular crystals from density-functional theory. *Phys. Rev. B*, 88:081204, Aug 2013.

[135] Daniel Lüftner, Sivan Refaely-Abramson, Michael Pachler, Roland Resel, Michael G. Ramsey, Leeor Kronik, and Peter Puschnig. Experimental and theoretical electronic structure of quinacridone. *Phys. Rev. B*, 90:075204, Aug 2014.

[136] Serge M Nakhmanson, M Buongiorno Nardelli, and Jerry Bernholc. Ab initio studies of polarization and piezoelectricity in vinylidene fluoride and bn-based polymers. *Physical review letters*, 92:115504, 2004.

[137] Nicholas J. Ramer and Kimberly A. Stiso. Structure and born effective charge determination for planar-zigzag $\beta$-poly(vinylidene fluoride) using density-functional theory. *Polymer*, 46:10431–10436, 2005.

[138] Anton Kokalj. Xcrysden—a new program for displaying crystalline structures and electron densities. *Journal of Molecular Graphics and Modelling*, 17(3-4):176–179, 1999.

[139] Manuel Cardona and Roberto Merlin. *Light scattering in solids IX*. Springer, 2007.

[140] R Loudon. Theory of the resonance raman effect in crystals. *Journal de Physique*, 26(11):677–683, 1965.

[141] Richard M Martin. Theory of the one-phonon resonance raman effect. *Physical Review B*, 4(10):3676, 1971.

[142] Thomas C Strekas and Thomas G Spiro. Hemoglobin: resonance raman spectra. *Biochimica et Biophysica Acta (BBA)-Protein Structure*, 263(3):830–833, 1972.

[143] Frank S Parker. *Applications of infrared, Raman, and resonance Raman spectroscopy in biochemistry*. Springer Science & Business Media, 1983.

[144] P Carey. *Biochemical applications of Raman and resonance Raman spectroscopes*. Elsevier, 2012.

[145] Leandro M Malard, Marcos Assunção Pimenta, Gene Dresselhaus, and Mildred Spiewak Dresselhaus. Raman spectroscopy in graphene. *Physics reports*, 473(5-6):51–87, 2009.

[146] R Saito, M Hofmann, G Dresselhaus, A Jorio, and MS Dresselhaus. Raman spectroscopy of graphene and carbon nanotubes. *Advances in Physics*, 60(3):413–550, 2011.

[147] V Zólyomi, J Koltai, and J Kürti. Resonance raman spectroscopy of graphite and graphene. *physica status solidi (b)*, 248(11):2435–2444, 2011.

[148] Y Yacoby and E Ehrenfreund. Resonant raman scattering in conjugated polymers. *Light Scattering in Solids VI: Recent Results, Including High-T c Superconductivity*, pages 73–135, 2005.

[149] H Kuzmany. Resonance raman spectroscopy of conjugated polymers what can we learn? In *Makromolekulare Chemie. Macromolecular Symposia*, volume 37, pages 81–97. Wiley Online Library, 1990.

[150] J Kastner, T Pichler, H Kuzmany, S Curran, W Blau, DN Weldon, M Delamesiere, S Draper, and H Zandbergen. Resonance raman and infrared spectroscopy of carbon nanotubes. *Chemical physics letters*, 221(1-2):53–58, 1994.

[151] PT Araujo, PBC Pesce, MS Dresselhaus, K Sato, Riichiro Saito, and A Jorio. Resonance raman spectroscopy of the radial breathing modes in carbon nanotubes. *Physica E: Low-dimensional Systems and Nanostructures*, 42(5):1251–1261, 2010.

[152] Erik H Hároz, Juan G Duque, Eduardo B Barros, Hagen Telg, Jeffrey R Simpson, Angela R Hight Walker, Constantine Y Khripin, Jeffrey A Fagan, Xiaomin Tu, Ming Zheng, et al. Asymmetric excitation profiles in the resonance raman response of armchair carbon nanotubes. *Physical Review B*, 91(20):205446, 2015.

[153] Pietro Marabotti, Matteo Tommasini, Chiara Castiglioni, Patrick Serafini, Sonia Peggiani, Mariagrazia Tortora, Barbara Rossi, A Li Bassi, Valeria Russo, and CS Casari. Electron-phonon coupling and vibrational properties of size-selected linear carbon chains by resonance raman scattering. *Nature Communications*, 13(1):5052, 2022.

[154] Alberto Milani, Matteo Tommasini, Daniele Fazzi, Chiara Castiglioni, Mirella Del Zoppo, and Giuseppe Zerbi. First-principles calculation of the peierls distortion in an infinite linear carbon chain: the contribution of raman spectroscopy. *Journal of Raman Spectroscopy: An International Journal for Original Work in all Aspects of Raman Spectroscopy, Including Higher Order Processes, and also Brillouin and Rayleigh Scattering*, 39(2):164–168, 2008.

[155] Alberto Milani, Matteo Tommasini, Valeria Russo, Andrea Li Bassi, Andrea Lucotti, Franco Cataldo, and Carlo S Casari. Raman spectroscopy as a tool

to investigate the structure and electronic properties of carbon-atom wires. *Beilstein journal of nanotechnology*, 6(1):480–491, 2015.

[156] Jun John Sakurai. *Advanced quantum mechanics*. Pearson Education India, 1967.

[157] Sven Reichardt and Ludger Wirtz. Theory of resonant raman scattering: Towards a comprehensive ab initio description. *Physical Review B*, 99(17):174312, 2019.

[158] Michele Lazzeri and Francesco Mauri. First-principles calculation of vibrational raman spectra in large systems: Signature of small rings in crystalline sio 2. *Physical Review Letters*, 90(3):036401, 2003.

[159] Stefano Baroni and Raffaele Resta. Ab initio calculation of the low-frequency raman cross section in silicon. *Physical Review B*, 33(8):5969, 1986.

[160] George Placzek. *The rayleigh and raman scattering*, volume 526. Lawrence Radiation Laboratory, 1959.

[161] Juan G Duque, Hang Chen, Anna K Swan, Andrew P Shreve, Svetlana Kilina, Sergei Tretiak, Xiaomin Tu, Ming Zheng, and Stephen K Doorn. Violation of the condon approximation in semiconducting carbon nanotubes. *ACS nano*, 5(6):5233–5241, 2011.

[162] Stefano Baroni, Paolo Giannozzi, and Andrea Testa. Green's-function approach to linear response in solids. *Physical review letters*, 58(18):1861, 1987.

[163] Francesco Mauri, Bernd G Pfrommer, and Steven G Louie. Ab initio theory of nmr chemical shifts in solids and liquids. *Physical review letters*, 77(26):5300, 1996.

[164] Xavier Gonze and Changyol Lee. Dynamical matrices, born effective charges, dielectric permittivity tensors, and interatomic force constants from density-functional perturbation theory. *Physical Review B*, 55(16):10355, 1997.

[165] Stefano Baroni, Stefano De Gironcoli, Andrea Dal Corso, and Paolo Giannozzi. Phonons and related crystal properties from density-functional perturbation theory. *Reviews of modern Physics*, 73(2):515, 2001.

[166] Xavier Gonze. Adiabatic density-functional perturbation theory. *Physical Review A*, 52(2):1096, 1995.

[167] Michele Lazzeri and Francesco Mauri. High-order density-matrix perturbation theory. *Physical Review B*, 68(16):161101, 2003.

[168] Jacques Des Cloizeaux. Energy bands and projection operators in a crystal: Analytic and asymptotic properties. *Physical Review*, 135(3A):A685, 1964.

[169] Paolo Giannozzi, Stefano Baroni, Nicola Bonini, Matteo Calandra, Roberto Car, Carlo Cavazzoni, Davide Ceresoli, Guido L Chiarotti, Matteo Cococcioni, Ismaila Dabo, et al. Quantum espresso: a modular and open-source software project for quantum simulations of materials. *Journal of physics: Condensed matter*, 21(39):395502, 2009.

[170] Andrea Dal Corso and Francesco Mauri. Wannier and bloch orbital computation of the nonlinear susceptibility. *Physical Review B*, 50(8):5756, 1994.

[171] Richard M Martin. Piezoelectricity. *Physical Review B*, 5:1607, 1972.

[172] DF Nelson and M Lax. New pyroelectric contributions to piezoelectricity. *Physical Review Letters*, 31:763, 1973.

[173] DF Nelson and M Lax. Linear elasticity and piezoelectricity in pyroelectrics. *Physical Review B*, 13:1785, 1976.

[174] Raffaele Resta. Manifestations of berry's phase in molecules and condensed matter. *Journal of Physics: Condensed Matter*, 12(9):R107, 2000.

[175] Xifan Wu, David Vanderbilt, and DR Hamann. Systematic treatment of displacements, strains, and electric fields in density-functional perturbation theory. *Physical Review B*, 72:035105, 2005.

[176] Gotthard Sághi-Szabó, Ronald E Cohen, and Henry Krakauer. First-principles study of piezoelectricity in pbtio 3. *Physical review letters*, 80:4321, 1998.

[177] Daniel Vilela Oliveira, Joachim Laun, Michael F Peintinger, and Thomas Bredow. Bsse-correction scheme for consistent gaussian basis sets of double- and triple-zeta valence with polarization quality for solid-state calculations. *Journal of Computational Chemistry*, 40:2364–2376, 2019.

[178] Elon Weintraub, Thomas M Henderson, and Gustavo E Scuseria. Long-range-corrected hybrids based on a new model exchange hole. *Journal of Chemical Theory and Computation*, 5:754–762, 2009.

[179] Claudio Marcelo Zicovich-Wilson, Fabien Pascale, Carla Roetti, VR Saunders, Roberto Orlando, and Roberto Dovesi. Calculation of the vibration frequencies of $\alpha$-quartz: The effect of hamiltonian and basis set. *Journal of computational chemistry*, 25(15):1873–1881, 2004.

[180] Fabien Pascale, Claudio Marcelo Zicovich-Wilson, F López Gejo, Bartolomeo Civalleri, Roberto Orlando, and Roberto Dovesi. The calculation of the vibrational frequencies of crystalline compounds and its implementation in the CRYSTAL code. *Journal of computational chemistry*, 25:888–897, 2004.

[181] A Erba, Kh E El-Kelany, M Ferrero, Isabelle Baraille, and Michel Rérat. Piezoelectricity of srtio 3: An ab initio description. *Physical Review B*, 88:035102, 2013.

[182] Alessandro Erba. The internal-strain tensor of crystals for nuclear-relaxed elastic and piezoelectric constants: on the full exploitation of its symmetry features. *Physical Chemistry Chemical Physics*, 18:13984–13992, 2016.